Impact of surface modification on the structure and dynamics of silica-polymer nanocomposites

Dafne Musino

THÈSE POUR OBTENIR LE GRADE DE DOCTEUR DE L'UNIVERSITÉ DE MONTPELLIER

En **Physique**

École doctorale **Information, Structure et Systèmes (I2S)**

Unité de recherche **UMR 5221/Laboratoire Charles Coulomb**

Impact of surface modification on the structure and dynamics of silica-polymer nanocomposites

Présentée par **Dafne MUSINO**

Le 24/11/2017

Sous la direction de Julian OBERDISSE
et Anne-Caroline GENIX

Devant le jury composé de

M. Paul SOTTA, Directeur de recherche, CNRS – LPMA Lyon	**Rapporteur**
Mme Silvina CERVENY, Chercheuse, CSIC – MPC San Sebastian	**Rapporteur**
M. Thomas HELLWEG, Professeur, Université de Bielefeld	**Examinateur**
M. Hubert MUTIN, Directeur de recherche, ICGM Montpellier	**Examinateur**
M. Julian OBERDISSE, Directeur de recherche, CNRS – L2C Montpellier	**Directeur de thèse**
Mme Anne-Caroline GENIX, Maitre de Conférences, L2C Montpellier	**Co-Directreur de thèse**
M. Thomas CHAUSSEE, R&D Manager, Solvay Silica	**Invité**

UNIVERSITÉ DE MONTPELLIER

Outline

General introduction

In 1839, Charles Goodyear discovered that mixing rubber with sulfur at high temperature allowed him to produce a material with higher elasticity. It was this finding that took him to develop the *vulcanization process* without which we would probably not have tires. In 1888, John Boyd Dunlop developed an air-inflated (pneumatic) tire using rubber as main component. He had invented the first commercial rubber tire. Few years later, André and Edouard Michelin adapted the pneumatic tire to cars.

From that moment on, the tire industry never stopped to look for new ideas to obtain rubber materials with enhanced properties, trying to satisfy more and more elevated standards. In this scenario, the development of synthetic rubbers and polymers, such as styrene-butadiene, represented one of the main evolutions in tire manufacturing. But the most important innovation is probably represented by the introduction of nanocomposite materials formulated adding fillers to a polymeric matrix. Since the early 1900s, carbon black at the individual particle scale has been added to rubber in order to increase its stability. More recently (1992), silica has been introduced as filler in tire manufacturing. Compared to carbon black, silica allows to reduce the rolling resistance and thus the vehicle fuel consumption and CO_2 production, which represents one of the main global worries of our times. At the same time, the improvement of some properties should not correspond to the impoverishment of other properties such as the wet grip. The replacement of the carbon black by silica remains one of the most challenging problems to solve, since the hydrophilic behavior of the silica reduces its compatibility with hydrophobic rubber or polymer compounds. Thus, the optimization of the filler-polymer interactions by modifying the nanoparticle surfaces represents one of the most promising solutions to enhance tire properties.

In this PhD-work, we present a study concerning non-crosslinked silica-polymer nanocomposites where the compatibility between fillers and polymer is tuned by the introduction of small molecules, such as silane coating agents. These molecules are able to modify the surface properties of silica particle making them more hydrophobic and improving their interaction with a hydrophobic polymer. This approach allows to better control the filler dispersion into the polymer matrix, which affects the structural, dynamical and mechanical properties of the final material.

A more detailed outline of this PhD dissertation is presented here:

Chapter 1: *State of the art*

In this section, some basics of polymer physics, characteristics of silica fillers and their surface-modification a introduced. Then, a literature overview on silica-polymer nanocomposite materials is presented, focusing on their preparation and showing how they can be characterized from a structural, dynamical and mechanical point of view.

Chapter 2: *Materials and experimental methods*

The main characteristics of the polymer (i.e., styrene-butadiene polymer) and the silane coating agents used in this work are presented. In particular, we focus on the formulation of the two nanocomposite systems: i) simplified industrial nanocomposites, obtained by solid mixing of styrene-butadiene, millimetric silica pellets, silanes and a catalyzer; ii) model nanocomposites, made by solvent casting technique using colloidal silica nanoparticles (NPs). In this second system, developed to be "equivalent" to the industrial one, the fillers are surface-modified by a brand new grafting reaction using different silane molecules. Finally, the main techniques used in this PhD work are presented: i) Small Angle X-ray Scattering (SAXS) coupled with Reverse Monte Carlo (RMC) simulation, for the structural analysis; ii) Broadband Dielectric Spectroscopy (BDS), for the dynamical characterization.

Chapter 3: *Synergistic effect of small molecules on large-scale structure of simplified industrial nanocomposites*

The structural characterization of simplified industrial nanocomposites is proposed. We shed light on the effect of the coating agents with different alkyl chain length (C_8, C_{12}, and C_{18}) on filler structure in terms of aggregate formation. The impact of different silane concentrations (up to 8%wt with respect to silica), and the influence of a commonly added catalyzer (DPG) have been investigated, revealing the existence of a strongly synergetic effect of both DPG and silane coating agents. Most of the results presented in this chapter have been recently published (Musino et al. 2017).

Chapter 4: *Impact of the surface modification of silica nanoparticles on dispersion in precursor solvents and model polymer nanocomposites*

This chapter mainly focuses on the model nanocomposite system. A description of the structural organization of colloidal silica NPs surface-modified by different silane molecules will be proposed. According to the preparation protocol, the main aim is to propose a quantitative analysis of the aggregation state of surface-modified silica NPs in precursor solvents and a polymer matrix, by a combined SAXS-reverse Monte Carlo approach. One of the key characteristics of such an approach is the possibility to extract aggregate mass in presence or absence of interactions between aggregates, by analyzing real space particle configurations obtained by RMC simulations. We show that the filler dispersion is influenced by the characteristics of the silane molecules and that the quality of the dispersion state is maintained from the precursor suspension to the final nanocomposite.

Chapter 5: *Silane coating agents as plasticizers in model silica-polymer nanocomposites*

In this chapter, Broadband Dielectric Spectroscopy (BDS) is used to investigate the role of silane coating agents in the segmental dynamics of model nanocomposite systems. We show that the silane molecules can act as *plasticizers* in pure styrene-butadiene matrices, inducing a significant decrease of the glass transition temperature T_g. Then, we prove that the chemical surface-modification of the fillers in

nanocomposites does not affect the segmental dynamics, while the presence of "free" silane molecules in the polymer bulk of the nanocomposite can induce a detectable plasticization effect.

At the end of the manuscript, appendices are proposed. Some of them (Appendices A1, A2, A3, A4, A6) report complementary information which can be useful to the support the comprehension of the main chapters. Others (Appendices A5, A7) are related to results still under quantitative analysis.

1. State of the art

1. State of the art

In recent years, materials with enhanced mechanical properties have attracted both fundamental and industrial interest. The present study concerns nanocomposites made by dispersion of nanometric fillers (i.e. silica nanoparticles) in a soft polymer matrix, focusing on the link between structural and dynamical properties which are strongly influenced by the characteristics of the polymer matrix, the fillers and the interactions between them.

In this chapter, a short overview on the polymer physics, the properties of the fillers, their surface-modification, and the characterization methods of the final polymer nanocomposites (PNCs or more synthetically NCs) will be presented.

1.1. Polymer physics

1.1.1. Basics on polymer physics

A polymer is a large molecule (i.e., macromolecule) made up of many small, simple chemical units called the "monomers". The number of these units in the sequence defines the "degree of polymerization", indicated as N. A molecule is usually defined as a polymer if the degree of polymerization exceeds 100 (Doi and Edwards 1988). The polymerization process allows to link monomers into a chain (i.e., polymer chain) and it usually occurs in presence of a catalyst. In chemistry, different polymerization processes are used, like for instance: i) the *addition polymerization*, where monomers link together without losing any atoms. This method is widely used to create synthetic polymers such as polyethenes, polypropylene, polyacrylates and polystyrene; ii) the *condensation polymerization*, which occurs when monomers join together but losing some atoms as reaction product (i.e., monomers with two functional groups or a distinct group of atoms within a molecule). Polyester can be produced by this method.

Polymers can be classified as a function of their composition. When the polymer chains contain monomers of only one type are called *homopolymers* even if they can differ by their microstructure, degree of polymerization or architecture. The combination of different types of monomers into a chain leads to the formation of a new macromolecule defined as *heteropolymer*. Macromolecules which contain at least two different monomers are called *copolymers*, which can be defined as alternating, statistical, random block or graft, depending on the sequence in which their monomers are bond together (Rubinstein and Colby 2003), as shown in Fig. 1.1.

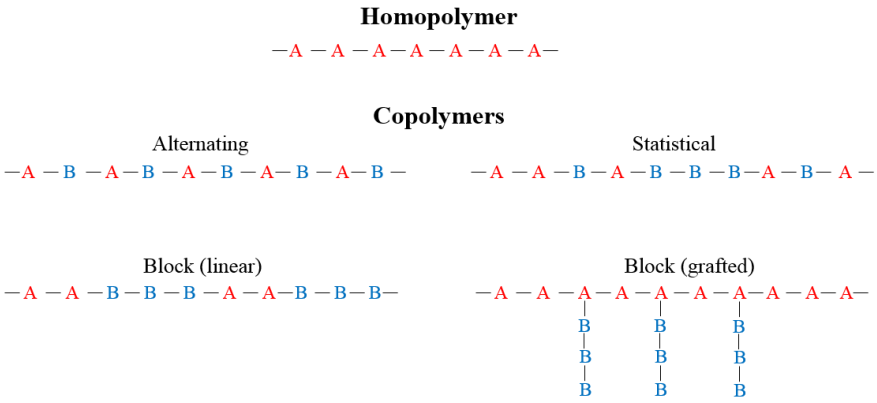

Figure 1.1 Schematic structure of different kinds of polymer chains.

Many natural polymers, such as proteins, are composed of macromolecules with the same degree of polymerization, N. In this case, the polymer can be considered as "monodisperse". Most of synthetic polymers are made up of individual macromolecules with a distribution of degrees of polymerization and they are thus characterized by a certain *polydispersity* which can be described by:

i) The number-average molar mass M_n, which corresponds to the first moment of the size distribution of polymer chains defined as

$$M_n \equiv \sum_N n_N M_N \qquad [1.1]$$

where n_N is the number of molecules with degree of polymerization N and M_N is their molar mass.

ii) The weight-average molar mass M_w, which corresponds to the second moment of the size distribution of polymer chains defined as

$$M_w \equiv \frac{\sum_N n_N {M_N}^2}{M_n} \qquad [1.2]$$

The polydispersity index I_p can be expressed as the ratio of the weight-average and number-average molar masses, as shown in formula [1.3]

$$I_p = \frac{M_w}{M_n} \qquad [1.3]$$

In a monodisperse sample, M_w results equal to M_n and the polydispersity of the system is equal to 1. Higher polydispersity values indicate systems with broader molar mass distribution. The entire molar mass distribution (characterized by M_w and M_n) can be experimentally evaluated by size-exclusion chromatography (SEC, also called gel permeation chromatography, GPC).

Due to its several internal degrees of freedom, a polymer molecule can be represented as a very long strings. When there are no net interactions between atoms separated by a sufficient number of bonds along the chain, the polymer is considered in its ideal state (i.e., ideal chain model) and its configuration will be the same as a random walk. This ideal model only considers the short range interactions between segments close to each other along the polymer chain, assuming that a chain could loop back onto itself.

In the real case, this is not physically possible since each segment has its own finite volume. This condition is called "excluded volume effect" which implies that if the polymer is modeled as a connected path on a lattice, this path cannot pass through any sites that have been previously traversed (i.e., excluded volume chain).

The size of linear chain can be characterized by its mean-square end-to-end distance, represented by a vector which joins one end of the polymer chain to the other (i.e., "end-to-end vector", **R**). As shown in Fig. 1.2, its average length is indicative of the size of the polymer and it can be defined as sum of N bond vectors $\mathbf{r}_n$ in the chain

$$\mathbf{R} = \sum_{n=1}^{N} \mathbf{r}_n \qquad [1.4]$$

For polymers characterized by too many ends or no ends at all (e.g., branched or ring polymers), this quantity is not well defined.

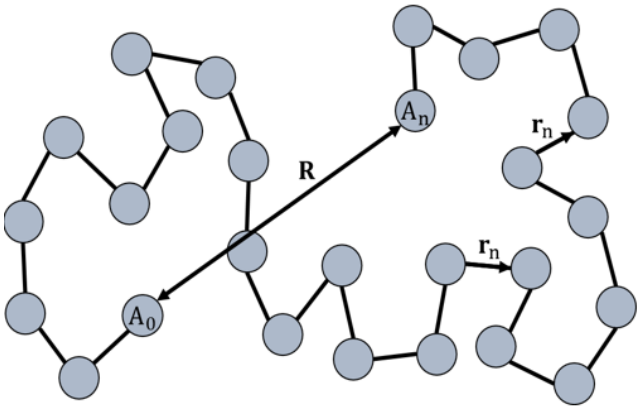

Figure 1.2 Conformation of flexible polymer, where **R** represents the end-to-end vector.

Every finite-size object has a radius of gyration R_g whose square value is defined as the average square distance between monomers in a given conformation ($\mathbf{R}_i$) and the center of mass of the polymer ($\mathbf{R}_{cm}$).

$$R_g{}^2 \equiv \frac{1}{N}\sum_{i=1}^{N}(\mathbf{R}_i - \mathbf{R}_{cm})^2 \qquad [1.5]$$

For an ideal linear chain, the mean-square radius of gyration and the mean-square end-to-end distance are related as

$$\langle R_g{}^2 \rangle = \frac{\langle R^2 \rangle}{6} \qquad [1.6]$$

The size of a real chain is much larger than the one of an ideal chain with the same number of monomers. The statistical properties of excluded volume chains have been extensively investigated in numerical simulation and for large N values, it has been found that the radius of gyration obeys to a power law

$$R_g \cong bN^{\nu} \qquad [1.7]$$

where the prefactor b takes into account the quality of the solvent with respect to the polymer and the scaling exponent ν has been calculated equal to 1/2 for an ideal chain and 3/5 for a swollen linear polymer (i.e., from experimental data, ν=0.59 for polymer in a good solvent).

1.1.2. Viscoelasticity and polymer dynamics

In linear, amorphous non-crosslinked polymers such as poly-methyl methacrylate (PMMA), poly-styrene (PS) or styrene/butadiene (SB), polymer chains can be connected by physical junctions named *entanglements* (Fig. 1.3) which develop from the interpenetration of random-coil chains, strongly affecting the mechanical, structural and dynamic properties of the polymer. (De Gennes 1979; Wool 1993).

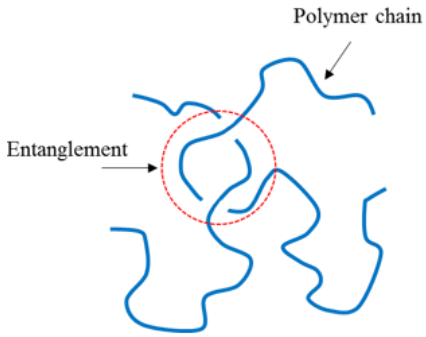

Figure 1.3 Schematic representation of an entanglement between polymer chains.

In the linear regime, these polymers show a viscoelastic behavior which is generally investigated by rheology, allowing the evaluation of the viscoelastic properties of a polymeric system, following the evolution of: i) the elastic modulus G' of the polymer, which represents the measure of its elasticity and of its ability to store energy; ii) the viscous modulus G" of the polymer, which is related to its ability to dissipate energy as heat.

The state of these polymers varies with the temperature. In Fig. 1.4, the change of the elastic modulus as a function of the temperature is schematically reported. Three main regimes can be identified: i) the glassy state; ii) the rubber state; iii) the liquid-flow state.

The glassy state is observed for temperatures below the glass transition temperature T_g, which defines the transition of the system from a viscous liquid to a glass and it is usually determined by Differential Scanning Calorimetry (DSC). In such conditions (i.e., $T<T_g$), the polymer acts like a glass since the chain mobility is completely blocked (Angell 1995; Bower 2002). This state is generally associated to the local vibrations of the methyl groups of the polymer chains and it is described by a relaxation process commonly named as β-relaxation, which can be detected by Broadband Dielectric Spectroscopy (BDS) (Capponi 2011).

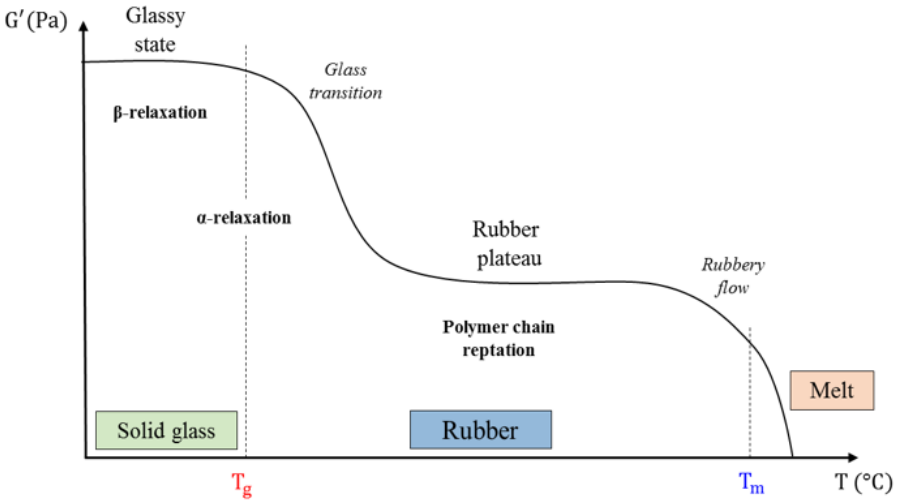

Figure 1.4 Schematic representation the evolution of the elastic modulus G' (Pa) of an amorphous polymer as a function of the temperature. The different states of the polymer at different temperatures are indicated.

The evolution as a function of the temperature of the characteristic relaxation time τ_β of this process (i.e. the time that the system needs to get back to the equilibrium state after a perturbation) can be described by the Arrhenius law

$$\tau_\beta = \tau_0 \exp\left(-\frac{E_a}{k_B T}\right) \qquad [1.8]$$

where τ_0 is a pre-exponential factor (e.g., 10^{12} - 10^{13} Hz for localized motional processes), E_A is the activation energy which depends on both the internal rotational barriers and the environment of a fluctuating unit (i.e., typical values for E_A are 20 to 50 kJmol^{-1}), k_B is the Boltzmann constant and T is the temperature.

When the temperature is close to the T_g, the system approaches the glass transition region where the elastic modulus G' dramatically decreases reaching a value around 1MPa. This change can be identified with the onset of structural relaxation, named segmental or α-relaxation, which can be well detected by both rheology and BDS. The evolution of the relaxation time of the α-process as a function of the temperature can be described by the William-Landel-Ferry law (Williams et al. 1955), which predicts the temperature dependence of mechanical and dielectric properties at temperatures between T_g and T_g+100°C, as shown in formula [1.9]

$$\log(a_T) = \frac{-C_1(T - T_{ref})}{(C_2 + T - T_{ref})} \qquad [1.9]$$

where C_1 and C_2 are two empirical constants characteristic for each polymer; a_T is generally defined as $\tau(T)/\ \tau(T_{ref})$ (Manke and Ferry 1968; Klüppel 2008) where $\tau(T)$ is the relaxation time at a genetic temperature and $\tau(T_{ref})$ is the relaxation time at the reference temperature. In rheological measurements, a_T is a temperature dependent horizontal shift factor used in the Time-Temperature Superposition (TTS)

to overlap measurements at different temperatures with the one at T_{ref}. This method is commonly used to construct a master curve which covers a bigger frequency/temperature range.
The evolution of the relaxation time of the α process can be also described by the Vogel-Fulcher-Tamman (VFT) equation (Vogel 1921),

$$\tau_\alpha = \tau_{\infty\alpha} \exp\left(\frac{DT_0}{T-T_0}\right) \quad [1.10]$$

where $\tau_{\infty\alpha}$ is the relaxation time in the high-temperature limit. T_0 is the so-called ideal glass transition or Vogel temperature which is found to be 30–70 K below the calorimetric glass transition temperature T_g. The coefficient D parametrizes the departure from the Arrhenius behavior and it is useful to distinguish between strong and fragile glasses, at high or low D, respectively (Angell 1991; Böhmer et al. 1993).

At T >T_g, the system enters in the rubber state. In this region, the elastic modulus is constant (rubber plateau). Here, the large scale motions of polymer chains are promoted and their mobility has been described by De Gennes as *reptation* (De Gennes 1979; Doi and Edwards 1988): the motion of a polymer chain in a tube of diameter *a* is defined by adjacent chains which represent physical obstacles for its motion, the abovementioned entanglements.
The value of the elastic modulus at the rubber plateau G'_0 can be estimated as

$$G'_0 = \frac{\rho RT}{M_e} \quad [1.11]$$

where ρ is the polymer density, R is the gas universal constant (8.314 $JK^{-1}mol^{-1}$), T in the temperature and M_e is the molecular weight between entanglements. According to the De Gennes model, the elastic modulus can be also defined as

$$G'_0 = \frac{k_B T}{\xi^3} \quad [1.12]$$

where ξ is the *mesh size* of the polymer (i.e., the mean distance between two adjacent entanglement points (Stöckelhuber et al. 2017). The extension of the rubber plateau is related to the time that a chain needs to reptate along the tube (reptation time).

Once temperature reaches the melting temperature T_m (i.e., the temperature at which a substance changes from solid to liquid state), the polymer chains have enough energy to easily reptate out through the entanglements and to finally flow reaching the liquid state. This reorganization of the system leads to a strong decrease of G', since only the Van der Waals interactions occur.
In cross-linked polymers, the final flow regime cannot take place because of the presence of chemical links between the polymer chains (see section 1.1.3).

1.1.3. Rubbers

In nature, rubber, or *natural rubber*, is essentially a hydrocarbon which is found in *hevea brasiliensis* latex in form of small polymer globules suspended in a watery liquid (Treloar 1975). Nowadays, the term rubber is also associated to any material having mechanical properties similar to the ones of natural rubber, regardless of its chemical constitution. From the chemical point of view, natural rubber hydrocarbon is composed of a regular repetition of isoprene monomer, C_5H_8, with every fourth carbon atom in chain carrying a methyl $–CH_3$ group. The structural formula of isoprene monomer and poly-isoprene polymer are represented in Fig.1.5.

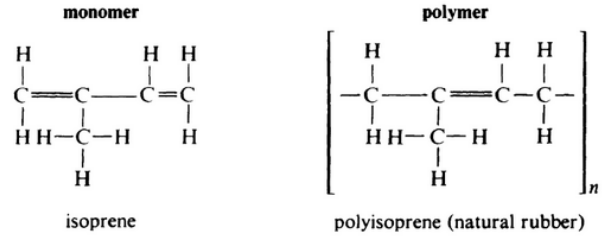

Figure 1.5 Relationship between the isoprene monomer (left) and poly-isoprene polymer (right) (Morton 2013).

Since the half of the XX century, a lot of interest has been shown for the production of synthetic polymers from a wide variety of monomers. One of the most used synthetic rubbers is styrene-butadiene rubber SBR (Morton 2013) which is used in the tire industry (Paul and Newman 1978; Mark et al. 2013). This is a linear statistic copolymer which is commonly synthetized by anionic polymerization. Its properties (e.g., the glass transition temperature) are influenced by the ratio between of styrene, 1-4 butadiene and 1-2 butadiene groups. The molecular formula of SBR copolymer is shown in Fig.1.6.

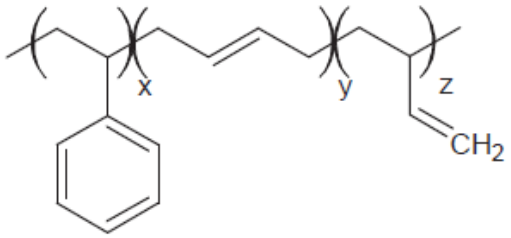

Figure 1.6 Molecular formula of SBR copolymer (Vieyres 2013).

Most of the rubbers used in tire manufacturing are *crosslinked* or *vulcanized*, since the un-vulcanized rubbers are generally not resistant and they do not come back to the original shape after a strong deformation. The crosslinking process allows to create chemical junctions between polymer chains by the insertion of crosslinks (i.e., bridges between chains), as shown in Fig. 1.7. Such a process induces the formation of a tridimensional network, enhancing the retractile force of the polymer and reducing the residual deformation after an applied stress (Mark et al. 2013) and thus forming an elastomer. In order to crosslink a polymer, some chemical agents (i.e., *crosslinkers*) have to be added to the system.

The nature of the crosslinkers can strongly influence the structure of the final network and the crosslink density. Sulfur and peroxide are some of the most common crosslinkers.

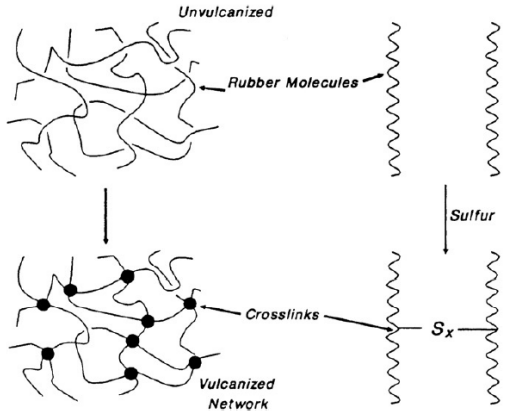

Figure 1.7 Scheme of crosslinking or vulcanization process between rubber chains (Mark et al. 2013).

1.2. Fillers

As already mentioned, the development of advanced materials, such as nanocomposites, depends on the use of fillers. Fillers, also named as *reinforcements*, can be defined as a solid phase which differs from the bulk where it is dispersed in composition and structure (Wypych 2016). They are usually added to polymers in order to enhance their mechanical, electrical or thermal properties and they can be classified according to: i) their mineral or chemical composition: mineral, glass, carbon black, organic or metal; ii) their properties, such as electrical and thermal conductivity or optical properties; iii) their preparation method (e.g., precipitated, fumed or hydrated fillers); iv) their size and shape (e.g., spherical particles, fibers, layers). Some most used fillers in industrial applications are silica (Katz and Mileski 1987), clays (Zhang et al. 2000), and carbon black (Donnet 1993).

1.2.1. Silica particles

Silica (SiO_2) is widely used as filler because of chemical inertness and durability. In addition to the natural products such as quartz, silica can also be synthetized. Here, we focus on:

1- Precipitated silica (used in simplified industrial nanocomposites, see Chapter 2.2)
2- Colloidal silica (used in model nanocomposites, see Chapter 2.3)

Precipitated silica is produced from sodium silicate through the reaction with sulfuric and hydrochloric acids, which usually takes place in a stirred reactor under alkaline pH conditions (Katz and Mileski 1987). This procedure allows to avoid the gelation and to enucleate silica particles (micelles) whose size increases with the silica precipitarion. The interactions between single primary particles can induce the formation of aggregates which cannot be simply dispersed because of the presence of strong

chemical bonds (Si-O-Si bonds). Moreover, aggregates can be linked by hydrogen bondings, forming agglomerates (Fig. 1.8).

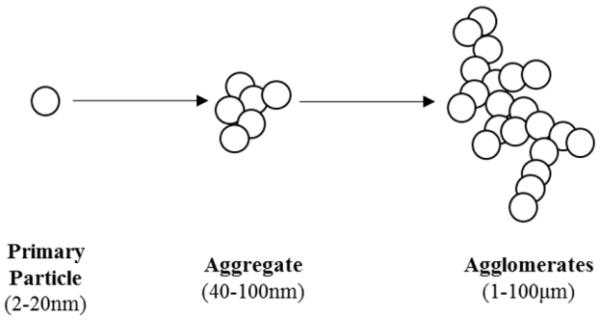

Figure 1.8 Evolution of size and sturcture of silica: from primary nanoparticles to agglomerates (Yrieix 2016).

Several parameters such as the concentration of the reactants, their rate of addition, the temperature of reaction, determine the characteristics of the final silica (specific surface area, porosity, primary particle size and shape, density and hardness). At the end of the preparation process, precipitated silica appears like a millimetric white dust and it is charaterized by a high polydispersity in size and shape.

Colloidal systems are mostly based on very small silica particles (micro- or nano-particles) dispersed in a suspending medium. In this system, the main aim is to preserve the colloidal stability: a colloidal suspension is defined as stable if its solid particles do not sediment or agglomerate (Bergna and Roberts 2005). Colloidal silica particles are usually synthetized by sol-gel process in basic medium (pH > 7) or in reverse micro-emulsions (Burns et al. 2006). One of the most widely used method for the synthesis of silica nanoparticles is the Stöber process (Stöber et al. 1968) which is based on the hydrolysis and condensation of a molecular precursor (typically tetraethoxysilane, TEOS) in ethanol or water/ethanol mixture, using ammonia as catalyst. This reaction allows to produce monodispersed and stable silica particles with a diameter ranging from 50 to 2000 nm. Nowadays, colloidal suspensions of silica nanoparticles in water at high concentration are commercially available (e.g., Ludox® synthetized by Sigma-Aldrich).

According to the DVLO theory (Derjaguin and Landau 1993), silica particles in suspension are stabilized considering the superposition of Van der Waals attraction upon repulsion forces (e.g. charges on the surface, ions) which occur when particles approach each another (i.e., below a critical distance at which particles "feel" each other). Thus, the evolution of the interaction energy between particles can be described as a function of their distance. The development of surface charge on the particle is accompanied by the formation of a countercharge in the surrounding medium which results in an electro-chemical double layer which is essential in the stabilization of colloids in suspension (Wypych 2016).

In addition to their stability, silica particles in colloidal suspensions are generally characterized by a well-defined spherical shape and very low polydispersity (< 15%) (Russel et al. 1989). These colloidal particles are usually stabilized in water or ethanol but they can be transferred in other solvents by a solvent exchange procedure or distillation of the initial suspending medium (Liff et al. 2007; Meth et al.

2011). The change of the surrounding medium can destabilize the particles inducing their aggregation. The common trend is to modify the surface of the particles to avoid agglomeration and obtain a good filler dispersion in a polymer matrix (see section 1.2.3).

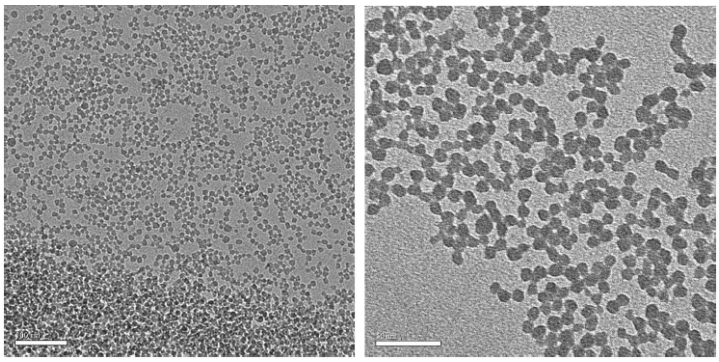

Figure 1.9 Transmission Electron Microscopy (TEM) images of silica nanoparticles (Ludox SM30). Scale-bar equals to 100 nm on the left, and 50 nm on the right (Wolf et al. 2007).

1.2.2. Properties of silica nanoparticle surface

The properties of the fillers, such as the size, the surface area and the surface chemistry, strongly influence the interactions among particles and between the particles and the solvent or the polymer in which they are dispersed.

The surface of silica particles is essentially characterized by the presence of surface siloxane groups Si–O–Si and silanol groups Si–OH. According to Zhuravlev (Zhuravlev 2000), -OH surface groups can be subdivided in: i) isolated/single silanols, ≡ SiOH; ii) germinal silanols, $=Si(OH)_2$; iii) vicinal, or bridged, or OH groups bound through an hydrogen bond. All the type of silanol groups and siloxane bridged on silica surface are represented in Fig. 1.10.

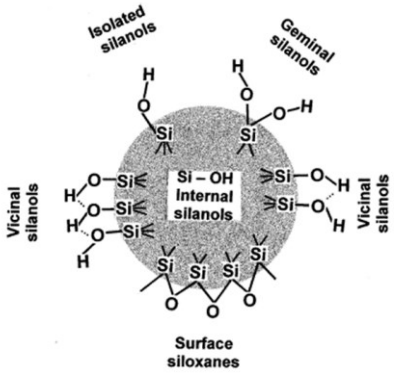

Figure 1.10 Type of silanol groups and siloxane bridges on the surface of amorphous silica (Zhuravlev 2000).

In colloidal suspension, the nature of silica surface can be influenced by several parameters, such as the pH of the liquid phase which can modify the electric charge distribution (i.e., zeta potential) on the filler surface (Hunter 2013). The pH at which the zeta potential is equal to zero is called isoelectric point or

point of zero charge. For silica particles, the theoretical isoelectric point is at pH equal to 2 (Kosmulski 2001). The evolution of the zeta potential for particles in water as a function of pH is shown in Fig. 1.11.

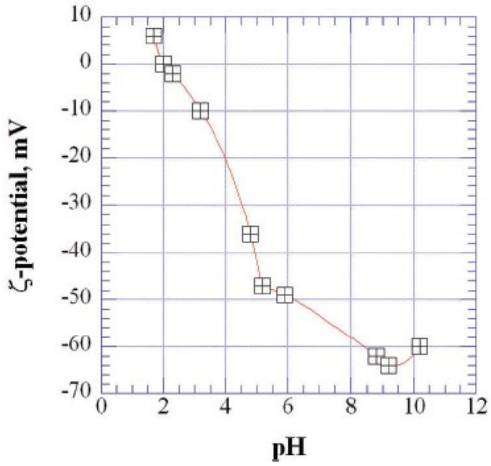

Figure 1.11 Zeta-potential of bare nano-silica in water (Wypych 2016). At pH=2 the zeta-potential is zero.

1.2.3. Surface-modification of silica nanoparticles

Silica fillers usually show a hydrophilic behavior and do not easily combine with most of the polymers which are usually hydrophobic (e.g., styrene-butadiene). Thus, the increase of the compatibility between fillers and polymer is a key point to obtain a material with homogeneous enhanced properties (Pukánszky and Fekete 1999). To overcome this polarity mismatch, the surface-modification of the particles is widely used to minimize the particle aggregation and promotes the particle-polymer interactions. Because of their numerous surface groups, silica particles can easily react with a *modifier* by: i) physical methods, which result in secondary forces between the particles and the modifier (Van der Waals, hydrogen and electrostatic forces); ii) chemical methods, which provide the covalent attachment avoiding the desorption of the modifier from the particle. The surface-modification can be performed on both precipitated and colloidal silica (Chen et al. 2005; Ramier et al. 2006). Once modified, fillers become reactive with other chemical groups or change their surface character from hydrophilic to hydrophobic (or vice versa). The surface-modification is commonly quantified by the grafting density (i.e., number of silane molecules per nm^2 of silica surface).

Different families of modifiers can be used. The silica particle surface can be grafted by polymer chains and thus, polymer-grafted nanoparticles are synthetized (Chevigny et al. 2009; Kumar et al. 2013; Lin et al. 2016). In this case, two approaches are possible: i) “grafting-to”, where end-functionalize polymer chains are grafted on the particle surface (Ranjan and Brittain 2007); ii) “grafting-from”, where a polymerization reaction starts from the particle surface where an initiator is grafted (Prucker and Rühe 1998; Carrot et al. 2006). Hasegawa et al. (Hasegawa et al. 1996) investigated polybutadiene particles grafted with polyacrylonitrile-co-styrene (AS) in a AS matrix, showing that there is a grafting density which optimizes the filler dispersion in the polymer matrix. These authors observed that in a polymer melt, if the “brushes” on the filler surface touch each other, the interface between the brush and the

matrix disappears leading to a decrease of the free energy of the system, favoring aggregation between grafted nanoparticles.

The surface-modification can be also performed using *organosilanes* which are low molecular weight compounds which can be grafted on silica (Mittal 2007). They can act as:

- Coupling agents, interacting with both polymer chains and inorganic fillers, providing covalent links between them (Wolff and Wang 1992), as shown in Fig. 1.12a. One of the most used coupling agent is the Bis[3-(triethoxysilyl)propyl] Tetrasulfide (TESPT or Si69). Its chemical formula is represented in Fig. 1.12b. Dohi et al. (Dohi and Horiuchi 2007) used TESPT as coupling agent in silica-styrene/butadiene composite expecting the formation of a coupling interlayer at the interface between these two compounds.

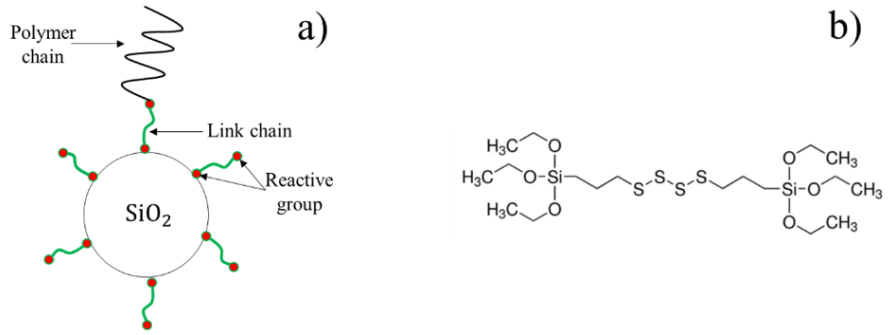

Figure 1.12 (a) Reaction mechanism of a coupling agent with surface of silica particle and polymer chain. (b) Structure formula of Bis[3-(triethoxysilyl)propyl] Tetrasulfide (TESPT).

- Coating agents, playing a role analogous to surfactants in microemulsions, inducing a decrease of dispersive and polar contributions of surface energy. These molecules are characterized by one or several functional groups which can react with silica surface forming covalent Si-O-Si bonds and by an alkyl chain which contributes to constitute a layer on the particle (Fig. 1.13a). One of the most used coating agent is the Octyltriethoxysilane (commercially known as OCTEO, also named OTES), Fig. 1.13b.

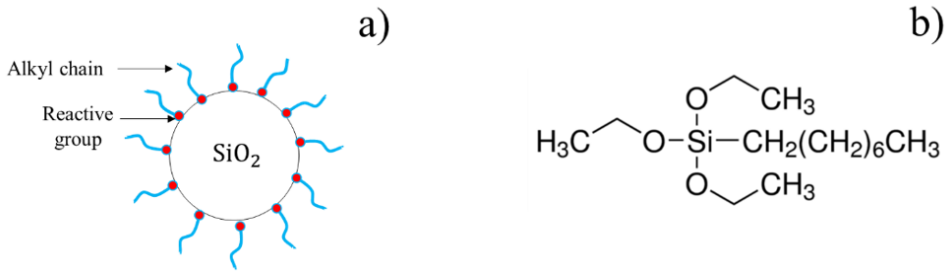

Figure 1.13 (a) Reaction mechanism of a coupling agent on silica particle surface. (b) Structure formula of octyltriethoxysilane (OCTEO).

Both coupling and coating agents are commonly used in modern car tires manufacturing since several studies have evidenced their impact on dispersion and macroscopic properties (Sternstein and Zhu 2002; Wu et al. 2008).

Reaction mechanism of silane agents on silica surface

The grafting of silane molecules on filler surface is influenced by the characteristics of the modifiers and the experimental conditions of the grafting process.

Among the parameters affecting the grafting reaction, such as pH, temperature (Goerl et al. 1997), the presence of water in the system and on the silica surface is one of the most important. It is essential to hydrolyze the functionalized groups of the silane molecules (e.g., Si-O-CH_2-CH_3 groups of the octyltriethoxysilane molecules) which can then react with the filler surface groups (e.g. –OH groups). This hydrolysis-condensation reaction induces the formation Si-O-Si bonds between the alkyl chain of the silane coating agent and the silica particle (Osterholtz and Pohl 1992; Brochier Salon and Belgacem 2011).

The surface modification can be performed before or after the incorporation of the fillers in the polymer matrix. For amorphous precipitated silica, Castellano et al. (Castellano et al. 2005) proposed to perform the surface-modification in a CH_2Cl_2 solution of TESPT, which is then thermally treated at 120°C after the complete evaporation of the solvent to promote the condensation of TESPT molecules. In another work (Castellano et al. 2007), same authors proposed a filler surface-modification by triethoxysilane (TES), octadecyltriethixysilane (ODTES) and TESPT/ODTES mixture using the same method and thus to evaluate the dispersion in a styrene-butadiene copolymer matrix. Other authors suggest that the surface-modification of the fillers with silanes can also take place during the mixing with a polymer. Ramier and co-authors (Ramier et al. 2006; Ramier et al. 2007b) affirmed that the treatment of the silica by TESPT can be performed during the incorporation of the fillers in a styrene-butadiene matrix using an internal mixer (i.e. *solid-phase mixing*, see Chapter 2.2). The same solid-phase mixing method has been used by Baeza et al. (Baeza et al. 2013a), to promote the reaction of the OCTEO on the silica, and by Stockelhuber et al.(Stockelhuber et al. 2011) to modify several kind of fillers (i.e., fumed, precipitated silica and carbon black). Using this method, the common opinion is that the process has to be performed at high temperature: at low temperature the solid-phase mixing could only promotes the adsorption of the silane molecules on the filler surface while the chemical grafting of the silanes on the silica is promoted at high temperatures. During the mixing, Qu and co-authors (Qu et al. 2013) kept the temperature in the range of 145-160°C for 10 minutes to ensure the reaction of the silane with the silica surface while Vilmin (Vilmin et al. 2014) suggested that the direct condensation of the silane can be reached also in absence of residual water on filler surface working at temperature higher than 140°C.

Suspensions of bare colloidal particles in water are commercially available or they can be synthetized via the sol-gel method of TEOS (Tabatabaei et al. 2006) based on TEOS-ethanol-water-ammonia

mixture according to the Stöber method (Stöber et al. 1968). For these colloidal systems, the critical point is that the surface-modification by silane agents can induce the modification of the electrical double layer which stabilizes the particles, leading to their aggregation.

In 1990, Badley (Badley et al. 1990) proposed to perform the surface-modification of non-porous silica particles of 58 nm by different silanes such as TESPT and octadecyltrimethoxysilane, working at room temperature for 20h. The final octadecylsilica (i.e., silica modified by octadecyltrimethoxysilane) precipitated after the synthesis, providing a method to purify and transfer the octadecylsilica to a nonpolar solvent. More recently, Wu et al. (Wu et al. 2007) indicated a one-step method adapted from the one of Wang (Wang et al. 2003) to control the hydrophobicity of sub-micrometer silica spheres by modifying their surface with different silane agents, such as methyltriethoxysilane, *n*-octyltriethoxysilane (OTES) or *n*-dodecyltriethoysilane (DTES). This method consists in the dropwise addition of the silane to the colloidal suspension to react with the SiO_2 surface which is under vigorous stirring for 19 h. They showed that the particles modified with OTES and DTES were the most hydrophobic from water vapor adsorption experiment, generally used to compare the hydrophobicity of the particles.

In most of the cases, the surface-modified silica particles are separated by centrifugation and washed by acetone or ethanol to remove the unreacted or physically absorbed silane molecules. Then, they can be dried and re-dispersed in another solvent or polymer (Chen et al. 2005). Another option is to transfer the grafted particle in a desired solvent by a solvent exchange procedure (Liff et al. 2007).

As for precipitated silica, also for colloidal silica some parameters such as temperature and pH can influence the grafting reaction. As general remark, the surface modification of colloidal silica does not require to reach high temperatures as for the precipitated silica. This could be explained considering the large presence of water in the suspending medium which promotes the hydrolysis of the silane molecules. Thus, a small increase of temperature could contribute to accelerate the reaction.

As already mentioned, the hydrolysis of the reactive groups of silane molecules is essential to achieve a good grafting (e.g., octyltriethoxysilane has three ethoxy groups ($-OCH_2CH_3$) that could participate to the reaction). Even if it is difficult to predict or determine the number of hydrolyzed reactive groups, the condensation reaction of individual silane molecules with silica surface or with other neighboring molecules can be explained by three different models (Goerl et al. 1997; Ramier et al. 2006):

- Model I (or vertical model), which assumes a reaction of the silane with the silica and admits the possibility that other silane molecules condense onto a silane molecules which is already bound to the silica surface.
- Model II, which predicts that all the silane reactive groups form siloxane bonds by reacting with the silanol groups on the silica surface. However, this model is not realistic since the geometry of the siloxane bonds prevents the formation of two or three of these bonds.

- Model III, which considers the formation of a single siloxane bond on the silica surface. This model is based on the assumption that a primary reaction occurs (i.e., single bond between silane and silica surface) and then followed by a condensation reaction between neighboring silane molecules already grafted to the silica surface (secondary reaction).

Characterization of surface-modified silica nanoparticles

The detection of the grafting reaction is an essential step to define the characteristic of the surface-modified fillers. When grafting is performed before the filler dispersion into a polymer matrix, grafted particles can be directly analyzed whereas the characterization of the surface properties is much more difficult when the filler grafting is performed during the mixing with the polymer (e.g., solid-phase mixing). In the latter case, the silica particles have to be extracted from the polymer bulk and the presence of the polymer adsorbed on the silica surface can mask the detection of the silane molecules. Here, some of the main techniques used for the characterization of the surface-modified silica nanoparticles are presented:

- *Thermogravimetric analysis* (TGA), which provides the sample weight loss as a function of the increasing temperature. For silica particles grafted with silane agents, two main stages of weight loss can be identified: i) at temperature below 200°C, the weight loss can be linked to the evaporation of the water physically adsorbed at silica surface; ii) between 200° and 900°C, the weight loss results from the condensation of the silanol groups and the decomposition of the grafted silane molecules. This technique allows to approximately estimate the silane grafting density. Chen et al. (Chen et al. 2005) used TGA to prove that new kinds of silica nanoparticles with different surface properties can be obtained by modifying the bare colloidal silica particles with different silanes (e.g., octyltriethoxysilane, vinyltriethoxysilane, methyltriethoxysilane), as shown in Fig. 1.14. Measurements are usually performed under air or azote with a temperature ramp of 5°C/min.

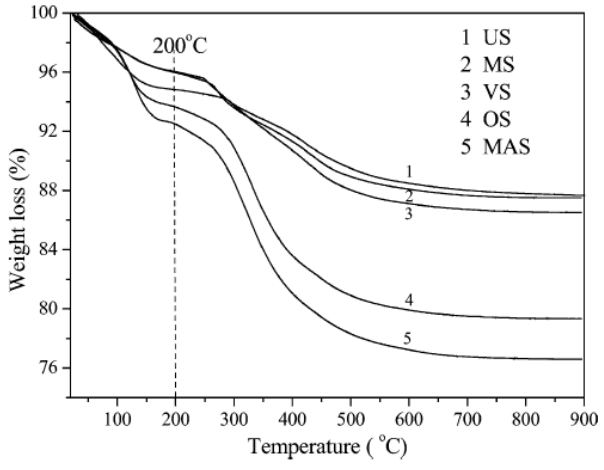

Figure 1.14 Thermogravimetric analysis curves of silica powders grafted with different silane agents (Chen et al. 2005).

- *Elemental analysis*, which allows to identify and quantify the elemental composition of the sample. This technique is widely used for the detection of the silane molecules grafted on the filler surface (Castellano et al. 2005), even if it does not allow to obtain accurate results which are often affected by sample contamination.
- *^{29}Si Solid-state NMR*, where the position of the chemical shifts allows to distinguish the chemical species in the sample. Several authors (Sindorf and Maciel 1983; Valentin et al. 2006) use this technique to identify the silanol groups or the siloxane bonds on the silica surface.
- *Infrared spectroscopy*, which involves the interaction of infrared radiations with matter. Techniques such as Raman spectroscopy, FT-IR (Fourier Transform Infrared Spectroscopy) or ATR (Attenuated Total Reflectance) are usually used to investigate and quantify the silane grafting. Vilmin and co-authors (Vilmin et al. 2014) performed FT-IR experiments on hydrated precipitated silica grafted by TESPT in temperature and atmospheric conditions which reproduce an industrial mixing process with an elastomer. Chen et al. (Chen et al. 2005) described the properties of surface-modified silica powders by FT-IR, probing that all the fillers became hydrophobic after the grafting reaction.

Other complementary techniques can be used to determine the surface properties of the surface-modified silica nanoparticles. For instance, Gauthier et al. (Gauthier et al. 1996) proposed to use Atomic Force Microscope (AFM) to investigate the mechanism of grafting alkoxysilane and chlorosilane molecules onto silica surface, showing that the influence of the tip velocity on the friction behavior is a good way to discriminate between the bare silica surface and the grafted one. The morphology of grafted silica particles can also be analyzed by Transmission Electron Microscopy (TEM) (Schmitt et al. 2015).

1.3.Nanocomposites

Polymer nanocomposite (PNCs) are formed by incorporating inorganic nanoparticles in a soft polymer matrix (Schmidt and Malwitz 2003; Genix and Oberdisse 2015). Even if these materials attract a lot of interest because of their significantly improved properties, the basic physical origin of the large property enhancement is still not clear (Kumar et al. 2013). The knowledge of these complex materials passes through a detailed knowledge of the characteristics of the polymer matrix and the fillers and also through the description of the particle dispersion which is controlled by the filler-filler and the filler-polymer interactions (Jancar et al. 2010).

1.3.1. Filler dispersion in polymer matrices

The dispersion of the fillers in a polymer matrix strongly affects the final characteristics of the material and it depends on thermodynamics of the sample and the kinetics of its preparation.

A homogenous dispersion would allow to obtain a material with perfectly homogenous physico-chemical properties. In the real case, the repartition of spherical particles in a polymer matrix can be described considering their dispersion and distribution, as shown in Fig. 1.15. For colloidal nanoparticles, the filler clustering is promoted by strong Van der Waals forces which occur between particles at short distances, while it may be prevented by long-range electrostatic repulsions which stabilize the single beads (Oberdisse 2006).

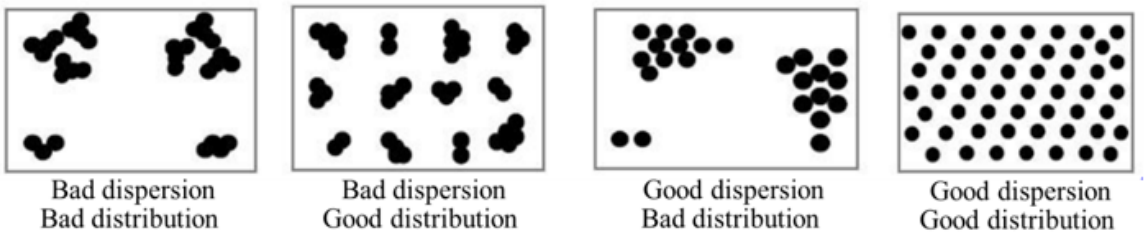

Figure 1.15 Distribution and dispersion of spherical particles in a continuous medium. A good dispersion is related to a feeble aggregation and a good distribution is linked to a homogeneous spatial repartition of the particle (adapted from (Baeza 2013)).

If aggregation occurs, the aggregates can have a tenuous, fractal like or more compact configuration (Fig. 1.16a). Their morphology strongly depends on the nanocomposite synthesis process which is influenced by several parameters such as: i) the size of the elementary nanoparticles, as shown in Fig. 1.16b; ii) number of particles which constitute the aggregate (i.e., *aggregation number*); iii) the amount of filler which is present inside an aggregate (i.e. *compacity*); iv) the fractal dimension; v) the percolation, which indicates the formation of a continuous filler path through the material that influences some physical characteristics of the material such as its conductivity (Feng et al. 2012) or its elastic modulus (Chen et al. 2015). These concepts will be detailed in Chapter 2.

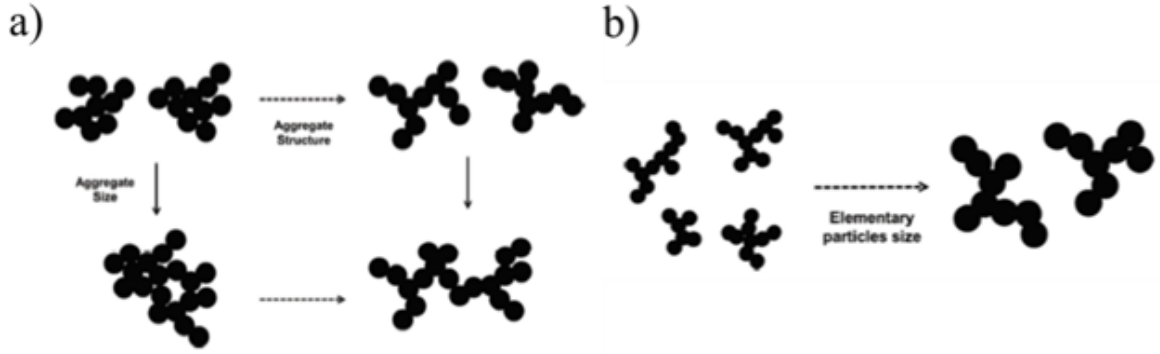

Figure 1.16 Schematic representation of (a) aggregate size and structure and (b) impact of elementary particle size on aggregate surface (Vieyres 2013).

In nanocomposite materials, aggregates can also interact between them. Baeza et al. (Baeza et al. 2013a) described the structure of the silica in a PNC starting from the primary silica NPs as basic units. By a combination of TEM, X-ray scattering and simulations, these authors proposed a complete structural characterization of the system, from the primary silica nanoparticles, to NP aggregates, up to

micrometer-sized branches (Fig. 1.17). They found that NPs aggregate in small clusters with a radius of about 40 nm and their interactions can be described with a hard core repulsive potential. These aggregates are themselves concentrated in a large-scale fractal branches where they repel each other (i.e., strong effect on the apparent isothermal compressibility which leads to the characteristic low-q depression in the scattering intensity).

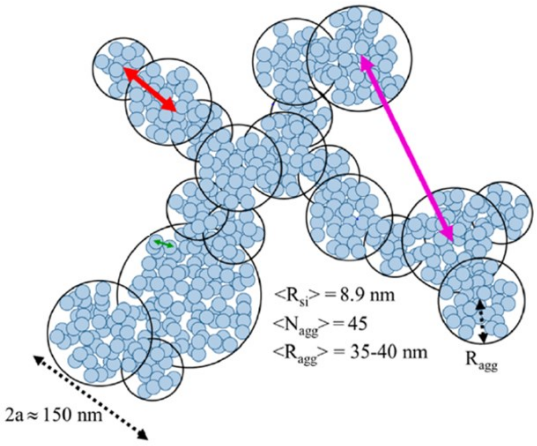

Figure 1.17 Real-space representation of multi-scale structure of the silica in a nanocomposite: from the interaction between particles inside an aggregate to the repulsion between fractal branches (adapted from (Baeza et al. 2013a)).

Grafting of polymer chains

The surface-modification of fillers can help to improve the compatibility between hydrophobic polymers and hydrophilic silica particles, promoting the polymer grafting or absorption. Unfortunately, the mechanism of reaction between the silanes grafted on silica surface and the polymer chain is not completely understood.

Dohi et al. (Dohi and Horiuchi 2007) proposed a schematic illustration of the coupling reaction of TESPT in a silica-rubber composite, expecting the formation of the coupling layer at the interface between the silica and the rubber (SBR), as shown in Fig. 1.18. In this representation, the ethoxy groups of TESPT condense with the silanol groups on the silica surface and the tetrasulfane group of TESPT covalently bonds with the rubber. The authors assume that the in situ reaction among the three components of the TESPT monolayer took place at the interface between silica and rubber (i.e., the silica is coupled with the rubber matrix via covalent bonds). At the same time, the reaction/interaction mechanism during the mixing can be complicated by other reactions: the polycondensation within the silane molecules, the suppression of the reaction between the silane and the silanol groups on silica or the trapping of silane molecules in the polymer matrix through the dissolution and chemical reaction between silane and rubber.

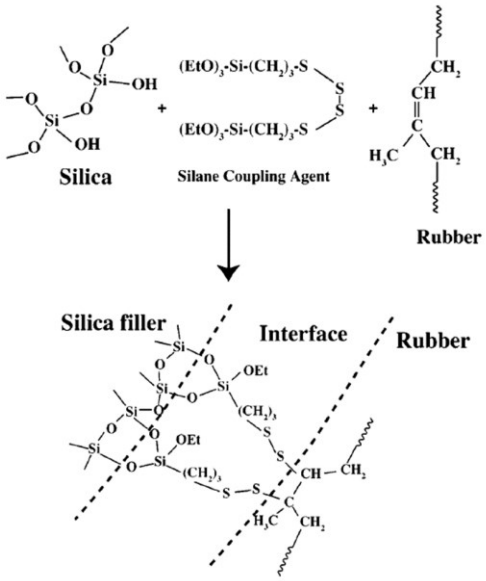

Figure 1.18 Coupling reaction of TESPT in a silica-rubber composite (Dohi and Horiuchi 2007).

Thus, the filler dispersion can be tuned by the addition of *graftable* polymer chains with a silanol end-function helping them to anchor to the filler surface. Baeza et al. (Baeza et al. 2013b) proposed a study of a un-crosslinked SBR system filled with precipitated silica nanoparticles as a function of the amount of graftable polymer chains. They show that the nanoparticles dispersion in the polymer matrix evolves from rather heterogeneous spatial distribution at 0% of graftable polymer chains to a much more homogenous dispersion when all the polymer chains are end-functionalized (Fig. 1.19).

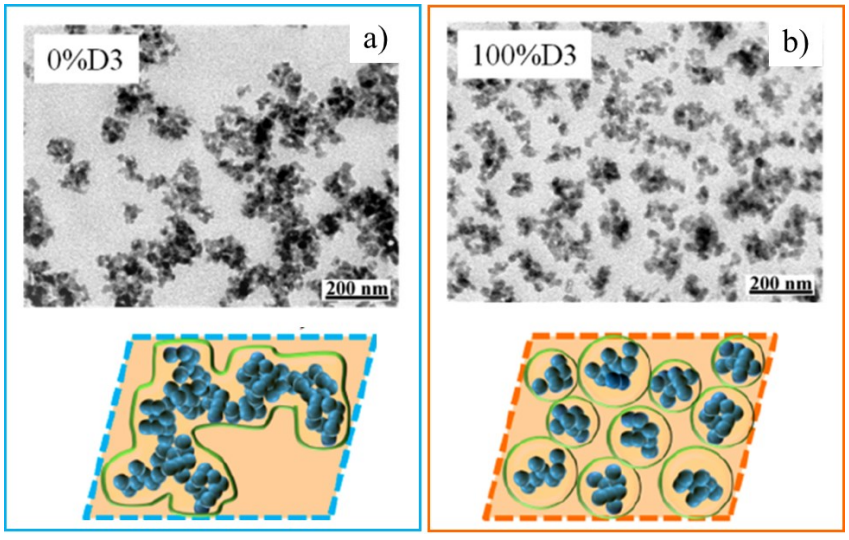

Figure 1.19 TEM images show the aggregation state of the silica NPs in a styrene-butadiene matrix with different amounts of graftable polymer chains: (a) 0% and (b) 100% of graftable chains (Baeza et al. 2013b).

The amount of polymer which is chemically grafted or strongly physically adsorbed on the filler surface can be estimated by Bound Rubber (BR) measurements. The BR is usually defined as the

fraction of polymer which is not extracted by a good solvent from a filled rubber and it is considered as a good estimation of the reinforcement and the filler activity towards the rubber (Wypych 2016). This kind of test is generally performed on un-crosslinked PNCs and the extraction of the non-grafted/non-adsorbed polymer can be performed using several solvents such as toluene, tetrahydrofuran, chloroform, hexane and xylene (Blow 1973; Ismail et al. 1995; Choi 2002b; Scotti et al. 2014). The temperature and the number of washes in the solvent also influence the BR results. A schematic representation of a bound rubber procedure is proposed in Fig. 1.20a. Baeza et al. (Baeza et al. 2013b) showed that the bound rubber amount increases linearly with the amount of end-functionalized polymer chains, probing the key role of the silanol end-groups in silica-polymer interactions, Fig. 1.20b. Wu et al. (Wu et al. 2008) proved that the surface-modification of silica fillers with a coupling agent (TESPT) induces the increase of the bound rubber and improves the dispersion of the silica since its stability is ensured by the chemical bonds between filler and rubber.

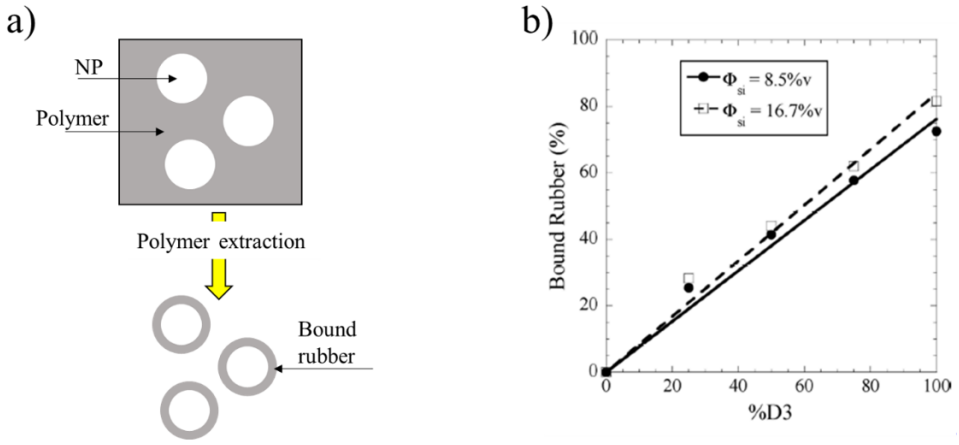

Figure 1.20 (a) Schematic representation of a bound rubber test (i.e., extraction of "free" polymer with solvent); (b) Bound rubber fraction as a function of the amount of end-functionalized polymer chains, for PNCs at two silica fractions (Baeza et al. 2013b).

1.3.2. Formulation methods of PNCs

According to the polymer and filler characteristics, nanocomposites can be produced using several methods, such as:

Solid-phase mixing: this method is commonly used in tire manufacturing. The solid polymer is introduced in a mixer equipped with two rotors, which is usually pre-heated at high temperature. Once the polymer is homogenized, the filler and other compounds (e.g. silane, catalyzers) are added. The mechanical action of the rotors coupled with the high temperature promotes the incorporation and the dispersion of the particles, inducing the fragmentation of macroscopic aggregates. The final dispersion state of the fillers in the polymer matrix can be also tuned using an external mixer.

The solid-phase method allows to produce:

i) Un-crosslinked PNCs, Genix et al. (Genix et al. 2016a) recently reviewed the structural and dynamical properties of the so-called "simplified industrial nanocomposites" (Chapter 2.2) made by un-crosslinked styrene-butadiene polymer, precipitated silica, octyltriethoxysilane as silane agent, and the Diphenylguanidine, DPG, as catalyzer (i.e., the number of ingredients is limited to the strict minimum).

ii) Crosslinked PNCs, where other ingredients such as cross-linkers, cure activators (e.g., ZnO nanoparticles), accelerator providing fast cure rate like sulfenamides (TBBS, CBS) are used to chemically linked the polymer chains between them (Choi et al. 2004; Ramier et al. 2007b; Conzatti et al. 2008; Stockelhuber et al. 2011). These compounds are usually indicated as "curing package" (Stockelhuber et al. 2011).

Even if the crosslinked PNCs are preferred in tire industry for their mechanical properties, the "simplified" formulation of the un-crosslinked PNCs with a reduced number of ingredients makes easier the evaluation of the impact of each compound on the final properties of the material.

As already mentioned in the section 1.2, the use of silane agents to surface-modify silica particles has been investigated in the case of solid-phase mixing since it can tune the filler-filler and filler-polymer interactions (Yatsuyanagi et al. 2002; Suzuki et al. 2005; Ramier et al. 2007b). Other studies have been dedicated to the impact of other ingredients, such as the DPG which is a basic molecule traditionally used as secondary accelerator. Schaal et al (Schaal et al. 2000) showed that the DPG also induces a retardation of the re-agglomeration of silica particles. It has also been found that DPG improves the silane reaction during the mixing (Penot and Roy 2006). This favors the curing process, since the higher coverage of the silica surface allows a better efficiency of the accelerators which otherwise tend to be adsorbed at the filler surface (Kaewsakul et al. 2012). As a consequence, the mixing order of the ingredients used for nanocomposite formulation is of primary importance. Several authors propose to introduce the DPG with the curing package at the end of the mixing process (Choi 2002a; Yatsuyanagi et al. 2002; Suzuki et al. 2005; Mujtaba et al. 2012) or later with the use of an external mixer (Schaal et al. 2000; Ramier et al. 2007b). Others (Baeza et al. 2013a; Bouty et al. 2014) suggest to incorporate the DPG at the beginning of the mixing process, following a patent innovation by Michelin (Penot and Roy 2006).

In this PhD work, the solid-phase mixing protocol proposed by Baeza et al. (Baeza et al. 2013a) has been used as reference to produce the "simplified industrial" PNCs made by styrene-butadiene polymer, silica pellets, a silane coating agent and DPG (see section 2.2).

Solvent casting technique: in this formulation method, suspensions of silica particles and polymers in a common good solvent can be mixed together by stirring or sonication. The final mixture is placed into a support to allow the solvent to evaporate (solvent casting) and to obtain the final nanocomposite, as schematically represented in Fig. 1.21.

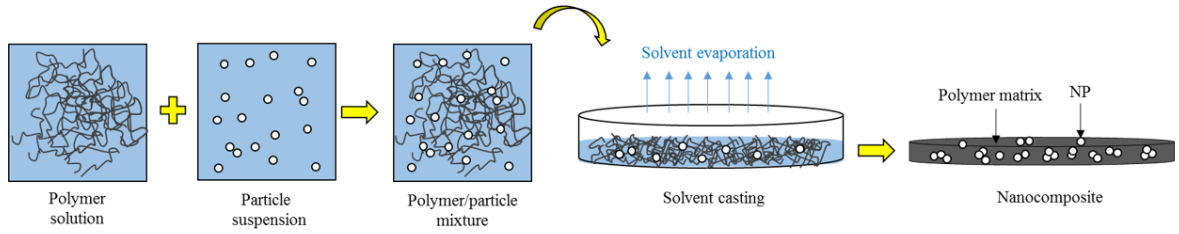

Figure 1.21 Drawing illustration of solvent casting technique. Polymer and silica dispersed in the same solvent are mixed together and put into a support to allow the complete evaporation of the residual solvent and obtain the final polymer-silica nanocomposite.

As already mentioned, silica particles are usually dispersed in water. When the polymer is soluble in an aqueous phase, it can be directly mixed with silica. This is the case of silica-latex (Rharbi et al. 1999; Oberdisse and Demé 2002; Oberdisse 2006; Tatou et al. 2011; Banc et al. 2014) and silica-PEO nanocomposites (Anderson and Zukoski 2009). On the other hand, several polymers (e.g. styrene-butadiene) show a hydrophobic behavior, resulting soluble in organic solvents while silica particles are usually stabilized in water. Thus, before the mixing, filler particles have to be stabilized in the same solvent where the polymer is dissolved. At present, suspensions of silica particles in organic solvents are commercially produced. For example, Nissan Chemical Industry synthetizes silica particles of 10-100nm directly stabilized in methyl-ethylketone, MEK (http://www.nissanchem-usa.com/products/organosilicasol) which are currently used in several scientific works, unfortunately with unknown organic surface modification (Rittigstein et al. 2007; Jouault et al. 2014; Baeza et al. 2016a). Another option is to replace the water where particles are originally stabilized with the organic solvent used for polymer dissolution. This procedure is named *solvent exchange method*. Liff et al. (Liff et al. 2007) proposed to use a solvent-exchange method (Kumar et al. 2005) to disperse polar nanoparticles, such as laponite, in organic solvents: particles are dispersed in a first solvent and then, a second solvent, miscible with the first one, is gradually added. Finally, all the first solvent is extracted from the second forming the final particle suspension. The solvent exchange can be performed using a dialysis tube which contains the particle dispersed in the first solvent and which is immersed in the second solvent for at least 24h (i.e., *dialysis* method).

In nanocomposites made by solvent-casting technique, the choice of the solvent plays a crucial role in NPs organization in the polymer matrix. Several studies report on the effect of the solvent on particle-polymer affinity and the resulting nanoparticle dispersion (Kim et al. 2009; Jouault et al. 2014; Zhao et al. 2014). Jouault et al. (Jouault et al. 2014) showed that a way to get a good dispersion is to use solvent where the polymer strongly adsorbs on silica surface, as for the poly(2-vinyl pyridine), P2VP, and methyl-ethylketone. Here, the formation of a polymer layer with a thickness comparable to the radius of gyration of the polymer imposes a strong steric repulsion between nanoparticles, preventing aggregation.

The organization of the filler in the polymer matrix can be also influenced by the evaporation rate of the solvent. By X-ray scattering, Kim et al. (Kim et al. 2016) recently investigated how silica NPs dispersion evolves during the drying in a polymer nanocomposite films (poly-vinyl-alcohol, PVA, matrix), focusing on the role of particle-polymer interactions in the structural development, tuned varying the pH, as shown in Fig. 1.22. They found that the inter-particle interactions can significantly evolve during the drying and alter the liquid structure to the point that the initial stable suspensions destabilize into the solid structure in the drying silica/PVA film. Also in this case, the polymer adsorbed at the filler surface plays a key role in the uniform dispersion of the NPs, as it sterically stabilizes them over short ranges during the drying, while depletion attraction dominates at longer ranges.

In this PhD work, the solvent casting technique allowed us to develop our model nanocomposite system (see section 2.3).

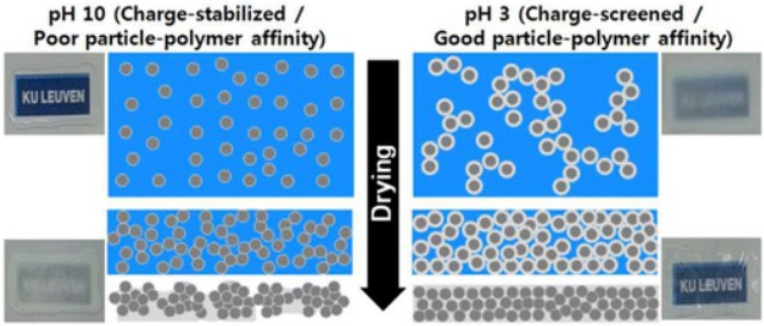

Figure 1.22 Schematic illustration of the structural development of silica dispersion during the drying of silica/PVA films. The polymer-particle affinity is tuned by pH value (at pH=10 on the left and at pH=3 on the right), inducing a different polymer absorption on the filler surface which governs the filler short-range stabilization (Kim et al. 2016).

1.3.3. Characterization of PNCs

The macroscopic properties of nanocomposite materials (e.g., mechanical or electrical) are intrinsically linked to their: i) structural characteristics, such as the filler organization in the polymer matrix and the polymer conformation which determines how the stresses are transmitted across the sample; ii) dynamical properties of both particles and polymer chains, which are defined by typical time scales of mobility and relaxation phenomena (Genix and Oberdisse 2015).

Here below, a short overview of the structural, dynamical and mechanical properties of nanocomposite materials is presented, focusing on the main techniques used for PNC characterization.

Structural characterization of PNCs

Structural properties of PNCs are generally related to the filler organization in the polymer matrix and they can be studied using several techniques.

Many authors use direct imaging methods, such as Transmission Electron Microscopy (TEM) (Suzuki et al. 2005; Castellano et al. 2007; Stockelhuber et al. 2011; Pérez-Aparicio et al. 2013a), or Scanning Electron Microscopy (SEM) (Baeza et al. 2016b), to obtain a direct real-space picture of a small region

of the nanocomposites. TEM pictures are usually analyzed to determine the NP size distribution (Banc et al. 2014). An example of TEM picture of bare NPs dispersed in a poly(ethylacrylate) matrix is shown in Fig. 1.23a. Fig. 1.23b represents an isolated aggregate of the same image.

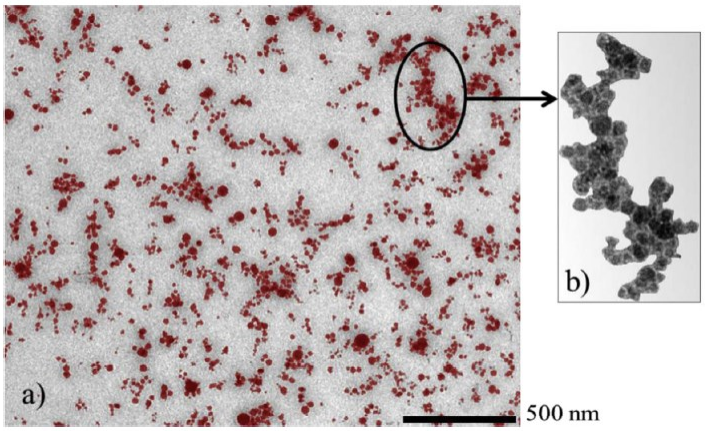

Figure 1.23 (a) TEM picture of bare NPs dispersed in a poly(ethylacrylate) matrix; (b) Zoom on an isolated aggregate (Schmitt et al 2016).

Other works proposed to investigate nanocomposite structure combining direct imaging methods with Small-Angle X-ray Scattering and Small-Angle Neutron Scattering (Genix and Oberdisse 2015). Even if the interpretation of the scattering data is quite challenging, they allow to obtain structural information also for samples with high filler content, where structural characteristics become hardly distinguishable by TEM. More technical details about these techniques are reported in Chapter 2.4.

Jouault et al. (Jouault et al. 2009) investigated the fractal organization and interactions between aggregates in silica-PS nanocomposites by SANS and TEM, providing structural information to understand the small- and large- scale deformations in these samples. Tatou et al. (Tatou et al. 2011) proposed an aggregation diagram based on SANS experiments and TEM observations of silica-latex nanocomposites as a function of the filler content and the pH of the precursor suspensions. Even if in most of the cases SANS experiments allow to investigate filler structure, this technique can be also used to follow the evolution of the polymer structure during the formation of the nanocomposite, as proposed by Genix et al. (Genix et al. 2012) in silica-latex system, using the zero-average contrast conditions to suppress the silica nanoparticles contributions. Janes et al. (Janes et al. 2011) used SAXS and TEM analysis to prove that the thermal history of Poly(methyl acrylate)/silica nanocomposites is a critical factor in nanoparticle dispersion. Banc et al.(Banc et al. 2014) coupled SAXS-TEM with simulations (i.e., Monte-Carlo simulations) to investigate the silica distribution in poly(ethyl methacrylate)-nanolatex matrices of different chain mass, as schematically indicated in Fig. 1.24. They showed that the best dispersion was obtained with the highest chain mass since a slowed-down kinetics of silica spatial reorganization is induced. A similar approach is used by Baeza et al. (Baeza et al. 2013a) who propose to use: i) the analysis of SAXS data to extract the average aggregate radius R_{agg} using the Kratky plot ($q^2I(q)$ versus q); ii) the TEM analysis to reveal the volume fraction of fractal branches Φ_{fract}, which

refers to the essential input for the independent Monte-Carlo simulations which allow to describe the inter-aggregate structure factor for polydisperse spheres. This method will be extensively applied in Chapter 3. Schmitt et al. (Schmitt et al. 2015) proposed a study on aluminia-coated silica NPs grafted with phosphonic acids of different hydrophobicity and dispersed in a poly(ethylacrylate) matrix. They evidenced the NP aggregation by SAXS, SANS, TEM and simulations, showing that the micrometer-scale inhomogeneities depend on the surface/polymer matrix compatibility. They focused on the analysis in the intermediate q-regime where local interactions between NPs override. They observed the evolution of the compacity which describes the internal density of NP in the aggregate, quantifying the depth of the correlation hole in the scattered intensity, a rather novel method described in Chapter 2.4 (Schmitt et al 2016; Genix et al 2017 in preparation). All these scattering studies confirm the presence of a multi-scale tridimentional structure of the silica particles in the nanocomposite material (see section 2.4).

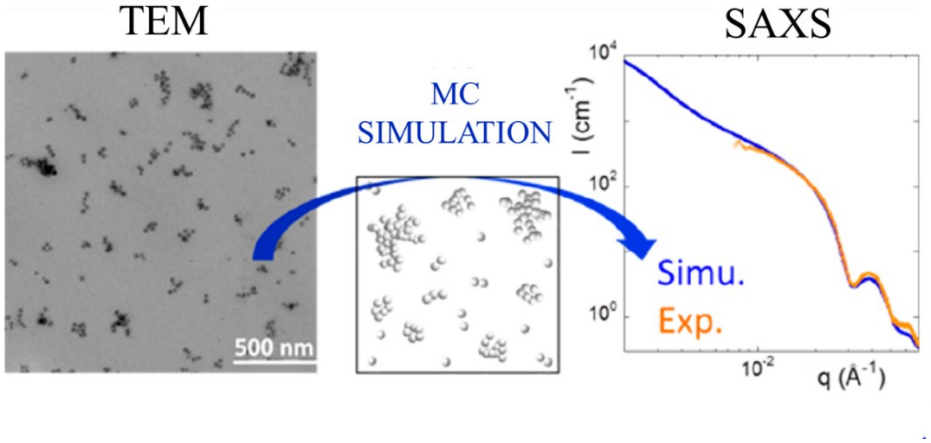

Figure 1.24 Schematic representation of the multi-technique approach used by (Banc et al. 2014) which coupled TEM and SAXS experiments with Monte-Carlo simulations.

Another technique used to obtain information about the structural organization of the filler in a nanocomposite material is Atomic Force Microscopy (AFM). This technique allows to characterize the structure and morphology of the sample surface and to investigate properties of a material from the nanometric to the millimetric scale. Zhang et al. (Zhang et al. 2001) used AFM to shed light on the main properties of nanocomposites made by polypropylene and silica treated by irradiation grafting polymerization. Lapra et al. (Lapra et al. 2003) proposed an AFM study of nanocomposites made by SBR and Polydimethylsiloxane (PDMS) and silica, stretched at different strain values, showing that the material becomes more homogeneous in term of local strain distribution after pre-cycling. Mélé et al. (Mélé et al. 2002) focused on a AFM-SAXS quantitative morphological analysis of the spatial distribution of fillers in silica-SBR nanocomposites, investigating the role of fractal aggregates in the reinforcement. Le Diagon et al. (Le Diagon et al. 2007) used AFM to study model acrylate/silica nanocomposites which have been uniaxial stretched. These authors focused on the analysis of the displacement field of the near surface particles which presents distortions from the affinity related to

the mechanical confinement of the matrix between particles. On the other hand, it can be noticed that this technique allows only to obtain 2D-information related to the surface of the observed sample.

Characterization of dynamics of PNCs

In PNCs, dynamical properties have the same importance as the structural ones since the viscoelastic properties of these materials are strongly temperature and frequency dependent.

The polymer dynamics as well as the polymer-filler interactions in PNCs have been largely investigated by Broadband Dielectric Spectroscopy (BDS), a technique that allows measuring the dielectric response of a material over a wide temperature and frequency range. A detailed description of this technique will be presented in Chapter 2.5.

As already mentioned, in a pure polymer matrix such as styrene-butadiene rubber (Cerveny et al. 2002), two main relaxation processes can be identified: i) the α-relaxation, or segmental relaxation, linked to the glass transition; ii) the β'-relaxation, usually related to localized non-cooperative processes in polymer segments.

In PNCs filled with silica, clay or carbon black (Böhning et al. 2005; Mijović et al. 2006), additional processes appear at frequencies lower than the α-relaxation because of the presence of the filler. One of these processes is commonly attributed to the Maxwell-Wagner-Sillars (MWS) polarization due to the charge carrier diffusion through the different phases of the composites (i.e., polymer and fillers). It is linked to the trapping and accumulation of charges at the polymer/filler interfaces. (Genix et al. 2016a).

In silica-SBR industrial nanocomposites, Otegui et al. (Otegui et al. 2013) observed that the MWS polarization is directly related to the water layer adsorbed at the surface of silica particles: for high water content, the MWS peak moves to higher frequencies; the same process can be completely removed from the frequency window if the water content is consistently reduced and it can be observed again in case of re-hydration of the sample, i.e., MWS is a reversible process. To describe this behavior, the same authors used the interlayer model proposed by Steeman (Steeman and Maurer 1990). Moreover, they showed that the increase of the relative humidity (RH) induces a decrease of the relaxation time of the MWS processes, while the α-relaxation is unperturbed. This is consistent with the results found by Baeza et al. (Baeza et al. 2015b) for similar silica-SB industrial nanocomposites. In their case, the increase of the filler content leads to an increase of the water content of the sample, as it can be deduced from the relaxation maps of the MWS process (i.e., the evolution of the relaxation time of the process as a function of the temperature), here indicated as MWS1 (Fig. 1.25).

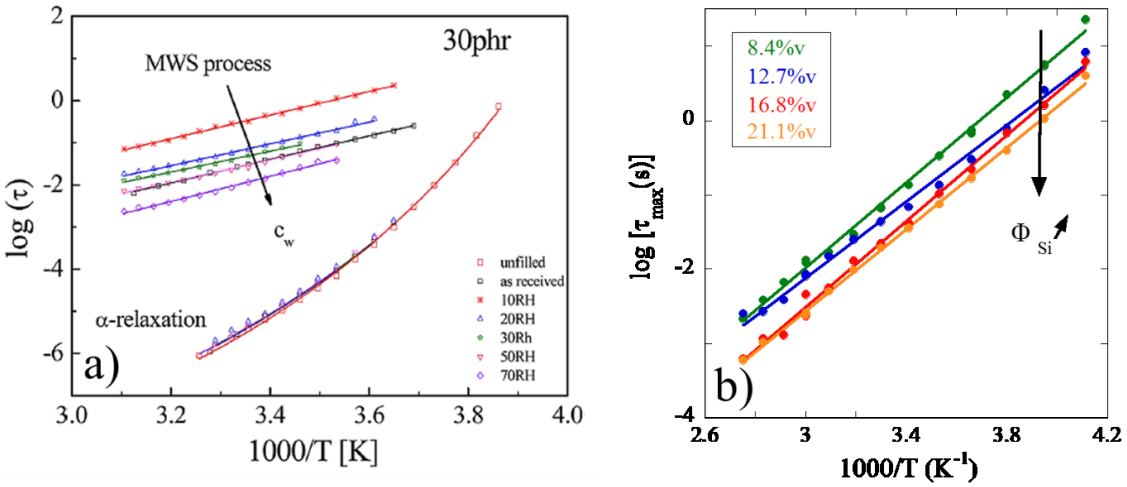

Figure 1.25 (a) Temperature dependence of the relaxation times for the MWS and α-relaxation processes at different water contents for a sample at fixed filler content (Otegui et al. 2013); (b) Dynamics of MWS1 process as a function of temperature for different filler fractions(Baeza et al. 2015b).

In particular, the same authors have reported the existence two different interfacial polarization processes (Baeza et al. 2015a): i) the already mentioned MWS1, which is the lower-T/higher-frequency interfacial process associated with the water layer at the filler interface and referred to local phenomena on the scale of few NPs; ii) the MWS2, the second - higher-T/lower frequency - interfacial process which is independent from the sample water content. The dynamics of the MWS2 process is primarily controlled by the polymer matrix, even if both conductivity and MWS2 time scales depend on the silica content (i.e., two conduction mechanisms, one through the matrix between aggregates, and another along the aggregate surface). Moreover, the MWS2 process is sensitive to depercolation (i.e., network destruction) upon polymer grafting, and it can be used to characterize the latter (Baeza et al. 2015b). Fig. 1.26 illustrates the frequency dependence of the real (ε') and imaginary (ε'') part of the complex dielectric permittivity for a silica-SB with 8.4%v of silica. The α-relaxation, MWS1 and MWS2 processes are showed in the caption.

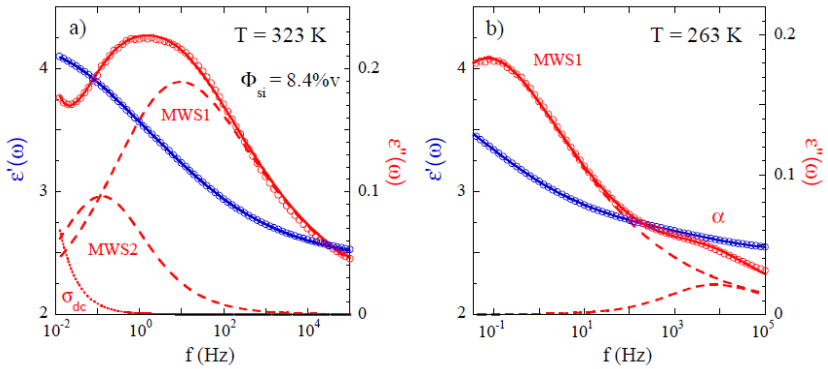

Figure 1.26 Frequency dependence of the real (ε') and imaginary (ε'') parts of the complex dielectric permittivity measured on a nanocomposite with 8.4%v silica: (a) at T=323K, a strong and broad peak described by two distinct contributions (MWS1 and MWS2) and a low-frequency upturn characteristic of the ionic conductivity are visible; (b) at T=263K, all dielectric processes are shifted to lower frequencies, which consequently makes visible the MWS1 process on the low-frequency side jointly with the primary α-relaxation. (Baeza et al. 2015b).

The filler-polymer interfacial properties have a key role in the dynamical processes of nanocomposite systems.

In the early 2000s, the presence of a "glassy" polymer fraction at the interface of particles in PNCs has been proposed to better describe the structural and dynamical characteristics of nanocomposite systems. This "glassy layer" is formed by grafted or adsorbed polymer chains that dramatically slow down their dynamics, creating a separation between the bulk polymer and the filler particle. The glassy layer has been mainly studied by Nuclear Magnetic Resonance and it has been estimated that the glassy layer has its typical thickness is around 2-3 nm (Berriot et al. 2003; Papon et al. 2011; Papon et al. 2012b). In a work of 2012, Papon et al. (Papon et al. 2011) highlighted that the presence of the glassy layer induces a slowing down of the polymer dynamics at longer range (i.e., 7-10 nm), as reported in Fig. 1.27, and this can affect the mechanical behavior of the sample..

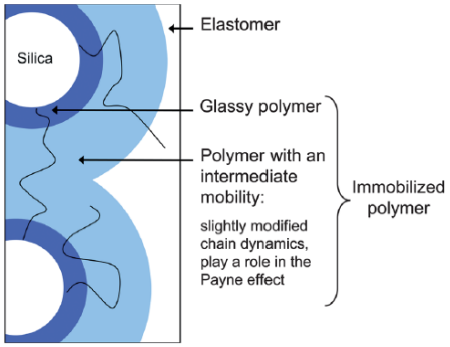

Figure 1.27 Schematic representation of glassy and immobilized polymer (Papon et al. 2012a)

Baeza et al. (Baeza et al. 2015a; Baeza et al. 2015b) showed that the presence of the silica in a styrene-butadiene matrix did not affect the α-relaxation, in agreement with Otegui et al. (Otegui et al. 2013). Moreover, the same authors proved by NMR that even if the amount of rigid polymer close to the filler surface increases with the filler fraction, it results rather low as compared with other systems (Papon et al. 2011). This is in agreement with another work by Mujtaba et al. (Mujtaba et al. 2014) where the amount of immobilized polymer in industrial silica/styrene butadiene nanocomposites had been correlated to the mechanical properties of the sample. For un-crosslinked polymer filled nanometric silica, Robertson et al. (Robertson and Rackaitis 2011) proposed an alternative approach according to which the reduced motions close to filler surface are due to a limitation in flow relaxation for chains adsorbed on filler surface, while the segmental motions are not altered by small particles

More recently, Holt et al. (Holt et al. 2014) investigated the dynamics in poly(2-vinylpyridine) (P2VP) silica- nanocomposites by BDS and Temperature Modulated Differential Scanning Calorimetry (TMDSC), showing that whereas the calorimetric glass transition temperature changes weakly with the addition of NPs, the segmental mobility of the interfacial layer is slower than the one of the polymer bulk. The same authors investigated the investigated the influence of different oxide attractive

nanoparticles (i.e. titanium, aluminum, silica, and magnesium NPs) on the P2VP segmental dynamics (Holt et al. 2013). They observed that the addition of NPs has no significant influence on the P2VP segmental dynamics, even at high loadings (e.g., 28%vol). The authors only revealed a slight reduction (of a factor 2) in the segmental relaxation time at lower temperature which had been linked to the suppression of the segmental mobility.

The impact of the filler presence on the segmental relaxation linked to the glass transition has also been investigated by Lin et al. (Lin et al. 2016). The authors studied the dynamics of nanocomposite systems made with un-grafted or PS-grafted silica NPs dispersed in a PS or PMMA matrix. To describe the dynamics in PNCs filled with silica particle surface-modificed by PS, they proposed that the presence a three-layer structure composed by: i) a "glassy" polymer layer, which consists in grafted chains immobilized at the filler interface; ii) an interfacial layer between the grafted and the free polymer chains caused by repulsive interactions, which is characterized by an enhanced mobility (α'-relaxation which fast dynamics); iii) free polymer chains in the bulk of the sample (related to the main α-relaxation). In another recent contribution, Cheng et al. (Cheng et al. 2016) also focused on the properties of the interfacial layer identifying a α'-relaxation process which corresponds to the dynamics in the interfacial layer, revealing that the increase of the molecular weight of the polymer induces a decrease of the thickness of the filler-polymer interfacial region where the segmental relaxation is slower (i.e. reduction in mass density in the interfacial region linked to the complex interplay between the adsorption of the long chains, nano-confinement and bridging effects).

In last years, the reduced dynamics at filler-polymer interface have been also investigated by Quasi-elastic Neutron Scattering (QENS). This kind of measurement indicates the presence of immobilized polymer segments close to the filler surface, according to an increase of the calorimetric glass transition temperature (Kropka et al. 2008; Akcora et al. 2010).

Mechanical characterization of PNCs: hydrodynamic reinforcement

The introduction of fillers in a polymeric matrix induces an improvement of the mechanical properties of the nanocomposite material, which is generally described by the concept of reinforcement (Heinrich et al. 2002; Stöckelhuber et al. 2017). In the linear regime, where the elastic modulus and the viscous modulus are independent of the applied strain, the reinforcement can be described as the ratio between the value of the elastic modulus at the rubber plateau for the PNC ($G'_{0\ PNC}$) and for the pure polymer matrix ($G'_{0\ PURE}$) (Oberdisse 2002).

Several models have been proposed to describe the mechanism of reinforcement in PNCs. For systems at low filler fraction (i.e., no interactions between particles), the reinforcement can be defined in analogy with hydrodynamics: for composite materials, Smallwood (Smallwood 1944) proposed a generalization

of the Einstein model for the viscosity of a colloidal suspension of rigid spheres (Einstein 1906), which is written as

$$G'_{0\,PNC} = G'_{0\,PURE}\,(1 + 2.5\Phi\,) \qquad [1.13]$$

where Φ is the filler volume fraction.

The Guth-Gold prediction (Guth 1945) can be applied to systems at higher Φ. The filler-filler interactions have been taken into account introducing a second order term

$$G'_{0\,PNC} = G'_{0\,PURE}\,(1 + 2.5\Phi + 14.1\,\Phi^2\,) \qquad [1.14]$$

Batchelor and Green (Batchelor and Green 1972) proposed to fixed the coefficient of the second order term equal to 6.2 in order to consider the effective shear modulus of the suspensions of the hard spheres in low shear limits.

A variation of the Einstein-Guth-Smallwood equation had been proposed using an effective filler volume fraction Φ_{eff} (e.g. carbon clack fillers, (Medalia 1970)). This approach considers that the particles cannot approach each other more than a certain distance, due to the repulsive forces between them. This means that fillers have an apparent or effective radius, a_{eff}, which is bigger than the real one, a, where $a_{\text{eff}} > a$ (Genovese 2012). As a consequence, the apparent or effective volume fraction is defined as

$$\Phi_{\text{eff}} = \Phi\,\left(\frac{a_{\text{eff}}}{a}\right)^3 \qquad [1.15]$$

and it results higher that the Φ. Thus, Φ can be replaced by Φ_{eff} in the models preciously introduced.

In concentrated suspensions of hard spheres, the Krieger-Dougherty, KD, model (Krieger and Dougherty 1959) introduces the maximum packing fraction $\Phi_{\max}$ for the system

$$G'_{0\,PNC} = G'_{0\,PURE}\,\left(1 - \frac{\Phi}{\Phi_{max}}\right)^{-2.5\Phi_{max}} \qquad [1.16]$$

which is usually simplified with the Quemada approximation (Quemada 1977; Nusser et al. 2013)

$$G'_{0\,PNC} = G'_{0\,PURE}\,\left(1 - \frac{\Phi}{\Phi_{max}}\right)^{-2} \qquad [1.16]$$

A recent review of Song et al. (Song and Zheng 2016) proposed a complete summary of the different models that can be used for the description of the hydrodynamic reinforcement in nanoparticle-filled polymers.

At a critical filler amount (Φ_C), the system reaches the *percolation* threshold, modifying its behavior in the viscoelastic regime since the particles start forming a tridimensional network through the sample (Fig. 1.28). Thus, a contribution related to the new interactions has to be considered and the reinforcement can be written as

$$G'_{0\,PNC} = G'_{0\,PURE}\,\left[1 + 2.5\Phi + \Theta\,(\Phi - \Phi_C)\,P\left(\Phi\,,\Phi_C\right)\right] \qquad [1.17]$$

where Θ is 1 if $\Phi \geq \Phi_C$ and 0 if $\Phi < \Phi_C$ and $P(\Phi, \Phi_C)$ is a function which depends on the critical volume fraction Φ_C and from the value of G' at the plateau modulus of the pure polymer and the PNC.

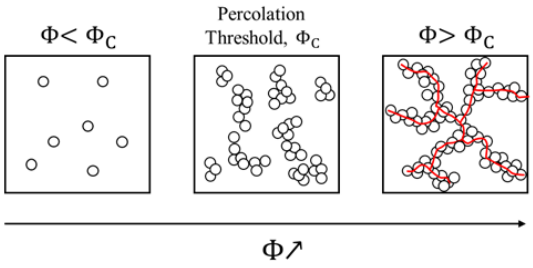

Figure 1.28 Reinforcement in PNC as a function of the filler content: from isolated particle to a percolated system.

Associated to the reinforcement, some non-linear effect can be detected in nanocomposites materials. The Payne effect is one of the most extensively studied effect (i.e., strain amplitude typically between 1-10%) which describes the viscoelastic properties of filled elastomers depending on the amplitude of applied solicitation (Payne 1965): with the increase of the deformation amplitude, the stiffness decreases because of the changes in the filler network. In Fig. 1.29a a schematic representation of a Payne effect experiment is reported. This effect can be detected by the presence of a large drop of the storage modulus and a peak in the loss modulus (Fig. 1.29b). Another well-studied non-linear effect is the Mullins effect which refers to a drop of the elastic modulus after a large amplitude stress-strain cycle, showing that the material can recovery to the initial value on a long time scale (Merabia et al. 2010).

These effects have been largely studied in filled elastomers, also in cross-linked systems whose behavior is less affected by the presence of the filler particles. The surface-modification of the fillers, which influences the filler-polymer interactions, can impact on these effects (Ramier et al. 2007b; Mujtaba et al. 2012; Papon et al. 2012a; Pérez-Aparicio et al. 2013b).

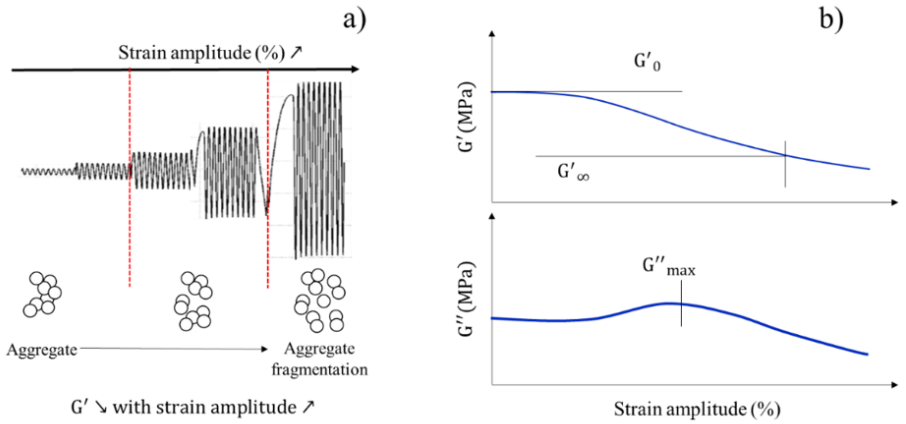

Figure 1.29 (a) Payne effect experiment: the increase of the strain amplitude induces the aggregate fragmentation and thus a decrease of the elastic modulus; (b) Schematic representation of the evolution of the elastic and viscous modulus (G' and G", respectively) as a function of the strain amplitude. G'_0 represents the G' value close to zero strain, G'_∞ is taken where there is no further change in G' with the increase of the strain (usually around the 50% strain), G''_{max} is the value of the viscous modulus at the maximum. The intensity of the Payne effect is usually estimated as $\Delta G' = (G'_0 - G'_\infty)/ G'_0$ (Papon et al. 2012a).

2. Materials and experimental methods

2. Materials and experimental methods

In this PhD thesis, we focus on two silica-polymer nanocomposite systems: the first one is the so called simplified industrial system, formulated using millimetric silica pellets and polymer by a solid mixing procedure which is commonly used in tire industry; the second one is a new model system, obtained mixing polymer dissolved in an organic solvent with of silica nanoparticles stabilized in the same solvent (solvent casting technique).

In this chapter, the components, the formulation and processing methodology used to elaborate simplified industrial and model nanocomposites (NCs) are reported. Moreover, the main techniques used to characterize these nanocomposite systems will be presented: i) Small Angle X-ray Scattering (SAXS) coupled with Reverse Monte Carlo (RMC) simulation, for the structural analysis; ii) Broadband Dielectric Spectroscopy (BDS), for the dynamical characterization.

2.1. Materials

2.1.1. Styrene-butadiene polymer

Both nanocomposite systems have been formulated using a styrene-butadiene (SB) statistic co-polymer. In particular, we worked with two different SBs (by Synthos), which have the same microstructure (same glass transition temperature, T_g) and the same molecular weight (M_w), but they differ from the end-functionalization of their polymer chains. In this regard, we used a pure non-functionalized SB (SB_NF) and another one (SB_F) with 100% of graftable polymer chains functionalized with hexa-methylcyclotrisiloxane (HMCTS or $SiMe_2$-OH) group, as shown in Fig. 2.1.

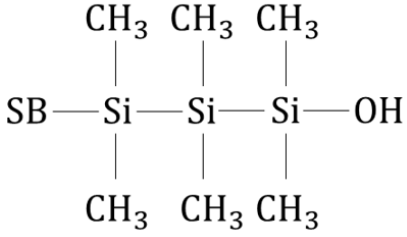

Figure 2.1 Schematic representation of SB polymer chain, end-functionalized with a $SiMe_2$-OH group.

A physical-chemical characterization of NF and F styrene-butadiene has been performed and their main properties are summarized in Table 2.1 (see more details in appendix A1).

	SB_NF	**SB_F**
% styrene	19%	20%
% butadiene	81%	80%
M_w (Molecular weight)	177 Kg/mol	170 Kg/mol
I_p (Polydispersity)	1.02	1.02
ρ (density)	0.9 g/cm^3	0.875 g/cm^3

T_g (glass transition temperature)	-24.7°C	-24.6°C
n (refractive index)	1.52	1.50

Table 2.1 Physical-chemical properties of NF and F styrene-butadiene polymer synthetized by Synthos.

2.1.2. Silane coating agents

During the preparation of silica-polymer NCs, different silane coating agents (SCAs) have been used to tune filler-filler and polymer-filler interactions.

Silane molecules characterized by ethoxy groups (O-CH_2-CH_3) have been mainly used in this work. These agents differ by the mass of their short aliphatic (or alkyl) chain, i.e., from octyl- to dodecyl- and octadecyl-triethoxysilane. According to this characteristic, they will be synthetically indicated as C_8, C_{12} and C_{18}. The main properties of these products are reported in Table 2.2 and their structure formula are shown in Fig. 2.2.

Silane coating agent (SCA)	Short name	Linear formula	M_w (g/mol)	d (g/ml)	n
Triethoxyoctylsilane	**C_8**	$C_{14}H_{32}O_3Si$	276.5	0.88 (at 25°C)	1.417
Dodecyltriethoxysilane	**C_{12}**	$C_{18}H_{40}O_3Si$	333.6	0.89 (at 20°C)	1.433
n-Octadecyltriethoxysilane	**C_{18}**	$C_{24}H_{52}O_3Si$	416.7	0.89 (at 25°C)	1.438

Table 2.2 Chemical properties of silane coating agents with ethoxy groups.

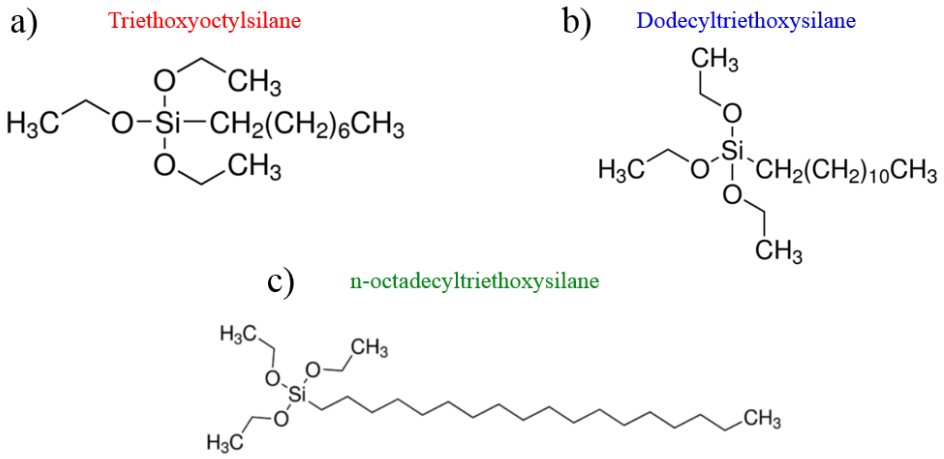

Figure 2.2 Structural formula of silane coating agents indicated in Table 2.2.

We also used C_8 coating agents with 8 carbons in the alkyl chain (C_8-) where the ethoxy groups of molecules indicated in Table 2.2 are replaced by a methoxy group (-OCH_3). The characteristics of trimethoxyoctylsilane (C_{8m}) , and methoxydimethyloctylsilane (C_{8mm}) are reported in Table 2.3 and their structural formulae are shown in Fig. 2.3a and Fig. 2.3b, respectively.

Silane coating agent (SCA)	Short name	Linear formula	M_w (g/mol)	d (g/ml)	n
Trimethoxyoctylsilane	C_{8m}	$C_{11}H_{26}O_3Si$	234.4	0.91 (at 25°C)	1.416
Methoxydimethyloctylsilane	C_{8mm}	$C_{11}H_{26}O\,Si$	202.4	0.81 (at 25°C)	1.423

Table 2.3 Chemical properties of silane coating agents with methoxy groups.

a) Trimethoxyoctylsilane

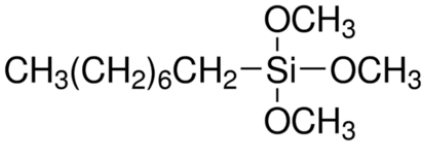

b) Methoxydimethyloctylsilane

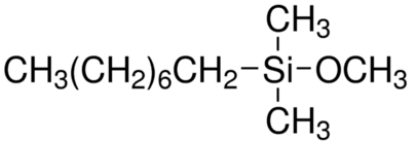

Figure 2.3 Structural formula of coating agents indicated in Table 2.3.

2.2.Simplified industrial nanocomposites

Simplified industrial nanocomposites have been prepared at the "Laboratoire d'application" of Solvay Silica (Collonges au Mont-D'Or, France). These samples have been obtained following a procedure close to the industrial one, commonly used for tire production. At the same time, these NCs have been formulated using a reduced number of components in order to simplify their characterization, identifying the impact of each ingredient on NC properties.

2.2.1. Formulation of simplified industrial nanocomposites

Simplified industrial nanocomposites are prepared using a reduced number of components:

- Styrene-Butadiene polymer (SB) - by Synthos
- Zeosil 1165MP: millimetric silica pellets with nominal specific surface of 160 m^2/g; the size distribution of the primary nanoparticles obeys a log-normal law with R_0=8.55nm, σ=27% and an average bead volume V_{Si}=3.6 10^3 nm^3 (Baeza et al. 2013a) - by Solvay
- A silane coating agent: octyl-, dodecyl- or octadecyl-triethoxysilane, indicated as C_8 (from Sigma-Aldrich, M_w=276 g/cm^3), C_{12} or C_{18} (from Alfa Aesar, M_w=332 g/cm^3 and M_w=417 g/cm^3), respectively.
- A catalyzer: Diphenyl guanidine, DPG (from Bayer, M_w =211.3 g/mol).

In order to test the influence of each component on NC properties, some key-parameters have been tuned, such as:

- Polymer matrix composition: variation of amount of SB with end-functionalized polymer chains: 0%v (SB_NF), 50%v (50/50 mixture) or 100%v (SB_F)
- Silica volume fraction (Φ_{Si}) from 0%v to 22.2%v

- Coating agent addition: C_8 is usually added as 8%w with respect to silica (Baeza et al. 2013a). Using this reference, NCs have been formulated with isomolar amounts of C_8, C_{12} and C_{18} in order to obtain the same grafting density on filler surface taking into account the different molecular weight of coating agents
- Coating agent amount: C_8 has been added as 0%w, 4%w or 8%w with respect to filler content
- Catalyzer addition: without or with DPG as 1%w with respect to polymer

All the formulated simplified industrial NCs are indicated in Table 2.2. All simplified industrial NCs have been produced by a stepwise procedure, as represented in Fig. 2.4.

a)

Φ_{Si}	0%v	8.3%v			13.30%v	18.3%v			22.2%v
SB_NF	X	C_8	C_{12}	C_{18}	C_8	C_8	C_{12}	C_{18}	C_8
50/50						C_8			
SB_F		C_8				C_8	C_{12}	C_{18}	

b)

%w silane coating agent (C_8)	0%w	4%w	8%w
Φ_{Si} = 18.3%v SB_F	DPG	DPG	DPG
	No DPG		No DPG

Table 2.4 (a) Simplified industrial NCs formulated using different polymer matrices (SB_NF,50/50 and SB_F), at different filler content (Φ_{Si} from 0%v to 22.2%v). All the samples have been performed with different coating agents (isomolar C_8, C_{12} or C_{18}) and with DPG (1%w with respect to polymer); (b) Simplified industrial NCs in a fully functionalized polymer matrix (F) at various C_8 contents and with or without DPG (1%w with respect to polymer). In these tables, the indicated filler fraction have been determined by TGA (see end of this section).

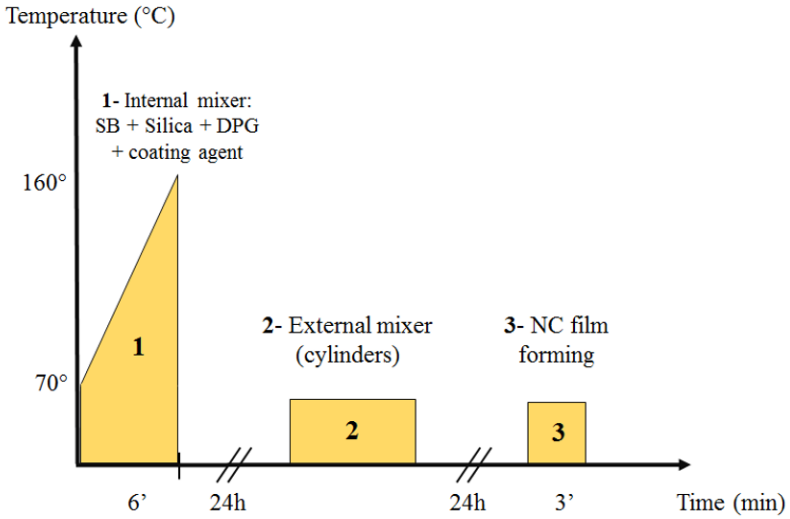

Figure 2.4 Temperature profile of formulation steps for simplified industrial NCs. Firstly, SB, silica pellets, coating agent and catalyzer are mixed (1); after that, samples are passed between rotating cylinders at 70°C and then another eleven passages after cooling at room temperature (2); finally, samples are pressed in order to obtain the final simplified industrial NC.

Firstly, the pure SB polymer has been mixed for about 1 minute and 20 seconds into an internal mixer (Thermo-Scientific Haake Rheomix OS equipped with two Banbury R3000 rotors) pre-heated at 70°C. After that, silica pellets previously mixed with coating agent and DPG, have been introduced inside the

mixer chamber by a piston and thus incorporated to the SB. During the mixing process, the speed of the rotors has been adapted between 90 and 130rpm to reach the final temperature of 160°C (Fig. 2.4, phase 1). Reaching this temperature, coupled with the mechanical action of the rotors, is essential to promote the grafting reaction of the coating agent and end-functionalized SB chains on filler surface.

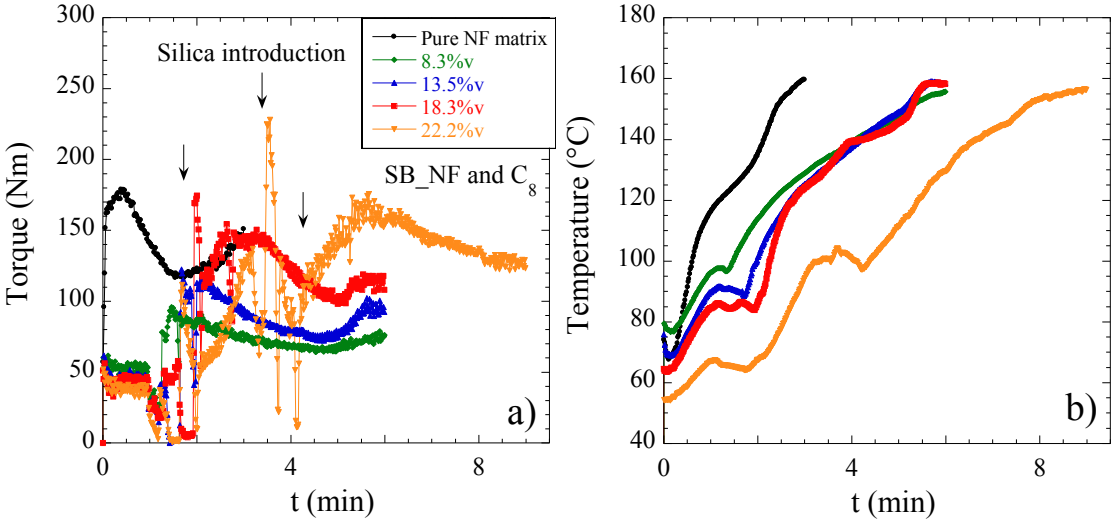

Figure 2.5 Torque (a) and temperature (b) inside the internal mixer have been monitored as function of time during the preparation of simplified industrial NCs at different silica content (Φ_{Si} from 0% to 22%v).

This mixing process can be characterized from a thermo-mechanical point of view: the evolution of torque as estimation of material viscoelasticity together with the temperature of the internal chamber have been monitored as a function of time. Torque and temperature curves for NCs at different Φ_{Si} (from 0% to 22.2%v) formulated with SB_NF matrix and C_8 as coating agent are shown in Fig. 2.5a and 2.5b, respectively. Except for the pure polymer matrix, which has been mixed just for about 3 min, the introduction and thus fragmentation of silica pellets lead to an important increase in torque and then in temperature. The final torque value increases with the increase of the filler content. The instants of introduction of silica pellet into the internal chamber can be easily identified observing the torque curve, as indicated by arrows in Fig.2.5a. For NCs at high filler content (Φ_{Si}=18.3%), silica pellets have been introduced in two times in order to obtain a better incorporation of fillers into the polymer matrix. For NCs at 22.2%v, filler addition has been performed in three times and, thus the final preparation time results a bit longer (about 8 min in spite of 6 min).

The other NC tuning parameters, such as the coating agent or polymer matrix variation, seem not to impact the torque and temperature trends as function of time (see more details in appendix A2). The appearance of a NC after the internal mixer is shown in Fig. 2.6a.

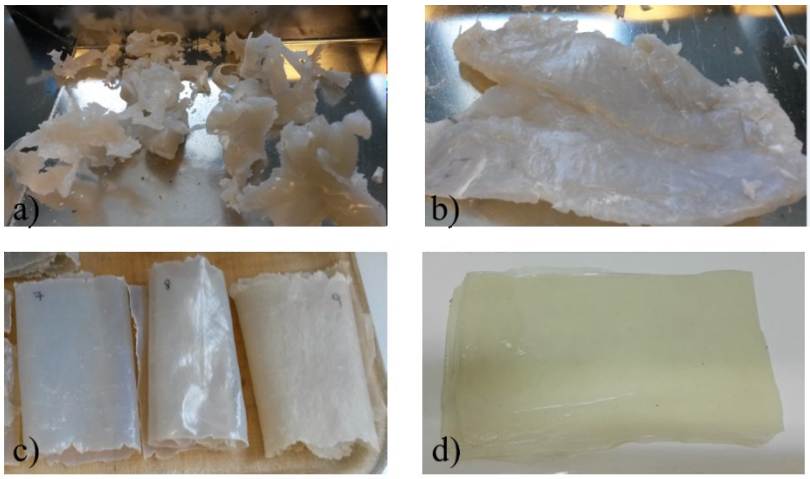

Figure 2.6 Simplified industrial NCs after the formulation inside the internal mixer (a); then after the first two (b) and the other eleven (c) passages between the rotating cylinders. The final NC is shown in figure (c).

The internal mixer step has been followed by two first passages between rotating cylinders (2mm) at 70°C (Fig. 2.6b). Then, after cooling up to room temperature, another eleven passages have been performed with a 1.5 mm gap to fix the final sample thickness (Fig. 2.4, phase 2). This procedure allows to improve the filler dispersion into the polymer matrix. The aspect of the sample after this step is shown in Fig. 2.6c. As last step (Fig. 2.4, phase 3), samples have been pressed using a caliber of 2 mm working at T=60°C, P=60 bar for 3 minutes in order to reduce the surface roughness and to obtain the final simplified industrial NCs which have an average thickness of 1.5mm (Fig. 2.6d).

The silica volume fractions of simplified industrial NCs have been determined by thermo-gravimetric analysis (TGA Star System, Mettler Toledo) applying a first ramp at 30 K/min from 25°C to 550°C under nitrogen, followed by a second ramp at 20 K/min from 550 to 950°C under air. These temperature ramps allow to achieve the complete thermal decomposition of the polymer. From the sample weight loss as a function of the temperature, the silica mass fraction $\Phi_{Si,w}$ can be determined. Then, the silica volume fraction $\Phi_{Si,v}$ (or Φ_{Si}) can be determined by mass conservation according to

$$\Phi_{Si,v} = \frac{d_{SB}\,\Phi_{Si,w}}{d_{Si}\left(1-\Phi_{Si,w}\right) + d_{SB}\,\Phi_{Si,w}} \qquad [2.1]$$

where d_{SB} is the styrene-butadiene density (Table 2.1) and d_{Si} is the silica density (d_{Si} =2.3 g/cm^3). Unless otherwise noted, our filler contents are always reported as volume fraction.

For each NC sample, the glass transition temperature (T_g) has been determined by Temperature Modulated Differential Scanning Calorimetry (TMDSC, Q2000 TA Instrument), taking into account the reverse heat capacity curve (modulated ramp at 3 K/min, ±0.5°C, 60s, under nitrogen). The T_g values are reported in Table 2.5a and 2.5b. No significant T_g variations can be observed for loaded samples as compared to the pure SB_NF matrix (T_g = -24.0°C).

a)

Φ_{Si}	0%v	8.3%v			13.30%v	18.3%v			22.2%v
SB_NF	-24.7	-24.0°C	-25.0°C	-25.0°C	-24.6°C	-24.2°C	-25.0°C	-25.0°C	-24.0°C
50/50						-24.8°C			
SB_F	-24.6	-25.0°C				-24.9°C	-25.0°C	-25.0°C	

b)

%w silane coating agent (C_8)	0%w	4%w	8%w
Φ_{Si} = 18.3%v SB_F	-25.0°C	-24.3°C	-24.9°C
	-24.9°C		-24.7°C

Table 2.5 (a) Glass transition temperature (T_g, °C) of simplified industrial NCs (corresponding to Table 2.4a); (b) Glass transition temperature (T_g, °C) of simplified industrial NCs (corresponding to Table 2.4b).

2.2.2. Bound rubber measurements

The amount of polymer grafted or adsorbed on the filler surface after the mixing process has been determined by bound rubber (BR) measurements. The quantity of non-extractable chains, or BR fraction, has been determined by the extraction of the free chains in xylene and measuring the resulting sample mass after evaporation of the solvent (i.e., Solvay registered protocol). The outcome of the BR tests is summarized in Table 2.6a and 2.6b.

a)

Φ_{Si}	8.3%v			13.30%v	18.3%v			22.2%v
SB_NF	16%	26%	25%	38%	46%	61%	41%	73%
50/50					57%			
SB_F	88%				96%	98%	99%	

b)

%w silane coating agent (C_8)	0%w	4%w	8%w
Φ_{Si} = 18.3%v SB_F	88%	92%	88%
	69%		88%

Table 2.6 (a) BR fraction of simplified industrial NCs (corresponding to Table 2.4a); (b) BR fraction of simplified industrial NCs (corresponding to Table 2.4b).

Due to the absence of antioxidant agent in the formulation, some weak crosslinking of SB occurs during the mixing resulting in an incomplete dissolution of the matrix polymer in a good solvent (e.g., tetrahydrofuran, THF). It can be observed that the BR fraction is higher for PNCs formulated with end-functionalized styrene-butadiene, according to Baeza et al. (Baeza et al. 2013b). Moreover, the quantity of non-extractable chains increase with the silica volume fraction but it is slightly affected by the DPG presence and by the C_8 amount variation.

2.3. Model nanocomposites

During my PhD work, a new silica-polymer model nanocomposite system has been developed. In this system, silica pellets used in the simplified industrial system have been replaced by colloidal silica nanoparticles (NPs). The well-defined shape (R_{Si}=12.5nm) and low polydispersity (σ=12%) of these fillers facilitate the investigation of silica structure and dispersion in a polymer matrix.

Model silica-SB nanocomposites have been formulated using the following components:

- Styrene-butadiene polymer (by Synthos)
- Colloidal silica NPs (Ludox TM40®, 40%w suspension in water, by Sigma-Aldrich) at Φ_{Si}=23.2%v
- A silane coating agent: octyl-, dodecyl- or octadecyl-triethoxysilane, indicated as C_8 (from Sigma-Aldrich, M_w=276 g/cm^3), C_{12} or C_{18} (from Alfa Aesar, M_w=332 g/cm^3 and M_w=417 g/cm^3), which differ by the length of their alkyl chain. Trimethoxy(octyl)silane, C_{8m} (from Sigma-Aldrich, M_w=234 g/cm^3), and methoxy(dimethyl)octylsilane, C_{8mm} (from Sigma-Aldrich, M_w=202 g/cm^3), have been also used.

As for the simplified industrial system, the impact of some key-parameters has been tested also for model NCs:

- Polymer matrix composition: variation of amount of SB with end-functionalized polymer chains
- Silica volume fraction (Φ_{Si}) from 0%v to 20%v (nominal)
- Coating agent addition: C_8 is usually added at 8%w with respect to silica (Baeza et al. 2013a). Using this reference, NCs have been formulated with isomolar amounts of C_8, C_{12}, C_{18}, C_{8m} and C_{8mm} in order to obtain the same grafting density on filler surface (ρ, number of molecules per nm^2) taking into account the different molecular weight of the coating agents.

2.3.1. Experimental method for surface-modification of colloidal silica NPs by silane coating agents

To develop a silica-SB model system equivalent to the simplified industrial one, the first objective was to surface-modify silica NPs using coating agents in order to tune filler-filler and then the filler-polymer interactions.

To this aim, a multi-step procedure has been optimized to obtain the efficient surface-modification of silica NPs in suspension. As first step, 4.6ml of Ludox TM40® have been diluted in water (Φ_{Si}=2.1%v), keeping the pH around 9 by the addition of sodium hydroxide (NaOH by Carlo Erba). Because of their hydrophobicity, silane coating agents have been previously dissolved in ultra-pure ethanol (EtOH, 85ml). Then, this mixture has been dropwise added to the diluted suspension of NPs in water. The ethanol/water ratio has been optimized to allow the good dissolution of all silane coating agents. The final hydro-alcoholic suspension is composed by 63%v of EtOH and 37%v of H_2O (Φ_{Si} ~ 1%v) and it

is stirred at 50°C for 24h in order to promote the grafting reaction on surface of silica NPs in suspension. The same procedure also allows to stabilize raw NPs (without coating agent addition) in H_2O/EtOH mixture.

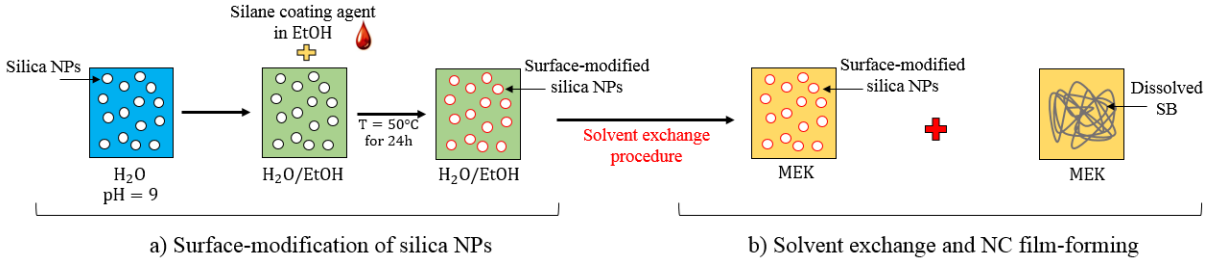

Figure 2.7 Multi-step method for surface-modification of silica NPs in suspension by grafting of silane coating agent molecules.

This multi-step method, schematically represented in Fig. 2.7, shows several key-points. First of all, the water in the hydro-alcoholic suspension allows to obtain the hydrolysis (i.e., breaking of a bond in a molecule using water) of lateral groups -O-CH_2-CH_3 of silane molecules. Then, it can react on filler surface which is negatively charged. The basic pH of the initial colloidal suspension (NPs in water) provides the prevalence of negative charges (-O^-) on particle surface (Wyss 2003) preserving the colloidal stability. Moreover, the dropwise addition of EtOH/coating agent mixture together with the stirring allows to slowly incorporate the coating agent in a hydrophilic environment avoiding phase separation phenomena.

2.3.2. Characterization of surface-modified silica NPs

Once the surface-modification has been performed, an evaluation of the grafting reaction has been carried out estimating the silane grafting density on silica NP surface.

Following the washing steps (i.e., in ethanol for three times), only silane molecules attached to the NP surface can still be present in the suspension. By running infra-red experiments under attenuated total reflection (ATR), absorption bands specific to chemical bonds of these silane molecules have been detected, as shown in Fig. 2.8 for C_8, C_{12} and C_{18} silanes. The strong intensity around 1000 cm^{-1} is a superposition of silica signals, i.e. it is unspecific with respect to grafting. In the inset of Fig. 2.8, a zoom on peaks around 2950 cm^{-1} related to C-H stretching vibrations of the ethoxy group (-O-C_2H_5) of the silane molecules (Deshmukh and Aydil 1995; Mondragón et al. 1995) is shown. Note that in absence of any graft (i.e., raw NPs), only a baseline is detected here whereas a non-quantifiable intensity is found in presence of grafts. The presence of these groups after washing shows that the corresponding molecules are indeed attached, but that all lateral side groups have not been hydrolyzed. For the following estimations of the grafting density ρ, two lateral groups were assumed to have reacted, either with a surface SiOH, or a neighboring molecules.

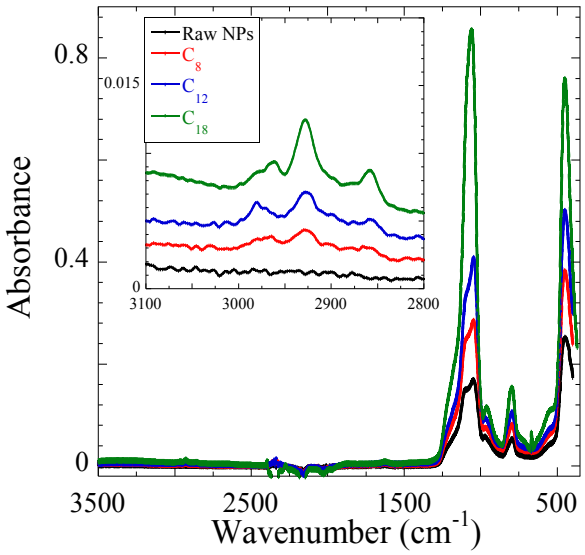

Figure 2.8 Evidence of silane grafting on NPs by ATR, with a zoom around 2950 cm^{-1} shown in the inset.

The samples analyzed by ATR have been then investigated by thermogravimetric analysis (TGA) applying a 5 K/min temperature ramp from 35°C to 900°C, under air. This technique allows to characterize the amount of organic material with respect to the silica. In Fig. 2.9a, the complete TGA curves for the tri-ethoxy grafts (C_8, C_{12}, C_{18}) at identical molar concentration are shown. It can be observed that the mass loss with increasing temperature is found to be strongly affected by the type of graft, and it is higher for the more massive molecules having a longer alkyl chain, which had been introduced in isomolar amounts. The mass loss can be translated into the silane grafting density recognizing that (a) the weight loss at low temperatures (< 200°C) is given by physisorbed water, and that (b) the weight loss above 550°C is affected by condensation of silanol groups on silica particle surface, as one can show by comparing to bare NPs (Chen et al. 2005). Assuming that the loss between 200°C and 550°C results from the decomposition of grafted coating agent molecules only, the relative weight loss with respect to bear NPs has been considered in this temperature range, as represented in Fig. 2.9a. Assuming the average hydrolysis of two lateral groups, the amount of reacted agent and the grafting densities can be estimated, as reported in Table 2.7. Details of the calculations are reported in Appendix A4. For completeness, the grafting densities would be approximately 0.15 nm^{-2} lower if only one lateral group were assumed to have reacted. Assuming for comparison the formation of a uniform monolayer on the filler surface of density 0.88 g/cm^3, its equivalent thickness can be estimated. The same approach has been used to evaluate the grafting densities also for NPs surface modified by C_{8m} and C_{8mm} silanes (Table 2.7). Obviously, for the monofunctionalized C_{8mm} agent the hydrolysis of one single group has been assumed. The TGA measurements for the NPs surface-modified by C_{8m} and C_{8mm} are reported in Appendix A4.

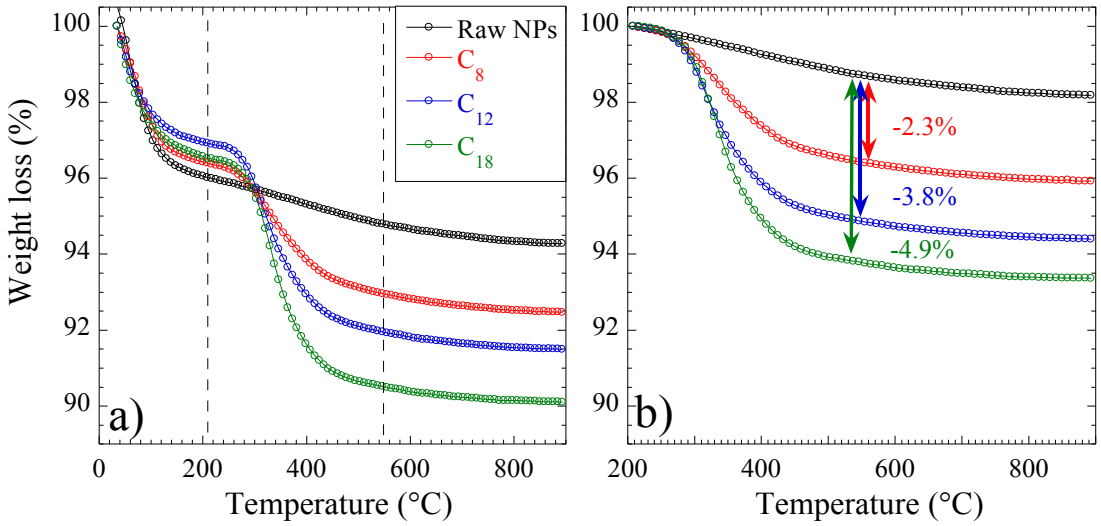

Figure 2.9 (a) Weight-loss curves between room temperature and 900°C is related to the evaporation of water physically absorbed on NPs (up to 200°C), to the decomposition of grafted silane molecules (between 200°C and 550°C) and to the condensation of silanol groups on silica surface (up to 900°C). (b) The weight loss between 200°C and 900°C for raw silica NPs and for NPs surface-modified with C_8, C_{12} or C_{18}. For the evaluation of the grafting density, only the weight loss between 200°C and 550°C has been considered.

Silane coating agent	%w reacted	grafting density (molecules/nm^2)	monolayer thickness (nm)
C_8	64.0%	1.1	0.55
C_{12}	72.2%	1.2	0.75
C_{18}	63.1%	1.1	0.84
C_{8m}	72.4%	1.2	0.51
C_{8mm}	77.3%	1.3	0.53

Table 2.7 Estimation of the amount of reacted coating agent, the grafting density and the equivalent monolayer thickness for different silanes.

2.3.3. Film formation: model PNCs

To obtain a model NC, the surface-modified silica NPs have to be dispersed into the SB matrix.

This polymer shows a hydrophobic behavior. It can be dissolved in several organic solvents (toluene, cyclohexane, methyl-ethylketone) but not in the in H_2O/EtOH mixture where NPs are previously dispersed. Thus, to stabilize the surface-modified NPs in the same solvent used for polymer dissolution, a solvent exchange method has been developed (Fig. 2.7, phase b).

As first step, the hydro-alcoholic suspension has been dialyzed for 24h in a pure ethanol bath. The concentration gradients allow to push out most of the water and eventual free coating agent molecules. Then, the suspension has been dialyzed two times for 24h in pure Methyl-ethylketone (MEK or 2-Butanone, by Sigma-Aldrich) to remove residual water and to replace ethanol with the selected organic solvent. Finally, the suspension of surface-modified NPs stabilized in MEK (dialysis suspension) is sonicated for 90 minutes at room temperature. In analogy with agent-coated particles, also bare colloidal silica can be transferred in MEK. The residual amounts of H_2O and EtOH in the final dialysis suspension

have been determined by liquid nuclear magnetic resonance (NMR) and they result equal to 2.2%v and 2.5%v, respectively. This solvent exchange procedure allows the stabilization of surface-modified or bare NPs in an organic solvent preserving the colloidal stability from the initial water suspension (see chapter 4). As last step, MEK suspension (Φ_{Si}=1%v about) is mixed w SB polymer previously in MEK at a volume fraction R=0.1. This mixture is stirred for 1h30 and then put into a Teflon support for 24h at 50°C to promote the complete solvent evaporation (solvent casting technique). Final model NCs at different silica contents are shown in Fig. 2.10.

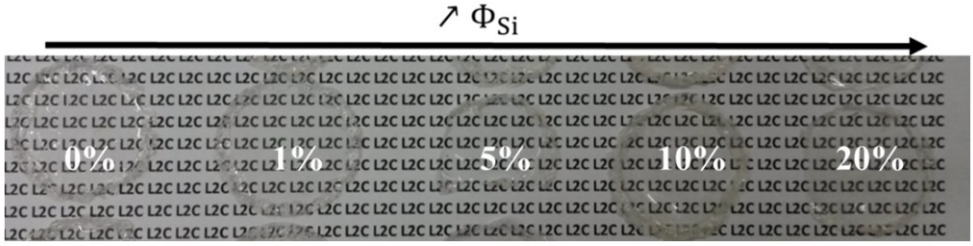

Figure 2.10 Model NCs at different filler content made by a solvent casting technique, using colloidal silica NPs stabilized in the MEK and SB dissolved in the same solvent. All the samples result transparent which means that there are no macroscopic aggregation or phase separation phenomena.

As for simplified industrial NCs, the silica volume fractions have been determined by TGA applying the same experimental conditions indicated in the previous section. In this case, the density of the silica particles d_{Si} is assumed equal to 2.2 g/cm^3.

The glass transition temperature (T_g) of each NC sample has been determined by TMDSC (modulated ramp on reverse heat capacity curve, at 3K/min, ±0.5°C, 60s, under nitrogen). As example, the T_g values for samples prepared at different Φ_{Si} (from 0%v to 20%v) using SB_NF polymer and C_8 as coating agent are reported in Table 2.8. No significant T_g variations can be observed for loaded samples as compared to the SB_NF matrix (0%v). The variation of coating agent or polymer matrix do not impact the T_g values.

Φ_{Si} (%v nominal)	**0%v**	**1%v**	**5%v**	**10%v**	**20%v**
T_g (°C)	-24.7	-24.8	-24.8	-24.7	-24.9

Table 2.8 Glass transition temperature (T_g) for model NCs formulated at different silica content using NF styrene-butadiene and C_8 as coating agent.

2.3.4. Bound rubber measurements

As for the simplified industrial nanocomposites (section 2.2), we try to estimate the amount of polymer grafted or adsorbed on the filler surface (i.e., BR fraction) also in model nanocomposites. In this case, the extraction of the free polymer chains has been performed by a multi-step procedure. Firstly, the initial mass of the NC has been evaluated. Then, the sample has been completely dissolved in MEK and centrifuged to promote the particle sedimentation and to keep the polymer in the supernatant. In order to remove all the free polymer, the sample has been washed and centrifuged for two times in MEK and

for two times in chloroform and between each step it has been sonicated. Finally, the residual silica has been dried and weighed. The BR fraction has been calculated as follows

$$BR = \frac{M_S - M_i \Phi_w}{M_i(1 - \Phi_w)} \quad [2.2]$$

where M_i is the initial mass of the sample, M_s is the mass of the dried sample after the extraction and Φ_w is the mass fraction of silica in the sample.

This kind of measurement has been performed just for few model nanocomposites formulated at high silica fractions with SB_F or SB_NF polymer. The very low values of BR fraction summarized in Table 2.9 proves that the both SB_NF and SB_F polymers are not grafted or adsorbed on the filler surface. This result will be recalled in Chapter 5.

NC sample	Φ_{Si} (%w)	BR (%)
SB_NF, C_{18}	23.1	0.0113
SB_F, C_{18}	22.3	0.0173
SB_NF, C_{18}	35.4	0.0202
SB_F, C_{18}	30.2	0.0294

Table 2.9 BR fractions of model NCs formulated at two different silica contents using SB_F or SB_NF polymer.

2.4. Structural characterization of PNCs

Small angle scattering (SAS) techniques are commonly used in soft matter studies to determine structural characteristics of systems at nanometric scale. For silica-polymer PNCs, this analytical method allows to obtain fundamental information such as average size, shape and polydispersity of primary particles or aggregates.

In this PhD work, Small Angle X-Ray Scattering (SAXS) measurements have been performed and analyzed. In particular, experiments have been done on beamline SWING at Synchrotron Soleil (Saint Aubin, France) using standard conditions: sample-detector distances of 2m, 5m and 6,5m and the wavelength λ=1Å giving a q-range from 6.2 10^{-4} $Å^{-1}$ to 5.6 10^{-1} $Å^{-1}$. Standard data reduction tools given by Soleil were used (Foxtrot 3.1).

In this section, the physical concepts of SAXS are reported (Lindner and Zemb 1991).

2.4.1. Basics of Small Angle Scattering

During a SAXS measurement, an X-ray beam is sent through the sample and thus it can interact with it in three ways: transmission, absorption, and scattering. When X-rays hit a material, a fraction is transmitted in the same direction of the incident ray, a part will be absorbed and transformed into other forms of energy (heat, fluorescence radiations, etc.) and another one will be scattered into other directions of propagation. In this last case, every object inside the X-ray beam will contribute to a "scattering" signal which is collected at different angles by a 2D-detector (Fig. 2.11)

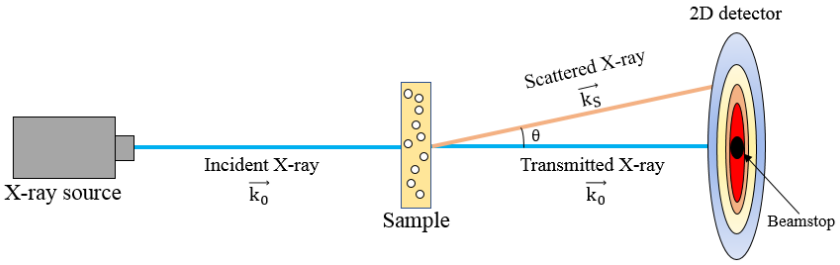

Figure 2.11 Schematic representation of Small Angle X-ray Scattering (SAXS) measurement. The wave vector of the incident X-ray ($\vec{k}_0$) and the one of the scattered X-ray ($\vec{k}_s$) do not have the same direction but they have the same magnitude $|k_0| = |k_s|$ (elastic scattering).

During an experiment, only the intensity of the scattering signal is measurable (i.e. only the squared amplitude of the scattered wave $I = |\vec{E}|^2$) which can be used to evaluate the average structure of all objects illuminated by the beam. This intensity is commonly represented as a function of the scattering vector q [nm^{-1}] which is defined as

$$\vec{q} = \vec{k}_s - \vec{k}_0 \qquad [2.3]$$

where $\vec{k}_0$ is the wave vector of the incident X-ray and $\vec{k}_s$ is the one of the scattered X-ray.

The magnitude of the scattering vector is defined as

$$|q| = \frac{4\pi}{\lambda}\sin(\theta/2) \qquad [2.4]$$

where λ is the wavelength of the X-ray beam and θ is the angle between the incident and the scattered radiation.

The scattering intensity I(q) is defined as the differential scattering cross-section per unit sample volume ($d\Sigma/d\Omega$). Such a parameter is expressed in [cm^{-1}] and it represents the probability of a particle of the incident beam being scattered out from the unit sample volume into the solid angle ΔΩ. In few words, the intensity I(q) provides the quantitative representation of the sample-radiation interaction and contains information on the structure of the sample. Moreover, for a monodisperse system of object with spherical symmetry, I(q) can be expressed as

$$I(q) = \Delta\rho^2 \Phi V_o P(q) S(q) \qquad [2.5]$$

where Δρ is the scattering contrast between sample phases (e.g., objects and medium), Φ is the volume fraction of objects in the medium (e.g., particles in polymer matrix), V_o is the object volume, P(q) is the form factor of the object and S(q) is the structure factor. The latter is related to the spatial arrangement and interactions between objects.

Scattering contrast

As shown in formula 2.5, the measured intensity depends not only on the structure of the individual scattering elements and their interactions, but also on the so-called scattering contrast Δρ. It can be considered as the visibility of the object in the medium. It is given by the difference between the

scattering length density (ρ_o) of an object and the one the medium (ρ_m) where it is dispersed (e.g. silica particle in a polymer matrix or solvent)

$$\Delta\rho = \rho_o - \rho_m \quad [2.6]$$

where ρ_o is the scattering length density of the object and ρ_m is the one of the suspending medium.

In particular, the scattering length density is linked to the way each atom scatters which is represented by the scattering length (b). The scattering length for an atom b_i can be used to calculate the total b and then the scattering length density ρ of a molecule, as shown in formula [2.7].

$$\rho = \frac{\rho_m N_A}{M} \Sigma_i n_i b_i \quad [2.7]$$

where ρ_m is the mass density of the object, N_A is the Avogadro number (6.022 10^{23} mol^{-1}), M is the molecular weight, b_i is the scattering length of atom *i* and n_i number of atoms of type *i* in the molecule.

In SAXS experiments, because of the interactions of the X-ray beam with the electron cloud of atoms, the scattering length is defined as

$$b_i = Z_i b_e \quad [2.8]$$

where Z_i is the atomic number of atom *i* and b_e is the scattering length of an electron which is equal to 2.85 10^{-5} Å.

For neutrons, values of bi can be found on the NIST Center for Neutron Research (https://www.ncnr.nist.gov/resources/n-lengths/list.html). The neutron and X-ray scattering length densities for some components used in this thesis are reported in Table 2.10.

	$\rho^{Neutron}$ (cm^{-2})	ρ^{X-ray} (cm^{-2})
H_2O	$-5.61\ 10^9$	$9.45\ 10^{10}$
D_2O	$6.33\ 10^{10}$	$9.47\ 10^{10}$
C_2H_6O (EtOH)	$-3.44\ 10^9$	$7.58\ 10^{10}$
C_2D_6O	$6.22\ 10^{10}$	$7.73\ 10^{10}$
C_4H_8O (MEK)	$1.66\ 10^9$	$7.66\ 10^{10}$
SiO_2	$3.48\ 10^{10}$	$18.89\ 10^{10}$

Table 2.10 Neutron and X-ray scattering length densities for some of components used in this work. The relevant difference between the neutron scattering length densities of water and deuterated water underline the possibility to enhance system characteristics using a protonated or a deuterated solvent. For X-ray, silica shows a ρ high value (high number of protons) resulting well detectable.

Form factor P(q)

In a diluted system, objects (e.g., particles) are widely separated and it is possible to assume that their positions are not correlated. In this case, the structure factor S(q) linked to interactions between objects can be assumed equal to 1 and the form factor P(q) of a single object can be determined using the formula [2.9].

$$P_0(q) = \frac{I(q)}{\Delta\rho^2 \Phi V_o} \quad [2.9]$$

For a homogenous sphere with radius R, the normalized form factor $P_0(q)$ can be written as

$$P_0(q) = \left[3\frac{(\sin qR - q\,R\cos qR)}{(qR)^3}\right]^2 \qquad [2.10]$$

The form factor of a sphere of radius R=12.5 nm is shown in Fig. 2.12.

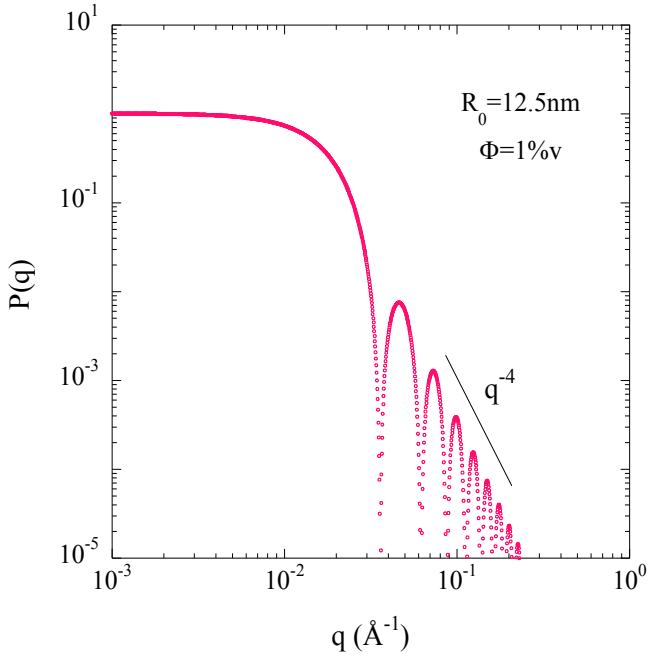

Figure 2.12 Form factor P(q) for a spherical object of radius R=12.5nm.

Different regimes can be described as a function of the scattering vector q.

The behavior at low q values (q→0, qR<<1, also called forward scattering) is particularly interesting for particulate systems in a diluted regime. When q tends to zero, the form factor P(q) obeys a general expression which depends only on the radius of gyration of the particle R_g. In these conditions, the scattering intensity for a diluted suspension decreases around the central beam as

$$I(q) \approx \Delta\rho^2 \Phi V_o e^{-(qR_g)^2/3} \qquad [2.11]$$

following the so-called **Guinier approximation** (Guiner et al. 1955; Lindner and Zemb 1991). The radius of gyration can be measured by looking at the intensity limit behavior when q→0. Moreover, using the radius of gyration R_g, the radius of the equivalent sphere (what we call Guinier radius R_G) can be evaluated knowing that

$$R_g = \sqrt{\frac{3}{5}} R_G \;\; ; \quad qR_g<1 \qquad [2.12]$$

In the monodisperse case, R_G corresponds to the "geometrical" radius of the scattering spherical object. Also the behavior in the large q limit ($q>1/r_c$ where r_c is the curvature radius) can be evaluated. For a two- phase system the intensity can be expressed by the **Porod approximation**

$$I(q) = \frac{A}{q^{6-D_s}} \qquad [2.13]$$

where D_s is the fractal dimension associated with the surface of the scattering object. For a perfectly smooth surface D_s is equal to 2. This means that the intensity decreases as q^{-4} at large q and the Porod law in its final form can be written as

$$\lim_{q\to\infty} I(q) = A = \frac{2\pi(\Delta\rho)^2}{q^4}\frac{S}{V} \qquad [2.14]$$

where $\Delta\rho$ is the contrast between scattering objects and the medium and S/V is the cumulated specific surface area of the scattering objects. Thus, the Porod's law allows to measure the specific surface of objects. This result persists also for concentrated systems or for systems no more made of separated particles. Moreover, for spherical objects the specific surface S/V allows to obtain the radius (Porod radius, R_P) for a known object volume fraction Φ

$$\frac{S}{V} = \frac{3\Phi}{R_P} \qquad [2.15]$$

For a monodisperse system composed of identical spherical elements, the Porod radius is equal to the geometrical radius of the sphere.

Structure factor

Let us consider a system composed of identical, spherical objects. The average distance between them depends on the object concentration in the system. When it becomes comparable to the distance inside the objects, this means that the interference pattern will contain contributions from neighboring particles as well and thus the spatial correlation between objects has to be taken into account. Thus, for N identical scattering particles correlated in the space, their interactions can be represented by the structure factor S(q) which is defined as

$$S(\mathbf{q}) = 1 + \frac{1}{N}\langle\sum_{i=1}^{N}\sum_{j\neq i}^{N} e^{i\mathbf{q}\cdot(\mathbf{r}_j-\mathbf{r}_i)}\rangle \qquad [2.16]$$

where N is the number of objects in the system, $\mathbf{r}_j$ and $\mathbf{r}_i$ are the center position of the object j and i, respectively.

For q=0, the structure factor S(q=0) allow to evaluate the mass of the scattering objects. In particular, using the equation [2.16], S(q=0) is equal to N which means that all the objects scatter in phase and all amplitudes add up constructively. For hard-sphere with short-range interaction potential, the Percus-Yevick approximation can be applied (Hansen and Mcdonald 1990; Lindner and Zemb 1991) and the so-called Percus-Yevick structure factor $S_{PY}(q\to0)$ can be used. In particular, its low-q limit $S_{PY}(q\to0)$ can be written as

$$S_{PY}(q\to 0) = \frac{(1-\Phi)^4}{(1+2\Phi)^2} \qquad [2.17]$$

where Φ is the object volume fraction.

Polydispersity

The assumption that the N objects in a system are all identical is rarely true. They usually have different sizes and shapes. This non-uniformity is called polydispersity and it is a common problem in practical applications. In principle, it is not possible to determine simultaneously shape and size distribution of a polydisperse system by scattering data. To approach to this problem, different ways can be considered. For example, it is possible to assume the shape and then determine the object size distribution or define the shape fixing the size distribution. In the first case, it is hypothesized that all the objects have the same shape and internal structure and their characteristics only depend on a size parameter (i.e., sphere radius R). For a system composed by spherical objects, which is one of the most common case, the total scattering intensity I(q) of a dilute suspension can be written as the sum over the contributions from objects of different sizes for a continuous distribution

$$I(q) = c_i \int_0^\infty D\,(R) \cdot P_0(q,R)\, dR \qquad [2.18]$$

where c_i is a normalization constant and $P_0(q,R)$ is the normalized form factor of a sphere of radius R. The term D(R) represents a size distribution which can be approximated by an analytical model where only few parameters need to be estimated, such as the mean size, the center of the distribution or its width (standard deviation). For example, a log-normal distribution function can be used to describe the probability to find an object of size R (Despert and Oberdisse 2003).

$$D(R, R_0, \sigma) = \frac{1}{\sqrt{2\pi}R\sigma} \exp\left[-\frac{1}{2}\left(\frac{\ln(R/R_0)}{\sigma}\right)^2\right] \qquad [2.19]$$

where R is the radius of the object and R_0 is defined as the "scaling radius" typical of the log-normal distribution, giving the average radius $\langle R \rangle = R_0 e^{\sigma^2/2}$. The σ term is the geometrical standard deviation which allows to define the polydispersity index (PI) as

$$PI = \frac{\langle R^2 \rangle - \langle R \rangle^2}{\langle R \rangle^2} = \sqrt{e^{\sigma^2} - 1} \sim \sqrt{\sigma^2} = \sigma \qquad [2.20]$$

where the last equation holds for small sigma. The influence of the polydispersity can be easily observed on the form factor P(q) of a sphere. In particular, the width of the oscillations decreases with the increase of the polydispersity, as shown in Fig. 2.13. Moreover, polydispersity can be taken into account in the Percus-Yevick S(q) (Lindner and Zemb 1991) which can be written as

$$S_{PY}(q \to 0) = \frac{(1-\alpha\Phi)^4}{(1+2\alpha\Phi)^2} \qquad [2.21]$$

where α is a parameter depending on system polydispersity.

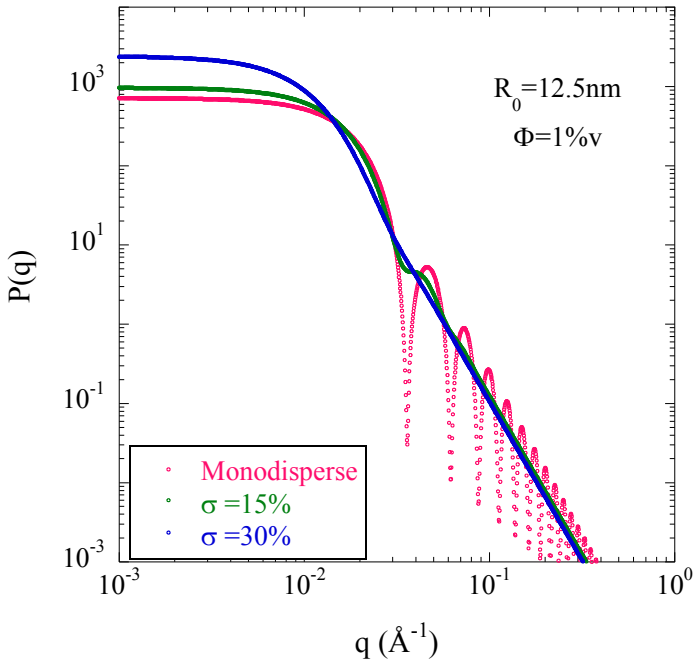

Figure 2.13 Form factor P(q) for a spherical object of radius R=12.5nm at different polydispersity values σ. These form factors have been obtained using the formula [2.10] for a polydipersity characterized by a log-normal distribution.

2.4.2. Useful tools for structural analysis of silica-polymer nanocomposites

In physics, a lot of systems, such as silica-polymer nanocomposites, cannot be described as "simple" dispersion of objects. Due to their complexity, the analysis and interpretation of their scattering data are not easy and thus some definitions and models result useful to well describe the structural properties of these systems (Genix and Oberdisse 2015).

Reduced representation: To compare SAXS data of samples characterized by different volume fractions Φ (i.e. NCs at different silica contents Φ_{Si}), their scattering intensities can be normalized for the real Φ in order to work with the so-called reduced representation I(q)/ Φ which gives direct access to the variations in the structure factor S(q), P(q) being fixed (Baeza et al. 2013a). Moreover, for silica-polymer NCs, matrix (pure polymer) contributions have been measured independently and subtracted from intensity signal of NC.

Aggregation number and compacity: Spherical objects inside a system can interact between them and eventually "stick" together forming aggregates (i.e., in NCs, aggregates are made of silica particles and polymer trapped between them), as shown in Fig. 2.14.

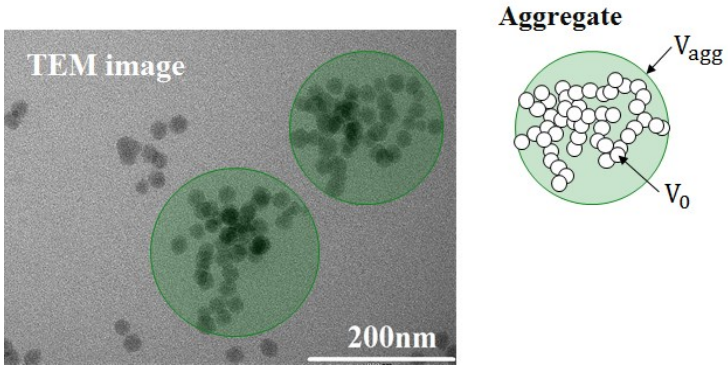

Figure 2.14 Transmission Electron Microscopy (TEM) image of a silica-polymer NC (Φ=1%v). The green circle defines the size of an aggregate inside the sample. On the right, the same aggregate is schematically represented to define the aggregate volume (V_{agg}) and the volume of a single particle or object (V_o).

In this case, a parameter called aggregation number N_{agg} can be introduced. It refers to the number of objects inside an aggregate and it is defined as

$$N_{agg} = \frac{V_{o\ in\ agg}}{V_o} \qquad [2.22]$$

where $V_{o\ in\ agg}$ is the effective volume of spherical objects in an aggregate and V_o is the average volume of a single object. For non-interacting aggregates, at low-q values, the value of N_{agg} can be evaluated as the ratio between the sample scattering intensity and the form factor P(q) intensity, following the equation [2.22]. Moreover, this parameter is linked to another one called local aggregate density or compacity κ which is related to the aggregate size and the amount of silica inside an aggregate (Baeza et al. 2013a; Genix et al. 2016a). In particular,

$$\kappa = \frac{V_{o\ in\ agg}}{V_{agg}} \qquad [2.23]$$

and

$$N_{agg} = \frac{4}{3}\pi {R_{agg}}^3 \frac{\kappa}{V_o} \qquad [2.24]$$

where $V_{agg} = \frac{4}{3}\pi {R_{agg}}^3$ is the total aggregate volume.

Local interaction region and correlation hole: For some complex systems, at intermediate-q range (q ~ 10^{-2} Å^{-1}) the scattering intensity starts decreasing with respect to the form factor P(q), as shown in Fig. 2.15 (inset). This is due to the repulsive local interactions between objects structured on the nanoscale (i.e., repulsive interactions between nanoparticles in close contact inside an aggregate) which determine a decrease of the structure factor in the intermediate-q range forming the so-called correlation hole (Schmitt et al. 2016). Thus, intensity at intermediate-q range can be interpreted using a numerical relationship between the structure factor at the correlation hole and the local volume fraction with the

Percus-Yevick structure factor $S_{PY}(q)$. In particular, the limiting value of $S_{PY}(q \to 0)$ can be re-written as

$$S_{PY}(q \to 0) = \frac{(1-\alpha\kappa)^4}{(1+2\alpha\kappa)^2} \qquad [2.25]$$

where α considers the polydispersity of the system objects and κ is the local compacity.

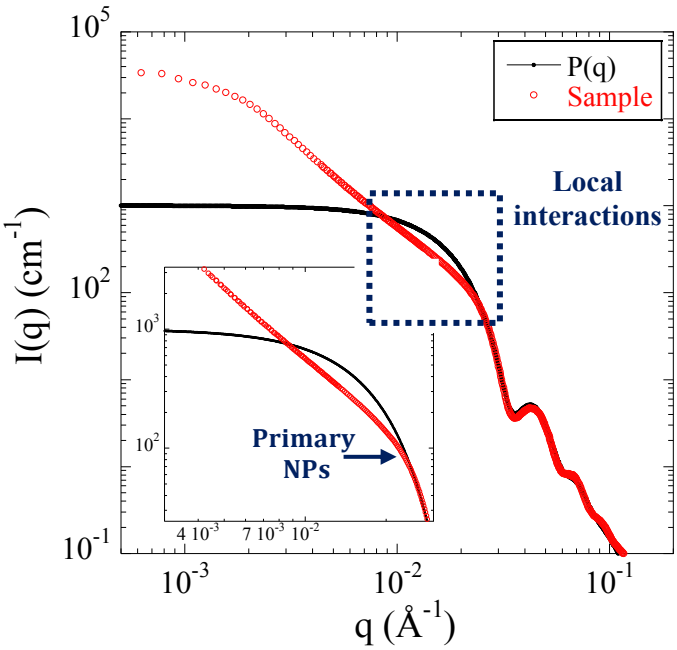

Figure 2.15 Example of scattering intensity I(q) for NCs (Φ=1%v) and form factor P(q) for a spherical object (i.e., silica nano-particle) with radius R=12.5nm and σ=12%. At a certain q value (q_p) in the intermediate-q range, the sample intensity starts decreasing with respect to the form factor (inset) defining the local interaction region (correlation hole). In this region, the structure factor $S_{PY}(q)$ can be evaluated using the Percus-Yevick approximation taking into account the polydispersity and the local compacity.

Fractal dimension: For diluted systems of identical aggregates, the low-q intensity increase can be described by a power law related to the fractal dimension d (i.e., aggregate fractal dimension) which relates the aggregate mass variation to the aggregate volume changing. Using this parameter d the aggregation number N_{agg} can be written as

$$N_{agg} = \left(\frac{R_{agg}}{R}\right)^d \qquad [2.26]$$

where R_{agg} is the aggregate radius and R is the radius referring to the average object volume in the polydisperse system.

Also the compacity can be related to the fractal dimension as

$$\kappa = \left(\frac{R_{agg}}{R}\right)^{d-3} \qquad [2.27]$$

The fractal dimension of a compact object is equal to 3 and thus for aggregates is generally between 1 and 3.

Cubic model: In some cases, a well-defined peak can be observed at low-q values, as shown in Fig. 2.16a. This peak represents the signature of a repulsive interactions between objects. In some cases which can be described by a Yukawa potential function.

A simplified description of this behavior can be obtain assuming that spherical objects of a system are organized in aggregates which are separated by a certain distance on a cubic lattice (cubic model, schematically represented in 2.16b). In this case, the position of the repulsive peak q_{rep} allows to determine the most probable distance d_{agg} between the mass centers of two aggregates, which can be defined as

$$d_{agg} = \frac{2\pi}{q_{rep}} \qquad [2.28]$$

Thus, the average aggregate volume can be determined as

$$\langle V_{agg} \rangle = \Phi \left(\frac{2\pi}{q_{rep}} \right)^3 \qquad [2.29]$$

and the aggregation number N_{agg} can be calculated as

$$N_{agg} = \frac{\langle V_{agg} \rangle}{V_o} \qquad [2.30]$$

where V_o is the average volume of a single object.

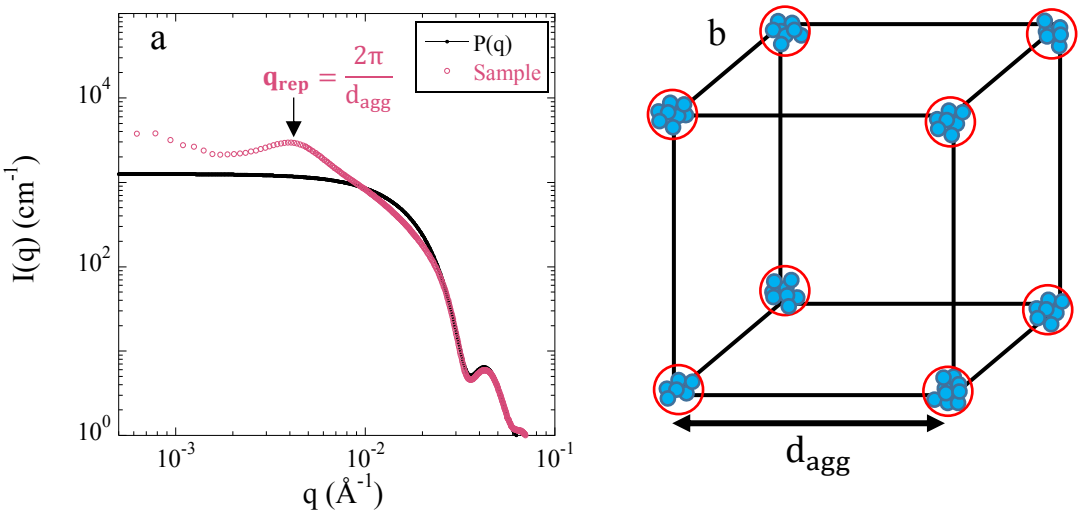

Figure 2.16 (a) SAXS curve of silica-polymer NC where a well-defined repulsive peak can be observed. This experimental curve is superimposed to the form factor P(q) of a spherical particle of radius R=12.5nm and polydispersity of 12%. (b) Schematic representation of cubic model.

2.5. Reverse Monte Carlo (RMC) simulations

Reverse Monte Carlo (RMC) simulations can be combined to SAXS measurements in order to extract detailed information on aggregate distribution functions in NP suspensions and polymer nanocomposites and to obtain a 3D-reconstruction of particle configuration compatible with the experimental scattering data. A new RMC method has been developed at the Laboratoire Charles Coulomb by Julian Oberdisse. Its application, coupled to the experimental SAXS measurements (see Chapter 4), reveals that all the interactions between particles which make aggregates can be described by focusing on particle configuration in real space. Then, an analysis in terms of aggregate distribution functions can be performed. Isolating aggregates thus allows ignoring interactions between potentially polydisperse aggregates, while describing the scattering consistently. The description reproduced in this section has been adapted from (Musino et al. b, submitted).

The main idea of reverse Monte Carlo applied to colloids is to produce configurations of polydisperse hard spheres in space, determine the scattering cross sections with special care to avoid finite size effects of the simulation box, and then adjust the configurations such that the experimental scattering curve is reproduced, within error bars. First, the box size needs to be set in agreement with the characteristics of the scattering experiment. In practice, L_{box} is set by the experimental minimum q-value, $L_{box} = 2\pi/q_{min}$. As the volume fraction of particles Φ_{Si} is an experimental key parameter, the total number of particles N is fixed by L_{box} and Φ_{Si}, as well as the average particle volume V_{si} deduced from the experimental particle size distribution function measured in an independent scattering experiment. In the experimental system described in Chapter 4, there are approximately 1200 particles in the simulation box for each percent of volume fraction, i.e. up to several thousand for the studied system.

In all the cases, the filler volume fraction has to be low enough to define an initial configuration by placing the beads with periodic boundary conditions in the box, avoiding particle overlap. Note that for too high concentrations, appropriate algorithms exist but have not been necessary here.

In order to study the impact of the initial configurations, pre-aggregated configurations have been generated, then checking their influence on the final result. These pre-aggregation states have been described introducing a parameter α, which is the fraction of NPs called 'seeds' that are distributed randomly in the beginning, without overlap, in the simulation box. Then, all following beads are put in contact with randomly chosen particles (seeds or not) that have already been positioned. For $\alpha = 100\%$ a random distribution without any pre-aggregation is generated, as every particle is a seed (but none is placed next to it). On the other hand, the lower limit $\alpha = 1/N$ gives a single aggregate made of all particles around a single seed, defining a highly non homogeneous configuration across the simulation box. This lack of homogeneity has been found to become dominant for $\alpha < 1\%$. Over a large range (i.e., $1\% < \alpha < 100\%$), it has been found that α value have only a little impact on the final result, as shown in Fig. 2.16. Thus, α has been set to 5% for the analysis developed in Chapter 4.

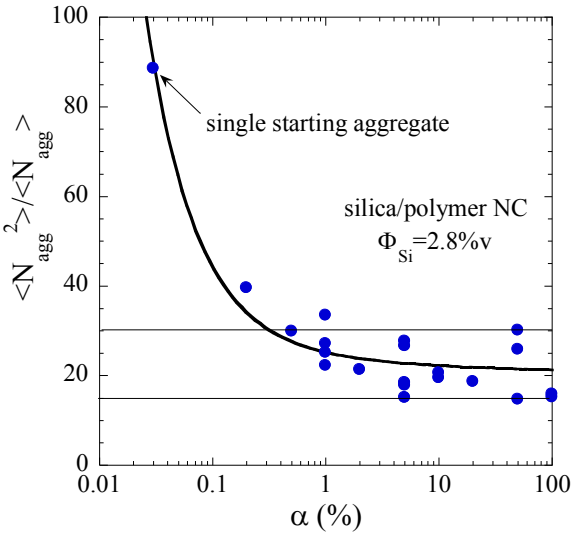

Figure 2.16 $\langle N_{agg}^2\rangle/\langle N_{agg}\rangle$ (i.e., average aggregation as measured in a low-q form factor experiment) as a function of the initial configuration parameter α. Only at the lowest α values, the $\langle N_{agg}^2\rangle/\langle N_{agg}\rangle$ seems to diverge, then the data points are scattered.

After defining an initial configuration, spatial distributions of polydisperse hard spheres of compatible with the measured scattering intensities have been determined using a reverse Monte Carlo simulation combined with simulated annealing. Individual Monte Carlo steps are performed by randomly choosing a particle in the box, and moving it in a random direction, with step-length, Δ. This has been repeated on average once for each NP in the box, defining one simulation time step. In order to access configurations with close contact more quickly, half of the steps have been chosen to be random jumps on the surface of another randomly chosen bead, as illustrated in Fig. 2.17a. A classical metropolis algorithm has been used to decide on the acceptance of each individual step (Metropolis et al. 1953), considering an exponential weight of the 'energetic' cost $\Delta\chi^2$ of the move, i.e., $\exp(-\Delta\chi^2/\chi^2_{eff})$. In particular, $\Delta\chi^2$ represents the difference between the experimentally measured $I_{exp}(q)$ and the calculated intensity $I_{RMC}(q)$ and it is defined as

$$\chi^2 = \frac{1}{N_q}\sum_{p=1}^{N_q}\left(\frac{I_{exp}(q_p)-I_{RMC}(q_p)}{\Delta I}\right)^2 \qquad [2.31]$$

where N_q is the number of the data points (including different directions, see eq. [2.33]) and ΔI is the experimental error of the scattered data. Here, χ^2 has been defined fir the intensity, but the same definition has been used for the apparent structure factor. The effective 'temperature' of the process is given by χ^2_{eff} which measures the acceptability of a move which might worsen the agreement between the intensities. The idea of simulated annealing is then to decrease this 'temperature' until a series of particle configurations with acceptable χ^2 is found. As the MC steps depend on Δ, this last parameter is also decreased in order to fine-tune the final structures accordingly, following an exponential decay:

$$\Delta \approx \Delta_0\,\gamma^n \qquad [2.32]$$

with $\gamma < 1$, n is the number of time steps, and Δ_0 is chosen at the particle scale to be the average radius. Both the imposed decrease of Δ and χ^2_{eff} are plotted in Fig. 2.17b. The resulting MC success rate (not taking collisions into account), and the decrease of χ^2 are also reported as a function of the number of MC attempts to move each particle. The decrease is stopped once a small χ^2 is found and a satisfying agreement between simulation and data is obtained. The simulation is continued with fixed parameters for averaging. During this averaging phase, multiple configurations compatible with the scattering are explored. This non-uniqueness of the configuration is a natural consequence of the ill-posed inverse scattering problem: there is much less information in the scattered intensity than in the particle configurations, and many configurations may correspond to the same scattering cross section, within error bars defined by the final χ^2_{eff}. The average is thus performed over many such configurations.

The details of the decrease of the parameters Δ and χ^2_{eff} may be of importance for which type of structure is selected. It is noted, however, that the final series of configurations is far from jammed (again, due to the low Φ_{Si}), and that therefore many statistically equivalent configurations are reached. In Fig. 2.17b, χ^2-values of different initial configurations (i.e., $\alpha = 5\%$, and one for $\alpha = 20\%$) have been superimposed and they are seen to converge to about the same final χ^2, i.e. the final fit quality is equally good.

The determination of χ^2 for each particle configuration is based on a trustworthy calculation of the scattered intensity. In principle, there are several ways of calculating such intensities. For monodisperse systems, the pair correlation function is usually determined and then the Fourier-transform is applied. Polydisperse systems require binning and this reduces the quality of the analysis. Staying in reciprocal space, this shortcoming can be avoided. A first method is based on the Debye isotropic averaging (Debye 1915). It is very efficient to calculate structure factors of aggregates (Oberdisse et al. 2007), but it is not appropriate for particle assemblies, as it includes the low-q upturn to the total mass of the assembly, which is treated as a big aggregate. A second method has been proposed by Frenkel in the 80s (Frenkel et al. 1986), and applied to different systems, e.g. to polymers by Pedersen (Pedersen and Schurtenberger 1999). This approach based on a calculation and squaring of the scattering amplitude in specific directions in space (usually 13) is very efficient, but it potentially lacks statistics at high q vectors due to the limited isotropic averaging. The structure factor was calculated taking into account polydispersity, i.e. correctly weighting all partial structure factors. (Genix and Oberdisse In preparation) The intensity then reads:

$$S(q_p) = \left|\sum_{j=1}^{N} \exp\left[-ip2\pi\frac{hx_j+ky_j+lz_j}{L_{box}}\right]\right|^2 \qquad [2.33]$$

where the N particles are located at positions (x_j, y_j, z_j), and the norm of the scattering vector is given by $q_p = p\,2\pi\frac{\sqrt{h^2+k^2+l^2}}{L_{box}}$, with p = 1, 2, 3… . One can include polydispersity via the sphere form factors in the above formalism, namely by multiplying the exponential by the normed form factor amplitude of sphere number j, $F_j(q_p)$, and the particle volume V_j.

The apparent (also called 'experimental', referring here to the simulation result) structure factor can be obtained by dividing the intensity by the average form factor P(q).

A sequence of statistically equivalent particle configurations is obtained by continuing the random particle displacements under the condition of agreement with the experimental intensity defined by the Boltzmann factor. These particle configurations result statistically independent, according to the time autocorrelation function of the low-q intensity. The intensities can then be averaged to obtain smooth intensities, and configurational averages. Moreover, all configurations can be analyzed, as done below for the state of aggregation. Alternatively, single snapshots of configurations in the box can be generated for illustration, and an example is reproduced in Fig. 2.17a.

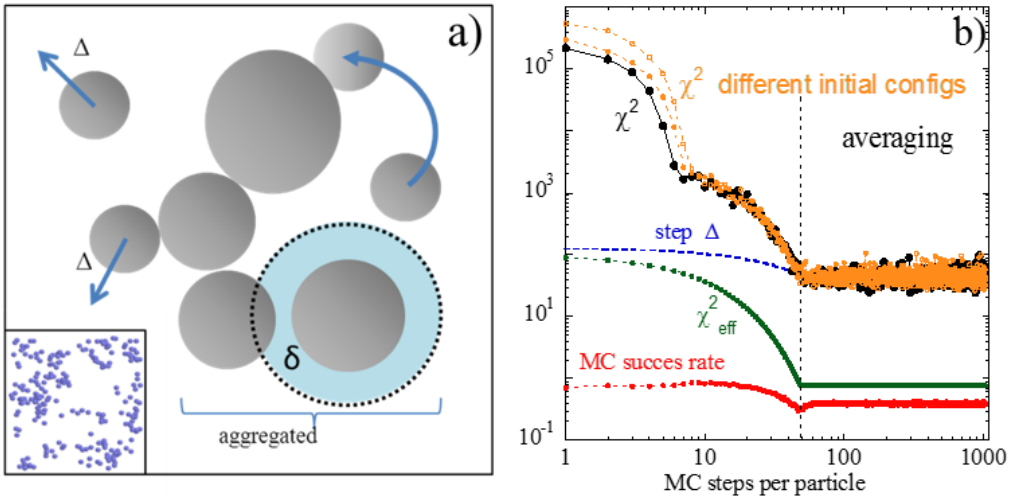

Figure 2.17 (a) Illustration of Monte Carlo moves (Δ, or jump to contact), aggregate recognition parametrized by δ, and a snapshot of a 70 nm-slice of the simulation box. (b) Example of simulated annealing as a function of the number of MC attempts to move each particle. χ^2 expresses the quality of the fit (different initial configurations with α = 5% and 20% are shown), Δ is the step-length of moves in Å, and χ^2_{eff} is the effective temperature. The MC success rate takes only χ^2-decisions into account. Once χ^2 crosses a critical value (after around 70 MC attempts), averaging starts.

In order to access the average aggregation state which corresponds to the scattered intensities, an aggregate recognition algorithm can be run on the particle configurations. This algorithm allows to recognize if two given particles have a surface-to-surface distance lower than some critical distance δ, as illustrated in Fig. 2.17a. Note that particles may be in touch across the periodic boundary conditions. One would expect that δ = 0 might be the appropriate choice. However, since the small-angle scattering is a low-resolution method, it is impossible to distinguish particles close-by from effectively touching particles. Accordingly to this, a non-zero δ allows counting particles as 'in contact' even if they are at a small distance. The natural length scale of the problem is the particle radius, and thus δ has been set equal to <R>. Note that the effective volume fraction of the particle plus a layer of thickness δ/2 increases with the effective radius to the third power, and choosing δ = 2<R> would result in an 8 times

higher volume fraction, virtually aggregating the entire simulation box for the experimentally relevant Φ_{Si}. The range of meaningful values for δ is thus rather restrained, and δ = <R> seems appropriate.

2.6. Dynamical characterization of PNCs

To completely characterize a system, not only its structural but also its dynamical properties have to be studied. For a lot of soft matter system, such as silica-polymer nanocomposites (NCs), dynamical (relaxation) processes are commonly investigated by Broadband Dielectric Spectroscopy (BDS), a technique which is sensitive to the molecular fluctuations of dipoles and displacement of charge carriers within the system in presence of an electric field.

For this PhD work, BDS measurements have been performed at the Centro de Fisica de Materiales of the University of Basque Country (San Sebastian, Spain) using a broadband high-resolution dielectric spectrometer (Novocontrol Alpha Analyzer System) to measure complex dielectric permittivity (see details below), performing isothermal measurements in the frequency range from 10^{-2} to 10^{7} Hz, under nitrogen atmosphere.

Here below, the physical basics of BDS (Kremer and Schönhals 2003) and the main dynamical processes in NCs will be described.

2.6.1. Broadband Dielectric Spectroscopy (BDS)

Broadband Dielectric Spectroscopy (BDS) is an experimental technique which allows fundamental investigations of dielectric response of a material in presence of an electric field (EF) over a broad temperature (from about 100K to 680K) and frequency range (from 10^{-6} to 10^{12} Hz). When an EF is applied to a dielectric material across the faces of a parallel plate capacitor, its atomic and molecular charges are displaced from their equilibrium positions and the material becomes polarized.

In this vast frequency domain where BDS works, there are several mechanisms that can induce polarization phenomena (Fig.2.18): i) electronic polarization, which arises because of the small shift of the electron cloud in presence of an external EF and it is extremely fast; ii) atomic polarization, which is found in molecules with an asymmetrical electron distribution and where the application of an EF induces a dipole moment; iii) orientational polarization, which is related to the rotation of the pre-existing molecular dipole moments when an EF has been established inside a dielectric material. This last polarization phenomenon can only take place at relatively low frequencies since it requires motions of bigger entities.

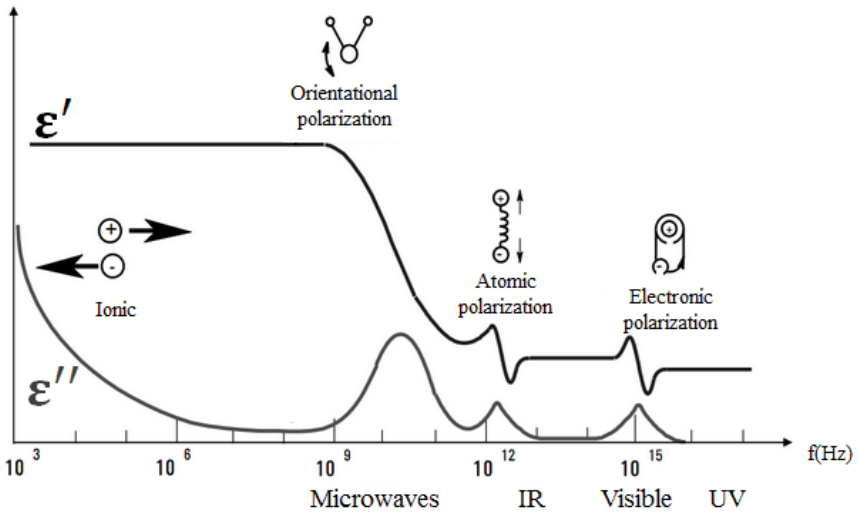

Figure 2.18 The real and the imaginary part of complex dielectric permittivity over a wide frequency range. Different polarization mechanisms are shown as a function of frequency: ionic conductivity, orientational, atomic and electronic polarization.

While electronic and atomic polarization result from induced dipoles, there are many materials that contain permanent dipoles. When such materials are placed in an electric field, dipole orientation is produced as dipole alignment in the direction of the electric field. Unlike electronic and atomic polarizations that are considered instantaneous by dielectric spectroscopy, the orientation of permanent dipoles involves cooperative motions of the molecular segments with a time-scale measurable by BDS. The time-dependent loss of orientation of these dipoles when the EF is removed is called *dipole relaxation*.

Another polarization mechanism which must be considered is the conductivity, which is related to the charge migration, such as proton transfers along hydrogens bonds.

Most of dielectric measurements are performed putting a sample of thickness d between two disk-shaped gold electrodes of surface A. Then, a tension is applied to electrode interface and the amplitude and phase shift of the resulting current are measured (Fig. 2.19a, 2.19b and 2.19c).

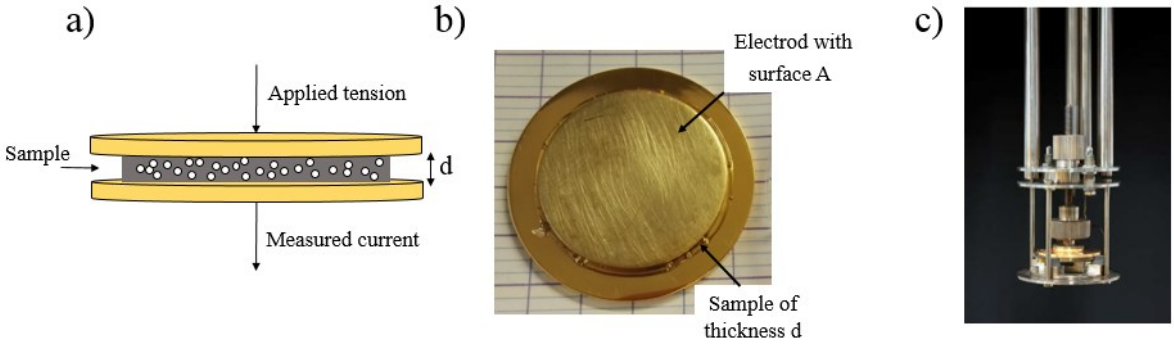

Figure 2.19 (a) Schematic representation of BDS measurement: the sample of thickness d is put between two disk-shaped gold electrodes of surface A to form a capacitor system; (b) Image of a nanocomposite sample ready for BDS measurement; (c) sample between gold electrodes put in a low frequency sample holder of BDS experimental setup.

The ratio of the output (current) and the input (tension) signal is the system impedance Z*(ω), a function of the angular frequency ω= 2πf (where f is the measuring frequency). This parameter can be expressed as a sum of the resistance term R(ω) and capacitance term C(ω) and it can be represented as a complex number since both amplitude and phase of the output current can be different from the ones of input voltage.

$$Z^*(\omega) = Z'(\omega) - iZ''(\omega) \qquad [2.34]$$

where $i = \sqrt{-1}$ and $Z'(\omega)$ and $Z''(\omega)$ are the real and the imaginary part of the impedance, respectively. From Z*(ω), other complex dielectric quantities can be deduced such as the complex dielectric permittivity ε*(ω). In particular, considering a plate-plate capacitor filled with a dielectric material, the ε*(ω) can be defined as

$$\varepsilon^*(\omega) = \varepsilon'(\omega) - i\varepsilon''(\omega) = \frac{C^*(\omega)}{C_0} \qquad [2.35]$$

where C_0 is capacity of the system without the sample, $C^*(\omega)$ is the complex capacity in presence of the material; $\varepsilon'(\omega)$and $\varepsilon'(\omega)$ are the real and the imaginary part of the complex permittivity, respectively. When a sinusoidal electric field $E^*(\omega) = E_0 \exp(i\omega t)$ is applied, $\varepsilon^*(\omega)$ can be written as

$$\varepsilon^*(\omega) = \frac{J^*(\omega)}{i\omega\varepsilon_0 E^*(\omega)} = \frac{1}{i\omega C_0 Z^*(\omega)} \qquad [2.36]$$

where ε_0 is the permittivity of free space (8.85×10^{-12} F/m) and $J^*(\omega)$ the complex current density.
In most of the cases, experimental impedance can be matched with the impedance of an equivalent circuit composed of ideal resistors R (dissipative component, related to ε″) and capacitors C (storage component, related to ε'). The simplest equivalent circuits can be obtained by combining resistance and capacitance in parallel or series.

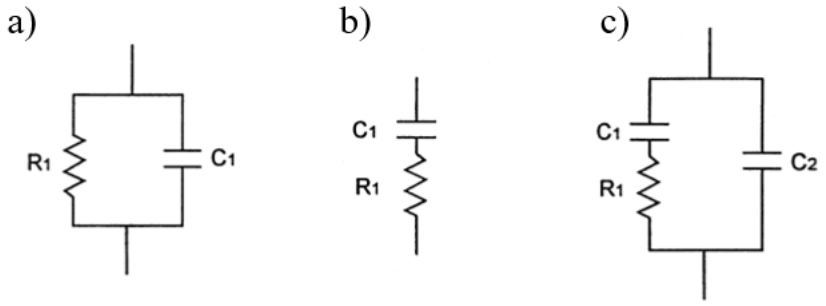

Figure 2.20 Equivalent circuit diagrams for modeling of material properties: an R-C parallel circuit (a), an R-C series circuit (b) and the overall impedance of a circuit considering where the contribution of atomic and electric polarization is represented by an additional capacitance C_2 (c)

For the RC parallel circuit (Fig. 2.20a) the overall impedance $Z^*(\omega)$ is given by

$$Z^*(\omega) = \frac{1}{\frac{1}{R_1}+i\omega C_1} \quad [2.37]$$

The real and the imaginary components of this complex impedance are, respectively

$$Z'(\omega) = \frac{R_1}{1+(\omega R_1 C_1)^2} \quad [2.38]$$

and

$$Z''(\omega) = -i\frac{\omega {R_1}^2 C_1}{1+(\omega R_1 C_1)^2} \quad [2.39]$$

where R_1C_1 is the circuit characteristic time τ. In the case of dipole polarization, τ is called relaxation time.

When a resistance R and a capacitor C are in series (Fig. 2.20b) it is possible to obtain $Z^*(\omega)$ for a single dipole or many dipoles with a single relaxation time. However, also the contribution of atomic and electric polarization to the stored energy affects the dielectric response and it is typically represented by an additional capacitance (C_2), as represented in Fig. 2.20c. The overall impedance of this circuit can be expressed as

$$Z^*(\omega) = (i\omega C_2)^{-1} + \left[\frac{i\omega C_1(1-\omega\tau)}{1+(\omega\tau)^2}\right] \quad [2.40]$$

where $\tau = R_1C_1$.

The equation [2.40] can be also expressed in terms of dielectric complex permittivity as

$$\varepsilon^*(\omega) = \varepsilon_\infty + \frac{\varepsilon_S-\varepsilon_\infty}{1+\omega\tau} \quad [2.41]$$

where ε_S is the static permittivity defined $\varepsilon_S = \lim \varepsilon'(\omega)$ if $\omega << 1/\tau$ and ε_∞ is the high frequency permittivity defined as $\varepsilon_\infty = \lim \varepsilon'(\omega)$ if $\omega >> 1/\tau$. The real and imaginary part of $\varepsilon^*(\omega)$ can be respectively written as

$$\varepsilon'(\omega) = \varepsilon_\infty + \frac{\varepsilon_S-\varepsilon_\infty}{1+(\omega\tau)^2} \quad [2.42]$$

and

$$\varepsilon''(\omega) = \frac{(\varepsilon_S - \varepsilon_\infty)\omega\tau}{1+(\omega\tau)^2} \quad [2.43]$$

Equations [2.42] and [2.43] are commonly referred to as **Debye equations**, where the existence of one relaxation time is assumed. For some systems (e.g., polymeric materials) the dipole mobility depends on the local restrictions due to their surroundings. The spatial variation of this restrictions determines a distribution of relaxation times (i.e., relaxation time mapping).

Analysis of dielectric specta

Information about relaxation processes linked to fluctuations of molecular dipoles can be obtained by analyzing the dielectric function (i.e. complex permittivity). In particular, relaxation processes are generally characterized by a peak in the imaginary part ε ″ and a step-like decrease of the real part ε ′ of the complex dielectric function $\varepsilon^*(\omega)$ with increasing frequency, as shown in Fig. 2.21.

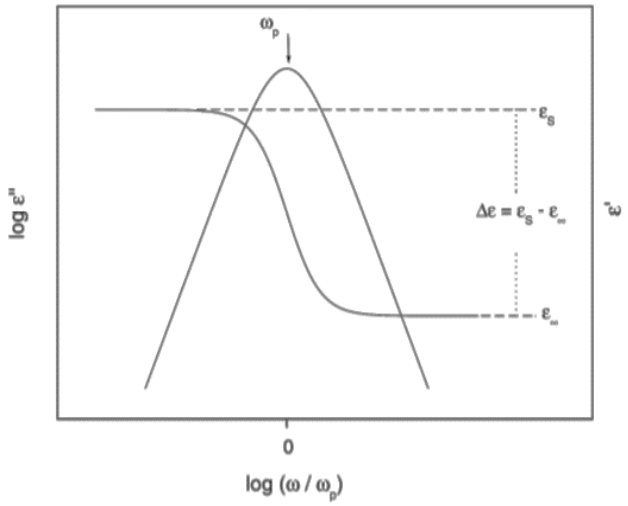

Figure 2.21 Real ε ′ and imaginary part ε ″ of the complex dielectric permittivity as a function of normalized frequency.

The essential quantities which characterize a dielectric relaxation process can be extracted from that behavior. The frequency of maximal loss f_P is related to a characteristic relaxation rate $\omega_P = 2\pi f_P$ or relaxation time $\tau_P = 1/\omega_P$ of the fluctuating dipoles. From the shape of the loss peak the distribution of relaxation times can be deduced (i.e. deviations from Debye behavior with single relaxation time translate into distribution of times).

Moreover, the dielectric strength Δε of a relaxation process can be determined from the step in ε ′(ω). In this last case, Δε can be written as

$$\Delta\varepsilon = \varepsilon_S - \varepsilon_\infty \quad [2.44]$$

Dielectric relaxation processes are usually analyzed using model functions theoretically founded on Debye equations, which can be written as

$$\varepsilon^*(\omega) = \varepsilon_\infty + \frac{\Delta\varepsilon}{1+i\omega\tau_D} \quad [2.45]$$

where τ_D is the Debye relaxation time and it is related to the position of maximal loss by $\omega_P = 2\pi f_P = 1/\tau_D$.

In most of the experimental spectra, the half width of measured loss peaks is much broader than predicted by equation 2.45 (up to six decades) and their shapes are asymmetric with a high frequency tail (i.e., non-Debye relaxation behavior). In the literature, several empirical model functions, based in the Debye function, have been developed (i.e., Cole-Cole, Cole/Davidson) and the most general model, introduced by Havriliak and Negami (HN-function) (Havriliak and Negami 1967), is defined as

$$\varepsilon^*_{HN}(\omega) = \varepsilon_\infty + \frac{\Delta\varepsilon}{(1+(i\omega\tau_{HN})^\gamma)^\delta} \qquad [2.46]$$

where γ and δ are fractional shape parameters which describe the symmetric and asymmetric broadening of the complex dielectric function ($0 < \gamma, \delta\gamma \leq 1$), as shown in Fig. 2.22.

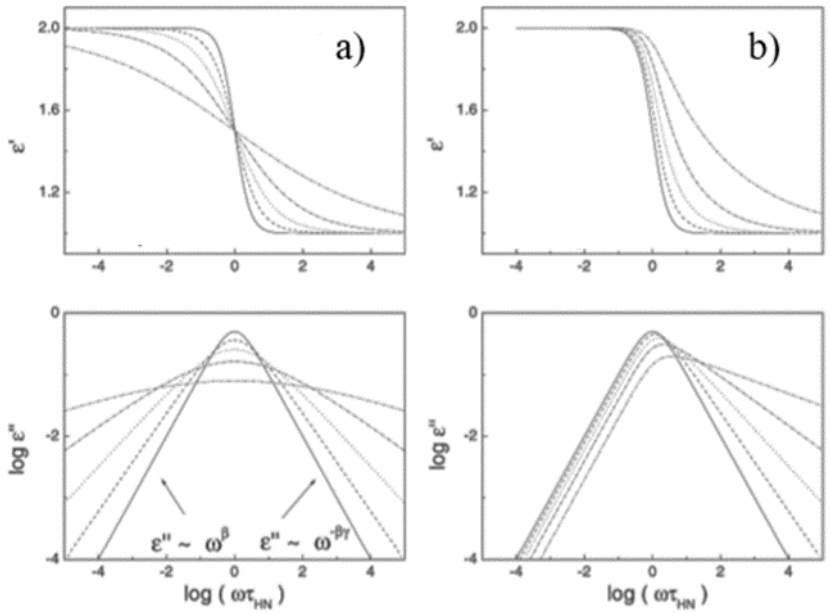

Figure 2.22 Complex dielectric permittivity (real and imaginary part) for an Havriliak/Negami function with fixed parameter: (a) $\delta = 1$ with variation of γ; (b) $\gamma = 1$ with variation of δ.

2.6.2. Relaxation processes in silica-polymer nanocomposites

Polymeric materials, such as silica-polymer NCs, are rather complex systems and the analysis and interpretation of their dielectric spectra are not trivial. The knowledge of some of fundamental dielectric process (reported below) results essential for the interpretation of the BDS results.

α –relaxation: Dielectric α -relaxation process is linked to the calorimetric glass transition, involving cooperative motions. In polymeric systems (e.g., pure polymer matrix or silica-polymer NCs), this process usually dominates the dielectric response whose relaxation time increases when temperature decreases toward the glass transition temperature T_g (Cerveny et al. 2002). Close to T_g, α -relaxation can be described by the Vogel/Fulcher/Tammann (VFT) law (Vogel 1921; Fulcher 1925), see formula 1.10.

As for other dynamical processes (see below), the evolution of the segmental relaxation time as a function of the temperature represents the *relaxation map* of a sample.

β–relaxation: Besides the α–relaxation, secondary relaxations (i.e., dielectric β–relaxation) with different characteristics can be active at faster time scales. In polymeric systems, this process is usually related with the motions of the side groups on polymer chain (Cerveny et al. 2002). The temperature dependence of the relaxation time $\upsilon_{P\beta}$ of the β-relaxation can be described in general by an Arrhenius law (formula 1.8).

Maxwell-Wagner-Sillars: In reinforced materials, such as silica-polymer nanocomposites, additional dielectric processes can be observed at frequencies lower than the α–relaxation (Böhning et al. 2005; Otegui et al. 2013) at polymer-filler interface. These phenomena can be considered as high-temperature interfacial processes due to the filler presence and thus they can be attributed to the so-called Maxwell-Wagner-Sillars (MWS) polarization. These processes are linked to the polarization effects due to the charge carrier diffusion through the different phases of a NCs (Baeza et al. 2015a; Genix et al. 2016a) and they result in the trapping and accumulation of charges at polymer/silica interface (resulting in a structure dependency). In particular, ions can diffuse on the surface of NPs within aggregates, or on a larger scale, on aggregate surface or across polymer between aggregates. The evolution of the MWS process with the temperature follows an Arrhenius law (formula 1.8) describing a thermally activated process. The typical values for E_A are generally about 50-60 kJmol^{-1} (Otegui et al. 2013; Lin et al. 2016).

Interlayer model (ILM): The use of fillers (e.g., silica nanoparticles, clay) frequently introduces a water sensitive component at polymer-filler interface which can influence interfacial process such as MWS (Baeza et al. 2015a). This means that a composite material can be considered as a three-phase system where the absorbed water forms an interlayer between fillers and polymer matrix gives electrical polarization since it is electrically conductive. This behavior can be modeled using the so-called interlayer model (Steeman and Maurer 1990)for the complex dielectric constant, using the equation [2.41]. In this case, the static dielectric permittivity ε_S is defined as

$$\varepsilon_S = \varepsilon_m \left(\frac{1+2\Phi_f}{1-\Phi_f}\right) \quad [2.47]$$

and the high frequency limit of dielectric permittivity is equal to

$$\varepsilon_\infty = \varepsilon_m \left(\frac{(\varepsilon_f+2\varepsilon_m)+2(\varepsilon_f-\varepsilon_m)\Phi_f}{(\varepsilon_f+2\varepsilon_m)-(\varepsilon_f-\varepsilon_m)\Phi_f}\right) \quad [2.48]$$

and the relaxation time is expressed as

$$\tau = \left(\frac{\Phi_f}{1-\Phi_f}\right)\left(\frac{3\varepsilon_0}{2\sigma_l\Phi_l}\right)[(\varepsilon_f + 2\varepsilon_m) - (\varepsilon_f - \varepsilon_m)\Phi_f] \quad [2.49]$$

where Φ_f is the filler volume fraction, ε_m is the frequency-independent dielectric constant of the medium (e.g., equal to the square of the refractive index n of the pure polymer $n^2 = (1.5)^2$) and ε_f the frequency-independent dielectric constant of the filler (e.g. silica permittivity ε_{SiO2} =4.5 according to Grabowski et al. (Grabowski et al. 2013) or 5.5, according to Steeman et al. (Steeman and Maurer 1990; Steeman et al. 1991)); σ_l and Φ_l are the conductivity and the volume fraction of the layer, respectively.

3. Synergistic effect of small molecules on large-scale structure of simplified industrial nanocomposites

3. Synergistic effect of small molecules on large-scale structure of simplified industrial nanocomposites

The formulation of nanocomposite materials used for modern car tires is of great complexity. Despite the fact that these materials have been deeply investigated from a fundamental point of view, little is known about the impact of each ingredient on their final structure and performance. In this chapter, we focus on simplified industrial nanocomposites prepared with un-crosslinked styrene-butadiene (SB) matrix and "small molecules", such as silane coating agents and a curing additive (i.e. *Diphenyl*-Guanidine, DPG). A multi-scale quantitative analysis on these PNCs is proposed to shed light on the impact of such small molecules on the spatial organization of fillers inside the polymer matrix. Main results of this chapter are reported in a recent publication (Musino et al. 2017).

3.1. Analysis method

As already mentioned in Chapter 1, in recent contributions (Baeza et al. 2013a; Baeza et al. 2013b; Genix et al. 2016a) a multi-scale analysis method has been developed to characterize primary nanoparticles (NPs) and aggregates in systems consisting of disordered silica in a styrene-butadiene copolymer matrix. This structural model has as central element the aggregate defined by its internal characteristics, namely average compacity κ and aggregation number N_{agg} (see section 2.4) and it is based on a combined use of:

i) Small-Angle X-ray Scattering (SAXS): this technique allows to reveal the multi-scale filler structure of PNCs, showing that NPs form aggregates which can be concentrated within fractal branches extending over micrometers. The analysis of SAXS data permits to extract the average aggregate radius R_{agg} using the Kratky plot ($q^2I(q)$ versus q). For a fixed silica fraction, changes in the SAXS spectra are mainly related to a different aggregate form factor (mass and size). The comparison with the SAXS intensity at a low-q value leads to the determination of the average aggregate compacity (Baeza et al. 2013b).

ii) Transmission Electron Microscopy (TEM): the treatment of TEM images reveals the volume fraction of fractal branches Φ_{fract} (or equivalently the volume fraction of pure polymer zones, given by $1 - \Phi_{fract}$).

iii) Independent Monte-Carlo simulation: the simulation of the inter-aggregate structure factor for polydisperse spheres representing aggregates is provided assuming the presence of excluded volume interactions between aggregates. The essential input in this simulation procedure is the value of Φ_{fract} obtained from the treatment of TEM images, since it allows to estimate aggregate internal volume fraction as $\Phi_{agg} = \Phi_{Si}/(\kappa\,\Phi_{fract})$, where Φ_{Si} is the volume silica fraction (Baeza et al. 2013a).

Pure polymer matrix contribution

The characterization of pure polymer matrix is an essential step in SAXS data treatment. The matrix spectrum is multiplied by the real polymer content Φ_p of each PNC (i.e., Φ_p =1-Φ_{Si}), and then systematically subtracted from PNC intensity signal. This data treatment is useful to stress the real contribution of silica particles and aggregates inside the PNCs.

As described in Chapter 2, simplified industrial nanocomposites have been formulated following a solid mixing procedure, using an internal and external mixer. A "simplified industrial matrix" made of un-functionalized styrene-butadiene (Matrix SB_NF) has been prepared following the same preparation steps. As shown in Fig. 3.1, the SAXS spectrum of this matrix has been compared to the one of a piece of pure SB_NF polymer to verify that the preparation procedure did not strongly impact the structural characteristics of the matrix.

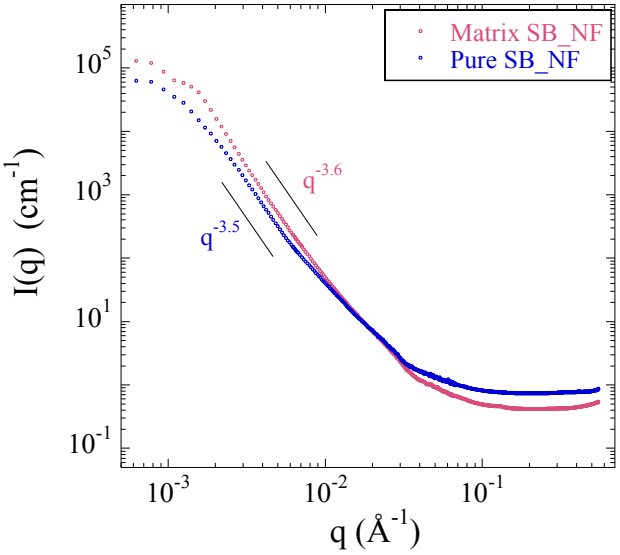

Figure 3.1 Small Angle X-Ray scattering spectrum of SB_NF matrix prepared following the same experimental conditions of simplified industrial PNCs. This curve has been compared to the one of a piece of pure SB_NF polymer to show that the solid mixing procedure does not impact the structural properties of the polymer matrix.

At high-q regime, both the Matrix SB_NF and the pure polymer show a well-defined plateau. At decreasing q values, both the intensity increases following a power law Aq^{-d}, where the fractal dimension d is equal to 3.6 and 3.5 for the "industrial matrix" and the pure polymer, respectively. This intensity increase can be related to the presence of impurities or bubbles inside the samples, but the intensity of these spectra always results lower than the PNC one.

As a general remark, no relevant differences can be observed between these two spectra, confirming that the solid mixing procedure does not impact the structural properties of the polymer matrix.

3.2. Impact of silica content variation on nanocomposite structure

As already show in some recent works (Baeza et al. 2013a; Genix et al. 2016a), the variation of the silica volume fraction (Φ_{Si}) influences PNC structural properties.

In the present study, simplified industrial nanocomposites have been formulated at different silica volume fractions (Φ_{Si} = 8.3%v, 13.3%v, 18.3%v and 22.2%), using un-functionalized styrene-butadiene (SB_NF), octyl-triethoxysilane as coating agent (C_8) and DPG.

At large-scale, structure investigation for NCs at different silica volume fractions have been carried out by Transmission Electron Microscopy (TEM). In Fig. 3.2, TEM images of nanocomposites from the lowest (Φ_{Si} = 8.3%v) to the highest (Φ_{Si} = 22.2%v) filler content are shown.

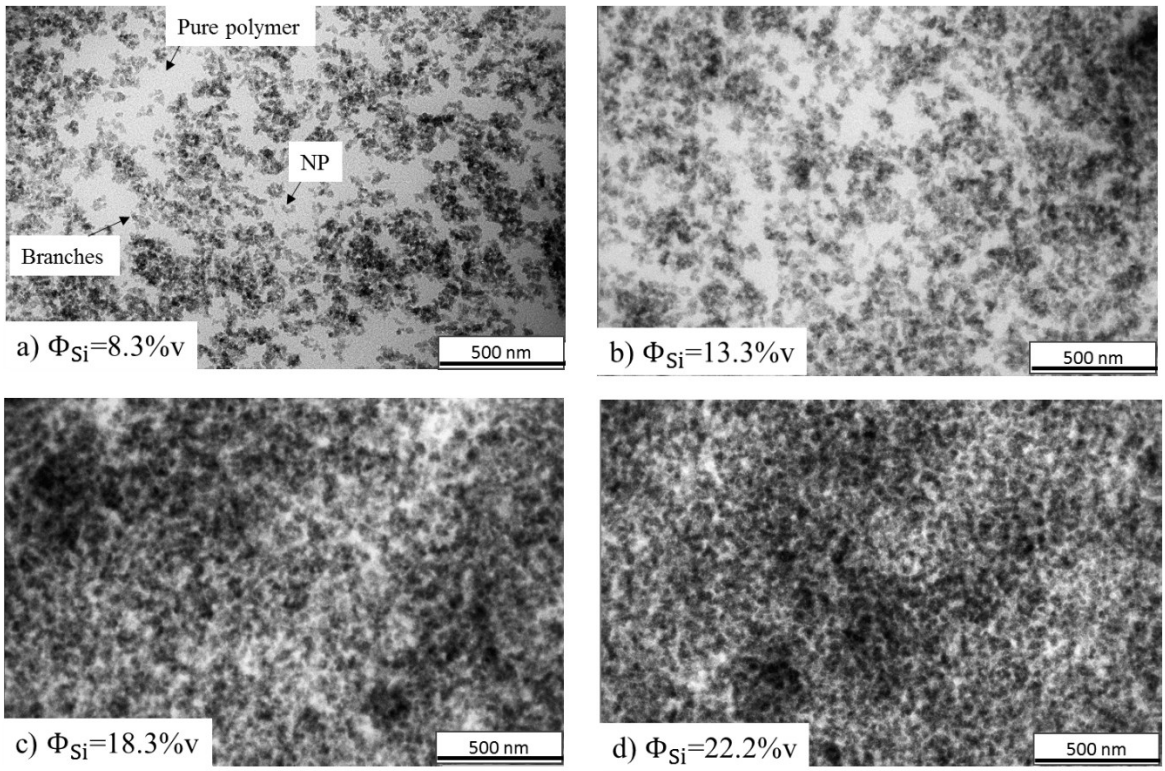

Figure 3.2 Silica structure of simplified industrial PNCs formulated with SB_NF polymer, using DPG and C_8 as coating agent: (a) TEM picture with Φ_{Si} = 8.3%v, where pure polymer regions are well visible. According to the grey scale, some primary NPs can be observed while other ones overlap giving a darker grey. (b) TEM picture of same NC formulated at Φ_{Si} = 13.3%v; (c) and (d) show TEM image of PNC at Φ_{Si} = 18.3% and Φ_{Si} = 22.2%v, respectively. Here, silica organization results much dense and structural features become hardly distinguishable just by TEM observations.

As expected, the polymer matrix occupies more space in NC at Φ_{Si} = 8.3%v and 13.3%v, with respect to other samples at higher filler content. Here, according to the grey scale estimation, some primary NPs can be observed, while overlapping NPs are represented by darker grey shades. Furthermore, some branched structures separated by pure polymer region can be detected (Fig. 3.2a). At higher silica content, Φ_{Si} = 18.3%v and 22.2%v, silica particles display a much denser arrangement and structural characteristics become hardly distinguishable just by mere observation of TEM images.

As a consequence, SAXS measurements are essential to better characterize silica organization inside the polymer matrix. Scattering spectra in reduced representation $I(q)/\Phi_{Si}$ for series of PNCs at different silica volume fractions are reported in Fig. 3.3a.

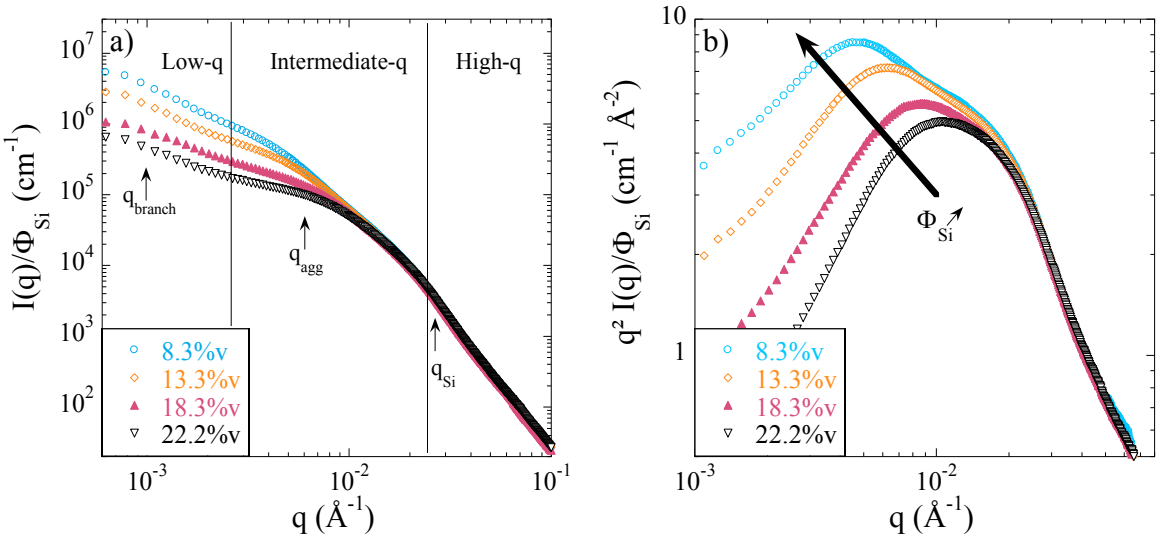

Figure 3.3 Reduced scattered intensity $I(q)/\Phi_{Si}$ for a series of PNCs at different silica volume fractions (Φ_{Si} from 8.3%v to 22.2%v) formulated using SB_NF polymer. Arrows qualitatively indicate the break in slope characterizing different q-regimes. (b) Same data as Figure (a) in Kratky representation of the reduced intensity $q^2I(q)/\Phi_{Si}$ to easily recognize breaks in slope as maxima of the curves.

The high-q regime can be defined above the first break in slope, which corresponds to a critical scattering vector value q_{Si}. For crowed NPs in contact, this q value is equal to π/R_{Si}, where R_{Si} refers to the average particle radius. The reduced representation shows that all SAXS curves are perfectly overlapped, thus implying that the same primary nanoparticles are in close contact in all the samples. Naturally, this is due to all the investigated PNCs being made with the same primary NPs.

At intermediate q-regime, another break in slope can be observed around q=0.01 A^{-1} and it is linked to the superstructures made by NPs. For aggregates in close contact, the position of this sudden change in slope is indicated as q_{agg} and it is equal to π/R_{agg}, where R_{agg} is the average aggregate radius.

The strong low-q upturn can be described by a power law Aq^{-d}. The fractal dimension d results equal to 2.49 ± 0.05 and A is a pre-factor which decreases with the increase of the filler content. This is in agreement with the decrease of isothermal compressibility at intermediate q-values, following the increase of repulsive interactions with increasing Φ_{Si}.

Above the q_{agg} bump, aggregate scattering results dominant and the decrease of scattering intensity with Φ_{Si} can be related to polydisperse aggregates which interact between them inside the branches. This proves the existence of an additional crowding within the fractal branches for higher silica loadings, in agreement to the results found by Baeza et al. (Baeza et al. 2013a; Baeza et al. 2013b). Fig. 3.3b shows the same SAXS data of Fig. 3.3a using the Kratky representation $q^2I(q)/\Phi_{Si}$, to determine the average aggregate radius R_{agg}. This plot allows to easily recognize breaks in slope of scattering intensities which correspond to the maxima of the curves. The structural evolution for PNCs is

highlighted by the shift position of the maximum as a function of the different volume fraction. Outcomes of SAXS-TEM-simulation analysis for samples at Φ_{Si}=8.3%v and Φ_{Si}=18.3%v are summarized in Table 3.1. They show the Φ_{fract} values increase with the silica content, highlighting the formation of small aggregates of average radius ranging between 30-40 nm.

Φ_{Si} (%v)	Φ_{fract}	$\langle R_{agg} \rangle$ (nm)	κ (%)	$\langle N_{agg} \rangle$ (nm)
8.3	0.35*	38.5	65	96
18.3	0.58	33	70	67

Table 3.1 Structural characteristics of simplified industrial PNCs formulated with SB_NF, C_8 and DPG at Φ_{Si}=8.3%v and 18.3%v: volume fraction of fractal branches (Φ_{fract}), average aggregate radius ($\langle R_{agg} \rangle$) from Kratky analysis, compacity (κ) and average aggregation number $\langle N_{agg} \rangle$. * Note: Φ_{fract} value assumed from (Baeza et al. 2013b).

These results can be compared to the ones obtained for an equivalent sample in a previous work of Baeza et al. (Baeza et al. 2013b). As illustrated in Table 3.2, the results for NCs at $\Phi_{Si} \approx 18$%v referring to two systems show a quite good agreement demonstrating that: i) there is a structural similarity of our system (Solvay NC) with the one developed by Baeza et al. in collaboration with Michelin (Michelin NC) (Baeza et al. 2013a), which means that we correctly reproduced this formulation procedure and the polymer synthesis; ii) the SAXS-TEM-simulation analysis method can be consistently extended also to our case.

System	Φ_{Si} (%v)	Φ_{fract} (%)	R_{agg} (nm)	κ (%)	N_{agg}
"Solvay NC"	18.3	58	33	70	67
"Michelin NC"	16.7	52-63	49.4	58-51	150-171

Table 3.2 Structural features of simplified industrial PNCs formulated in collaboration with Solvay compered to results obtained by Baeza et al. (Baeza et al. 2013b) for the same system developed with Michelin (volume fraction of fractal branches Φ_{fract}, average radius of aggregates R_{agg} from Kratky analysis, compacity and aggregation number).

3.3. Impact of matrix composition on nanocomposite structure

In recent studies of simplified-industrial nanocomposites, the impact of chain parameters on the filler aggregate structure has been investigated by SAXS, focusing on chain end-functionalization (Baeza et al. 2013b) and chain mass (Baeza et al. 2014). In order to test the influence of the coating agent and DPG, a matrix composition had to be chosen. As the chains had been newly synthesized with a slightly different chain mass (170Kg/mol, PI=1.02), the impact of end-functionalization was studied first, in order to choose the most promising system in terms of structural evolution. For the same reason, a high volume fraction of silica filler (Φ_{Si} = 18%v) has been chosen to work with. Here, we present results concerning simplified industrial PNCs made using as polymer matrix of styrene/butadiene with non-

functionalized (SB_NF) or end-functionalized polymer chains (SB_F), or a 50/50 mixture of them (50%w SB_NF and 50%w of SB_F).

Fig. 3.4 shows TEM images for NCs prepared with un-functionalized (SB_NF) and functionalized polymer chains (SB_F). From a first qualitative observation of these pictures, the simplified industrial NCs formulated with functionalized SB seem to show a better dispersion of silica in the polymer matrix. From the image data treatment, the Φ_{fract} has been evaluated. For PNCs at Φ_{Si} =18%v, Φ_{fract} has been estimated equal to 80±2% for samples with functionalized polymer chains (SB_F), while for NF and 50/50 Φ_{fract} = 58 and 73% have been evaluated, respectively.

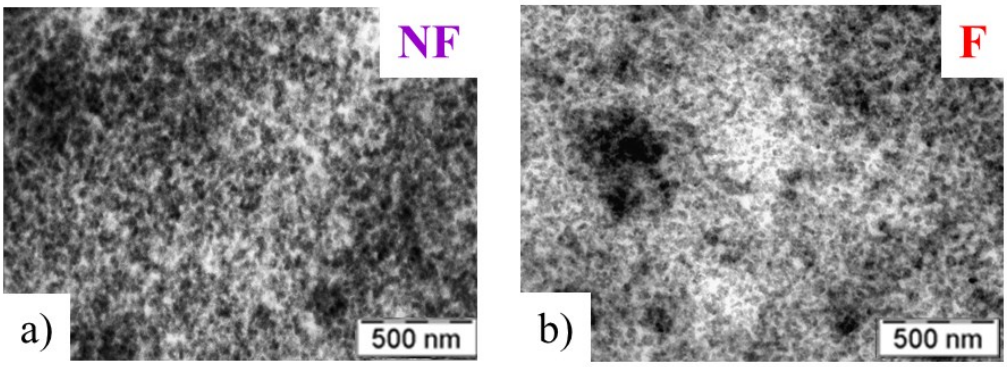

Figure 3.4 TEM images which reveal silica structure of simplified industrial NCs prepared using DPG and C_8 as coating agent, with a NF (a) or F (b) styrene-butadiene polymer matrix.

In Fig. 3.5, three normalized SAXS intensity curves are shown, corresponding to either pure non functionalized matrix (SB_NF), fully functionalized one (SB_F), and a 50/50 mixture. The structural features of these nanocomposites are clearly recognized in the scattered intensities: the high-q scattering is reminiscent of the primary silica NPs, identical in all formulations. A small bump in the range 0.02 – 0.03 $Å^{-1}$ (well visible in a Kratky representation) characterizes the interactions between particles in contact, and below that q-value aggregate scattering is dominant. A much stronger change in slope around 0.01 $Å^{-1}$ is indicative of aggregate-aggregate interactions, and this position in q-space is used to extract the average aggregate radius R_{agg} from the scattering. In this intermediate q-range, the strong influence of the matrix composition on the structure is visible. Finally, a low-q upturn typical for large-scale filler structures is visible.

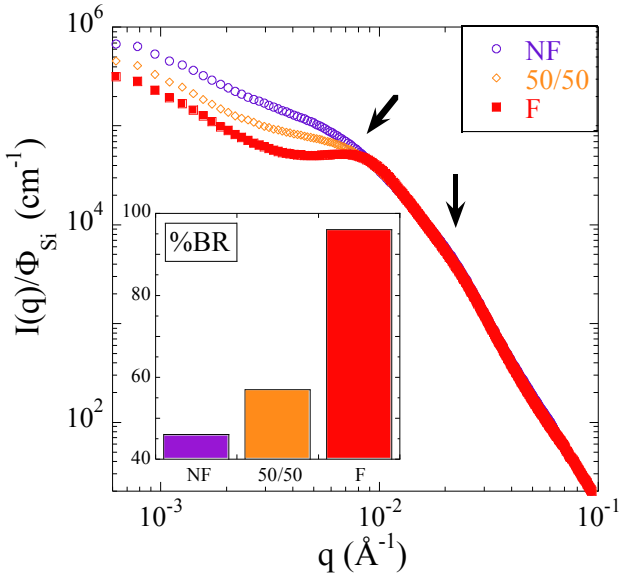

Figure 3.5 Reduced SAXS intensities I(q)/Φ allowing the structural comparison between nanocomposites containing 18.0±0.3%v of silica, coating agent octeo (8%wt), and DPG, made with different polymer matrices SB_F (squares), SB_NF (circles), and a 50/50 mixture (diamonds). Arrows indicate the q-ranges of nanoparticle- and aggregate-scattering, respectively. Inset: Bound rubber results for the corresponding samples.

A quantitative analysis confirming the impact of matrix composition has been performed following the method proposed by Baeza et al. (Baeza et al. 2013a). It allows the determination of not only R_{agg}, but also the aggregate density (compacity κ), and thus the average aggregation number N_{agg}, all given in Table 3.3. As reported in literature (Baeza et al. 2013b), the more functionalized chains form the matrix, the lower the aggregate radius determined through the Kratky representation, and the lower the κ. This tendency results in a decrease of the aggregation number by a factor of three. The evolution towards smaller aggregates is accompanied by the formation of a well-defined shoulder around 0.01 $Å^{-1}$: nanocomposites formed with the end-functionalized polymer chains thus present the most prominent signature in I(q), indicative of the best dispersion of smallest possible aggregates. Moreover, the effect of the graftable chains can also be evidenced by bound rubber measurements, the results of which are also summarized in Table 3.3 and in the inset in Fig. 3.5. Even with only un-functionalized polymer (SB_NF), about half of the chains are not desorbed in a BR measurement. This is probably due to weak crosslinking of the chains during mixing, or possibly chain adsorption on the filler. The high fraction of bound rubber with graftable chains indicates that grafting took place. Thus, the fully-functionalized graftable matrices (SB_F) has been principally chosen to study the impact of the small molecules, silane and DPG, by investigating how the dispersion evolves as the quantity of small molecules is reduced.

Sample	Silane coating agent	Φ_{Si} (%v)	R_{agg} (nm)	κ (%)	N_{agg}	%BR
NF	C_8	18.3	33	70	67	46
50/50	C_8	18.2	33	51	47	57
F	C_8	18.1	30	44	31	96

F	C_{12}	18.1	30	45	31	98
F	C_{18}	18.3	31	45	34	99
F	4%wt C_8	17.8	32	46	39	92
F	-	17.5	34	47	48	88
F, no DPG	C_8	18.1	36	50	61	88
F, no DPG	-	17.4	38	48	67	69

Table 3.3: Nanocomposite formulations with silica content $\Phi_{Si} = 18.0 \pm 0.3$%v. Average radius of aggregates from Kratky analysis, compacity, aggregation number, and bound rubber of NCs. All samples contain 8%wt C_8 with respect to silica (resp., isomolar C_{12}, C_{18}) and DPG, unless otherwise stated.

3.4. Impact of hydrophobic character of coating agent on nanocomposite structure

Subsequent to the choice of the polymer matrix, the coating agent needed to be chosen. We have varied the chemical nature of the coating molecule, via the length of its alkyl chain. The macroscopic bound rubber values are almost identical (96 – 99%) and are given in Table 3.3. This suggests that the chain length of the coating agent has only little influence on polymer grafting, which is an important driver of the PNC microstructure, as shown in Fig. 3.5. The scattering results for an 18%-nanocomposite, in a fully functionalized polymer matrix, with DPG and isomolar amounts of C_8 (octeo, 8%wt with respect to silica), C_{12}, or C_{18}, are shown in Fig. 3.6.

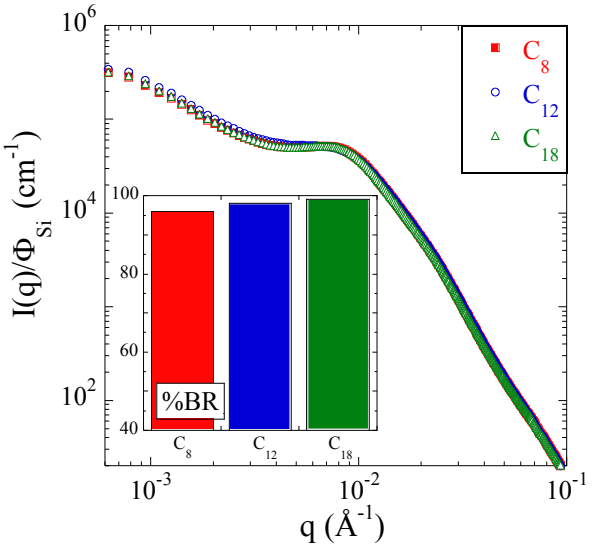

Figure 3.6 Reduced SAXS intensities allowing the structural comparison between nanocomposites containing 18.0±0.3%v silica in a fully functionalized matrix with DPG, for three different isomolar silane coating agents: octeo (C_8), C_{12}, and C_{18}. The inset shows the bound rubber of the same NCs.

Contrarily to what one might expect based on the formation of a more hydrophobic layer on the filler surface, potentially inducing a better compatibilization (and thus dispersion), there is no significant effect of the nature of the coating agent on the aggregate structure. Indeed, the three intensity curves superimpose almost perfectly. This surprising result is thought to be due to a saturation effect, i.e.,

adding the same number of higher-mass agents does not increase the silica surface coverage. This suggests that C_8 molecules already reach a perfect coverage, and C_{18} only modifies the thickness of the interfacial layer. Also, bound rubber measurements seem to show no impact on the efficiency of polymer grafting on the silica surface, further indicating similar surface coverage. In the following paragraphs, the surface modification is thus performed with the C_8 coating agent (octeo), which incidentally is also the industrially relevant one.

For a qualitative comparison, the scattering spectra of PNCs in a fully non-functionalized (SB_NF) polymer matrix, with DPG and isomolar amounts of C_8 (octeo, 8%wt with respect to silica), C_{12}, or C_{18} at Φ_{Si}=8.5%v ±0.2 and 18%v ±0.4 are shown in Fig.3.7a and Fig.3.7b, respectively. Also in this case, at both silica volume fractions, the nature of the coating agent does not have a significant effect on filler dispersion (i.e., at each Φ_{Si} intensity curves superimpose almost perfectly). At large-scale, TEM images of these samples (Fig. 3.8) confirm the coating agent variation does not impact the silica organization in the polymer matrix.

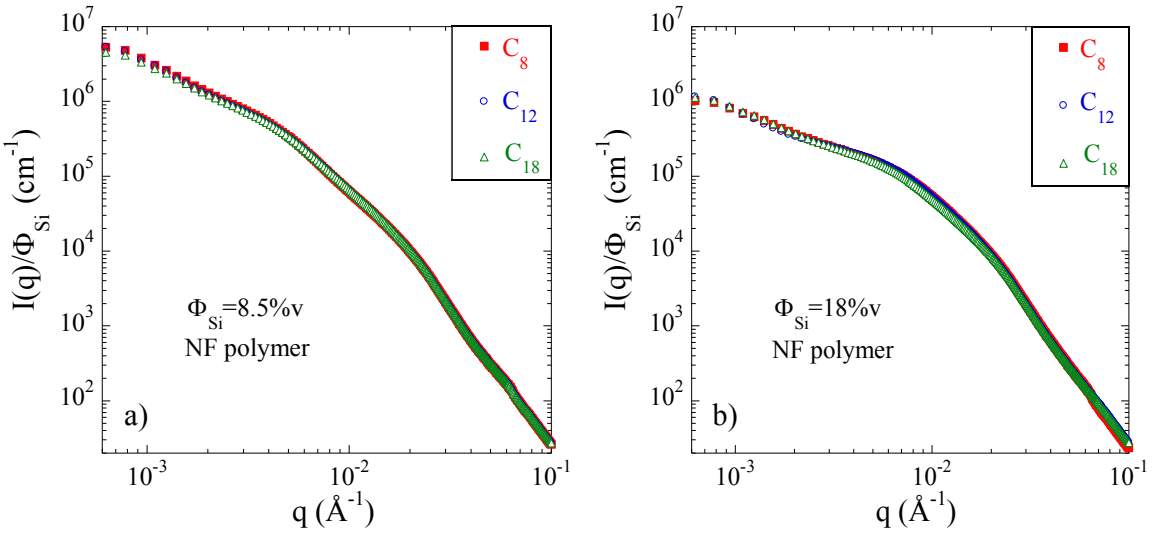

Figure 3.7 (a) Reduced SAXS intensities allowing the structural comparison between nanocomposites containing 8.5±0.2%v silica in a fully un-functionalized (SB_NF) matrix with DPG, for three different isomolar silane coating agents: octeo (C_8), C_{12}, and C_{18}. (b) Reduced SAXS intensity for PNCs at 18.0±0.4%v silica.

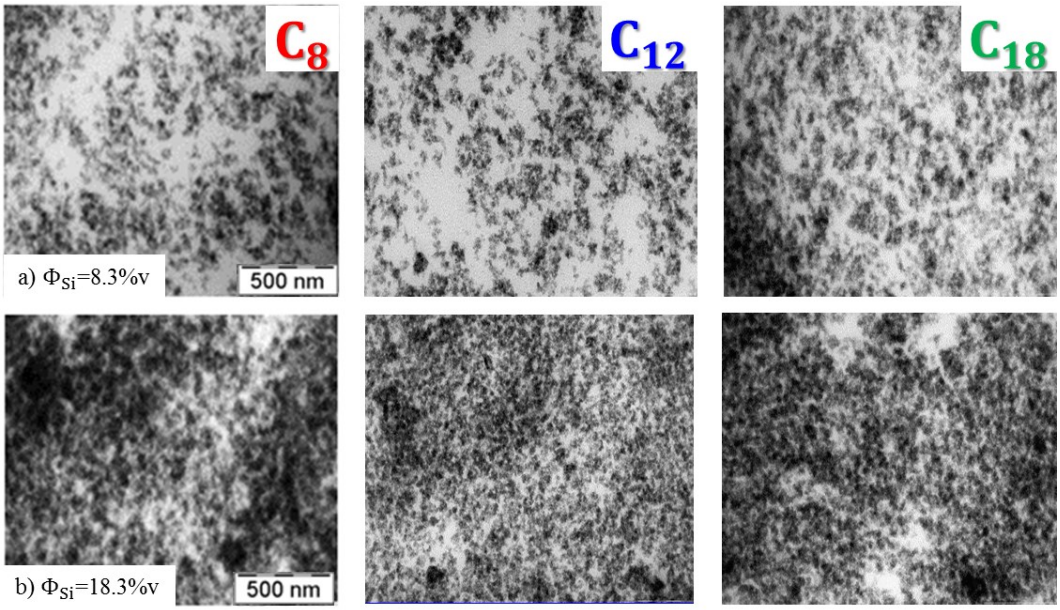

Figure 3.8 TEM images of simplified industrial PNCs prepared using an NF polymer matrix, DPG , and three different isomolar silane coating agents: octeo (C_8), C_{12} and C_{18}. Figure (a) shows samples at 8.3%v and (b) samples at 18.3%v of silica.

3.5. Impact of amount of coating agent on nanocomposite structure

The reduced representation of small-angle intensities scattered by nanocomposites with various octeo contents used during the formulation (i.e. 0, 4, and 8%wt with respect to the filler), are shown in Fig. 3.9a. All other parameters have been fixed, namely the filler content (Φ_{Si}=18.3%v) and DPG content (1%wt with respect to polymer).

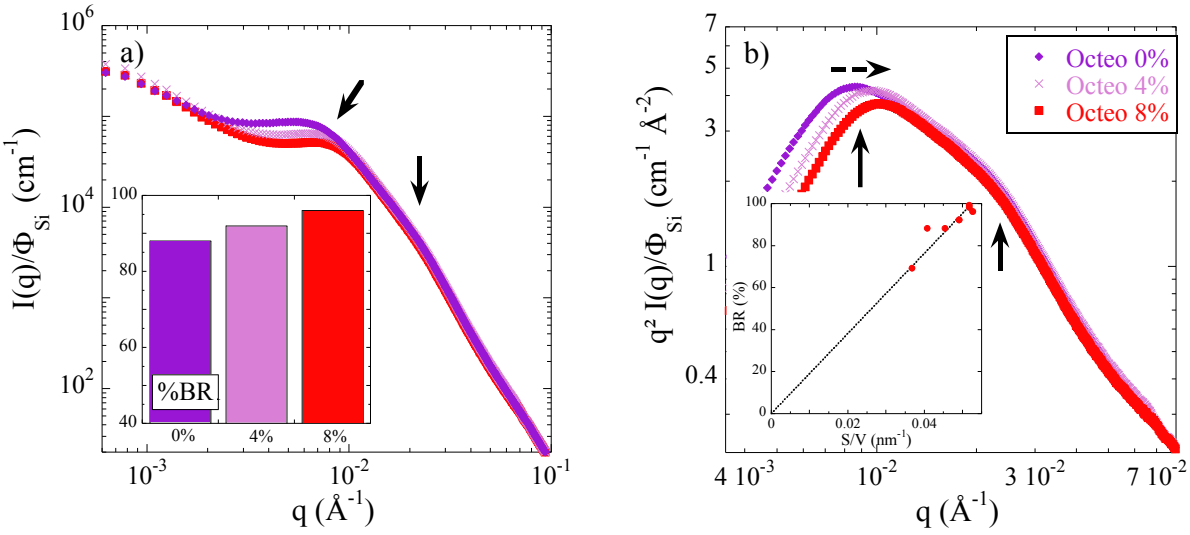

Figure 3.9 (a) Reduced SAXS intensities allow the structural comparison between nanocomposites containing 18.0±0.3%v silica in a fully functionalized matrix with DPG, made with different amounts of coating agent octeo: 0 (circles), 4 (crosses), and 8%wt (squares). The inset shows the bound rubber of the same NCs. Arrows indicate the q-ranges of particle- and aggregate-scattering, respectively. (b) Kratky plot $q^2I(q)$ vs q highlighting the structural evolution (dashed arrow). Inset: All BR for functionalized polymers versus the specific surface of aggregates.

The scattered intensities in Fig. 3.9a are characteristic of the same type of structure as discussed with Fig. 3.5: obvious changes are induced by the presence of the coating agent, inducing better filler dispersion. A similar result has been reported in the literature for an ungrafted polymer matrix (Bouty et al. 2014). In parallel, the fraction of bound rubber shown in the inset is seen to increase with the amount of octeo. Fig. 3.9a is a key result of our study, since it reveals the delicate impact of the coating agent on structure in graftable matrices. The results of our quantitative analysis are given in Table 3.3. It reveals a decrease by more than 10% in the average aggregate radius R_{agg}, which is also seen in the Kratky representation in Fig. 3.9b, with the shift of the maximum to higher q illustrated by the dashed arrow. This maximum is the direct consequence of the break in slope in I(q), indicative of the aggregate interaction, highlighted by the arrow around 0.01 $Å^{-1}$. From the analysis of the height of the signal in the 'aggregate region' up to 0.01 $Å^{-1}$, using the volume fraction of fractal branches determined independently from TEM pictures shown in Fig. 3.10 ($\Phi_{fract} \approx 80\%$), the compacity is also found to decrease, as given in Table 3.3. As a result of the combination of decrease both in size and density, the average aggregation number N_{agg} is seen to diminish by 35%, from 48 to 31. In the inset of Fig. 3.9a, the bound rubber results are seen to slightly increase with increasing octeo content. As this coating agent does not contribute to any grafting of the polymer, this is a priori surprising. The interpretation of this behavior is that the decrease of N_{agg} favors polymer-filler interactions, via a higher specific surface S/V estimated by $3*\Phi_{agg}/R_{agg}$ in the inset of Fig. 3.9b. Indeed, both bound rubber and S/V increase by some 10%. It cannot be decided, however, if the higher bound rubber is only adsorbed to the aggregates, possibly entangled with grafted chains making it difficult to desorb, or if the higher S/V favors polymer access to surface and grafting. In parallel, the TEM images of the octeo-series in Figure 3.10 illustrate the progressive formation of smaller and smaller structures with increasing octeo content. Homogeneity on larger scales has been checked with lower resolution pictures. As expected, compatibilization of the originally hydrophilic filler surface with the hydrophobic polymer matrix through the coating agent induces the formation of smaller aggregates, i.e., a better – more "nano" – dispersion.

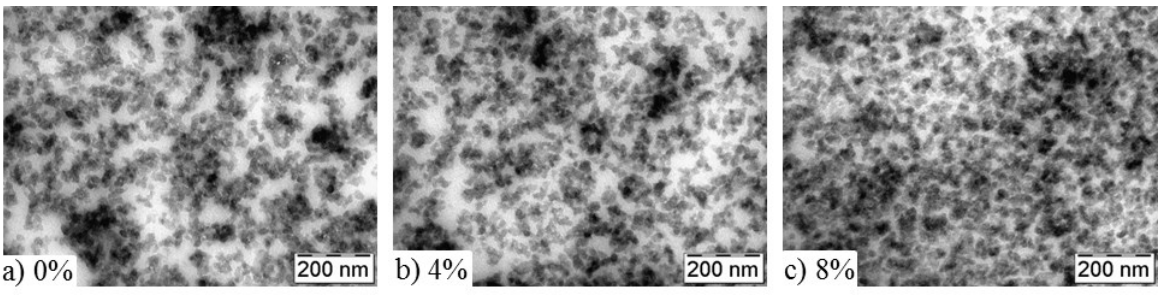

Figure 3.10: TEM images of nanocomposites containing 18.0±0.3%v silica in a fully functionalized matrix with DPG, made with different amounts of coating agent octeo: 0, 4, and 8%wt with respect to silica.

3.6. Synergetic effect of coating agent and catalyzer on nanocomposite structure

Once the impact of the coating agent octeo is characterized, the role of DPG can be evaluated. Four different samples, containing either no agents, only octeo, only DPG, or both DPG and octeo have been formulated and compared. Concentrations have been set to the nominal values, i.e., 8%w octeo with respect to silica (≈ 18%v filler fraction), and 1%w DPG with respect to polymer mass. The TEM images in Fig. 3.11 seem to indicate that the characteristic size is larger in absence of both octeo and DPG, or only with octeo, than in presence of only DPG or both agents. For quantitative analysis, however, SAXS is needed.

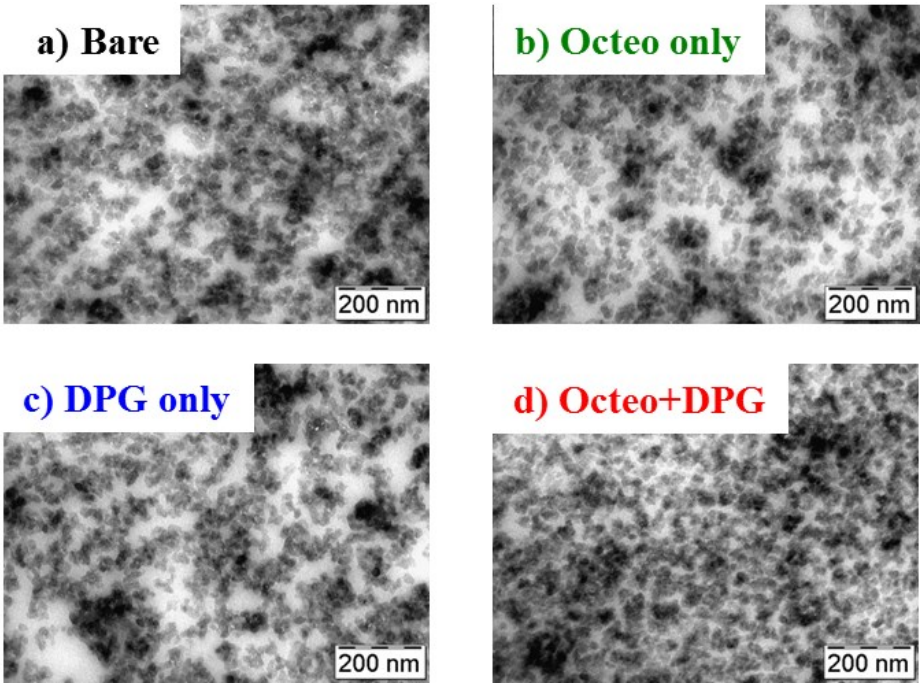

Figure 3.11: TEM images of nanocomposites containing 18.0±0.3%v silica in a fully functionalized matrix (F): (a) without small molecules (bare), (b) with octeo only (8%wt with respect to silica, no DPG), (c) with DPG only (1%wt with respect to polymer, no octeo), (d) with with both octeo and DPG

In Fig. 3.12a, the normalized scattered intensities are plotted for these samples, and the Kratky plots in Fig.3.12b highlight the structural evolution.

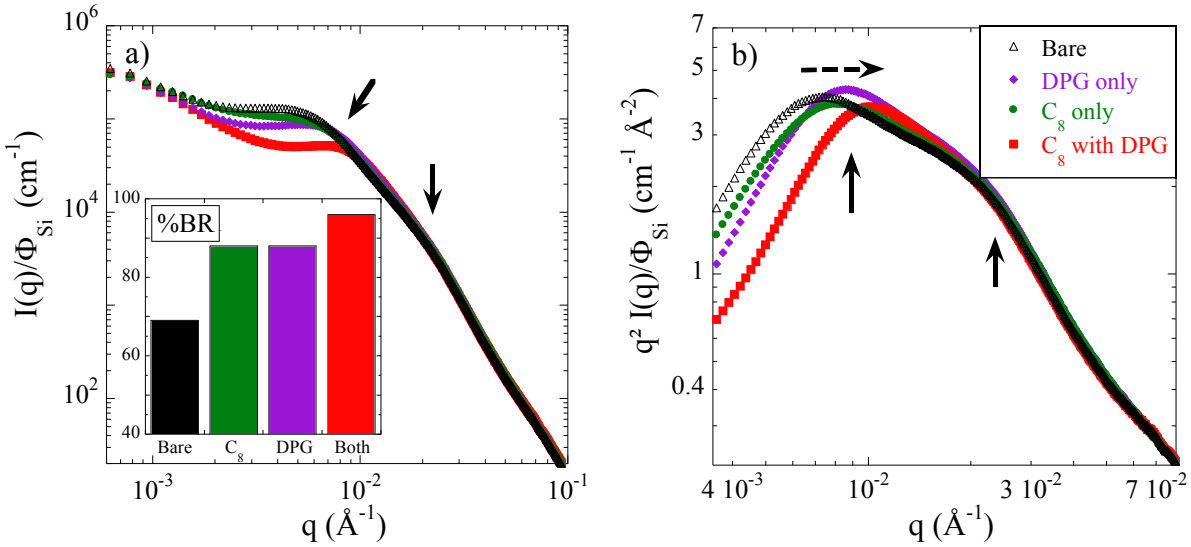

Figure 3.12 (a) Reduced SAXS intensities comparing the structure of nanocomposites containing 18.0±0.3%v silica in a fully functionalized matrix: without small molecules (bare, triangles), with DPG only (diamonds), with octeo only (circles), and with both octeo and DPG (squares). The fraction of octeo (when present) is 8%wt. The inset shows the bound rubber of the same PNCs. (b) Kratky representation.

All the structures characterized by scattering in Fig. 3.12a are again typical for this type of simplified industrial nanocomposites. The coating agent and DPG have a pronounced impact on the aggregate structure probed at intermediate q, as one can see from the different intensity levels – keeping in mind the logarithmic scale: without any DPG or coating agent, the dispersion is worst, with the highest intensity in Fig. 3.12a, while in presence of both – cf. the lowest, red curve in the figure –, the best dispersion is obtained. This is confirmed by the quantitative analysis of the Kratky plot (Fig. 3.12b) presenting a shift to the right with added molecules, which is given in Table 3.3: the average aggregate radius R_{agg} decreases from 38 (no agents) to 30 nm (both agents). Simultaneously, the compacity and the aggregation number evolve from κ = 48% to 44%, and N_{agg} from 67 to 31, respectively, while the bound rubber fraction increases from below 70% to above 95%. The decrease in N_{agg} is indicative of a better compatibility of the filler with the matrix, as there is more polymer in contact with fillers for smaller aggregates, and this leads to the highest bound rubber value in Fig. 3.12a.

One might wonder if octeo and DPG produce a synergetic effect on the microstructure, or if only one of them might be effective. The two intermediate samples with either one of them have also been analyzed; cf. Fig. 3.12 and Table 3.3. Adding only octeo decreases the aggregate radius to 36 nm and the aggregation number N_{agg} to 61, whereas the bound rubber fraction increases. This behavior is consistent with the variation observed for different octeo contents in presence of DPG, cf. Fig. 3.9, and probably has the same causes – a higher specific surface. Finally, adding only DPG has an unexpected effect on the structure, as it leads to a better dispersion than without any agent: the average aggregate radius is about 34 nm, while compacity is 47% and the aggregation number $N_{agg} \approx 48$. Such results may be due to the strong affinity of the basic DPG with the silica surface, which displays acidic character. DPG

therefore preferentially adsorbs on the (untreated) silica, preventing by this way the formation of hydrogen bonds between hydroxyl groups of different nanoparticles (Kosmalska et al. 2003; Zaborski and Donnet 2003). Note that the number density of silanol groups on silica has been shown to be correlated with the aggregate size in SBR nanocomposites (Yatsuyanagi et al. 2001). Comparison between the structural results with DPG only and octeo only further indicates that the efficiency of the coating agent alone is not optimal. The addition of DPG together with octeo is required to obtain the better dispersion (see Fig. 3.12 and Table 3.3), the DPG promoting the grafting reaction of the silane (Penot and Roy 2006). On the other hand, one may wonder if DPG also has a catalytic action on the grafting reaction of the polymer chains on the silica nanoparticles (all chains carry a Si-OH end-function). This does not seem to be the case as the BR values for DPG only and octeo only are identical. It follows that the 40%-increase of the bound rubber fraction from no agents to both agents in Figure 12a is mostly driven by the structural evolution: the decrease of N_{agg} leads to a higher specific surface ($\approx$ +45%), favoring chain grafting. Confronting these findings with presence and absence of *both* molecules unambiguously proves that DPG and octeo are necessary to tune the large-scale filler structure efficiently.

Our discussion towards the influence of small molecules has been extended also on crosslinked samples as they may be used in applications. The details about the preparation of the crosslinked nanocomposites are reported in appendix A3.We have first investigated the vulcanization kinetics given by the curing curves (torque versus time) of the pure matrix with and without DPG, see inset of Fig. 3.13. As observed by Ramier et al. (Ramier et al. 2007a), using only CBS (without DPG) shifts the beginning of the vulcanization process to longer times, which means that both accelerators are required for a rapid cure. In the meantime, we found that the presence of DPG impacts the final crosslinking density only by a few percent. We have then formulated four crosslinked samples in analogy to the four samples compared in Fig. 3.12a. The experimental difficulty with such samples is that the curing agents are added in the two-roll mill process, inducing slight anisotropy in the samples and thus intensities. Luckily, the average level of these intensities as shown in the next plot, however, varies strongly with the composition, making conclusions robust independently of anisotropy. In Fig. 3.13, the same color code as for Fig. 3.12a applies, comparing crosslinked samples with both DPG and octeo, with only one, or neither. The scattering of the corresponding uncrosslinked samples (Fig.3.12a) is superimposed in grey for convenience.

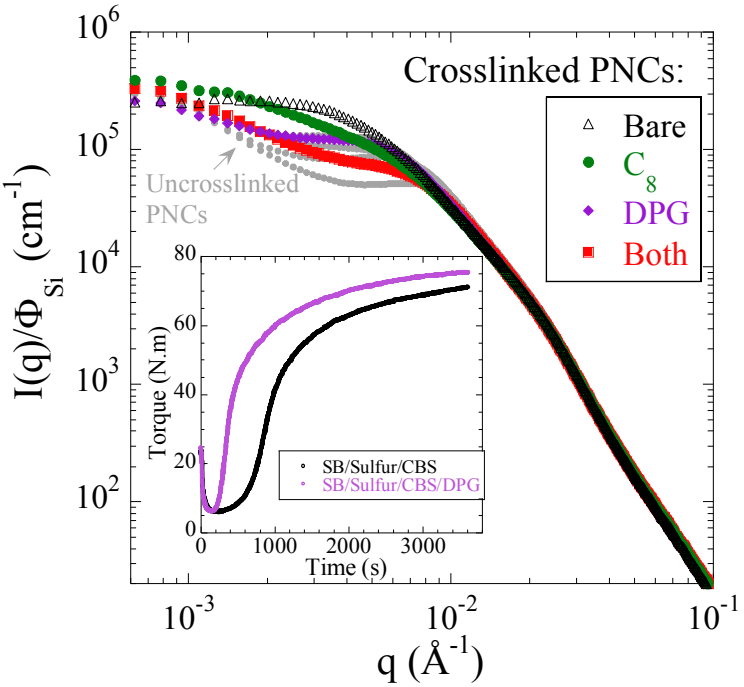

Figure 3.13 Reduced SAXS intensities comparing the structure of crosslinked nanocomposites containing 17.5±0.3%v silica in a fully functionalized matrix: without small molecules (bare, triangles), with DPG only (diamonds), with octeo only (circles), and with both octeo and DPG (squares). The fraction of octeo (when present) is 8%wt. The uncrosslinked curves shown in Fig. 3.12 are superimposed in grey. Inset: Curing curves of unfilled polymer: SB+Sulfur+CBS, and SB+Sulfur+CBS+DPG.

In Fig. 3.13, crosslinked and uncrosslinked structures are identical at high q, and at low q intensities tend to converge. In the intermediate q-range, all four intensity curves of crosslinked samples are higher by less than a factor of two than the uncrosslinked ones. This means crosslinking favors slightly the aggregation of silica nanoparticles, similarly to previous results (Baeza et al. 2016c). For instance, comparing the intensity levels of the samples having both small molecules, the crosslinked one has bigger aggregates R_{agg} (34 nm, uncrosslinked: 32 nm), about the same compacity (κ = 47%, resp. 44%), and a higher N_{agg} = 46 (resp. 31). It is unclear, however, if this increase in aggregation is due to the crosslinker which might influence interactions between particles, or if mechanical action during crosslinking has this effect. The most remarkable fact in Fig. 3.13 is that the order of the curves is unchanged with respect to the uncrosslinked case. Our findings that both small molecules, DPG and octeo, are necessary to tune the large-scale filler structure efficiently thus remain valid also for crosslinked samples.

3.7. Conclusion

We have investigated the impact of small molecules – coating agents and DPG added during formulation by solid-phase mixing – on the bound rubber fraction and on the microstructure of polymer nanocomposites made with disordered silica filler of industrial relevance. The bound rubber is found to be correlated with the microstructure (see inset of Figure 3b), suggesting a specific-surface effect,

smaller aggregates offering more possibilities to bind polymer. The microstructure is characterized by small-angle scattering and TEM, with a particular focus on aggregates of primary NPs, which we have shown to be the fundamental structural units, cf. recent reviews (Genix and Oberdisse 2015; Genix et al. 2016a). Accordingly, the structure can be quantitatively described with two independent measures, the average aggregate radius R_{agg}, and the average aggregation number N_{agg}, or equivalently, the compacity κ. Both have been shown to evolve with the coating agent content, higher concentrations of this additive giving better dispersion, i.e., smaller aggregates, presumably due to a better compatibility with the matrix. There was surprisingly no impact of the chain length of the coating agent on the nanocomposite microstructure, suggesting that short chains are sufficient to cover the nanoparticle surface. Concerning this latter point, one might nonetheless expect a modification of the local dynamics, caused by a plasticizing effect of the matrix by the longer aliphatic chains, a point which we hope to address in a future study. Along the same lines, one could also investigate if the absence of effect is due to saturation of the surface, e.g., by performing a study of longer molecules as a function of (lower) concentrations.

By confronting the dispersion of nanocomposites with and without the amine DPG, this molecule was unambiguously demonstrated to be necessary to promote the compatibilizing effect of the coating agent: there is a strong synergy between the amine and the coating agent. This conclusion was shown to remain true even for industrially more relevant crosslinked samples. By comparing bound rubber and structure to a sample containing only DPG, it was further shown that DPG does not catalyze the matrix end-grafting.

4. Impact of surface modification of silica nanoparticles on dispersion in precursor solvents and model polymer nanocomposites

4. Impact of surface modification of silica nanoparticles on dispersion in precursor solvents and model polymer nanocomposites

The properties of nanocomposite materials are strongly influenced by the polymer-silica interactions which can be tuned by the surface-modification of the fillers using "small molecules", such as silane coating agents commonly used in industrial applications. In this chapter, a description of the structural organization of silica NPs surface-modified by different silane molecules will be proposed. Following the preparation protocol developed for model nanocomposites (NCs), the dispersion state of such fillers has been monitored in the precursor suspensions (EtOH/H_2O solution and methyl-ethyl-ketone) and then in the final nanocomposite by Small Angle X-Ray Scattering (SAXS) and Transmission Electron Microscopy (TEM). A further quantitative analysis of the scattering data has been thus performed using an original Reverse Monte Carlo (RMC) method (see section 2.5).

The main results of these chapters are reported in two papers close to submission (Musino et al. in preparation - a -, Musino et al. Submitted - b).

4.1. Impact of silane hydrophobicity on dispersion of surfaced-modified silica NPs

The combined SAXS-TEM-RMC method has been applied to investigate systems (i.e., solvent precursors and model NCs) where silica nanoparticles (NPs) have been surface-modified by silanes which differ by the length of their alkyl chain, and thus by their hydrophobicity: C_8, C_{12} and C_{18} (see section 2.1). It will be shown that the dispersion state of the NPs in the precursor suspension before the nanocomposite formation is transferred into the polymer matrix. Moreover, the molecular weight of the silane molecules (i.e., length of the alkyl chain) affects the final aggregate distribution since the use of the silane with the longest alkyl chain (C_{18}) leads to the biggest aggregates.

4.1.1. Dispersion of C_8-, C_{12}- and C_{18}- surface-modified nanoparticles in precursor solvents

As reported in section 2.3, the surface-modification of the silica NPs with silanes characterized by different hydrophobicity is performed in a hydro-alcoholic suspension (63%v EtOH). The same particles are then transferred in methyl-ethyl-ketone (MEK) for the subsequent mixing with the styrene-butadiene polymer dissolved in the same solvent. The dispersion state after grafting has been investigated by SAXS in both solvents. The scattering curves of NPs obtained at the end of the surface-modification and suspended in hydro-alcoholic medium and MEK (Φ_{Si} = 1%v) are reported in Fig. 4.1a and Fig. 4.1b, respectively. Both suspensions have been compared to the one of bare particles ("no agent") in the same solvent. In the hydro-alcoholic suspension, the scattering function of these bare NPs in Fig. 4.1a can be

described by the form factor P(q) of polydisperse spheres (black line, 1%v NPs in water, R_0=12.5nm, log-normal polydispersity σ=12%). This implies that it is not necessary to include the structure factor in the description, and thus that bare particles are well dispersed. At high q, P(q) is overlapped to the data, confirming that the same particles are present in all samples. This feature has been used to normalize all data sets on the form factor measured in water, allowing the comparison between particle scattering in different solvents and then in the polymer matrix, also at different concentrations. The normalized intensity $I_{norm}(q)$ is thus expressed as

$$I_{norm}(q) = I_{exp}(q)\ \frac{\Phi_{form}}{\Phi}\ \left(\frac{\Delta\rho_{form}}{\Delta\rho}\right)^2 \qquad [4.1]$$

where the index 'form' corresponds to the form factor measurement, and Φ and Δρ to the particle volume fraction and contrast of the originally measured intensity I_{exp}. The scattering length densities used to calculate the contrasts $\Delta\rho = \rho_{SiO2}-\rho_{medium}$ are: $\rho_{SiO2} = 18.9\ 10^{10}$ cm^{-2}, $\rho_{H2O} = 9.5\ 10^{10}$ cm^{-2}, $\rho_{EtOH} = 7.6\ 10^{10}$ cm^{-2}, $\rho_{MEK} = 7.7\ 10^{10}$ cm^{-2}, and $\rho_{SB} = 8.9\ 10^{10}$ cm^{-2}.

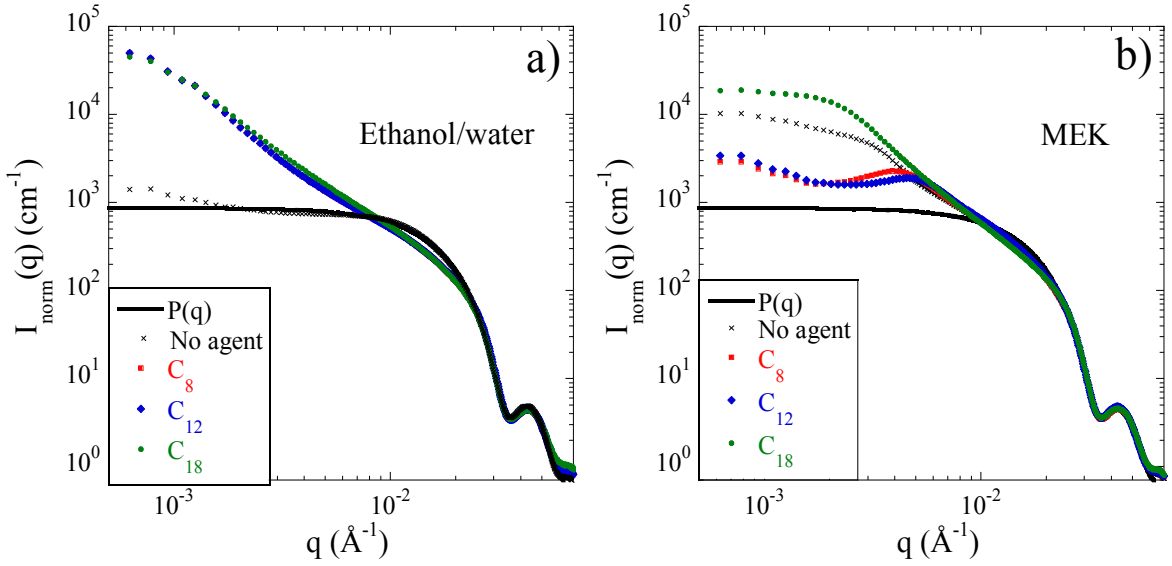

Figure 4.1 (a) SAXS scattered intensities normed to NP form factor in water (continuous line, R_0 = 12.5 nm, 12%) of bare and surface-modified NPs (C_8, C_{12}, C_{18}) in hydro-alcoholic suspension (63%v ethanol, Φ_{Si} = 1%v). (b) Same for NPs in MEK (Φ_{Si} = 1%v).

As soon as the grafting reaction with the trifunctional ethoxy molecules C_8, C_{12}, and C_{18} takes place in the ethanol-water mixture (Φ_{Si} =1%v), the dispersion state of the nanoparticles changes considerably. Together with the thermogravimetric analysis (TGA) and Attenuated Total Reflectance (ATR) results which allowed to reveal that the grafting density is just below 1 nm^{-2} independently of the coating agent (section 2.3), this observation represents another proof that the grafting reaction was successful, as otherwise the interaction between particles would not be modified. Incidentally, the scattering of the grafted monolayer is measurable at the highest q in Fig. 4.1a. The signal is 10'000 times weaker than the one at low q. However, a monotonic increase with layer thickness is visible in the Porod domain of the NP, showing that the particle surface has been modified. The considerable low-q increase of all the

scattering curves, up to ca. fifty times above the form factor, suggests the formation of small aggregates made with about the same number of NPs. Remarkably, this happens without any relevant difference for the different alkyl chain lengths, i.e. the layer thickness has no influence on the particle interactions in this solvent. At the same time, the samples become opaque (Fig. 4.2a), without showing any macroscopic destabilization like sedimentation by visual inspection, presumably due to the low particle concentration.

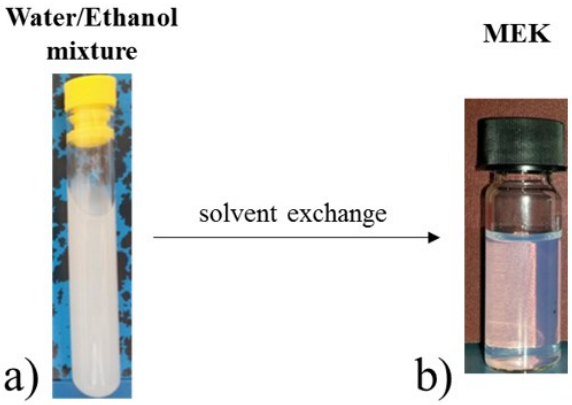

Figure 4.2 (a) Silica NPs surface-modified by C_8 suspended in water/ethanol suspension, i.e., "milky" suspension. (b) Same surface-modified NPs transferred in MEK by solvent exchange procedure form a "clear" translucent suspension.

As already mentioned, the same surface-modified NPs have been stabilized in MEK by a solvent exchange procedure based on dialysis. These suspensions became translucent again (Fig. 4.2b) suggesting that the NPs form again aggregates of finite and even smaller size. The silica volume fraction of MEK suspensions is about 1%v. The dispersion state of these surface-modified NPs in MEK has been evaluated by SAXS, as reported in Fig. 4.1b. A Kratky presentation $q^2I(q)$ of the scattering data indicates a low-q structure, with a peak close to 10^{-3} $Å^{-1}$, related to a finite size structure in suspension. Since MEK is a good solvent for styrene-butadiene, it is thus expected to solvate the grafted alkyl layer. At the same time, it is still a quite polar solvent ($\varepsilon_{MEK} = 18.5$), not too far below the water ethanol mixture ($\varepsilon_{EtOH} = 24.5$). In MEK, both steric stabilization and electrostatic interactions can contribute to the colloidal stability, which is found to be maintained by visual inspection for at least 45 days. Not surprisingly, the dispersion in this solvent is found to be more efficient than in the hydro-alcoholic suspension. Moreover, it appears to depend on the silane used for the grafting, as deducible from some variations in the shape of the curves. The overall intensity, however, stays in a finite range, indicating the formation of small aggregates of similar size in all cases. The scattering functions of the C_8 and C_{12}-samples, for instance, display a correlation peak around 0.0045 $Å^{-1}$, corresponding to small aggregates with long-range repulsive interactions. A simple cubic model gives $N_{agg} \approx 3 - 4$. Finally, the C_{18}-coating, finally, results in a less long-range repulsive interaction between NPs. From the low-q limit of the corresponding scattering function, an approximate aggregation number of $N_{agg} \approx 20$ can be deduced, indicating larger aggregates than with the other grafts. It is not trivial to compare the different scattering functions, in particular due to the absence or presence of interaction peaks. In the following section, a

quantitatively method based on RMC simulations (see section 2.5) will be applied to unify all the structures regardless of repulsive interactions. At the same time, it can be already observed from the presented scattering data that all the aggregates in MEK suspensions are smaller than the ones in hydroalcoholic solution. Such a result proves that aggregation is reversible, thanks to the steric hindrance induced by the grafted layer. Moreover, it can be concluded that for all grafts, the surface-modified particles form small aggregates which are well-dispersed in MEK before being incorporated into the polymer matrix.

4.1.2. Dispersion of C_8-, C_{12}- and C_{18}- surface-modified nanoparticles: from solvents to polymer matrices

Once the surface-modified silica NPs have been transferred into MEK, they can be dispersed in styrene-butadiene polymer dissolved in the same solvent. The final NC, indicated as "model" system due to the monodispersity of the silica, is obtained once all the residual solvent is evaporated, see section 2.3. The evolution of the dispersion of the NPs suspended first in hydroalcoholic solution, then in MEK, and finally in the polymer matrix is compared in Fig. 4.3a, 4.3b and 4.3c, for C_8-, C_{12}- and C_{18}-, respectively. As discussed in the previous section, the particles result to be somewhat aggregated in water/ethanol, then quite well-dispersed with visibly repulsive interactions in MEK, and finally slightly aggregated in the polymer. For all surface modifications, the dispersion in the final NC is intermediate between ethanol/water and MEK, somewhat closer to the structure in MEK, with namely the persistence of a shoulder in the q-range of the peak. It can be thus concluded that the good dispersion of the surface-modified NPs in MEK is mostly transferred into the polymer matrix, too.

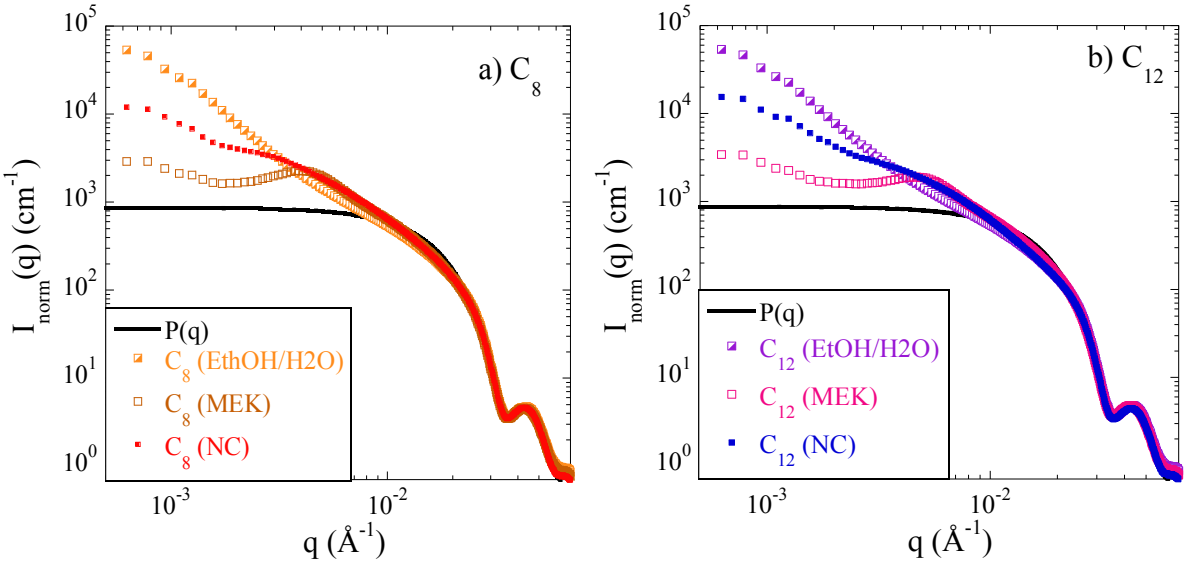

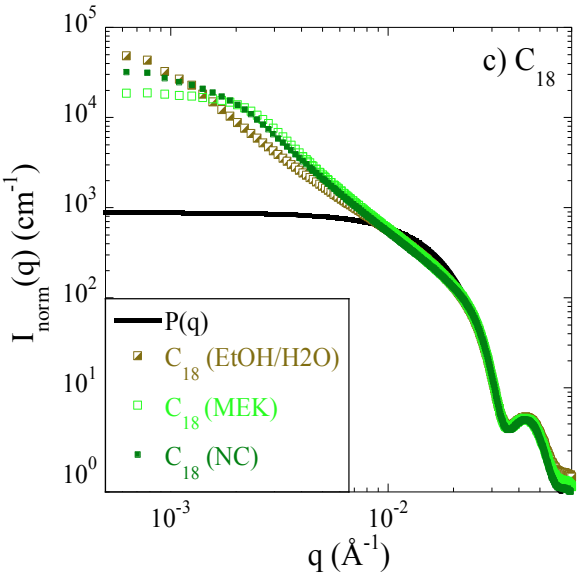

Figure 4.3 Evolution of SAXS scattered intensities normed to NP form factor in water (continuous line) of (a) C_8-, (b) C_{12}-, (c) C_{18}- surface-modified NPs from suspension in hydro-alcoholic solution, MEK, to polymer (Φ_{Si} = 1.1±0.1 %v).

The final dispersion state of the NPs in the nanocomposites has been systematically investigated for the three triethoxy grafts C_8, C_{12}, C_{18}, and for bare NPs and their SAXS curves are compared in Fig. 4.4. In a first approach, the lowest available volume fractions (Φ_{Si} ~ 1%v) are discussed, and concentration series will be shown below. The final silica volume fractions in the PNCs have been determined by thermogravimetric analysis. In each case, the data referring to model nanocomposites formulated with surface-modified NPs are compared to NCs made with bare NPs. As in MEK, the final dispersion in the polymer matrix is found to be rather similar for all grafts, roughly within a factor of two in low-angle scattering. This outcome suggests the formation of finite-sized aggregates. Some structural features can be extracted from the intensity curves: the C_8 and C_{12}-samples show a lower intensity at small angles, with a kink around 0.002 $Å^{-1}$. The C_{18}-sample displays a higher intensity with a Guinier-like shoulder in the same q-range, indicating that C_{18}-modification induces again the highest aggregation. It is difficult, however, to translate the intensity curves in direct space information, as they may result from a large distribution of aggregates, from single particles to bigger aggregates. Moreover, these aggregates interact differently, depending on the coatings, generating unknown structure factor contributions in the low-q intensity.

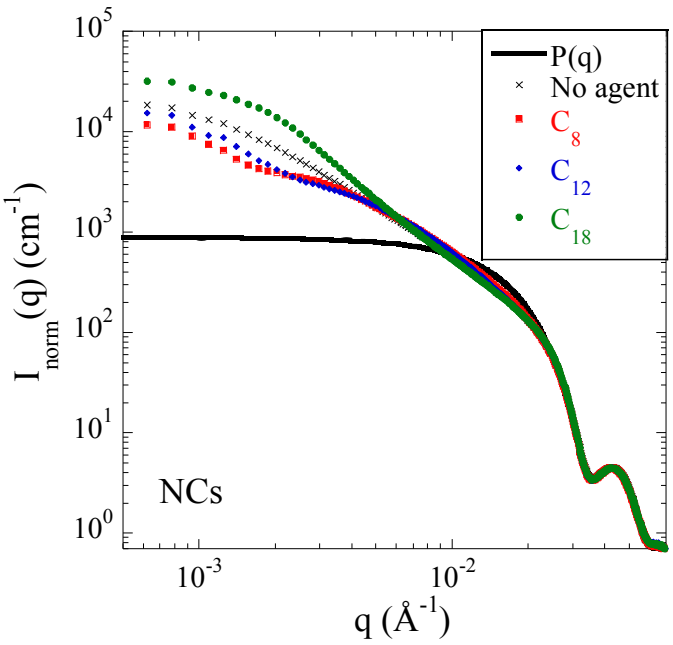

Figure 4.4 Intensities of bare and surface-modified NPs (C_8, C_{12}, C_{18}) in polymer nanocomposites at the lowest Φ_{Si} (2.6%v, 1.2%v, 1.7%v, 1.4%v, respectively).

Although they do not provide the statistical averages like SAXS, TEM pictures give an idea of the typical aggregation state of the particles in the nanocomposite. In Fig. 4.5, TEM images of NCs made with bare or surface-modified NPs are presented, at the lowest available particle volume fractions Φ_{Si}. Lower magnification pictures reveal the over-all homogeneity of the slices, as shown in the insets of Fig. 4.5. It can be observed that the nanoparticles are mostly individual, or form small aggregates, without any statistically relevant difference for bare or surface-modified NPs. At most, one may suspect that the C_{18}-modified NPs tend to aggregate more. In this respect, a visualization of a sample at Φ_{Si} around 5%v formulated with bare and C_{18}-surface modified NPs are nonetheless shown in the Fig. 4.6. It is obvious that is difficult to evaluate the influence of the silica volume fraction Φ_{Si} by TEM, due to the crowding effect even at moderate concentrations. Thus, the impact of the silica content has been mainly investigated by SAXS.

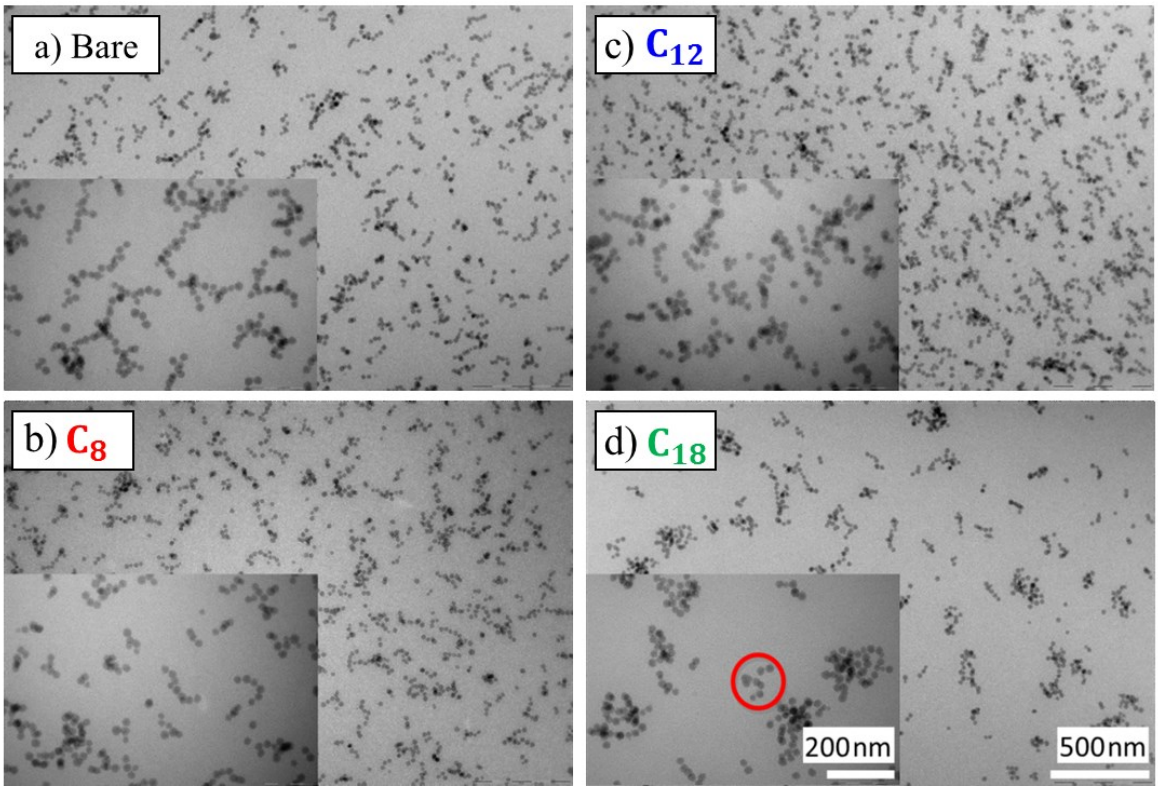

Figure 4.5 TEM pictures of NCs at low silica volume fraction, with bare (Φ_{Si} =2.6%v) (a) and (b-c) surface-modified NPs C_8 (Φ_{Si} =1.2%v), C_{12} (Φ_{Si} =1.7%v), C_{18} (Φ_{Si} =1.4%v), respectively, as indicated in the legend. The red circle in the inset of Fig. d shows how the resolution of TEM images does not allow to determine if the particles are part of the same aggregate.

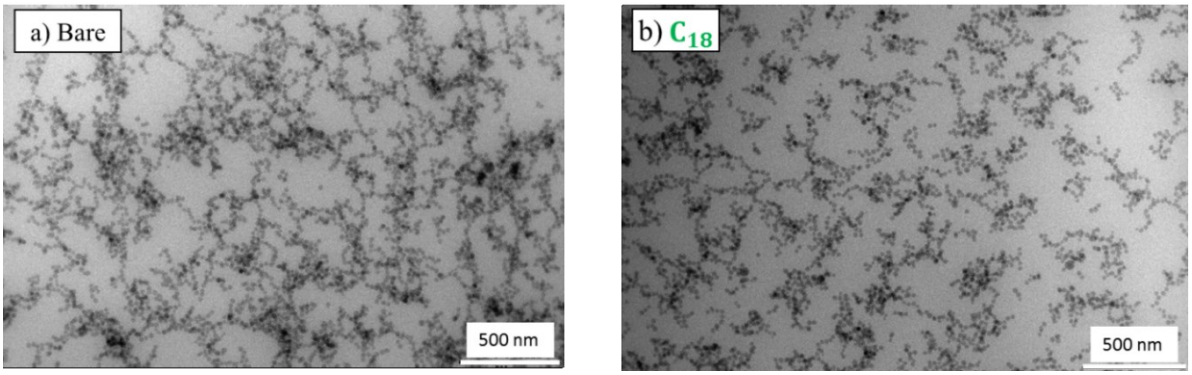

Figure 4.6 TEM pictures of NCs formulated with (a) bare silica (Φ_{Si}=6.0%v) and with (b) NPs surface-modified by C_{18} (Φ_{Si} =5.2%v).

The influence of the silica volume fraction Φ_{Si} on the structure of surface-modified NPs has also been investigated by SAXS. Series up to about 20%v are presented in Fig. 4.7, for the bare, and the C_8-, C_{12}- and C_{18}-coated samples. Our group recently proposed a method to extract the average local concentration of particles in aggregates from scattering (Schmitt et al. 2016; Genix and Oberdisse in preparation). Such a method is based on the depth of the "correlation hole", which is the intensity depression with respect to the form factor, around $q^* = 0.016$ Å^{-1} (see section 2.4). By the I(q)/P(q) ratio, the "experimental" (average) structure factor is obtained. Equating S(q) at the correlation hole with the structure factor expression obtained by fitting the Percus Yevick (PY) low-q limit to numerical

simulations (Genix and Oberdisse In preparation), the average local concentration κ (i.e. local compacity) can be found:

$$S_{PY}(q^*) = \frac{(1-\alpha\kappa)^4}{(1+2\alpha\kappa)^2} \qquad [4.2]$$

where α = 0.7 for the present nanoparticles of polydispersity 12%. As the intensities are rather close to the form factor, quite low κ-values are found. For all samples, independently of surface-modification, the compacity κ is estimated at 5±1% at the lowest Φ_{Si}, and it increases up to 9 – 12 % for the highest (global) silica volume fractions. This evolution represents a quantitative translation of the deepening of the intensity observed in the intermediate q-range with Φ_{Si} in Fig. 4.7. It indicates that a large fraction of the NPs forms a population of individually dispersed, or only slightly aggregated particles. Moreover, the presence of small aggregates of internal density of some 5-10% gives a picture of the overall structure, and in particular of the evolution of the structure factor: indeed, as the silica content is increased, zones representing aggregates of this density populate the sample. Due to conservation of matter, space becomes entirely filled when the global volume fraction Φ_{Si} equals the local one, κ. Then, the samples appear to be homogeneous on scales larger than the typical aggregate size, and the low-q intensity decreases, as observed for all surface-modifications in all the curves shown in Fig. 4.7.

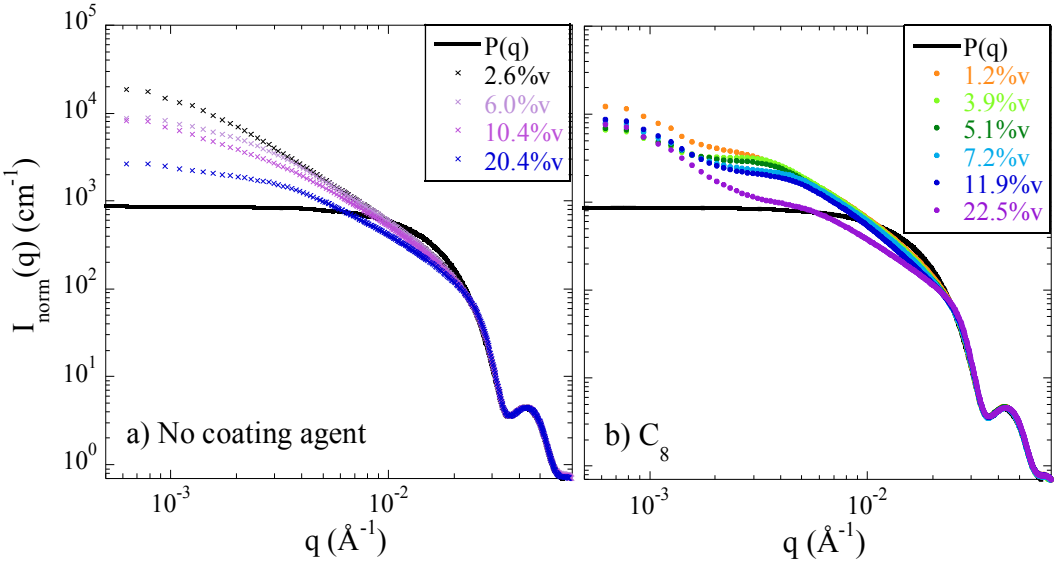

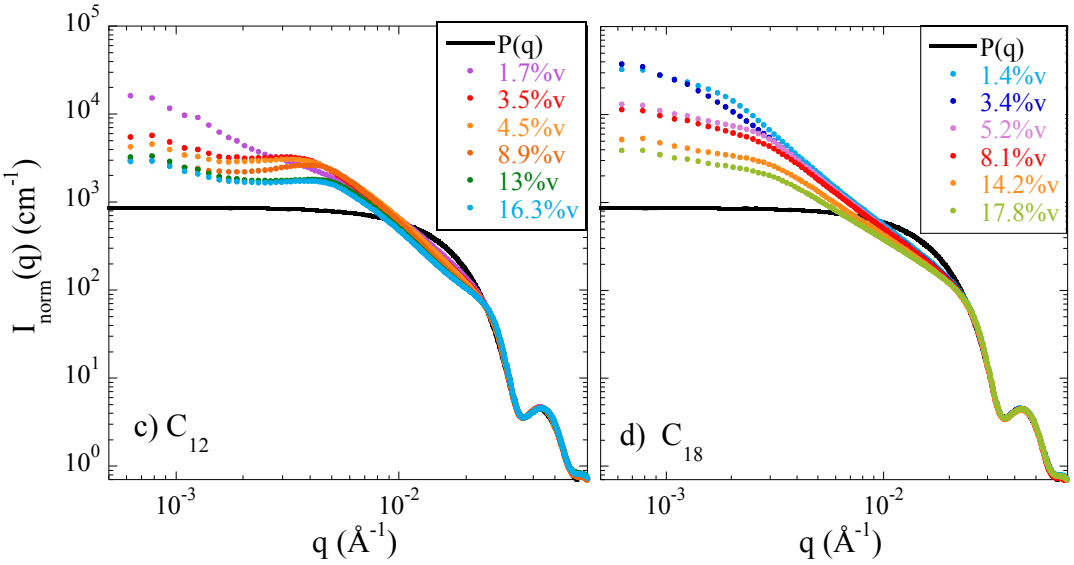

Figure 4.7 (a) SAXS scattered intensities normed to NP form factor in water (continuous line) of bare NPs in polymer, for different silica volume fractions as indicated in the legend. (b), (c), (d): Same comparison for C_8-, C_{12}-,C_{18}-grafted NPs in polymer, respectively.

The normalized scattered intensities for all series follow the same tendency: the higher the silica content, the lower the low-q intensity, and the deeper the correlation hole around 0.016 $Å^{-1}$. Moreover, the shape of the curves remains similar since there are no structural peaks, and the low-q shoulder stays approximately in the same q-range. From a first qualitative analysis, the intensities in Fig. 4.7a, 4.7b and 4.7c are lower than the one in Fig. 4.7d, leading to the conclusion that the increase in silica content does not alter the result obtained in Fig. 4.4, namely with the higher aggregation for C_{18}-coated NPs. At low-q, the intensity decrease is due to the repulsive interactions between NP aggregates which become predominant at higher concentrations. As already discussed, this is a consequence of the homogenization on large scales. The problem is difficult to analyze because the aggregate size distribution may change simultaneously, as well as the internal structure of aggregates. It is thus necessary to analyze scattering data with a more precise tool. The use of a stochastic inversion method is proposed to obtain quantitative information about the direct-space structure of NPs in the sample. This approach allows to quantitatively translate the shape of the scattering functions into real-space particle configurations, and thus aggregation distribution functions. The underlying inversion method of the intensity based on polydisperse NPs is called reverse Monte Carlo. The detailed description of the method has been outlined in section 2.5. In order to analyze the outcome of the RMC method, an aggregate recognition algorithm has been implemented. It relies on a critical surface-to-surface distance δ which must be defined. For the surface-to-surface distances below this value, particles are counted as aggregated. As already observed in section 2.5, it is tempting to set this distance equal to zero, but due to the finite resolution of the scattering experiment, non-contacting particles in close vicinity lead to a very similar scattering signature, i.e. one cannot discriminate 'real contact' from 'close-to-contact'. Moreover, looking at the TEM pictures in Fig. 4.5d, it appears that some NP assemblies (i.e., the one highlighted

by the ellipse) are likely to be counted as aggregates in scattering. At the same time, it is impossible to decide from the TEM if these NPs really touch since they possess centers-of-mass positions with a high degree of correlation, forming a dense zone. On the other hand, they clearly are not part of any of the groups on their left. Thus, the average particle radius seems to be an appropriate choice of the critical surface-to-surface distance. It may be added that different options have been tried to optimize this parameter: critical distances too close to zero fail in detecting about any aggregation, presumably due to the lack of resolution of the scattering experiments, in combination with polydispersity. On the contrary, taking the diameter as parameter results in aggregating all NPs in the simulation box already at low silica content.

For NCs of increasing silica contents formulated with the bare NPs or NPs surface-modified with C_8, and C_{18}, the distributions of aggregation numbers have been determined from the average of 100 RMC-configurations (i.e., application of the aggregate recognition algorithm to independent configurations). The results of this analysis are shown in Fig. 4.8. The results for C_{12}- surface modified NPs are not shown since they are extremely close to the one of C_8. Here, $p(N_{agg})$ represents the number of times that an aggregate of given aggregation number N_{agg} is found, divided by the total number of aggregates (including isolated NPs with $N_{agg} = 1$). It can be noticed that the functions in Fig. 4.8a, 4.8b and 4.8c are the real-space analogues of the intensities in Fig. 4.7a, 4.7b and 4.7c, in absence of interactions. These distribution functions describe the mass of the aggregates, but they disregard interactions between aggregates which are difficult to describe (although they are taken into account in the RMC code). The RMC procedure thus allows to identify aggregate mass distribution independently of any structure factor reflecting their dispersion in space. This result is remarkable since it could not have been obtained directly from the scattering.

Observing the generic shape of the distribution functions, it is found that a large fraction of the aggregates are individual particles. For each graft, the occurrence of aggregates then decreases strongly with aggregate mass. This decrease, and thus the width of the distribution function, evolves with the silica volume fraction. With higher Φ_{Si}, a tail of large aggregates is formed, in the range of aggregation numbers of several tens to hundreds: as the system becomes denser, more and more particles are pushed together. This is particularly visible in Fig. 4.8b, where the C_8-modified NPs at 7.2% build aggregates even up to about a few thousand particles. The densification results in an increase of the average aggregation number $\langle N_{agg} \rangle$, which is plotted in Fig. 4.9. Above a certain volume fraction, however, all aggregates cluster to form a giant aggregate. For nanocomposites made of bare NPs, e.g., this is found for the 10.4%-sample in Fig. 4.8a, and similarly at 11.9% with C_8-grafting, and earlier, at 8.1% with C_{18}. From these volume fractions on, the distributions of the small aggregates are close to the one of the low-silica sample, but with an additional aggregate with $N_{agg} > 10'000$ in each configuration. The presence of this big aggregate can be interpreted as the signature of percolation. Indeed, it represents more than 85% of all NPs in the simulation box at this volume fraction.

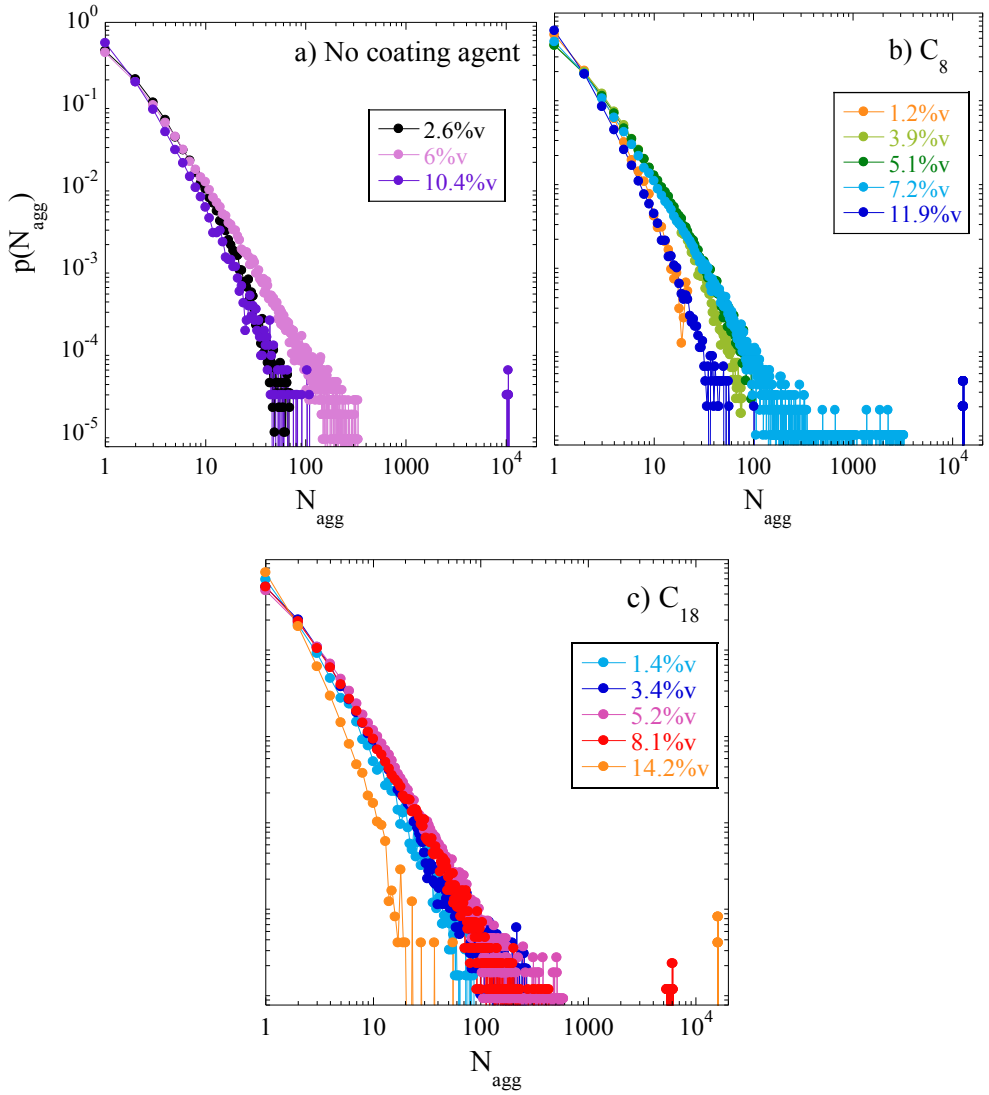

Figure 4.8 Distribution function of N_{agg} normalized to the total number of aggregates in each configuration, and averaged over 100 configurations, for nanocomposites with **(a)** bare, **(b)** C_8, and **(c)** C_{18} surface-modified NPs, for different silica volume fractions Φ_{Si}.

A quantitative interpretation of the distribution functions shown in Fig. 4.8a-4.8c leads to the definition of two indicators of dispersion for each surface-modification, and for different silica volume fractions (Fig. 4.9): the average aggregation number $<N_{agg}>$, and the next higher moment describing the width of the distribution, $<N_{agg}^2>/<N_{agg}>$. The latter combination is sensitive to the big aggregates formed at high volume fractions, and it corresponds also to the prefactor of small angle scattering intensity in absence of interaction. Indeed, it is found to reproduce the trends of the overall intensity prefactors of all samples quite well.

The main result of Fig. 4.9 is that all systems behave in a very similar manner concerning the average aggregation number. Indeed, all data points superimpose, and the same steady increase with Φ_{Si} is observed for all systems. However, the difference in scattering and thus structure is reflected in the much stronger increase of the second indicator, $<N_{agg}^2>/<N_{agg}>$, which can be considered as an average aggregation number favoring large aggregates in the average. Even if some scattering is detectable in

the data, the C_{18}-modified NPs produce the highest indicator, and above ca. Φ_{Si}=5%v the increase is even stronger. In comparison, the bare NPs show the same strong increase only at higher volume fractions. As already suspected with the raw data at low concentration (Fig. 4.4), the surface-modification with the longest graft thus produces the more aggregated polymer nanocomposites, whereas the bare NPs seem to resist aggregation up to higher volume fractions. At high volume fractions, finally, all samples seem to tend towards a common limiting function. This is a finite size effect of the simulation box, the linear dimension of which was fixed by the lowest measured q-value. The size of the box being fixed, the number of NPs in it increase with Φ_{Si}, which sets the upper bound for the number of particles that may potentially aggregate.

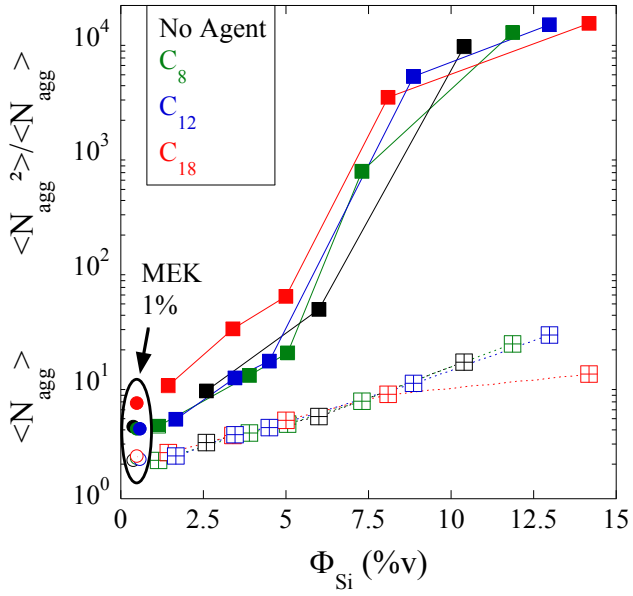

Figure 4.9 The average aggregation number $<N_{agg}>$ (empty symbols) and the normalized second moment of the distribution $<N_{agg}^2>/<N_{agg}>$ (plain symbols) as a function of silica volume fraction Φ, for different surface modifications. The data for suspensions in MEK (circles) are shown for comparison (Φ_{Si} = 1%v, shifted to ≈ 0.5%v for clarity).

Thus, it can be concluded that the quality of the dispersion in the MEK suspension is transferred into the polymer nanocomposites. This is one of the key findings of this study since it is not easy to extract such conclusions more than qualitatively from the scattered intensity curves (Fig. 4.1b and Fig. 4.4). The reverse Monte Carlo analysis allows to look at aggregates regardless of the (unknown) interactions that may exist between them. It shows that aggregate distribution functions are very similar in the precursor MEK suspension and in nanocomposites at equivalent low silica content. For comparison, the indicators $<N_{agg}^2>/<N_{agg}>$ and $<N_{agg}>$ for the four surface modifications in MEK (Fig. 4.1b) have been plotted in Fig. 4.9. It is striking to see that they predetermine the aggregate distribution of the low volume fraction nanocomposites, with C_{18}-modified particles being again the most aggregated ones. This confirms the intuition that aggregate structure in the precursor MEK suspension is indeed conserved in the nanocomposites.

4.2. Impact of silane function on dispersion of surfaced-modified silica NPs

The surface-modification of the silica NPs has also been performed using different type of C_8 silanes differing by their functional groups (i.e., silane function) but not for the length of their alkyl chain: octyl-triethoxysilane C_8, octyl-trimethoxysilane C_{8m}, and octyl-methoxy(dimethyl)silane C_{8mm}. The characteristics of these coating agents are reported in Table 2.1. Also in this case, a structural characterization has been performed for the surface-modified NPs in precursor solvents and then in the final polymer nanocomposite. It will be shown that the type of the silane function affects the dispersion state, in spite of unchanged alkyl chain.

4.2.1. Dispersion of C_8-, C_{8m}- and C_{8mm}- surface-modified nanoparticles in precursor solvents

As for the other silane agents, the surface-modification of the silica NPs with C_8, C_{8m} and C_{8mm} has been performed in a hydro-alcoholic suspension (63%v EtOH) and the grafting density was found to be about 1 nm^{-2}, for all the coating agent (see section 2.3).

Firstly, the SAXS normalized intensities of nanoparticles with these various surface-modifications suspended in water/ethanol mixture (63%v EtOH) are shown in Fig. 4.10a (Φ_{Si} =1%v). Each series of symbols is superimposed to a dotted line representing the average RMC fit. Note that the agreement is better than the size of the symbols. Intuitively, the low-q scattering intensities seem to indicate that the standard triethoxy silane C_8 forms the biggest aggregates. The trimethoxy C_{8m} sample displays lower scattering and thus an intermediate aggregation, while the monomethoxy C_{8mm} shows the lowest one. However, it is difficult to analyze quantitatively the 3D-structure corresponding to this family of scattered intensities, due to the superposition of aggregate formation as indicated by the increase of the low-q structure, and aggregate interaction which might add a low-q depression or enhancement. Moreover, the aggregate interaction is certainly different depending on the size of the aggregates. Thus, the analysis of aggregate mass distribution regardless of interaction is a non-trivial task due to the absence of any dominant scattering signature like a strong peak can be observed (i.e., large distribution of aggregate sizes).

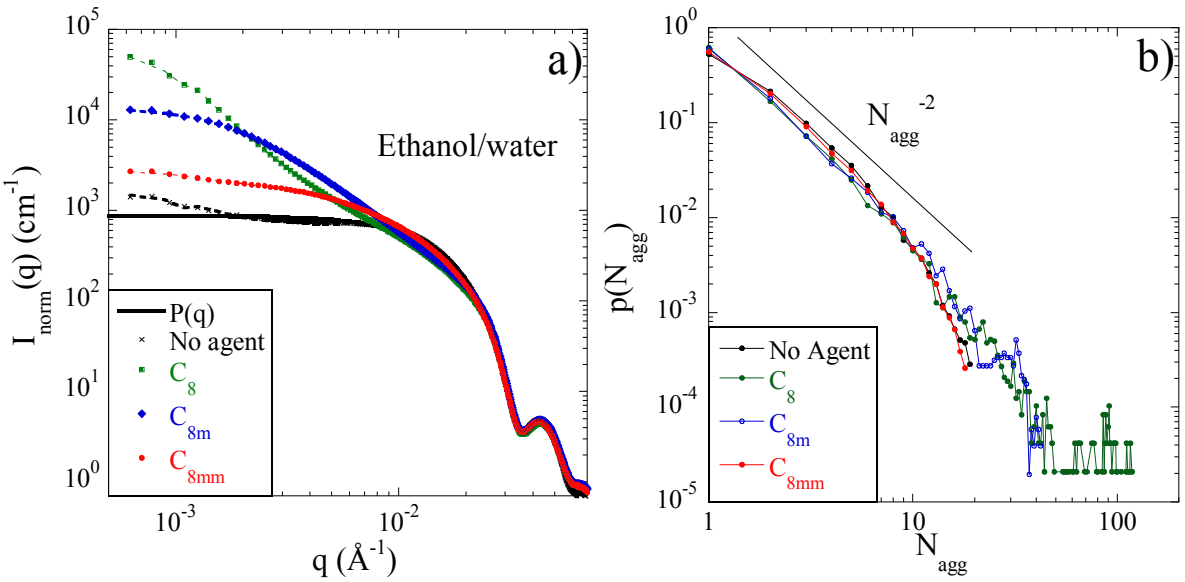

Figure 4.10 (a) SAXS scattered intensities normed to NP form factor in water (continuous line, R_0 = 12.5 nm, 12%) of bare and surface-modified NPs (C_8, C_{8m}, C_{8mm}) in hydro-alcoholic suspension (63%v ethanol, Φ_{Si} = 1%v). (b) Aggregate mass distributions of the same samples.

Nevertheless, the particle configurations generated by the RMC algorithm during the averaging phase (see section 2.5) can be used to extract the quantities of interest. In Fig. 4.10b, the aggregate size distributions corresponding to the SAXS intensities in Fig. 4.10a are plotted, using $\delta = \langle R \rangle$. These distribution functions represent the real-space analogues of the scattering intensities, without however the inter-aggregate interactions. In other words, it has been chosen to focus on the mass of the aggregates, by setting up an analysis which allows ignoring where aggregates are with respect to one another. This amounts to having taken out all partial structure factors between aggregates off the scattered intensity, a result which would not have been possible directly in reciprocal space. This will be of particular importance for higher volume fractions as encountered in the nanocomposites, where interactions become more and more dominant. The aggregate distribution function decays strongly for all surface modifications, following roughly a N_{agg}^{-2} power law. Above $N_{agg} \approx 10$, aggregates become even more rare. Bare NPs and C_{8mm}-modified ones do not exhibit aggregates above $N_{agg} \approx 20$, while C_{8m}-modified aggregates extend up to $N_{agg} \approx 40$, and C_8-modified even above 100. The distribution laws are thus mostly identical for small aggregates, and the differences become important only in the large N_{agg}-range. In hydroalcoholic suspension, C_8-surface modification favors the formation of bigger aggregates, whereas all others do not. This might be due to different grafting efficiencies and in particular remaining SiOH groups capable of inducing electrostatic repulsion, and thus limit aggregation.

According to the protocol presented in section 2.3, the surface-modified NPs are transferred in another solvent, methyl-ethyl-ketone (MEK). As for the silanes used in the previous section, this solvent change has been expected to considerably impact the dispersion of the surface-modified NPs. As already mentioned, MEK is still quite polar and an excellent solvent of the alkyl chains. In 4.11a, the scattering intensities of the C_8-, C_{8m}- and C_{8mm}-surface-modified NPs in MEK are plotted. Their behavior has been

compared to the one of the bare NPs in the same solvent. In MEK suspensions, the type of silane grafting function seems to have a strong influence on the NP dispersion, with an inverted order in this solvent with respect to the previous one (i.e., ethanol/water mixture): now the triethoxy silane C_8 seems to have the best dispersion, presenting a well-defined repulsive interaction peak at intermediate q. It is followed by the C_{8m}, which is thus again in the middle of the three, and also shows some structure at intermediate q. Finally, the monomethoxy C_{8mm} shows the highest low q scattering (i.e., intensity comparable to the one of the bare NPs). On the other hand, all intensities are of comparable magnitude, and the RMC analysis shows that the aggregates themselves are quite comparable, even if the interactions between aggregates are different for the different grafts.

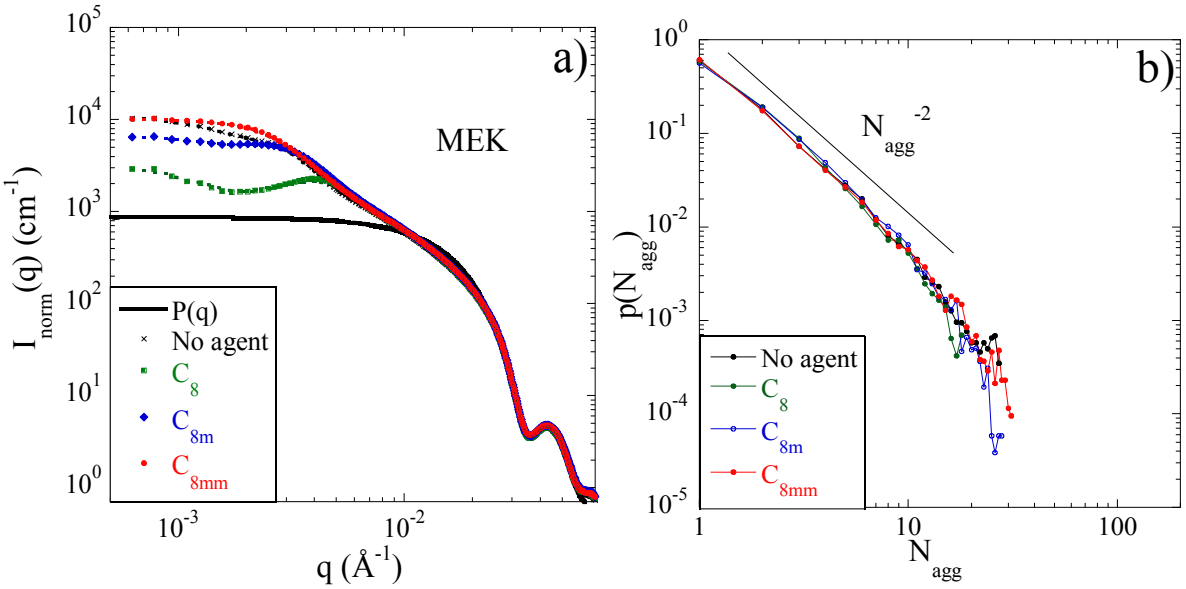

Figure 4.11 (a) SAXS scattered intensities normed to NP form factor in water (continuous line, R_0 = 12.5 nm, 12%) of bare and surface-modified NPs (C_8, C_{8m}, C_{8mm}) in MEK (Φ_{Si} = 1%v).
(b) Aggregate mass distributions of the same samples.

Also in this case, the dotted lines in Fig. 4.11a represent the RMC fits of the MEK-samples which are again not distinguishable from the symbols representing the experimental data points. After the application of the aggregate recognition algorithm, the corresponding average aggregate mass distributions are obtained, as reported in Fig. 4.11b. Given the differences in the scattering intensities, the mass distribution functions in MEK superimpose surprisingly well. Above some N_{agg} = 20 particles, there are no more big aggregates, for any surface modification. Below this value, the distribution function follows again approximately a N_{agg}^{-2} power law, as indicated in the Fig. 4.11b. The combined RMC and aggregate recognition approach thus allows to deliberately ignore the inter-aggregate interactions in this solvent, highlighting the aggregate distribution, which is found not to depend on the presence or type of surface modification. Apparently, MEK is a rather good solvent both for bare particles, and the grafts studied here. A high degree of detail is required to observe the presence of some bigger aggregates for particles surface-modified by C_{8mm}, which remain extremely rare. To summarize

the findings in solvents, surface-modified particles are mostly not well dispersed in ethanol-water mixtures, due to the hydrophobicity of the grafts, unless some electrostatic repulsion remains after grafting. In MEK, they are globally better dispersed, forming aggregates below N_{agg} = 20, due to the solvation of the layer. Our analysis shows that the mass distributions are similar, although the different interactions make the scattered intensities look different.

4.2.2. Dispersion of C_8-, C_{8m}- and C_{8mm}- surface-modified nanoparticles: from solvents to polymer matrices

The MEK suspensions can be used for the formation of nanocomposites. The latter are produced by mixing with the appropriate amounts of styrene butadiene molecules, followed by evaporation of the solvent. The final silica volume fractions in the PNCs have been determined by TGA, and lie between 1% and ca. 3%. The normalized scattering intensities of the NCs formulated using C_8-, C_{8m}- or C_{8mm}-surface-modified NPs are shown in Fig. 4.12a. To understand if also in this case the structural organization of the silica NPs in suspension predetermines their dispersion in the polymer matrix, the SAXS intensities shown in Fig. 4.12a can be compared to the ones in Fig. 4.11a. It can be observed that the intensities remain similar: the C_{8mm} sample is still the highest one which might indicate the highest aggregation; the C_8 and the C_{8m} seem to show some structural features (a shoulder), possibly reminiscent of the peaks observed in Fig. 4.11a. The overall conclusion is that aggregates in the nanocomposites are probably close in mass and structure to the ones in the precursor solution. However, it is very difficult to extract quantitative information from these scattering curves because of the occurrence of different large-scale organization in space which leads to different interactions and thus average structure factors also affected by changes in concentration. Using again the RMC simulation with aggregate recognition (see section 2.5) it is possible to obtain the aggregate mass distribution functions, regardless of inter-aggregate interactions, as shown in Fig. 4.12b. These distributions are now quite different for each surface-modification. The C_8-modification leads to the best dispersion, with a mass distribution falling quickly below the N_{agg}^{-2} power law. The other three samples (bare NPs, C_{8m} and C_{8mm}) follow this power law quite closely, but extend differently into the high-N_{agg} regime. In particular, the C_{8mm} sample is found to favor the formation of big aggregates, counting up to 200 nanoparticles.

The TEM images for NCs made with for C_8- and C_{8m}- surface modified NPs are shown in Fig. 4.13a and 4.13b, respectively. These pictures give an idea of the typical aggregation state of the particles even if the influence of the silica volume fraction Φ_{Si} is difficult to evaluate by this technique. Moreover, the difference in the real silica volume fraction between the two samples (C_8, Φ_{Si} =1.15%v; C_{8m}, Φ_{Si} =3.21%v) could modify the result of the visual comparison.

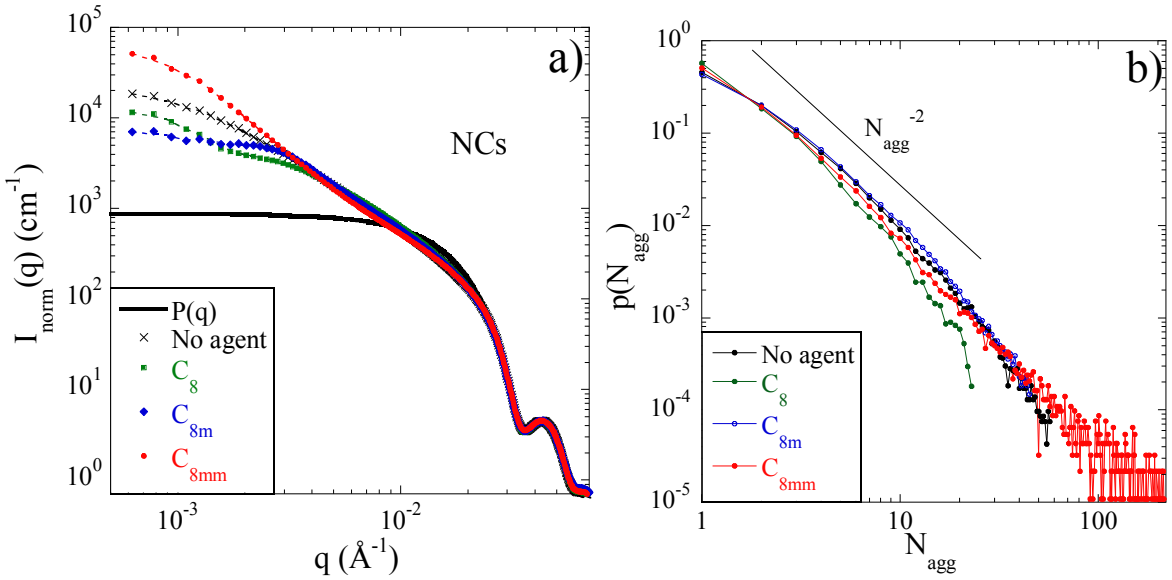

Figure 4.12 (a) SAXS scattered intensities normed to NP form factor in water (continuous line, R_0 = 12.5 nm, 12%) of bare (2.6%v) and surface-modified NPs (C_8, Φ_{Si} =1.15%v; C_{8m}, Φ_{Si} =3.21%v; C_{8mm}, Φ_{Si} =2.8%v) in PNCs. (b) Aggregate mass distributions of the same samples.

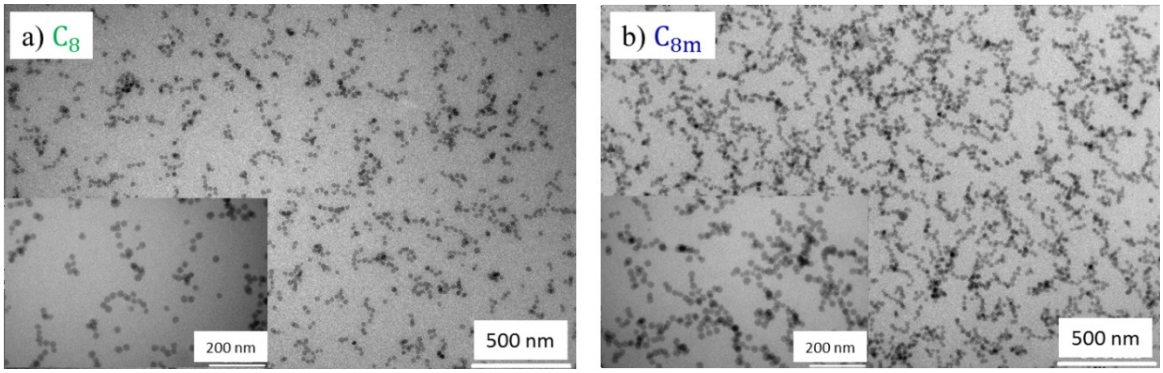

Figure 4.13 TEM images of polymer NCs formulated with silica surface-modified by (a) C_8 and (b) C_{8m}. The insets show a lower magnification images of the same samples (C_8, Φ_{Si} =1.15%v; C_{8m}, Φ_{Si} =3.21%v).

To further analyze the mass distribution functions, one may calculate their average and the width: The first moment gives the average, $\langle N_{agg} \rangle$, and the second moment $\langle N_{agg}^2 \rangle$ may be normalized by $\langle N_{agg} \rangle$ to obtain an indication of the width of the distribution. Moreover, it should also describe the low-angle scattering in absence of interaction, which is proportional to $\langle V^2 \rangle / \langle V \rangle$, where V is the volume of objects correlated in space, i.e. aggregates, and thus reduces to $\langle N_{agg}^2 \rangle / \langle N_{agg} \rangle$. One should keep in mind, however, that the present determination of aggregate distribution functions has a sharp cut-off parameter δ, and $\langle N_{agg}^2 \rangle / \langle N_{agg} \rangle$ are thus expected to be smaller than experimental low-q intensities in absence of interaction. Coming back to the first moment, $\langle N_{agg} \rangle$ evolves only slowly with surface modification and changes in the suspension medium. This is due to the similar predominance of aggregates with low aggregation numbers in all samples, leading to overlapping functions (Fig. 4.12b). In Figure 4.14, the parameter characterizing the width of the mass distribution functions $\langle N_{agg}^2 \rangle / \langle N_{agg} \rangle$ extracted from the data in Fig. 4.10b, 4.11b and 4.12b, is plotted for the three suspension media. As the

width is mainly related to the existence of large aggregates, the evolution observed in Fig.4.14 summarizes the evolutions discussed above. In the ethanol-water mixture, C_8-surface modification forms the biggest aggregates. In MEK, all aggregates are rather small, with C_{8mm} favoring aggregation. In polymer nanocomposites, finally, C_{8mm} induces the worst dispersion and C_8 the best.

Concerning a possible transfer of the characteristics of the dispersion from MEK into the polymer nanocomposites, it is true that the order of the width of the mass distributions seems to be conserved from MEK to the PNCs. On the other hand, only the C_8-modified NPs keep a comparable mass distribution, whereas the others become wider. In particular, the C_{8mm} one shows a strong evolution towards bigger aggregates in the polymer matrix.

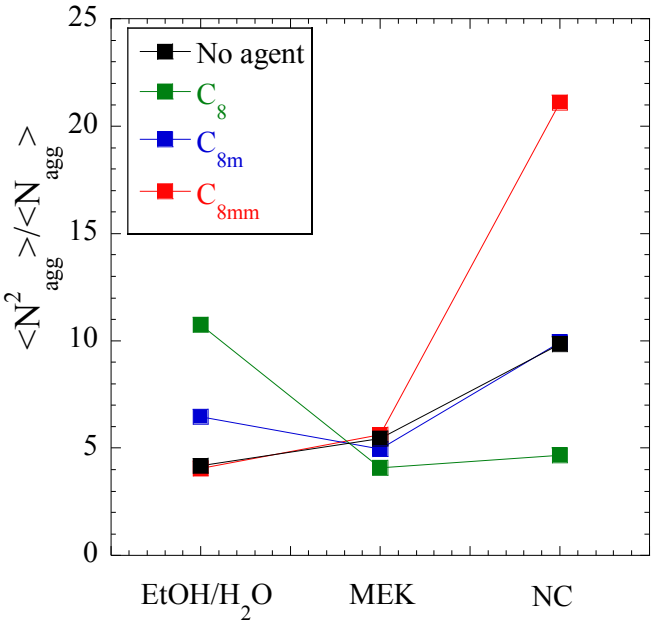

Figure 4.14: The width-parameter $<N_{agg}^2>/<N_{agg}>$ of the mass distribution functions in the three suspension media (hydro alcoholic mixture, MEK, and in polymer).

4.3. Summary of the impact of the surface-modification by different silanes on the NP dispersion in different media

In this section, we propose a brief summary of the main results of this chapter in order to highlight the impact that the NP surface modification has on the filler dispersion in different media.

We report the results obtained for the surface-modification obtained by silanes with different hydrophobicity (C_8, C_{12}, and C_{18}) and different silane functions (C_8, C_{8m} and C_{8mm}). Moreover, in the overall comparison we will also introduce the results obtain for the grafting reaction performed with coating agents which differ by their silane function but show a longer alkyl chain (C_{18}, C_{18m} and C_{18mm}). The chemical characteristics and the complete scattering intensity curves referred to these agents are reported in the appendix A5.

It results that the silane coating agents used in this work can be organized in three main classes according to their different functional groups: i) triethoxy-silane (C_8, C_{12}, and C_{18}); ii) trimethoxy-silane (C_{8m} and C_{18m}); iii) methoxydimethyl- or monomethoxy- silane (C_{8mm} and C_{18mm}).

Concerning the hydroalcoholic suspensions of surface-modified NPs, it has been noticed that all the scattering intensity curves (Fig. 4.1a, 4.10a, A5.2) show a low-q upturn, independently of the grafted silane molecule. This behavior has been interpreted as an additional proof that the grafting reaction took place and that the particle-particle and the particle-medium interactions are modified (i.e., surface-modification by a hydrophobic molecules performed in a still hydrophilic environment). On the other hand, when the grafting reaction has been performed with mono-functionalized silanes (i.e., C_{8mm} and C_{18mm}) the low-q scattering intensity resulted a bit lower with respect to the other surface-modifications. This different behavior might be related to a different reaction mechanism of these mono-functionalized molecules (e.g., no other lateral groups that can react with neighboring molecules) which could affect the final NP hydrophobicity (via the number of remaining silanol groups), and thus the dispersion in the hydroalcoholic suspension.

The dispersion state of surface-modified silica NPs has also been analyzed once they have been transferred in MEK. In Fig.4.15a, the width of the mass distribution functions $\langle N_{agg}{}^2\rangle/\langle N_{agg}\rangle$ are reported as a function of the different silane groups. As a general remark, the quality of the NP dispersion seems to be similar for all silane molecules. More in detail, while the C_{18m} favors the aggregation, the C_{18mm} allows to obtain a dispersion comparable to the one obtained for bare NPs or NPs surface-modified by C_8 and C_{12} (overlapped).
Concerning the nanocomposites at the lowest silica content ($\Phi_{Si} \sim 1\%v$), it can be observed that the quality of the NP dispersion in MEK is quite well transferred in polymer nanocomposite, in particular for silica nanoparticles which are surface-modified by C_8 and C_{12}. On the other hand, for the trimethoxy-agents a small increase of the $\langle N_{agg}{}^2\rangle/\langle N_{agg}\rangle$ from MEK suspension to nanocomposites suggests an enhancement of the NP aggregation, which is even more detectable for the mono-functionalized silane molecules.

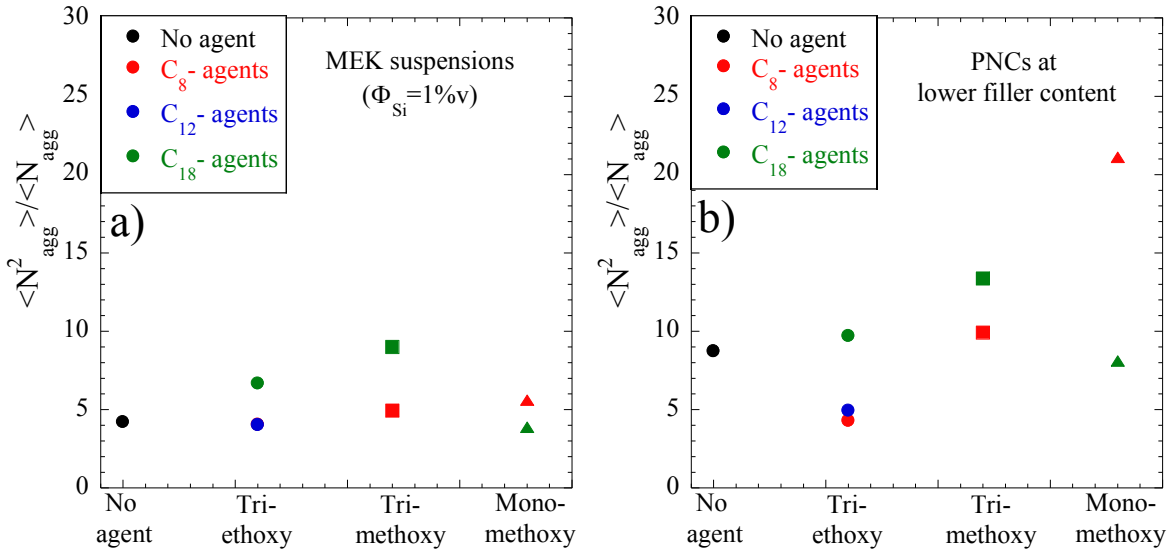

Figure 4.15 The width-parameter $\langle N_{agg}^2 \rangle / \langle N_{agg} \rangle$ of the mass distribution functions for the different groups of silane molecules in MEK suspensions (a) and in polymer nanocomposites at the lowest filler content.

4.4. Conclusions

This part of the PhD work focuses on a model nanocomposite system (see section 2.3) where the filler-filler and the filler-polymer interactions are tuned by grafting of small molecules (i.e., silane coating agents) of industrial relevance. The modification of these interaction is expected to induce changes in the aggregation behavior of the NPs. The main aim of this chapter is to propose a quantitative analysis of the aggregation state of surface-modified silica NPs in precursor solvents and a polymer matrix, by a combined SAXS-RMC approach. In particular, the determination of experimental distribution functions of aggregation numbers has been performed with SAXS data as input. One of the key characteristics of such approach is the possibility to extract aggregate mass in presence or absence of interactions between aggregates, simply by analyzing real space particle configurations obtained by RMC simulations.

Concerning the NP surface-modification by silanes with different hydrophobicity, the particle interactions in suspension were found to be only slightly affected by the type of graft, with C_{18} always yielding the highest aggregation numbers. For both the reaction solvent and the transfer solvent MEK, the average aggregation numbers as estimated from the low-q intensity indicate that the colloidal stability was maintained successfully. The propensity of NPs to aggregate, however, varies with the solvent. The normalization of the intensity to the form factor allows the comparison of the different aggregation states, enabling us to conclude on the grafting and on NP interactions. In particular, after the reaction in hydro alcoholic solution, the particles are rather aggregated, while after transfer into MEK, the low-q intensity is found to decrease, and the signature of repulsion appears. This shows that aggregation is reversible, and as particles possess a grafted layer, the latter probably protects NPs sterically from getting close enough for Van der Waals attraction to stick them irreversibly together.

Aggregation states have been quantitatively characterized by a novel reverse Monte Carlo technique, allowing the description of interacting polydisperse NPs and aggregates at arbitrary concentrations, in

solvents and nanocomposites. The series of particle configurations that satisfy the scattering condition have been analyzed in terms of the aggregate distribution functions. This method provided quantitative evidence for a stronger aggregation with C_{18}-surface modified NPs than for all others, at any concentration, in any medium. In particular, after incorporation of the NPs from MEK into the polymer matrix, the aggregation state was found to conserve the quality of the precursor suspensions. This can be understood as the consequence of the polymer chains solubilized in the MEK and surrounding all NPs and aggregates. Note that the precursor suspension is maintained at the low volume fraction of 1%, and that silica content is adjusted via the quantity of solution. During the drying procedure, the viscosity of the polymer solution increases considerably, and the polymer matrix freezes the aggregate distribution in space.

The same approach has been used to investigate the dispersion of silica NPs surface-modified by C_8-coating agents which differ by their silane function (i.e., triethoxy, trimethoxy, monomethoxy) in precursor solvents and polymer matrix. Also in this case, the combination of SAXS and RMC methods allows to obtain the distribution functions of aggregate mass, regardless of any possible interactions between the aggregates.

The physical chemistry of the surface-modified NPs can be understood along several complementary lines of reasoning. First, the solubility of the alkyl chains varies from ethanol/water, to MEK, and finally polymer. This explains why bare particles are quite well dispersed in water– the solvent they are sold in –, and hydro alcoholic mixtures, but less good in the other solvents. On the contrary, C_8-modified NPs are not well dispersed in ethanol/water, but much better in MEK and polymer. Secondly, the grafting reaction itself affects the number of silanol groups still available on the NPs, fostering repulsive electrostatic interactions between particles and aggregates. This is possible as long as the medium is polar enough, which is the case for both alcohol and MEK. For polymer, the situation is less clear, but due to the viscosity increase upon polymer addition, the particle configurations should be 'frozen' by the polymer in MEK. Nonetheless, namely C_{8mm}-modified samples aggregate upon transfer into polymer, and a third aspect must be accounted for, the type of the grafting function. While tri- methoxy and –ethoxy groups have slightly different reactivity, both molecules can anchor to more than one surface silanol, and also undergo side reactions with neighboring molecules, leading to polycondensation. This is probably the reason why C_{8mm}, the only graft which can under no circumstances undergo more than one reaction – with silanols or at most one other molecule – has such a peculiar behavior. Indeed, in ethanol/water, its surface-modified NPs are as well dispersed as the bare NPs, probably due to the lower number of consumed surface silanols, and thus the higher remaining electrostatic repulsion in this solvent. On the other hand, in polymer, the steric layer of surface grafts is probably less dense due to the absence of polycondensation, and aggregation sets in. The situation is however rather complex. In this view, the bare NPs should be even more aggregated, which following

Fig. 4.14 is not the case. Apparently, the dominating electrostatic repulsion of the bare nanoparticles is sufficient to keep aggregation low, although not the lowest.

5. Silane coating agents as plasticizers in model silica/polymer nanocomposites

5. Silane coating agents as plasticizers in model silica/polymer nanocomposites

The investigation of the glass transition of polymer nanocomposite materials is important for the development of their applications, due to its impact on the mechanical properties of the material. However, its fundamental physics still represents a challenge, since it can be affected by several parameters and in particular by the polymer-filler interactions (Rittigstein et al. 2007).

Broadband Dielectric Spectroscopy (BDS) is a powerful tool for investigating the polymer dynamics as well as the polymer-filler interactions. In this chapter, this technique will be used to shed light on the role of silane coating agents in the segmental dynamics of nanocomposite systems. It will be shown that silane molecules can act as *plasticizers* in pure styrene-butadiene matrices, inducing a significant decrease of the glass-transition temperature, T_g. Then, it will be shown that in model NCs the presence of the filler, as well as the chemical surface-modification of the filler do not affect the segmental dynamics, while the presence of *free* silane molecules in the bulk polymer induces a detectable plasticization effect.

5.1. Dynamics in pure styrene-butadiene polymer

In this work, an end-functionalized and a non-functionalized styrene-butadiene (named SB_F and SB_NF, respectively) of molecular weight 170 kg/mol have been used (see section 2.1). The dynamical properties of both these pure polymers have been investigated by BDS. As described in Chapter 1, the dielectric response in neat polymers is usually characterized by: i) a segmental relaxation (α-relaxation), associated with the cooperative motions of polymer chains, and thus with the glass-transition temperature; ii) a secondary relaxation (β-relaxation) which can be related to localized motion, like e.g., side-group reorientations.

For both the pure SB_F and SB_NF matrices, dielectric measurements have been performed in the frequency range from 10^{-2} to 10^{7} Hz. In this frequency window, the spectra display a prominent relaxation due to the α-relaxation, which is clearly visible from 253 K to 303 K. Fig. 5.1 shows the dielectric losses ($\varepsilon''(\omega)$) for SB_F as a function of the frequency for different temperatures between 253 K and 278 K (every 5 K). The segmental-relaxation peak shifts to higher frequencies as the temperature increases. In the high-frequency side of the low-temperature spectra (T between 153 K and 173 K), the tail of a second process can be detected. It corresponds to the secondary β-relaxation, which has been related in (uncured) SB to local motions within the butadiene units (Cerveny et al. 2002). In Fig. 5.1, the secondary-relaxation peak at T=173 K is visible. As expected for such a process (Kremer and Schönhals 2003), the data are well described by a symmetric HN function (δ=1 in equation 2.46), i.e., a Cole-Cole function.

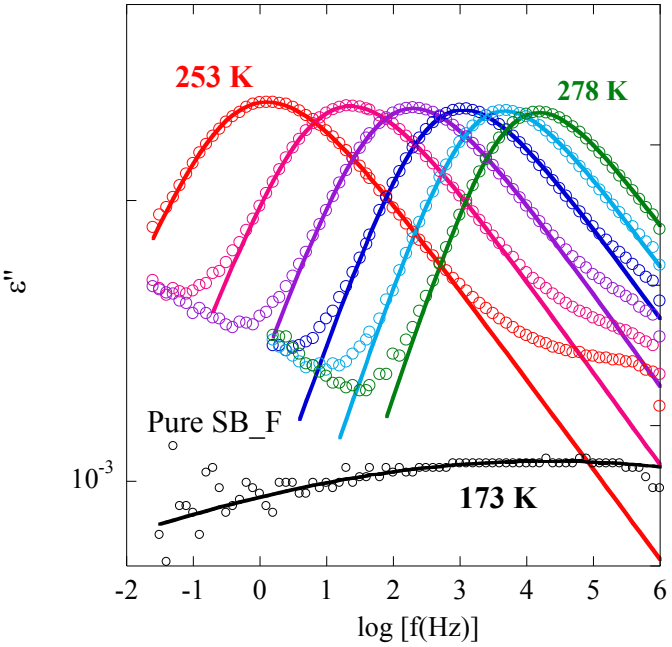

Figure 5.1 Dielectric loss ε'' as a function of frequency for pure SB_F between 253 K and 278 K every 5 K and at T=173 K (black circles). Solid lines represent fits with a HN function.

Firstly, the $\varepsilon''(\omega)$ spectra of the SB_NF matrix have been compared to the ones of the pure SB_F polymer. As shown in Fig. 5.2a, the spectra of the two polymer matrices at the same temperature (T=258 K) display a similar shape and the segmental relaxation peak at the same position. This suggests that they are virtually identical in their dielectric behavior.

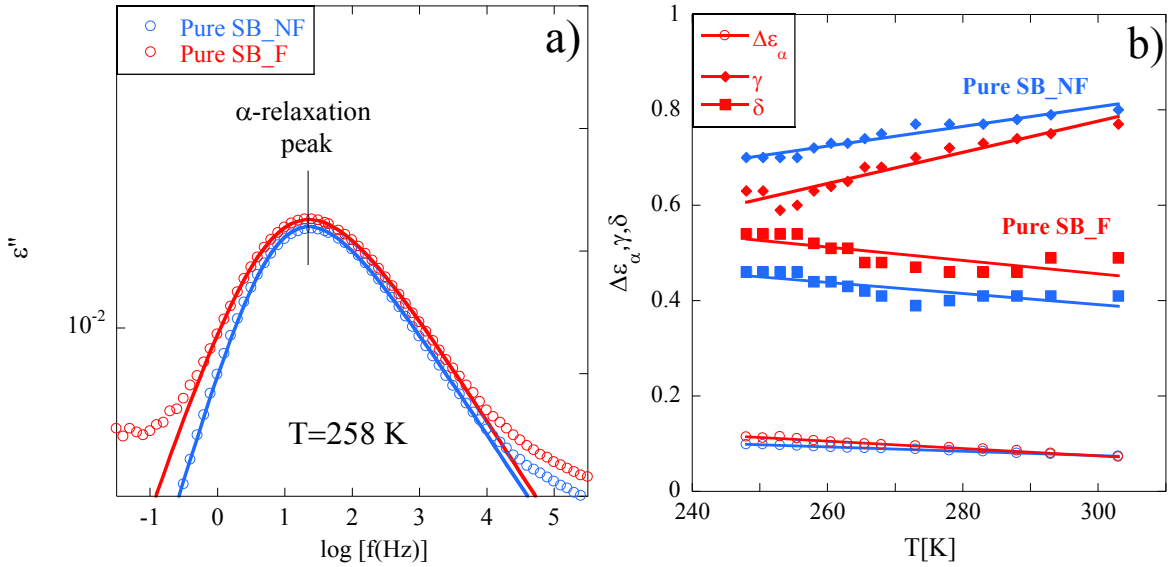

Figure 5.2 a) Dielectric loss ε'' as a function of frequency at T=258 K for pure SB_NF (blue circles) and pure SB_F (red circles). Solid lines represent fits with a HN function; (b) Fit parameters of the HN function used to describe the α-process in each SB.

To validate this result, the experimental data at different temperatures have been fitted by a HN function, as indicated by solid lines in Fig. 5.2a. Here, in order to determine the relaxation time of the α-process, the shape parameters (γ, δ) and the process intensity ($\Delta\varepsilon_\alpha$) have been used as free parameters in the fitting procedure. Their evolution as a function of temperature is shown in Fig.5.2b. For both SB matrices, the parameter γ linked to the peak width increases linearly with temperature, while δ and the dielectric strength $\Delta\varepsilon_\alpha$ decrease linearly with temperature. For each dielectric process, the relaxation time corresponding to the frequency of the maximal loss $\tau_{max} = \tau_\alpha = (2\pi f_{max})^{-1}$ was determined using this fitting procedure. As shown in Fig. 5.3, its evolution as function of temperature is well described by a Vogel-Fulcher-Tammann (VFT) law (eq. 5.1) which can be written as

$$\tau_\alpha = \tau_0 \exp\left(\frac{DT_0}{T-T_0}\right) \qquad [5.1]$$

where τ_0 is the relaxation time in the high-temperature limit, T_0 is the temperature where the relaxation time diverges; D parametrizes the divergence from the Arrhenius behavior and gives information about the glass fragility (Angell 1991; Böhmer et al. 1993). The correspondence between fitting and physical parameters is specified in Fig. 5.3 and the outcome is summarized in Table 5.1.

The results for SB_NF and SB_F polymers are very similar, thus confirming that the pure matrix dynamics are not strongly influenced by the end-functionalization of the polymer chains.

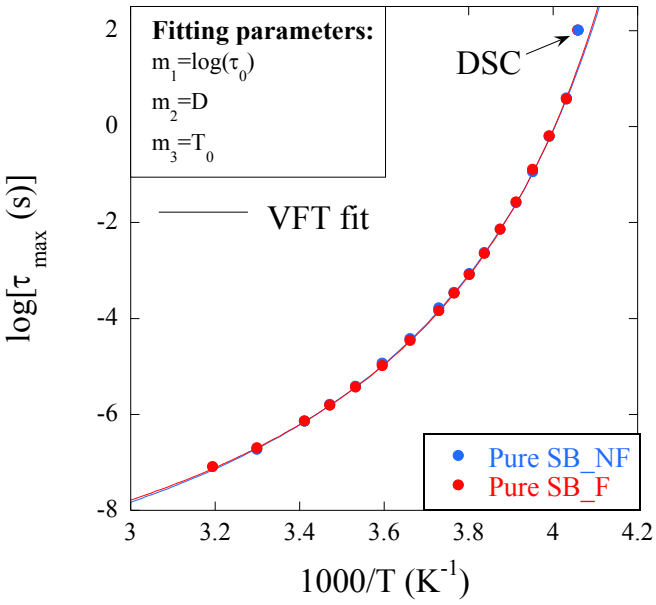

Figure 5.3 Relaxation map of α-process for pure SB_NF and SB_F. The solid lines through data points are fits by the VFT equation. The arrow indicates the relaxation time which corresponds to T_g estimated by DSC measurements ($T_{g,\,100s}$).

The extrapolation of the VFT formula to a relaxation time τ_α=100s allows obtaining a dielectric estimation of the glass-transition temperature, $T_{g,100s}$. According to several authors (Cerveny et al. 2002; Tung et al. 2016), this value is a good estimate of the calorimetric T_g evaluated by differential scanning

calorimetry (DSC, using a 20 K/min heating rate in our case). As shown in Table 5.1 and in Fig. 5.3, the dielectric and calorimetric T_g's are in good agreement. Moreover, they do not differ for SB_NF and SB_F. One may note that our results are in quite good agreement with the ones obtained by Cerveny et al. (Cerveny et al. 2002) for a similar styrene-butadiene polymer (Table 5.1). The small differences between them could be related to a slight variation in terms of microstructure (percentage of butadiene and styrene units in the chain).

Sample	D	T_0 (K)	$\log \tau_0$	T_g (K) (DSC)	$T_{g,100s}$ (K)	M
SB_NF	4.1	215.0	-11.1	246.4±0.3	244.5	108.3
SB_F	3.9	216.3	-10.9	246.3±0.2	244.61	111.5
SBR1 *	6.1	165.0	-11.5	208	197±0.3	84±3.0

Table 5.1 Outcomes from VFT fits for pure SB_NF and SB_F. The results have been compared to the ones obtained by *Cerveny et al. (Cerveny et al. 2002) for a styrene-butadiene with a similar composition similar to the one of SB_NF and SB_F. In terms of VFT parameters, the fragility can be also described by another parameter, m (Cerveny et al. 2002).

5.2. Plasticization of styrene-butadiene matrix

In Chapter 4, it has been shown that silane coating agents with different hydrophobicity can be used to surface-modify the silica particle in order to tune the filler dispersion in the final nanocomposite system. To shed light on the role that silane agent play on the segmental relaxation in NCs, the impact of these agents on the pure polymer matrix dynamics will be investigated first. Samples have been prepared by dissolving the pure SB_F polymer in methyl-ethylketone (MEK) and adding the selected coating agent, following the experimental protocol for model systems described in section 2.3.

5.2.1. Silane coating agent as plasticizer of the polymer matrix

For a first qualitative evaluation of the effect induced by the introduction of the silane in a polymer matrix, SB_F and SB_NF have been mixed with the silane with the longest alkyl chains (M_w SB=170 kg/mol; M_w C_{18} = 417 g/mol; Φ_{C18} = 7.6%w). These samples will be termed "SB_F+C_{18}" and "SB_NF+C_{18}", respectively. As shown in Fig. 5.4a, the dielectric loss spectra of both samples (T=258 K) have been compared to the one of the pure SB_F matrix. For both polymers, the addition of C_{18} shifts the segmental-relaxation peak to higher frequencies which indicates a shorter relaxation time of the α-process. Temperature-Modulated DSC measurements (TMDSC, cooling ramp 3 K/min, ±0.5°C every 60s), allowed to relate this dielectric behavior to a variation of the glass transition temperature T_g. While for the pure SB_F the T_g is -24.6 ± 0.3 °C, the T_g for the matrices mixed with C_{18} moves to -32.8 ± 0.3 for the SB_NF+C_{18} and to -33.0 ± 0.3 °C for the SB_F+C_{18}. This suggests that free silane molecules dispersed into the pure SB polymer behave like a *plasticizer* (Wypych 2004), thus inducing a decrease of the glass transition temperature. As established in the literature (Boyer and Spencer 1947; Immergut

and Mark 1965; Buera et al. 1992; Kadam et al. 2016) the plasticization effect can be induced by mixing a given polymer with a low molecular weight compound, in analogy with the samples presented here above. The complete relaxation maps of SB_NF+C_{18} and SB_F+C_{18} are compared to the one of the Pure SB_F in Fig. 5.4b. Since the relaxation times for SB_NF+C_{18} and SB_F+C_{18} samples are perfectly overlapped, this suggests that both polymers display the same behavior in presence of the C_{18} coating agent. Thus, in the next sections we will only work with the SB_F polymer.

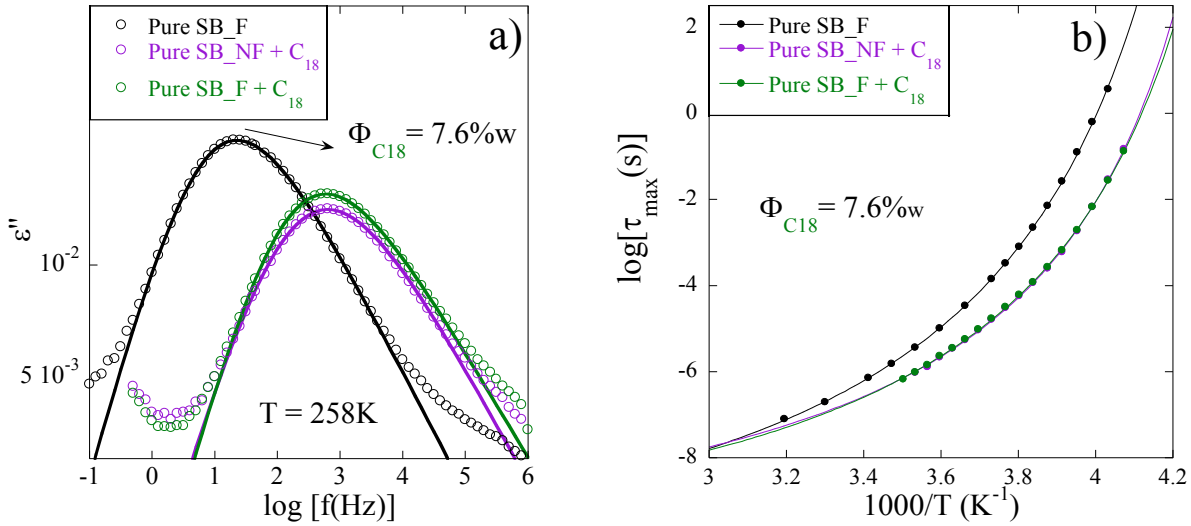

Figure 5.4 (a) Dielectric loss ε'' as a function of frequency at T=258K of pure SB_F (black circle) and pure SB_F mixed with C_{18}. Solid lines represent the HN fit functions. (b) Relaxation map for SB_NF + C_{18} and SB_F + C_{18}. Solid lines represent VFT fits.

5.2.2. Impact of coating agent amount on polymer matrix plasticization

The plasticization effect induced by the C_{18} has been studied as a function of its concentration in the polymer matrix. (Bradford and Vanderhoff 1963). The different silane concentrations correspond to different C_{18}/SB_F mass ratios (ζ), which have been varied from 0% to 8.2%. The dielectric loss spectra of these samples at T=258 K are shown in Fig. 5.5a. The segmental-relaxation peak moves to higher frequencies with the increase of ζ, which indicates that the plasticization effect is related to the amount of silane molecule dispersed in the SB matrix. In addition, the increase of the plasticizer concentration corresponds to a progressive reduction of the calorimetric T_g (Fig. 5.5b). In particular, the T_g values have determined at the inflection point on the modulated cooling ramp (3 K/min, ±0.5° every 60s). The error bars have been determined repeating the measurement on three independent samples.

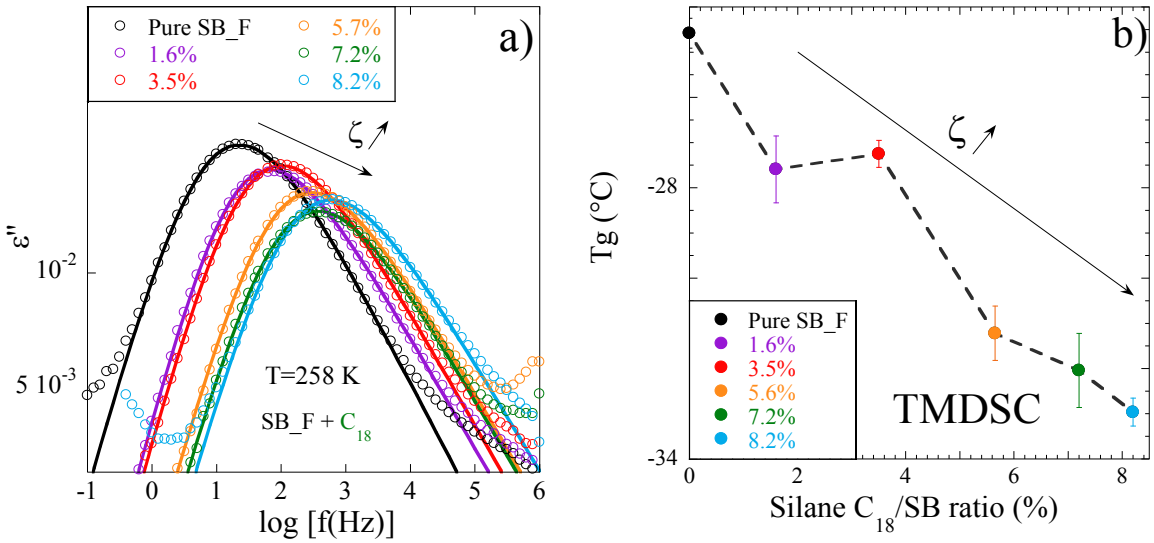

Figure 5.5 (a) Dielectric loss ε'' as a function of frequency at T=258 K of SB_F mixed with different amounts of C_{18} (silane/SB mass ratio, ζ). Solid lines represent the HN fit functions. (b) Evolution of glass transition temperature (T_g) as a function of silane C_{18} /SB mass ratio.

For each sample, the evolution of the segmental-relaxation time τ_α as a function of temperature (relaxation map) has been determined fitting the experimental data by a Havriliak-Negami function and it has been described by a VFT law (Fig. 5.6a). In Fig. 5.6b, the trend of τ_α has been plotted in a log scale as a function of the C_{18}/SB_F mass ratios at different temperatures (from 253 K to 278 K). The relaxation time of the α-process decreases linearly with the increase of ζ and this trend persists at all the investigated temperatures, i.e., where the peak in the frequency window.

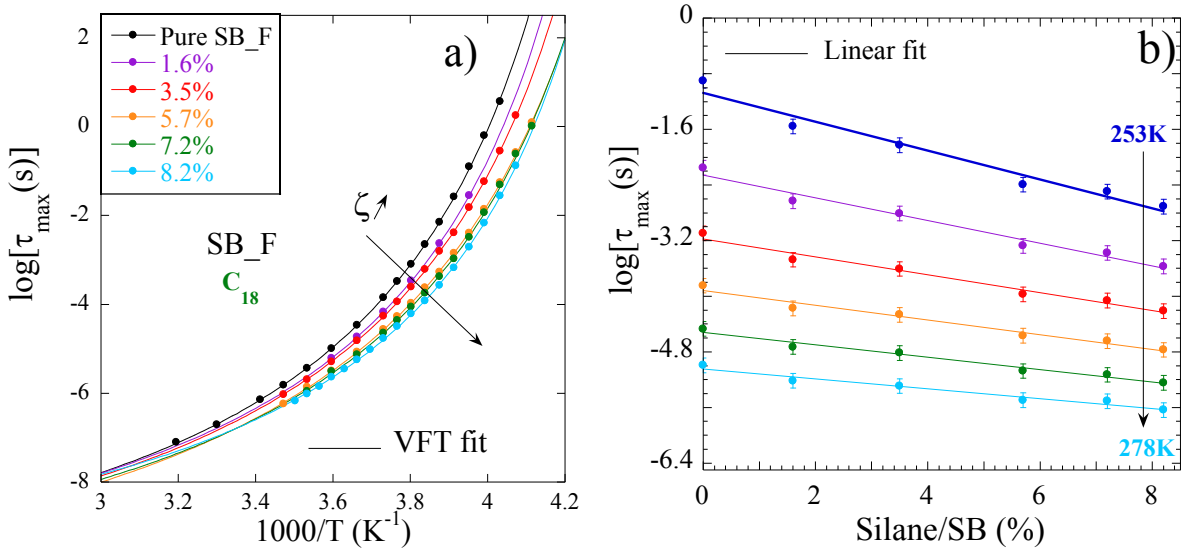

Figure 5.6 (a) Relaxation map of the α-process for SB_F mixed with different amounts of C_{18} (silane/SB mass ratio). The solid lines through the data points are fits to the VFT equation. (b) The relaxation times of the α-process as a function of the C_{18}/SB_F mass ratios at different temperatures (from 253 K to 278 K). The error bar has been estimated considering the variation of the relaxation time between two experimental points which are consecutive in frequency.

The VFT parameters are summarized in Table 5.3 with the extrapolated value of T_g, $T_{g,100s}$. The latter is found to be in good agreement with the calorimetric T_g.

Silane/SB (%)	D	T_0 (K)	$\log \tau_0$	T_g (K) (DSC)	$T_{g,100s}$ (K)	m
0%	3.9	216.3	-10.9	246.2±0.2	244.5	111.5
1.6%	3.7	215.3	-10.7	244.6±1.0	242.5	113.4
3.5%	4.0	212.3	-10.9	245.4±0.3	241.0	107.9
5.7%	4.4	207.9	-11.9	239.6±1.2	238.6	100.6
7.2%	4.0	209.9	-10.9	238.7±1.4	238.0	109.9
8.2%	3.1	214.3	-10.2	236.3±1.1	238.0	122.2

Table 5.3 Outcome from VFT fits for SB_F mixed with different amounts of C_{18} (C_{18} /SB mass ratio).

To summarize, it has been shown that the increase of the C_{18} amount in the polymer matrix induces a linear decrease of the segmental-relaxation time, which corresponds to a more and more intense plasticization effect. Such result will be used in the next section to build a calibration curve which will allow evaluating the plasticization effect in polymer nanocomposites.

5.2.3. Matrices equivalent to silica-polymer nanocomposites

As already mentioned in Chapter 2, three silane coating agents have been used in the preparation of the nanocomposites: octyl-triethoxysilane C_8 (M_w=276 g/mol), dodecyl-triethoxysilane C_{12} (M_w=332 g/mol) and octadecyl-triethoxysilane C_{18} (M_w=417 g/mol). These silane molecules differ for the length of their alkyl chain and therefore for their molecular weights. Several samples have been prepared by mixing pure SB_F polymer and isomolar amounts of the three selected coating agents. These SB_F+silane samples (named as "equivalent matrices") have been designed to have the same silane/polymer ratio as in nanocomposites with Φ_{Si}=10%v and Φ_{Si}=20%v. In the latter, the amount of silane coating agent is fixed with respect to the amount of *silica* (which is absent here, thus the term "equivalent matrix"). This will allow considering them as a reference to evaluate the plasticization effect in the correspondent nanocomposites.

For all SB_F + silane equivalent matrices, the evolution of τ_α as function of temperature has been determined by fitting the experimental data by a single HN function. The corresponding relaxation maps are shown in Fig.5.7a and 5.7b together with a VFT description.

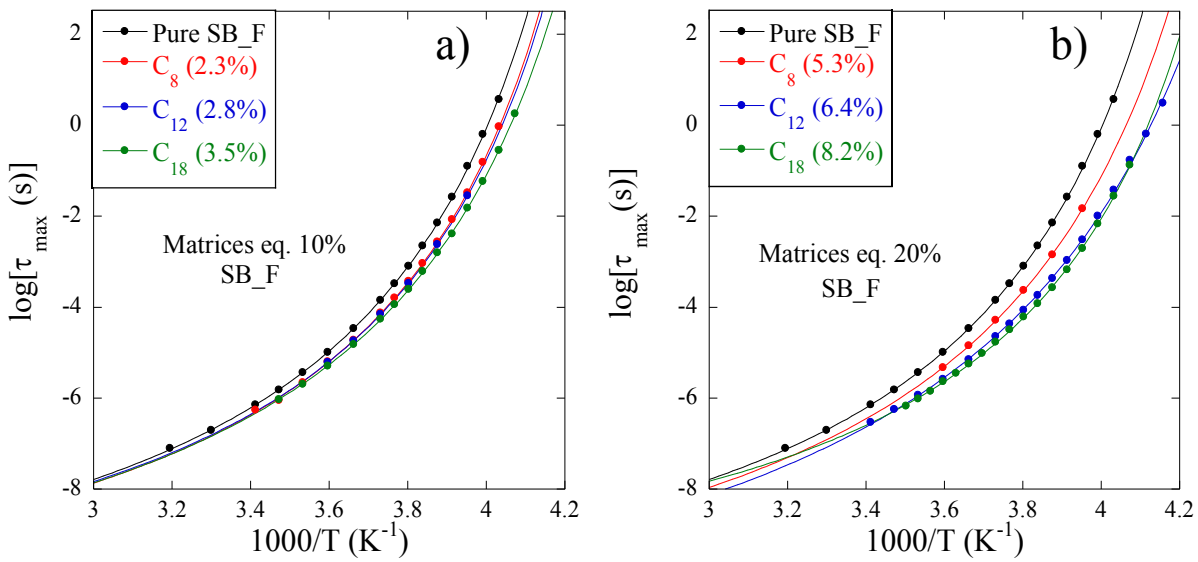

Figure 5.7 (a) Relaxation maps of the α-process for SB_F mixed with different coating agents (i.e., matrices equivalent to NCs) at Φ_{Si}=10%v (a), and Φ_{Si}=20%v (b). In the legend, each silane/SB ratio (%) is indicated. The solid lines through data points are fits to the VFT equation.

As for the pure polymer matrices, the outcomes obtained by the VFT fits are summarized in Table 5.4a for matrices equivalent to NCs at Φ_{Si}=10%v, and in Table 5.4b for matrices equivalent to NCs at Φ_{Si}=20%v. In both cases, there is a good agreement between the value of T_g obtained by calorimetry and the one extrapolated to τ=100s from the VTF fit, $T_{g,100s}$. One can see that the glass transition temperatures for matrices equivalent to NCs at Φ_{Si}=10%v are higher than the ones of the matrices equivalent to NCs at Φ_{Si}=20%v. Such a result is consistent with the fact that the amount of silane is higher in the 20%v-equivalents.

Matrices eq. to NCs at Φ_{Si} = 10%v	**D**	**T_0 (K)**	**log τ_0**	**T_g (K) (DSC)**	**$T_{g,100s}$ (K)**	**m**
C_8	3.8	215.1	-10.9	245.4±0.5	242.7	113.1
C_{12}	3.8	214.6	-10.8	243.9±0.6	242.4	111.1
C_{18}	4.0	212.3	-10.9	245.4±0.2	241.0	107.9

Table 5.4a. Outcomes of VFT fit for SB_F with different coating agents (matrices equivalent to NCs at Φ_{Si}=10%v).

Matrices eq. to NCs at $\Phi_{Si} = 20\%v$	D	T_0 (K)	$\log \tau_0$	T_g (K) (DSC)	$T_{g,100s}$ (K)	m
C_8	3.5	214.4	-10.5	244.5±1.0	240.2	117.6
C_{12}	3.7	209.9	-10.5	239.0±0.8	237.2	107.3
C_{18}	3.1	214.3	-10.2	236.3±1.1	238.0	122.2

Table 5.4b. Outcomes of VFT fit for SB_F with different coating agents (matrices equivalent to NCs at Φ_{Si}=20%v).

To summarize this section, the α-process has been studied for samples made of pure SB_F mixed with different amounts of C_{18} (Fig. 5.6a), and for equivalent SB_F matrices containing different coating agents C_8, C_{12} and C_{18} at isomolar amount (Fig. 5.7a and 5.7b). Since each sample is characterized by a specific silane/SB_F ratio, the value of the relaxation time τ_α at a given temperature (i.e., T=258 K) can be reported as a function of ζ, as shown in Fig. 5.8. One can see that the segmental-relaxation time decreases linearly with the increase of the silane/SB_F ratio, independently from the silane molecule. This result suggests that the plasticization effect is not affected by the length of the alkyl chain of the silane (from 8 to 18 carbons), but only by the silane coating agent amount (silane/SB_F ratio). Moreover, the result shown in Fig. 5.8 can be considered as a calibration curve which will allow to *quantitatively* estimate the strength of the plasticization effect in NCs in the following section.

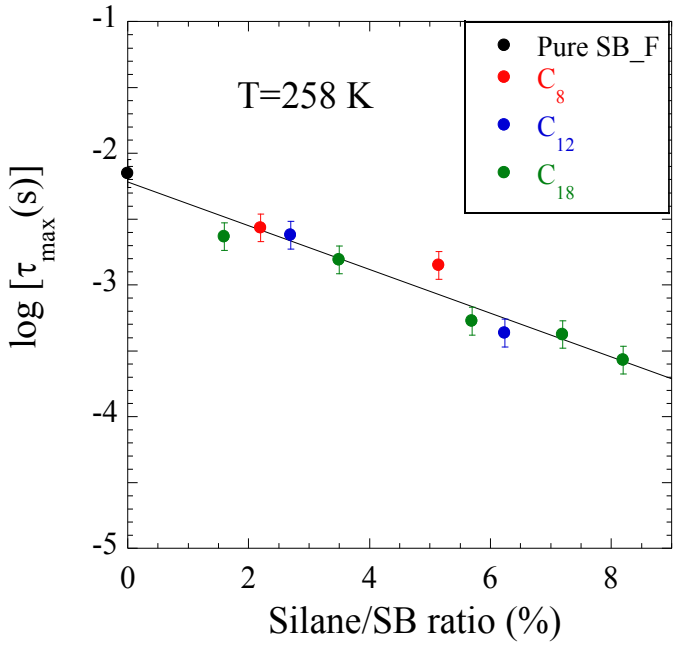

Figure 5.8 Segmental relaxation time at T=258K as a function of the silane/SB_F ratio for equivalent SB_F matrices containing different coating agents C_8, C_{12} and C_{18} (isomolar), and samples made of pure SB_F mixed with different amounts of C_{18}. The solid black line represents a linear fit. The error bar has been estimated considering the variation of the relaxation time between two experimental points which are consecutive in frequency.

5.3. Dynamics in silica/styrene-butadiene model nanocomposites

In previous studies (Steeman and Maurer 1990; Otegui et al. 2013; Baeza et al. 2015a), it has been shown that the introduction of the fillers in a polymer matrix implies the presence of additional dipoles (e.g., water trapped on hydrophilic filler, -OH groups on particle surface). Thus, in nanocomposite systems such as the one structurally investigated in Chapter 4, the β- and the α-relaxations are combined to additional interfacial processes that can be observed on a wide range of temperature and frequency (e.g., MWS interfacial processes (Kremer and Schönhals 2003).

In this section, the segmental α-relaxation in model nanocomposites is investigated to shed light on the plasticization effect induced by silane molecules when they are not chemically grafted on the silica surface. This phenomenon has been studied as a function of: i) the composition of the polymer matrix; ii) the filler content; ii) the amount of silane. The contribution of a low-frequency interfacial polarization process sensitive to the water content will be taken into account, since it partially overlaps with the α-relaxation.

5.3.1. Fitting of dielectric spectra

The fitting procedure applied to the dielectric spectroscopy data to extract the characteristic times of the relaxation processes is reported here. Special care has been given to the α-relaxation whose peak is clearly visible for temperatures ranging between 253K and 278K. This process partially overlaps with the much more intense interfacial process, which relates the hydration layer adsorbed on the filler surface (Fig. 5.9a and 5.9b). This process will be indicated as MWS1, according to Baeza et al. (Baeza et al. 2015a).

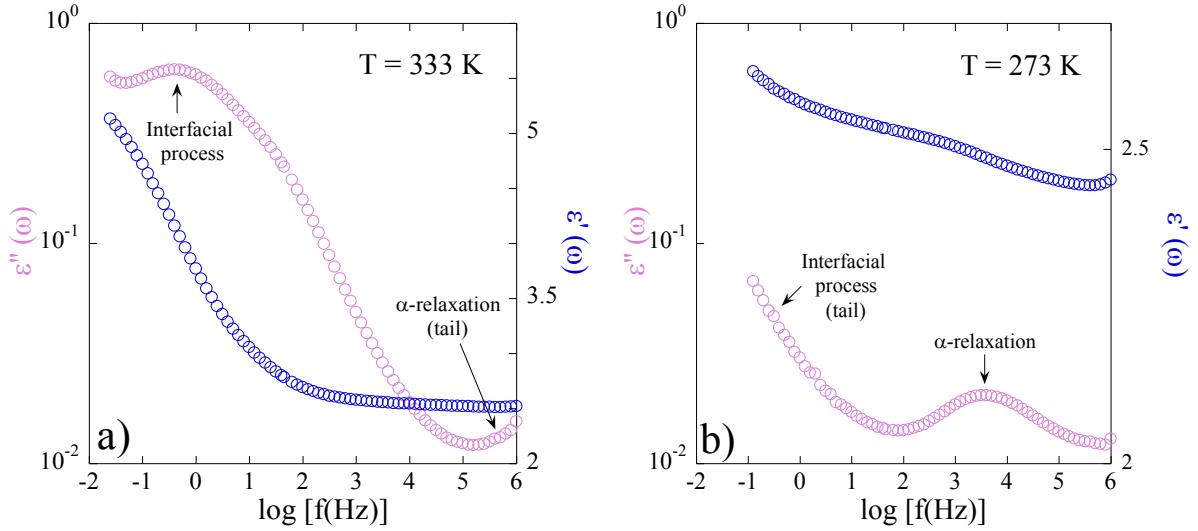

Figure 5.9 Real and imaginary part of the dielectric spectra at T=333 K (a) and at T=273 K (b) of a silica/SB_F model NCs (at Φ_{Si}=9.8%v, formulated using SB_F and silica nanoparticles surface-modified by C_8). The interfacial process MWS1 partially overlaps the α-relaxation.

In order to perform a quantitative analysis of the α-processes in the frequency domain, the dielectric spectra have been fitted by the HN function (Havriliak and Negami 1967). We found, however, that it is difficult to reproduce the broad maximum of the segmental relaxation with a single HN function, as shown in Fig. 5.10a, due to the strong influence of the MWS1-process. Therefore, we used the sum of two HN functions plus a purely dissipative dc-conductivity term $\varepsilon''_{dc} = \sigma_{dc}/\varepsilon_0\omega$, as given in Eq. 5.2, to describe the NCs data (see Fig. 5.10b).

$$\varepsilon^*(\omega) = \varepsilon_\infty + \sum_j \frac{\Delta\varepsilon_j}{\left[1+(\omega\tau_{HN_j})^{\gamma_j}\right]^{\delta_j}} - i\frac{\sigma_{dc}}{\varepsilon_0\omega} \qquad [5.2]$$

where ε_∞ is the high-frequency limit of the dielectric permittivity, ε_0 is the vacuum permittivity; τ_{HN_j} is the characteristic relaxation time and $\Delta\varepsilon_j$ the dielectric strength of the process. The parameters γ_j and δ_j are related to the shape and they range between 0 and 1 depending on the symmetric and asymmetric broadening of the j^{th} process, respectively. A fit example is given in Fig. 5.10b together with the different contributions.

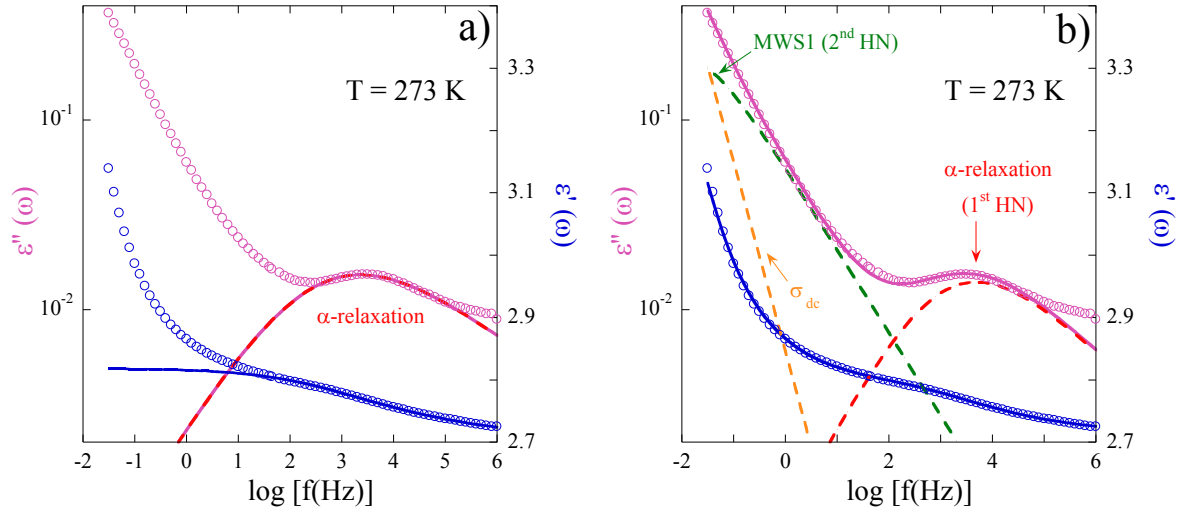

Figure 5.10 Example of frequency dependence of real and imaginary part of the dielectric permittivity in model NCs (at Φ_{Si}=21.0%v, formulated using SB_F and silica NPs surface-modified with C_{18}). The solid lines through the experimental data points represent the global fit based on Eq. 5.2 using one (a) or two (b) HN processes. The dotted lines represent the individual HN functions of each process which contribute to the global fit.

In this fitting approach, the number of free parameters has been controlled carefully in order to extract reliable information, in particular the relaxation time of each process. At first, the fitting parameters of the HN functions have been left free to identify the possible trends as a function of the temperature. For the PNCs, it has been found that the δ parameter can be fixed to 0.5 for the α-relaxation, which is the average of the δ values of the pure polymer matrix (see Fig. A6.1a). For the MWS1 process, δ has been fixed to 0.575 while γ has been specifically chosen for each sample and kept fixed at all the investigated temperatures. The fitting procedure has been applied to the full temperature range to obtain the relaxation map of each sample.

5.3.2. Where do the silane molecules go if they are not chemically grafted on the silica surface?

The impact of the silane coating agents on the dynamical properties of the model NCs is investigated here. A comparison is proposed between NCs where the silane molecules are chemically grafted on the silica surface, and NCs where the molecules are just added to the system without any grafting reaction on the filler surface. This should represent an original way to observe how a coating agent can be used to tune the properties of the system even when it is not grafted. One could think, e.g., to the first stage of solid-phase mixing with the polymer in an industrial system as the one studied in chapter 3.

In section 2.3, an efficient method to surface-modify the silica nanoparticles in suspension using silane molecules with different alkyl-chain length (C_8 – C_{12} – C_{18}) has been proposed. These colloidal suspensions have been mixed with the styrene-butadiene matrix, and the final model nanocomposites have been obtained by solvent casting (see section 2.3). Such NCs, with silane molecules which are chemically grafted on the silica surface, will be indicated as *grafted* NCs. On the other hand, model NCs can also be formulated using bare silica particles and adding the silane coating agent in the NPs suspension together with the polymer in organic solvent. Note that unless the input of specific parameters (T, pH), as done for grafted NPs in the nanocomposites and as indicated in the protocol in chapter 2.3, silanes that are simply added to the system cannot bound covalently to the silica. In this case, the silane molecules are *free* (i.e., not grafted on the filler surface) and this type of model nanocomposite will be named as *non-grafted* PNCs.

The comparison between these two types of model NCs will allow determining where *free* silane molecules distribute in the system and how it can modify the matrix or NC properties. Such information could be useful in the case of coating agents added directly during mixing of the fillers with the polymer (e.g., solid-phase mixing), since it is difficult to verify the grafting reaction *ex post* and the presence of unreacted silane molecules in the polymer bulk could influence the properties of the final NC (i.e., via the plasticization effect as observed for pure polymer in section 5.2).

Firstly, the relaxation maps of model NCs formulated with bare nanoparticles (i.e., no coating agent) at two filler contents (Φ_{Si}=11.2 and 19.0%v) have been compared to the one of the pure SB_F matrix, as shown in Fig. 5.11. One can see that the characteristic times of the α-process for both nanocomposites and the matrix are superimpose, which indicates that the addition of silica nanoparticles (up to $\Phi_{Si} \approx$ 20%v) does not affect the segmental relaxation dynamics and thus the glass-transition temperature. This result is in agreement with previous works using similar rubber systems (Otegui et al. 2013; Baeza et al. 2015b). This may be due to the non-attractive interaction between silica and SB chains, which leads to a negligible amount of interfacial polymer layer with slowed-down dynamics (*glassy* fraction of a few percent as determined by low-field NMR (Mujtaba et al. 2014; Baeza et al. 2015b)).

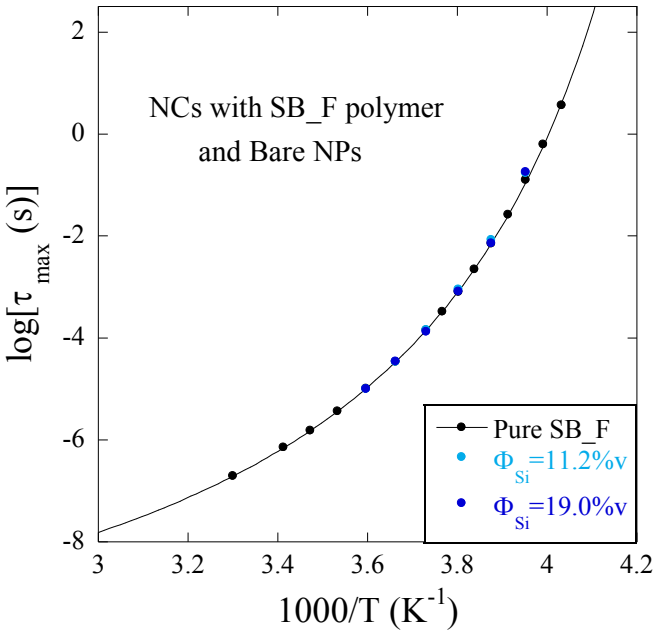

Figure 5.11 Relaxation map of model NCs formulated with bare NPs and SB_F matrix at two filler contents (11.2 and 19.0%v of silica, no coating agents). Solid lines represent VFT fits.

Then, the *grafted* and *non-grafted* nanocomposites formulated with SB_NF or SB_F polymer matrix and C_8, C_{12} or C_{18} as coating agent have been compared. All these samples have been prepared at the same filler content ($\Phi_{Si\ nominal}$ =10%v; $\Phi_{Si\ TGA}$= (10.5 ± 0.7) %v) and their segmental-relaxation times at T=258 K are shown in Fig. 5.12 as a function of the alkyl-chain length of the silanes. These characteristic times are compared to the ones of the equivalent SB_F polymer matrices (Fig. 5.7a).

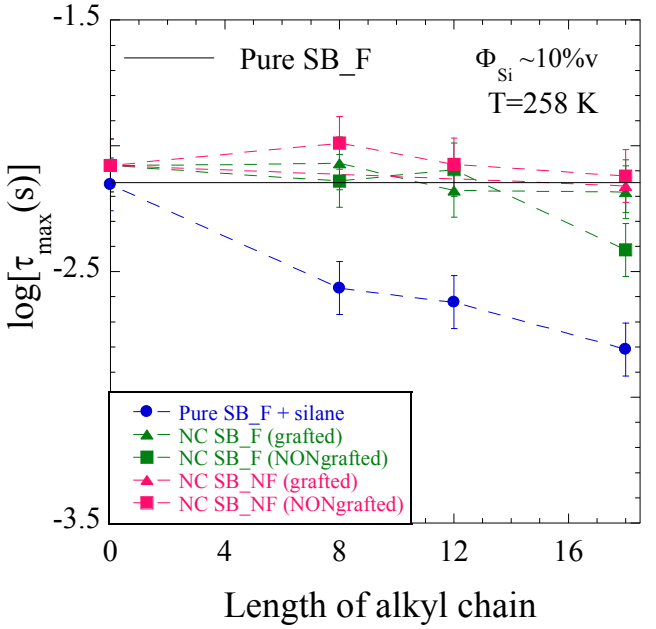

Figure 5.12 Relaxation time of the segmental relaxation at T = 258 K for *grafted* and *non-grafted* model NCs as a function of the alkyl-chain length of the silane. The black line indicates the level of the pure SB_F matrix. Error bars have been estimated considering the variation of the relaxation time between two experimental points which are consecutive in frequency.

The characteristic times for grafted nanocomposites in Fig. 5.12 do not evolve with the silane length (from 0 up to 18 carbons) and, within error bars, they are similar to the relaxation time of the pure SB matrix (SB_F or SB_NF, both being very close, see Fig. 5.4). Thus, surface-modification of the silica surface with any of the silane molecules investigated here does not seem to affect the dynamics of the segmental relaxation. Turning to the *non-grafted* NC (with *free* silanes), there is also no detectable change of the relaxation time, except for the sample formulated with the longest silane (C_{18}) and SB_F. This sample displays a faster dynamics as compared to the pure polymer matrix. According to what has been observed in section 5.2, this behavior suggests that ungrafted silane molecules may induce a plasticization effect also in NCs.

These results point out several interesting features: i) when the silane is grafted to the filler, there is no observable matrix plasticization; ii) the plasticization in presence of filler with ungrafted silane is observed only with the longest alkyl-chain (C_{18}) silane in SB_F, which highlights the role of the polymer matrix; iii) the plasticization in NCs with C_{18} is clearly less intense than the one detected in the pure matrix with same silane/SB ratio. It suggests that a certain amount of silane is not present in the bulk, but adsorbed on the filler surface. To better visualize the plasticization effect in presence of silica, the relaxation time of the NCs of interest at 258 K has been normalized by the relaxation time of the pure polymer, as summarized in Fig. 5.13a. The corresponding dielectric losses are reported in Fig. 5.13b.

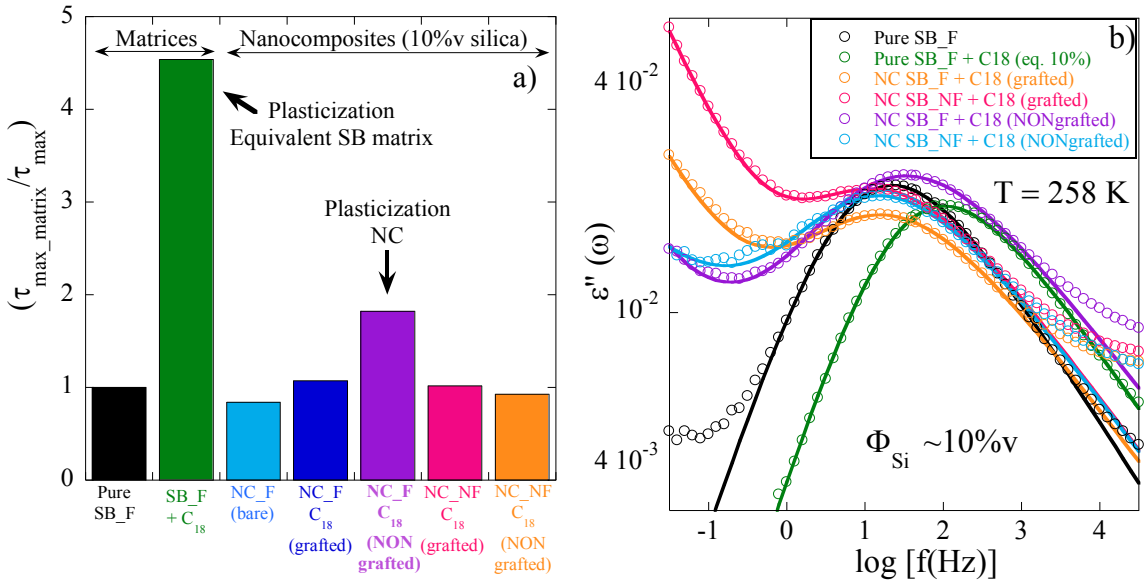

Figure 5.13 (a) Relaxation time of matrices and NCs (Φ_{Si} ~ 10%v) normalized by the one of the pure polymer to put in evidence the plasticization effect in the *non-grafted* sample formulated with SB_F and C_{18}. For these samples, the imaginary ε" part of the dielectric permittivity is shown in (b). The solid line represents the HN fit functions.

At this point, one may wonder if these NCs with different dynamics have a similar filler structure. Therefore, the structure of the *grafted* and *non-grafted* model NCs (10%v of silica) formulated with SB_F or SB_NF and C_{18} as coating agent has been investigated by SAXS. The results are shown in Fig.

5.14a. From a first qualitative analysis, the scattering curves overlap rather well in the intermediate-q regime. This is quantitatively confirmed by the analysis of the structure facture at the correlation hole, Fig. 5.14b (see section 2.4). For these four samples, the aggregate compacity is similar, $\kappa \sim 10\%$, as reported in the inset in Fig. 5.14b. This result confirms that grafting of the silane molecules does not modify the filler structure regarding local interactions, as already observed in Chapter 4. It follows that the *grafted* and *non-grafted* samples display a similar local structure. In addition, for each type of NC, the polymer variation (from SB_NF to SB_F) does not seem to impact the structural features, whereas it plays an important role regarding the plasticization of the polymer matrix, as seen in Fig. 5.13a and in the following.

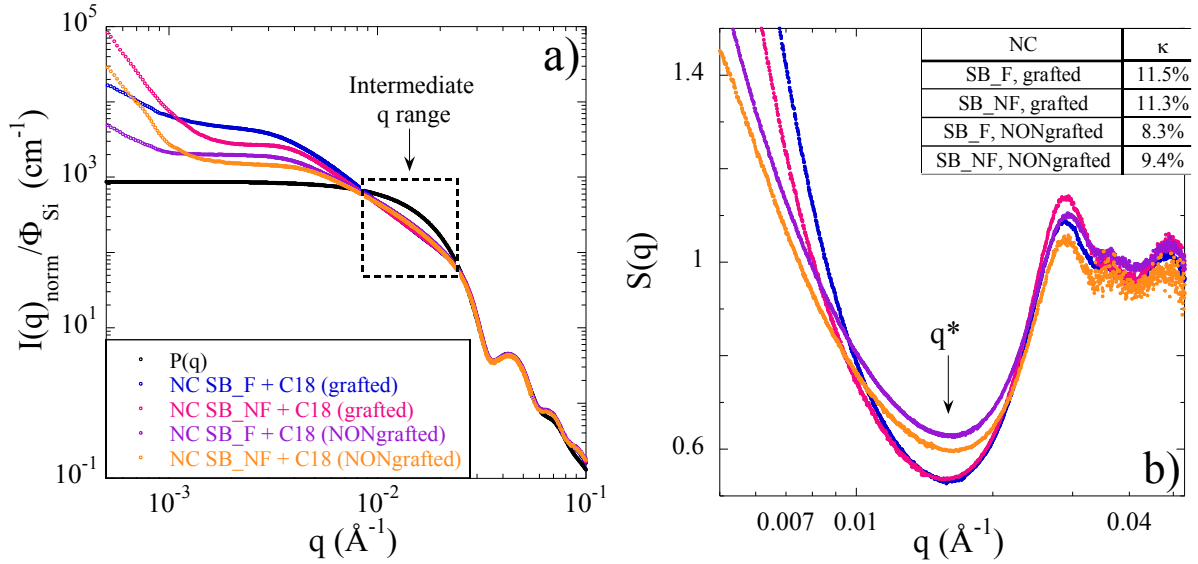

Figure 5.14 (a) Reduced representation of SAXS data for grafted and non-grafted model NCs formulated with SB_F or SB_NF polymer and C_{18} as coating agent. (b) Structure factor in the intermediate-q range for the same samples. Inset: aggregate compacity values. In this case, the SAXS experiments have been performed at the ESRF synchrotron (ID02 line; collimated beam at 12.46keV; SDD =1m, 10m, 30m).

In the light of the above results, we will focus from now on the study of plasticization in the *non-grafted* NCs formulated with C_{18} as coating agent. The impact of different parameters on the plasticization effect (e.g., composition of the polymer matrix, silica content variation, amount of silane) will be investigated in the next sections.

5.3.3. Impact of matrix composition on the plasticization effect in model PNCs

To determine the influence of matrix composition on the plasticization effect, *non-grafted* NCs with $\Phi_{Si} = (10.5 \pm 0.2)$ %v have been formulated with C_{18} and different amounts of end-functionalized chains in the matrix: 0% (= SB_NF), 50%, 75%, and 100% (= SB_F). The imaginary and real part of the dielectric permittivity of these samples at T=258K are reported in Fig. 5.15a and 5.15b, respectively.

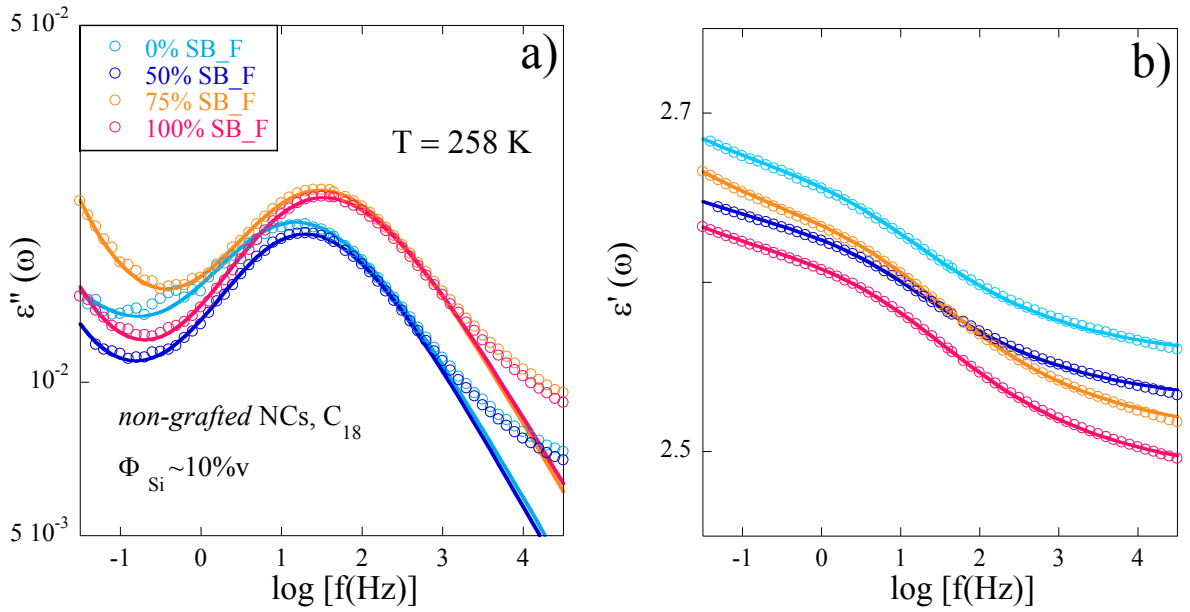

Figure 5.15 Imaginary (a) and real (b) part of the permittivity for *non-grafted* NCs with different amounts of end-functionalized chains in the matrix (from 0%v to 100%v of SB_F). The solid lines represent the HN fit function.

The dielectric loss spectra in Fig. 5.15a show a progressive shift of the α-relaxation peak towards higher frequency when increasing the fraction of SB_F polymer. This confirms that the amount of end-functionalized polymer chains in the nanocomposite is a key parameter for plasticization. The relaxation maps of these samples are given in Fig. 5.16a.

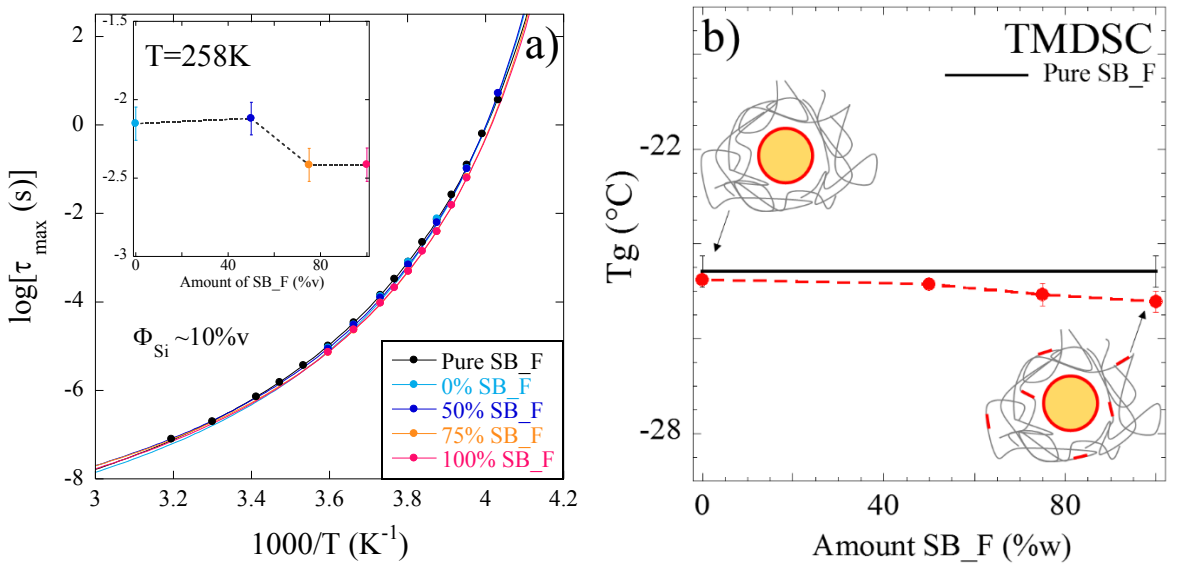

Figure 5.16 (a) Relaxation map of model NCs formulated with different amounts of end-functionalized polymer chains (fraction of SB_F polymer). Solid lines represent VFT fits. Inset: Characteristic times of the α-process as a function of the SB_F fraction at T = 258 K. Error bars have been estimated considering the variation of the relaxation time between two experimental points which are consecutive in frequency. (b) T_g values as a function of the SB_F fraction (TMDSC with cooling rate = 3 K/min). Red segments represent silane molecules in the bulk or around the silica NP (in yellow). Error bars have been determined repeating the measurement on three independent samples.

As long as the content of SB_F in the matrix is less than 50%v, the *non-grafted* NCs display a behavior comparable to the one of *grafted* nanocomposites, i.e., without plasticization. Thus, one may assume that for low SB_F fractions, all the C_{18} molecules are adsorbed on the filler surface. On the other hand, for SB_F contents higher than 50%v, a decrease of the segmental-relaxation time is observed in Fig. 5.16a. These BDS results have been confirmed by TMDSC measurements (Fig. 5.16b), which show a reduction of the glass-transition temperature when increasing the SB_ F fraction, and thus plasticization of the bulk polymer. Such a behavior could be explained considering that part of the C_{18} interacts with the silanol groups Si-OH on the silica surface, while another part is attracted by the functional end-group of the SB_F chains (Si-OH, see Fig. 2.1), inducing the observed plasticization effect. One may also wonder if the end-functionalized polymer chains could be grafted or adsorbed on the silica surface, reducing the effective surface available for the silane molecules to adsorb. We know from "bound rubber" tests (section 2.3), that the fraction of grafted polymer on the silica surface is negligible, as reported in Table 2.9. However, one cannot exclude a favorable interaction between the chain end-groups and the hydroxyl groups of the silica, which would imply that the silane molecules cannot access the silica surface and, therefore, stays in the bulk.

In the next sections, we choose to investigate the plasticization induced by C_{18} in *non-grafted* NCs with a fully end-functionalized matrix.

5.3.4. Impact of silica content on the plasticization effect in model PNCs

The influence of the silica content has been investigated in *non-grafted* NCs formulated with SB_F and C_{18} as coating agent. This combination has been shown in the above sections to exhibit the strongest plasticization effect. The silica volume fraction has been varied from 0 (pure polymer matrix) to 19.9%v. For all the samples, the C_{18} is added as 12%w with respect to silica (ψ = C_{18}/Silica ratio=0.12). This implies that while the C_{18}/Silica ratio is constant, the C_{18}/SB_F ratio, ζ, increases with the filler content. The characteristics of the NCs are summarized in Table 5.5. The silica content of each sample has been determined by thermogravimetric analysis (TGA), by the procedure reported in section 2.3.

%v Si (nom)	%v Si (TGA)	%w Si (TGA)	%w Silane (C_{18})	Ψ	ζ
1%	1.6%	2.5%	0.3%	12.0%	0.3%
5.0%	5.0%	11.7%	1.4%	12.0%	1.6%
7.5%	7.5%	17.0%	2.0%	12.0%	2.5%
10.0%	10.3%	21.9%	2.6%	12.0%	3.5%
12.5%	11.8%	26.5%	3.2%	12.0%	4.5%
15.0%	14.5%	30.8%	3.7%	12.0%	5.7%
20.0%	19.9%	38.7%	4.6%	12.0%	8.2%

Table 5.5 Characteristics of *non-grafted* NCs formulated with a fully end-functionalized SB matrix (SB_F) and C_{18} as coating agent at different silica contents.

For a first qualitative comparison, the imaginary and real parts of the dielectric permittivity of the NCs at T = 258 K are reported in Fig. 5.17 for the different filler fractions investigated. As shown in Fig. 5.17a, the peak of the segmental α-relaxation shifts to higher frequency with the increase of silica fraction up to Φ_{Si}=11.8%v. This indicates a reduction of the segmental-relaxation time, and reveals plasticization of the bulk polymer. Above Φ_{Si}=11.8%v, and up to the highest silica content (Φ_{Si}=19.9%v), the α-relaxation peak seems to move back to lower frequencies showing a relaxation time comparable to the one of the NCs at low filler content.

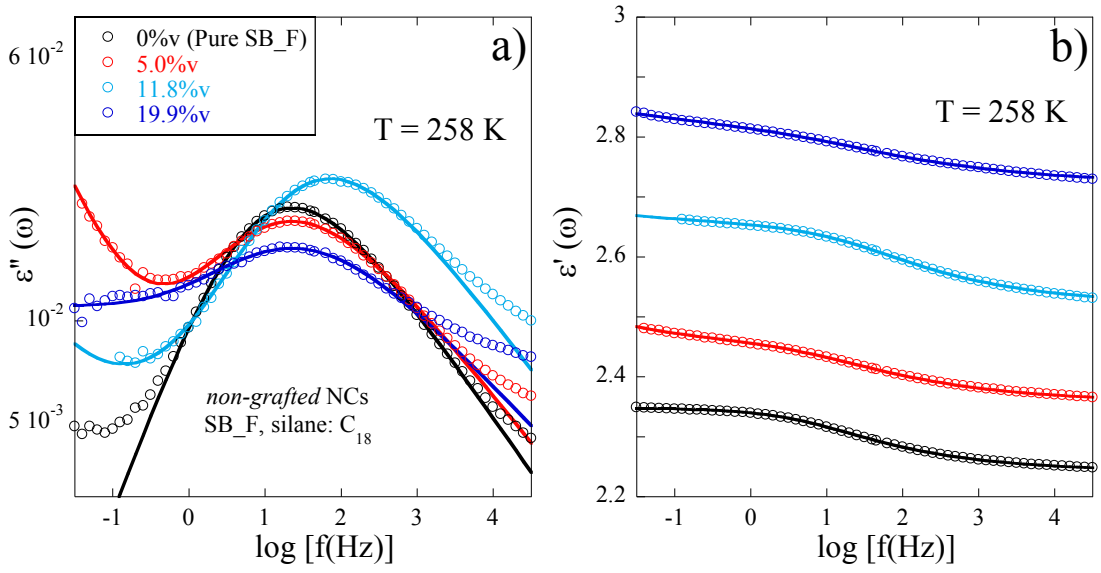

Figure 5.17 Imaginary (a) and real (b) part of the dielectric permittivity at 258 K for *non-grafted* NCs formulated at different silica contents (Φ_{Si}= 0, 5.0, 11.8 and 19.9%v) with SB_F matrix and C_{18} as coating agent. Solid lines represent HN fit functions.

The data in Fig. 5.17 have been described by HN functions, and the relaxation maps for the α-process are given in Fig. 5.18a for the NCs with different silica contents. To better visualize the evolution of the relaxation times, the values obtained at temperatures between 253 K and 278 K have been reported as a function of Φ_{Si} in Fig. 5.18b. This representation underlines that the segmental-relaxation times display a non-monotonous behavior with the filler content, with a minimum at Φ_{Si}=11.8%v corresponding to a maximum for the intensity of the plasticization. A similar behavior is found for all the temperatures

investigated, and it is also confirmed by TMDSC: the glass-transition temperature shows a similar trend to the one of τ_α, as reported in Fig. 5.18c.

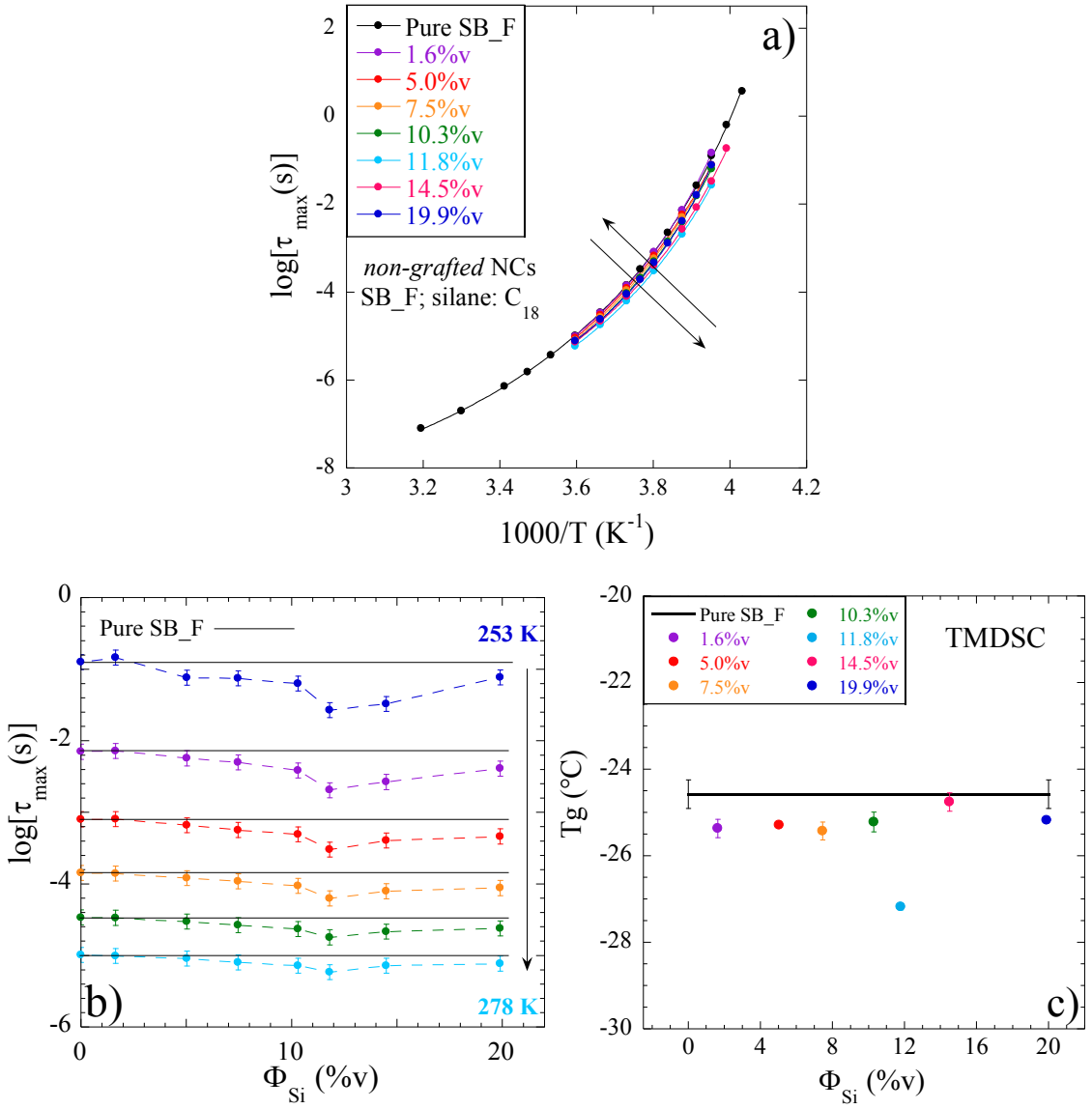

Figure 5.18 (a) Relaxation map of NCs at different silica contents. Solid lines represent VFT fit. The arrows represent the non-monotonic behavior. (b) Evolution of the segmental-relaxation time as a function of the filler content for several temperatures from 253 K to 278 K. Error bars have been estimated considering the variation of the relaxation time between two experimental points which are consecutive in frequency. (c) Evolution of T_g as a function of the silica content, estimated by TMDSC. Error bars have been determined repeating the measurement on three independent samples.

These results suggest that the silane molecules are distributed between the silica surface and the polymer matrix, where it interacts with the end-groups of the chains, because without end-functionalized groups (SB_NF) this effect is not observed (see section 5.3.3). We found that the most important silane fraction in the bulk is obtained for an intermediate silica fraction of about 12%v.

The segmental-relaxation times reported in Fig. 5.18b can be compared to the calibration curve constructed using the equivalent matrices (Fig. 5.8) in order to quantify the amount of *free* C_{18} in the bulk. An example is given Fig. 5.19a, showing how to obtain an equivalent C_{18}/SB_F ratio, indicated as "real ζ", by geometrical construction. This value is an estimation of the quantity of coating agent dispersed in the bulk polymer in presence of silica, which leads to the same plasticization as without silica. Normalizing this real ζ by the nominal one, the fraction of *free* C_{18} in the nanocomposite can be estimated. The outcome for all NCs with different filler contents is summarized in Fig. 5.19b. As in Fig. 5.18, two different regimes can be identified with a maximum silane content in the bulk at Φ_{Si}=11.8%v. At lower filler fractions, the quantity of silanes acting as plasticizer in the bulk increases with the increase of the filler. In this case, the increase of the nominal C_{18}/SB_F ratio, ζ, (Table 5.5) corresponds to an increase of the real ζ. This behavior can be explained considering that the increase of filler content is associated with a decrease of the polymer fraction in the nanocomposite. Thus, taking into account the constant nominal silane/Silica ratio (12%w in Table 5.5), this characteristic can be linked to an increase of the effective silane/polymer ratio in the bulk (i.e., amount of C_{18} molecules per polymer chains), which induces a stronger plasticization effect. In this sense, Φ_{Si}=11.8%v can be considered as the optimal filler fraction to obtain the maximum plasticization effect.

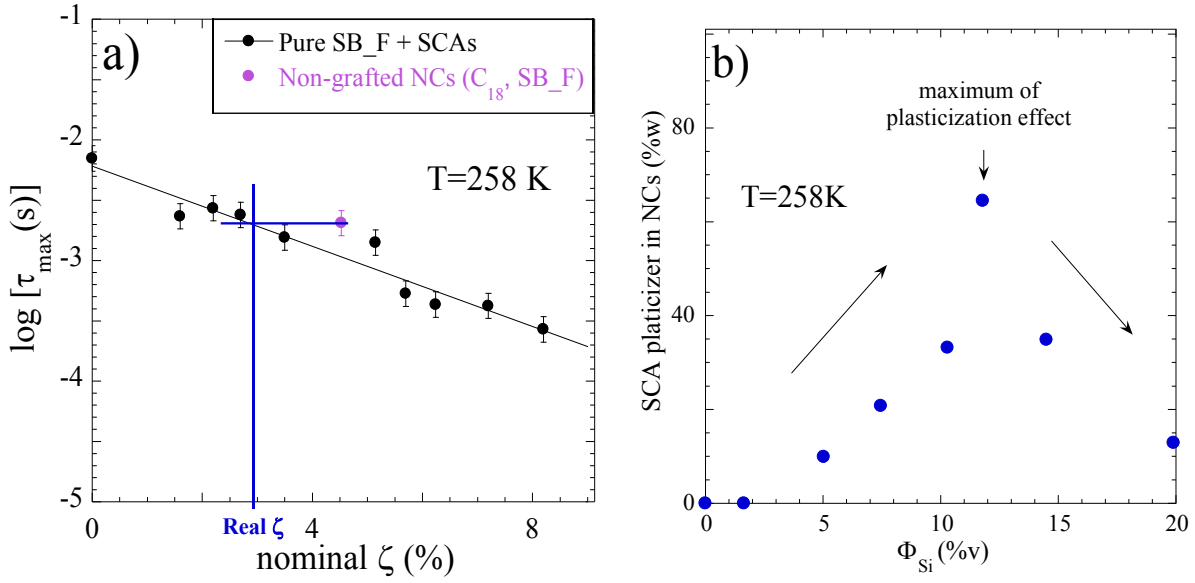

Figure 5.19 (a) The comparison between the NC relaxation time and the calibration curve allows determining the fraction of silane dispersed in the bulk polymer. The error bar has been estimated considering the variation of the relaxation time between two consecutive experimental points. (b) Fraction of silane which plasticizes the polymer matrix as a function of the silica volume fraction (%w of silane plasticizer in NCs are obtained from the real ζ values).

The still open question is why τ_α increases in the NCs with silica contents higher that 11.8%v (i.e., second regime), getting back to a value close to the one of the sample at 5.0%v of silica. The evolution of the segmental-relaxation time suggests that other mechanisms can prevail on the plasticization once the silica content overcomes Φ_{Si}=11.8%v. For example, rheological tests performed on the *grafted* NCs

at different filler contents (see Appendix 7, Fig. A7.10) underline that the system reaches the percolation threshold around this value of Φ_{Si}. The formation of a tridimensional network of nanoparticles may give rise to geometrical constraints for the polymer chains, leading to an increase of T_g and τ_α. Moreover, the presence of such a silica network could prevent the dispersion of the C_{18}, since the regions occupied by pure polymer in the NCs are reduced.

5.3.5. Impact of the amount of C_{18} on the plasticization effect in model PNCs

Another tuning parameter for the plasticization in nanocomposites is the amount of coating agent. In this section, *non-grafted* NCs with $\Phi_{Si} = (10.2 \pm 0.4)$ %v, formulated with SB_F or SB_NF matrix and C_{18} at different contents (12%w, 18%w and 24%w with respect to silica) are investigated. The C_{18}/Silica (ψ) and C_{18}/SB (ζ) nominal ratios of these samples have been summarized in Table 5.6. The relaxation map for the α-process is shown in Fig. 5.21.

C_{18}/Silica ratio, ψ (%)	C_{18}/SB ratio, ζ (%)
12	3.5
18	5.3
24	7.2

Table 5.6 The C_{18}/Silica and C_{18}/SB nominal ratios of *non-grafted* NCs at Φ_{Si}=10.2%v formulated with fully end-functionalized or fully non-functionalized SB matrix.

To better visualize the impact of the C_{18} amount on the plasticization, the segmental-relaxation times at T=258K have been represented as a function of the C_{18}/Silica ratio, ψ, in the inset in Fig. 5.20. In a previous section (par. 5.3.3), it has been shown that when C_{18} is added at 12%w with respect to silica, the plasticization effect in *non-grafted* NCs is detectable only if the amount of end-functionalized styrene-butadiene is higher than 50%v. On the opposite, no effect is detected when NCs are formulated with a fully SB_NF matrix, suggesting that all silanes are located at the filler interface (i.e., same behavior for *grafted* NCs and NCs prepared without silane coating agent). When the ψ ratio is increased, a more intense plasticization effect can be detected in the NC formulated with the SB_F matrix. One scenario to explain this result is to consider that in the NCs with end-functionalized styrene-butadiene, the plasticization could be promoted by an attractive interaction between the silane and the end-group of the polymer chains, leading to a distribution of the silane in the matrix. Another possibility is to consider that these end-groups display an attractive interaction with the hydroxyl groups at the silica surface, precluding the silane from adsorption on the silica.

Turning to the samples prepared with SB_NF, one can see a decrease of the relaxation time for $\psi >$ 18%w in Fig. 5.20, corresponding to an onset of plasticization. Such effect is most likely due to a saturation of the silica surface for the highest ψ values. As a consequence, the excess of C_{18} remains in the bulk, promoting plasticization even in the absence of end-functionalized polymer chains.

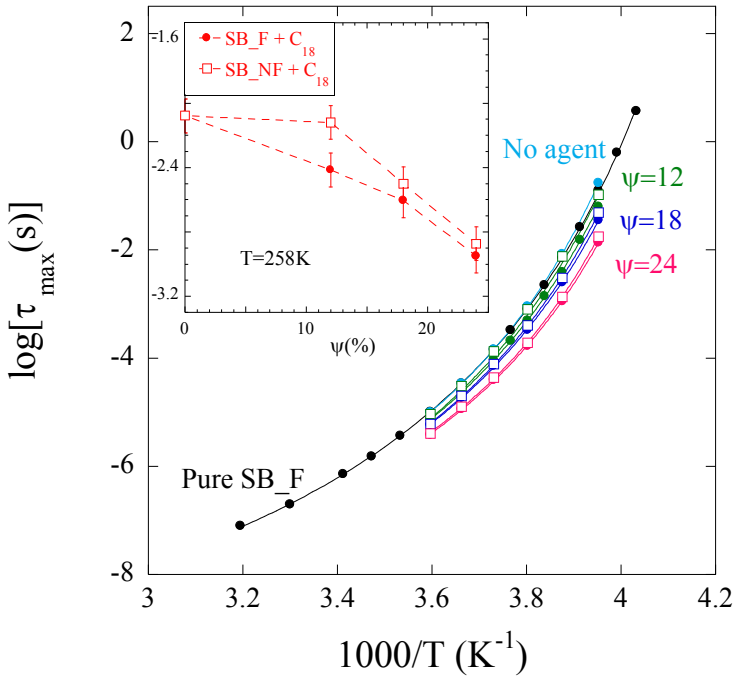

Figure 5.20 (a) Relaxation map of *non-grafted* NCs formulated at different C_{18}/Silica ratios with SB_F and SB_NF polymer matrix (Φ_{Si} = (10.2 ± 0.4) %v). Solid lines represent VFT fit. Inset: relaxation times at T=258K as a function of the C_{18}/Silica ratio. Error bars have been estimated considering the variation of the relaxation time between two experimental points which are consecutive in frequency.

Finally, when the ratio between silane and silica is increased to 24%w, the plasticization seems to become independent of the nature of the polymer matrix. We assume that a complete saturation of the filler surface is reached in both cases, resulting in a comparable plasticization effect of the bulk polymer. In Fig. 5.21a, the evolution of the C_{18} amount present in the bulk as a function the silane/SB ratio makes this effect even more evident. A schematic representation of this mechanism is given in Fig. 5.21b.

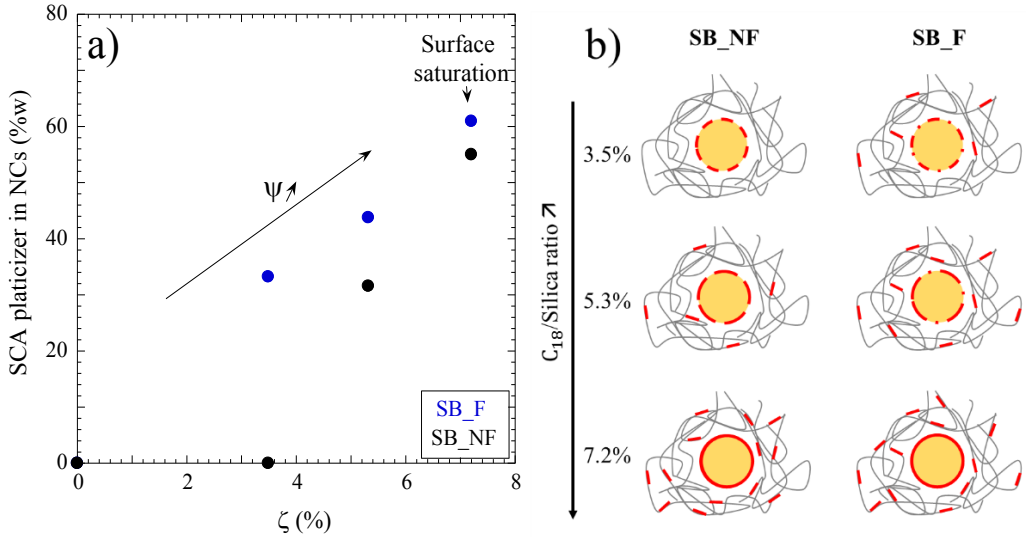

Figure 5.21 (a) Amount of C_{18} silane present in the bulk as a function of the silane/SB ratio. These values have been obtained using the calibration curve in Figure 5.8. (b) Schematic representation of the mechanism of distribution of silane coating agent as a function of the increase of the silane/Silica ratio. Red segments represent silane molecules in the bulk or around the silica NP (in yellow). The dotted and dashed-dotted red lines illustrate the increasing quantity of silane molecules around the silica NP from 3.5 to 5.3% of C18/silica ratio, and also from the left to right side of the figure at 5.3%

5.4. Conclusions

In this chapter, we have investigated the impact of the silane coating agent on the segmental dynamics in model silica/polymer NC systems, combining BDS and TMDSC. We observed that the dispersion of the silane molecules in a pure SB matrix (i.e., no fillers) leads to a decrease of both the segmental-relaxation times and the calorimetric T_g. This effect is associated with the plasticization of the polymer, and it is found to become more pronounced when increasing the amount of silane. On the other hand, plasticization is not affected by the variation of the alkyl-chain length of the silane.

In silica/SB nanocomposites, we found that there is no detectable modification of the segmental dynamics upon addition of silica nanoparticles (up to about 20% in volume). Then, two types of model NCs with similar (local) filler structure have been studied: i) *grafted* NCs, where the silanes are chemically bound to the NP surface; and ii) *non-grafted* NCs, where the silanes are simply added (without reaction) in the silica suspension before solvent casting. The comparison between these two systems revealed that surface modification of the silica (i.e., in *grafted* NCs) does not affect the segmental dynamics of the NCs. In this case, the silane agent (which cannot move) stays at the interface and does not modify the dynamics of the matrix. On the opposite, the introduction of *free* silane molecules with the longest alkyl group C_{18} (i.e., in *non-grafted* NCs) induces a clear plasticization effect, but only when the polymer matrix contains end-functionalized chains. It means that a fraction of the silanes is no longer adsorbed on the silica in the functionalized matrix. This fraction, which corresponds to the effective amount of molecules plasticizing the bulk in NCs, could be evaluated using a calibration curve. The presence of silanes in the bulk may be due either to a favorable interaction between the silanes and the functional end-groups of the polymer chains *in the bulk*, or to a favorable interaction of the polymer end-groups with the hydroxyl groups of the silica preventing the silanes from adsorption on the silica surface. At this stage, we are not able to discriminate between these two scenarios.

In *non-grafted* NCs formulated with SB_F polymer and C_{18} as silane, the increase of the filler content up to ≈ 12%v is associated with a stronger plasticization effect. Such an effect could be rationalized considering that an increase of the filler content corresponds to a decrease of the polymer fraction, i.e., a higher number of silane molecules per polymer chain. For silica fraction higher than 12%v, the formation of a percolated silica network seems to prevail on the plasticization since an increase of the segmental relaxation time was recorded. Moreover, the variation of the C_{18}/Silica ratio indicates that the plasticization can be induced also in a fully non-functionalized polymer matrix, once the silane content is high enough to induce the saturation of the silica surface.

This study proposes an original use of the silane coating agent as plasticizer, which allows tuning the segmental dynamics in pure polymers, but also in silica/polymer NCs. We have provided evidence for

a dependence on the amount of silane, its surface grafting, and the properties of the matrix (i.e., end-functionalized polymer chains). Moreover, we have proposed a quantitative measurement of the distribution of silane molecules in the bulk polymer in *non-grafted* NCs, evaluating the shift of the relaxation time of the α-process by BDS.

6. General conclusions and perspectives

6. General conclusions and perspectives

In the present PhD work, we investigated silica-styrene/butadiene nanocomposites, focusing on the impact that the surface-modification of nanoparticles by small molecules (e.g., silane coating agents, SCAs) has on the PNC properties. These SCAs allow to tune the filler-filler and the filler-polymer interactions which strongly affect the structure and the dynamics of the system.

Thanks to the partnership with Solvay, we successfully reproduced the formulation of simplified industrial nanocomposites, according to the protocol proposed in a previous PhD by Baeza et al.(Baeza et al. 2013a). In this system, obtained by solid mixing, the ingredients have been limited to the strict minimum allowing to shed light on the impact of each component on the structural properties of the final sample.

Firstly, we focused on the uncrosslinked simplified industrial nanocomposites. Using Small Angle X-ray Scattering (SAXS), Transmission Electron Microscopy (TEM) and a recently developed structural model, we quantified the effect of coating agents with different alkyl chain length (C_8, C_{12}, and C_{18}) on filler structure in terms of aggregate formation. We showed that SCA chain length has no impact on the nanocomposite microstructure. Moreover, we elucidated the role of the catalyzer, diphenyl-guanidine DPG, commonly used in tire manufacturing. We revealed that a strong synergic effect exists between both DPG and the silane coating agent: the DPG molecules are necessary to promote the compatibilizing effect of the SCA. We extended our discussion towards the influence of small molecules on crosslinked samples. Also in this case, we revealed that the synergistic action of DPG and SCA is essential to tune the large-scale filler structure influencing the filler dispersion.

The study of the simplified industrial nanocomposites has been extended to a new silica-styrene/butadiene model system, completely developed in the framework of my thesis at Laboratoire Charles Coulomb. This system has been formulated by a multi-step procedure, where colloidal silica NPs are dispersed in the polymer matrix and the final PNC is obtained by solvent casting. In order to realize a model system equivalent to the industrial one, the first aim was to surface-modify silica NPs using different silane molecules. We successfully developed an efficient method to surface-modify silica NPs in ethanol/water suspension, obtaining a grafting density of about 1 molecule/nm^2. By a solvent exchange procedure, we were also able to transfer the surface-modified particles in the same solvent (i.e., methyl-ethylketone, MEK) used to dissolve the polymer and then mix them to obtain the final model PNC. For this system, the surface-modification had been performed with silane molecules which differ: i) by the length alkyl chain length (C_8, C_{12}, and C_{18}), as for the simplified industrial nanocomposites; ii) the silane function, such as triethoxy-, trimethoxy-, monomethoxy- octylsilane (i.e., named C_8, C_{8m} and C_{8mm}, respectively).

For the structural characterization of this multi-step system, we proposed a combined SAXS-reverse Monte Carlo approach, which allowed to investigate the dispersion state of surface-modified silica NPs in precursor solvents (i.e., ethanol/water mixture and MEK) and in the final PNC material. In each medium, we were able to determine the experimental distribution functions of the aggregation numbers, extracting the aggregate mass in presence or absence of interactions between particle aggregates. We proved that, after the reaction in hydro-alcoholic solution, the particles were rather aggregated, while after transfer into MEK, the low-q intensity was found to decrease, and the signature of repulsion appeared. This suggests that aggregation is reversible, and as particles possess a grafted layer, the latter probably protects NPs sterically from getting close enough for Van der Waals attraction to stick them irreversibly together.

Concerning the NP surface-modification by silanes with different hydrophobicity, we proved that the particle interactions in suspension were found to be only slightly affected by the type of graft, with C_{18} always yielding the highest aggregation numbers. When the surface-modification was performed by silanes with different functions, the order of the width of the mass distributions seems to be conserved from MEK to the PNCs. On the other hand, only the C_8-modified NPs keep a comparable mass distribution, whereas it becomes wider for the C_{8m} and the C_{8mm}. In particular for this last silane agent, we showed a strong evolution towards bigger aggregates in the polymer matrix.

For the model nanocomposite, we also investigated by Broadband Dielectric Spectroscopy (BDS) the role of the silane coating agent molecules with different hydrophobicity on the segmental dynamics this system.

Firstly, we showed how SCA can be used to induce the *plasticization* of the pure polymer matrix, which arises from a decrease of the segmental relaxation time and thus induces a reduction of calorimetric glass transition temperature. As it concerns the nanocomposites, we investigated two type of systems: i) the *grafted* PNCs, where the silane is chemically grafted on the surface of silica nanoparticles before their dispersion in the polymer matrix. In this case, the segmental dynamics are not altered by the surface-modification of the nanoparticles; ii) the *non-grafted* PNCs, where the SCA is just added after the silica dispersion in the polymer matrix. Here, a plasticization effect is induced only when the sample is formulated with end-functionalized polymer chains and the silane molecules with the longest alkyl chain (i.e., C_{18}). We tried to interpret this experimental evidence considering the favorable interaction between the silanes and the functional end-group of the polymer chains in the bulk or the favorable interaction of the polymer end-group with the hydroxyl groups of the silica preventing the silane molecules from adsorption on the silica surface. Thus, in *non-grafted* model PNCs prepared with SB_F polymer and C_{18} we investigated the impact of the silica content variation. We quantified the amount of SCA agent in the polymer bulk, revealing that the amplitude of plasticization effect increased up to filler content of 11.8%v: the increase of the filler content corresponds to a decrease of the polymer fraction, and consequently to the increase of the number of the silane molecules per polymer chain. At filler

content higher than 11.8%v, the formation of a percolated silica network seemed to prevail on the plasticization since an increase of the segmental relaxation time is recorded. Moreover, the variation of the C_{18}/Silica ratio indicates that the plasticization can be induced also in a fully non-functionalized polymer matrix, once the silane content is high enough to induce the saturation of the silica surface.

All these findings could open the road to a fundamental understanding and rational design of model and industrial nanocomposite formulation with optimized coating agents.

Perspectives

For both nanocomposite systems investigated in this PhD work, several perspectives can be developed. Concerning the simplified industrial nanocomposites, the results proposed in Chapter 3 about NCs formulated with end-functionalized styrene-butadiene (SB_F) could be cross-checked with nanocomposites made only with a non-graftable matrix (SB_NF).

A more detailed characterization can be performed for the cross-linked version of the simplified industrial nanocomposites which can be characterized in term of linear and non-linear mechanical properties. Some preliminary tests have been already performed on crosslinked samples performed SB_NF polymer (not presented). Since the cross-linked nanocomposites are mainly used in car tire manufacturing, a deeper interpretation of these results and the comparison with the same system formulated with SB_F could highlight interesting properties of these materials.

Moreover, in the framework of the postdoctoral fellowship of A. Philippe (Laboratoire Charles Coulomb), the simplified industrial nanocomposites will be investigated by dynamic light scattering (DLS) techniques. This approach allows to follow the dynamics of the nanocomposite system under deformation, probing the local motion of the filler particles (e.g., thermal energy, rearrangements under strain) and identifying the extent of the filler reorganization resulting from an applied strain.

Regarding the model nanocomposite system, the SAXS-RMC approach proposed in Chapter 4 can be used to investigate the impact of the grafting density on the aggregate mass distribution, i.e. use of silanes with different hydrophobicity at a grafting densities lower and higher than the one investigated (1 molecule/nm^2). Some preliminary measurements have been already performed and they are reported in appendix A5. This study could be particular useful to better understand why the octadecyl-triethoxysilane C_{18} induces the formation of bigger aggregates.

Moreover, the effect of the variation of the silane functions can be also investigate in the case of coating agents with a longer alkyl chains, i.e. C_{18}- series. Such investigation could help to clearly reveal the role that the hydrophobicity and the silane function have in the NPs dispersion. Also in this case, some preliminary measurements have been performed, as reported in appendix A5.

Alternatively, it would be also interesting to investigate the reorganization of nanoparticles in dense assemblies or nanocomposites, like aging phenomena, under shear stress or at high temperature. For instance, this might open the road to detailed studies of the Payne effect (see section 1.3.3), where mechanical response of a nanocomposite system is found to evolve in a non-linear way, presumably due to particle reorganizations inducing changes in aggregate mass distribution.

A challenging extension of the mapping of the dynamical properties of both model and simplified industrial nanocomposites could be performed by Quasi-elastic Neutron Scattering (QENS), like Neutron Spin Echo spectroscopy (NSE), which is ordinarily used to probe coherent scattering. These rather sophisticated techniques are rarely used to investigate polymer-based nanocomposites. While QENS usually requires the use of deuterated polymer chains, we plan to use NSE to follow the self-correlation functions of the matrix polymer directly in time (i.e., up to 100 – 200 ns). In particular, we want to access the hydrogen self-correlation (i.e., incoherent NSE) on the protonated polymer-silica nanocomposites. Some incoherent NSE experiments have been scheduled in a next beam-time session at the Institut Laue-Langevin (ILL, line IN15, highlight proposal in the soft matter section).

7. Appendices

7. Appendices

7.1. Appendix 1: Characterization of styrene-butadiene polymer

Styrene-butadiene composition: In order to determine the exact percentage of styrene and butadiene (SB_NF and SB_F) a ^{1}H NMR spectrum has been recorded on a Bruker AVANCE Spectrometer-400MHz at the Laboratoire de Measures Physiques (UM2 -Plateau technique Max Mousseron). Chloroform D ($CDCl_3$) has been used as solvent to polymer dissolution and 1, 1, 2, 2, tetrachloroethane (from Fluka) has been chosen as tracer. In Figure A1.1, ^{1}H spectrum for the pure non-functionalized SB is shown.

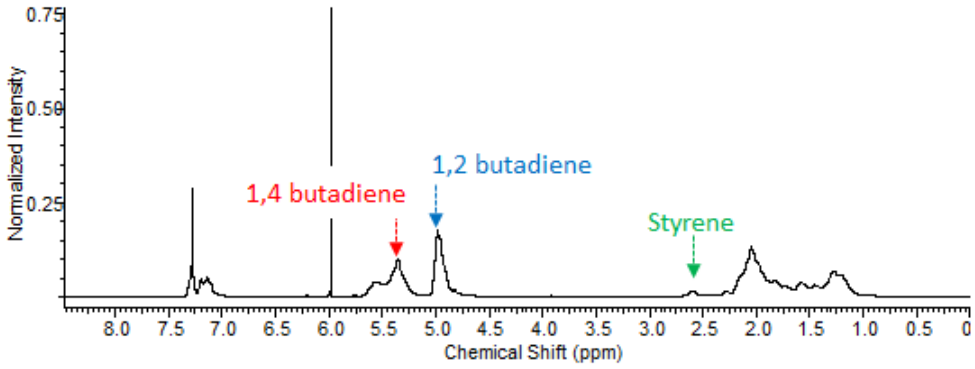

Figure A1.1 ^{1}H NMR spectrum recorded for non-functionalized SB.

Chemical shifts related to styrene and butadiene hydrogens have been identified using reference (Khoee and Sorkhi 2007). Peak integration allowed to verify that each polymer chain for both polymer is a statistical copolymer of styrene and butadiene (with 1, 2 and 1, 4 butadiene units). In particular mass fractions for both polymers are indicated below:

- SB_NF: 19.1%w of Styrene units and 80.9%w Butadiene units (where 42.6%w of which are 1, 4 units and 57.4%w are 1, 2units).
- SB_F: 20.4%w of Styrene units and 79.6%w of Butadiene units (where 43.3%w of which are 1, 4 units and 56.7%w are 1, 2 units).

Molecular weight and polydispersity: Molecular weight M_w and polydispersity index I_p of SB_NF and SB_F styrene-butadiene polymers have been determined by gel permeation chromatography (PL-GPC 50 Plus, Polymer Laboratories), using Tetrahydrofuran (THF) as eluent.

Density: Densities of SB_NF and SB_F styrene-butadiene polymers have been measured by a density kit for solids (Mettler-Toledo) set on a precision balance. The mass of a sample of each SB has been measured in dry conditions. Then, the test has been repeated after the immersion of the same sample in a solvent. In this case, ethanol has been used as solvent. Densities of unknown polymers have been calculated by an empirical formula [A1.1].

$$\rho_{SB} = \frac{A}{P}\rho_{EtOH} \qquad [A1.1]$$

Where ρ_{EthOH} is ethanol density, A and P are sample mass measured in dry and wet conditions.

Glass transition temperature: Temperature modulated differential scanning calorimetry (TMDSC) has been performed in order to evaluate glass transition temperatures T_g of both the SBs. To this end, the reverse heat capacity curve (modulated ramp at 3 K/min, ±0.5°C, 60s, under nitrogen) has been considered**.**

Refractive index: The measurement of refractive index (n) has been performed by an Abbe refractometer (Carl Zeiss). Methyl-ethylketone has been used as solvent in order to prepare solutions at different polymer volume concentrations. Then, the refractive index of both polymer has been deduced by a linear fitting of experimental data, as shown in figure A1.3.

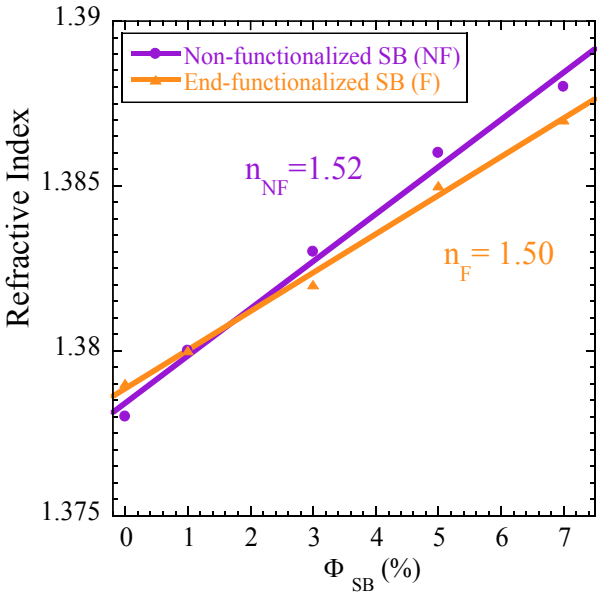

Figure A1.2 Refractive index values for SB_NF and SB_F styrene-butadiene, obtained from linear fitting of experimental data.

End-functionalization of polymer chains: Attenuated total reflectance analysis (ATR – Laboratoire Charles Coulomb, UM2) has been performed on samples of both SB in order to shed light on the end-functionalization of polymer chains. Acquired ATR spectra are shown in figure A1.3. In Table A1.1, wavenumber references used for peaks identification are indicated (Colthup et al. 1990).

Functional Group	Peak [cm^{-1}]	Notes
$Si-OH$	3670	Stretching vibration – OH
$Si-O-Si$	1050-1075	Asymmetric $Si-O-Si$ vibrations
$Si-CH_3$	1380-1450	CH_3 asymmetric stretch
$Si-CH_3$	1230-1380	CH_3 symmetric stretch

Figure A1.1 Wavenumber reference values used for peaks identification in ATR spectra.

In particular, only the SB_F is characterized by an absorbance peak around 3760cm^{-1}, as shown in the inset of fig. A1.3, which is typical of Si-OH vibrations and thus highlighting the signature of the hexa-methylcyclotrisiloxane (HMCTS or $SiMe_2$-OH) functionalization group of these polymer chains.

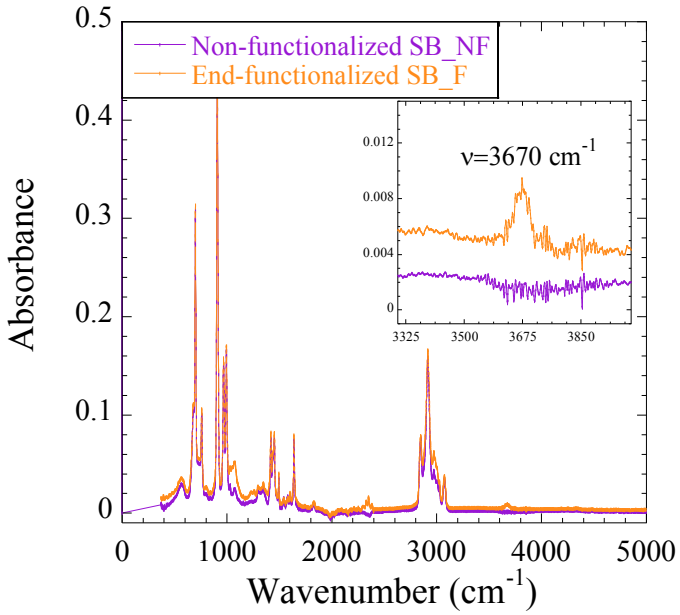

Figure A1.3 ATR spectra recorded for non-functionalized and end-functionalized SB. Inset: only the SB_F polymer shows an absorbance peak around 3670 cm-1, which is typical of Si-OH vibrations.

7.2. Appendix 2: Thermo-mechanical history of uncrosslinked simplified nanocomposites

In order to evaluate the impact of each key parameter variation on torque and temperature during the mixing process, torque/temperature curves as a function of time are reported in this appendix.

As a general conclusion, the variation of polymer matrix composition, coating agent, amount of coating agent or catalyzer/coating agent different combination seem not to impact of the thermo-mechanical history of simplified industrial NCs.

Variation of polymer matrix composition

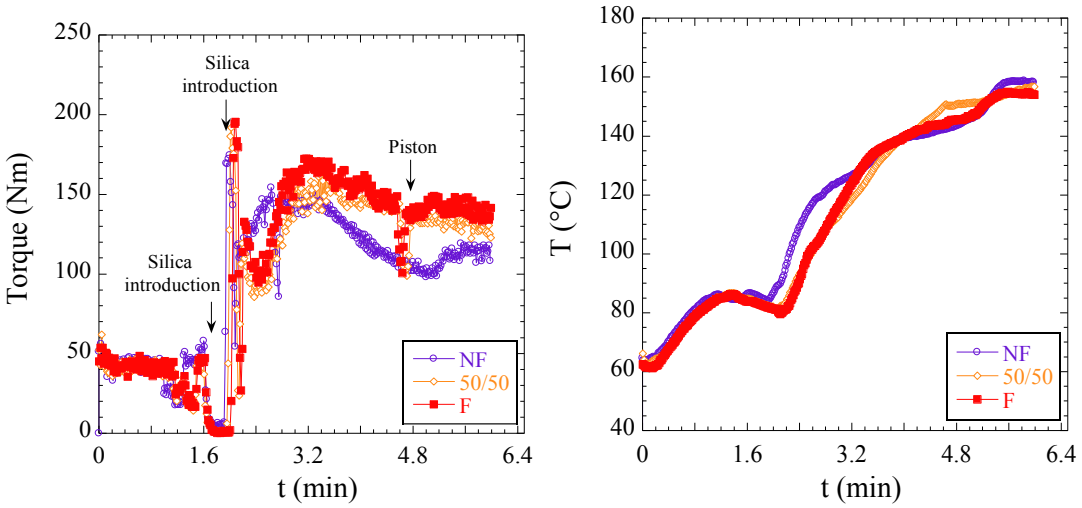

Figure A2.1: Thermomechanical history of simplified industrial PNCs formulated at Φ_{Si} =18%v, using C_8 as coating agent (with DPG) and varying the composition of the polymer matrix (SB_NF, SB_F and 50/50 mixture).

Variation of coating agent

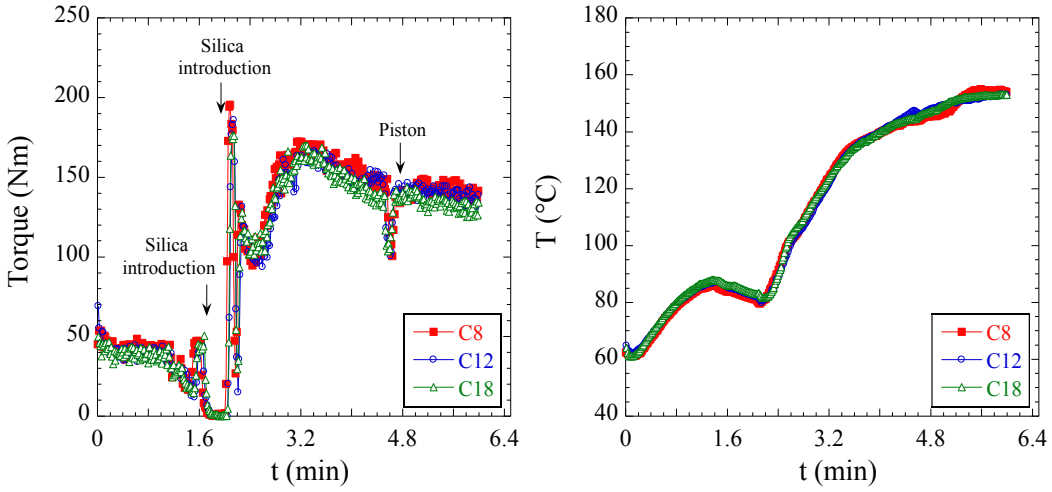

Figure A2.2: Thermomechanical history of simplified industrial PNCs formulated at Φ_{Si} =18%v, using a fully functionalized polymer matrix (F) and C_8 C_{12} C_{18} as coating agent (with DPG).

Variation of coating agent amount

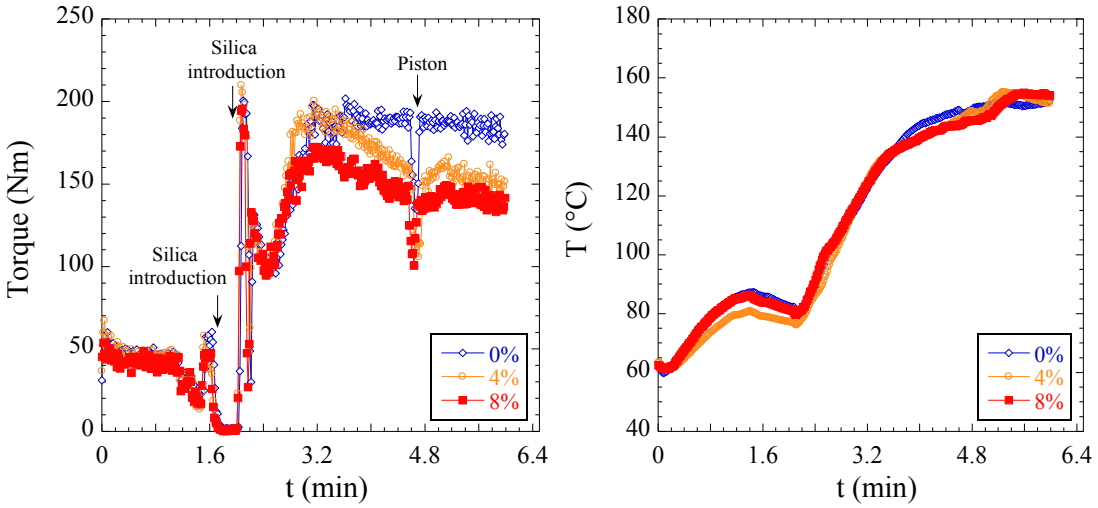

Figure A2.3: Thermomechanical history of simplified industrial PNCs formulated at Φ_{Si} =18%v, using a fully functionalized polymer matrix (SB_F) and varying the amount of C8 from 0%w to 8%w with respect to silica (with DPG).

DPG/Coating agent variation

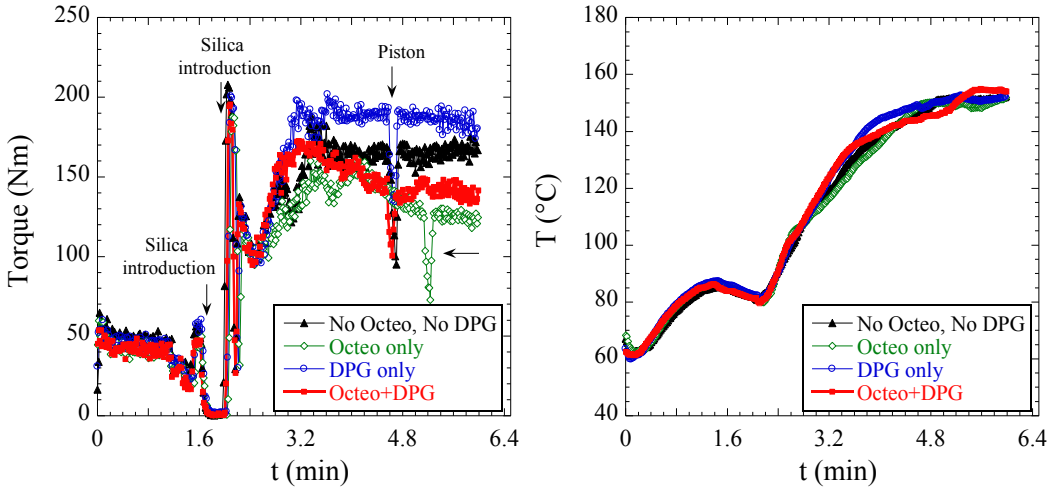

Figure A2.4: Thermomechanical history of simplified industrial PNCs formulated at Φ_{Si} =18%v, using a fully functionalized polymer matrix (SB_F). Different combination of DPG/C_8 have been used.

7.3. Appendix 3: Crosslinked simplified industrial nanocomposites

Vulcanization and crosslinking of the samples

The preparation of the uncrosslinked simplified industrial nanocomposite has been reported in Chapter 2. Once the samples have been passed through the hot cylinders (i.e., external mixer) to optimize the dispersion of the filler particles, some curing agents (or cross-linkers) can be added to promote the vulcanization process and to obtain a crosslinked nanocomposite. According to the procedure developed by Solvay Silica, sulfur and CBS80 (provided by Solvay) have been added as the 1.5%w with respect to the polymer mass. These two products have been incorporated in the silica/polymer nanocomposite using the external mixer (i.e., 20 passages between cylinders at T=50°C, 2 mm of distance).

In order to obtain the crosslinking of the nanocomposites, the *vulcanization time* (i.e., the time necessary to crosslink the 98% of the sample) has been determined using a Monsanto R100s Rheometer. For all the samples, this time has been estimated around 45 min. Thus, the simplified industrial nanocomposites with the incorporated Sulfur and CBS80 have been put at 160°C and P=280bar (45 min). The entire procedure described above is synthetized in Fig. A3.1.

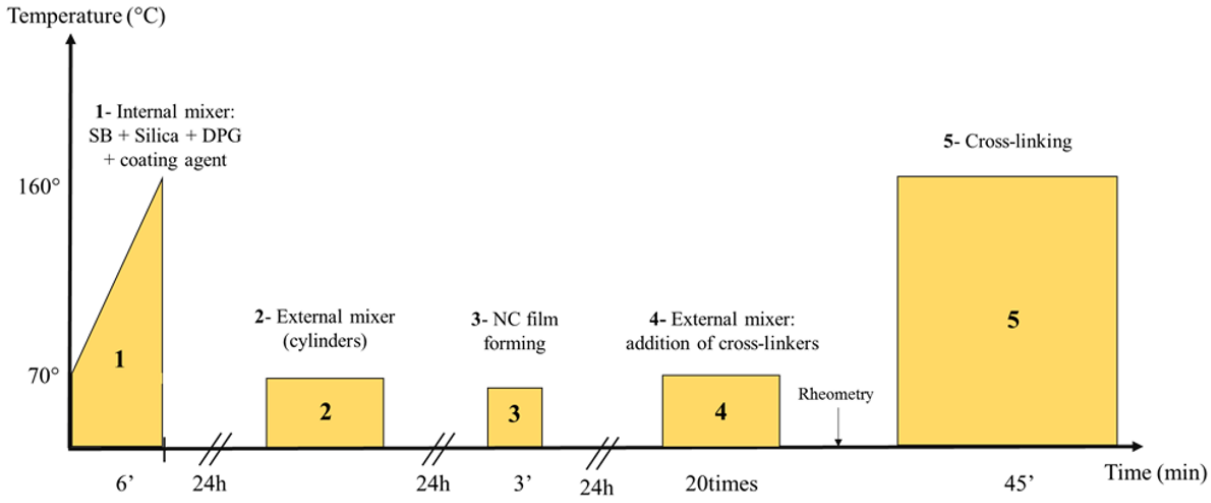

Figure A3.1 Temperature profile as a function of time of the formulation steps of crosslined simplified nanocomposites. Steps 1-2-3 summarize the preparation of the uncrosslinked simplified PNCs. Then, the curing agents Sulfur and CBS80 are incorporated in the sample using the external mixer (4). The vulcanisation time has been determined by rheometry (5) and the final crosslinking is performed at 160°C, P=280bar for 45 min.

7.4. Appendix 4: Model nanocomposite system: optimization of the surface-modification of silica nanoparticles in suspension and tuning of the silane grafting density

A TGA analysis has been performed on powders of silica NPs surface-modified by C_8 at different pH values to optimize the grafting of silane molecules on silica particle surface,

As shown in Fig. A4.1a, a basic pH resulted more efficient than an acid one. This proves that the particle surface charges play a main role for the silane grafting. A slight increasing of weight loss can be observed with the increase of the pH from 8 to 10. Unfortunately, at pH=10 the silica suspension starts gelling and for this reason the pH has been fixed around 9. Moreover, the kinetic of the grafting reaction has been studied, performing TGA tests on powders of silica NPs surface-modified by C_8 obtained collecting hydro-alcoholic suspension at different reaction time. As shown in Fig. A4.1b, after 24h at 50°C there is no detectable variation of weight loss.

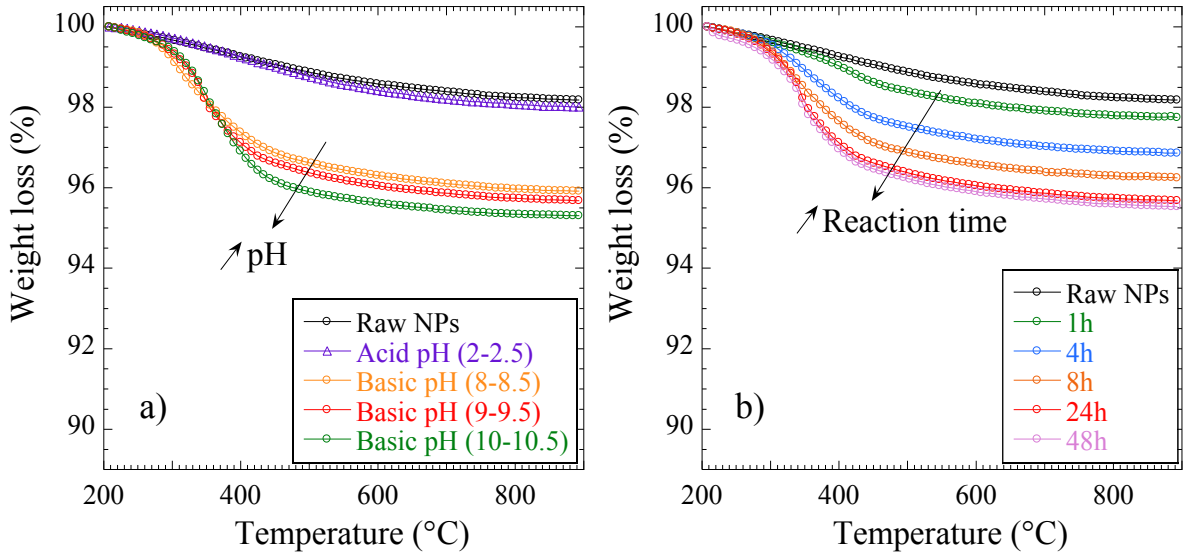

Figure A4.1 Weight-loss curves between 200°C and 900°C for raw silica NPs and for NPs surface-modified with C_8 at (a) different pH, and, (b) at different reaction times.

Evaluation on grafting density for surface-modified silica NPs

To determine the amount of reacted coating agent and thus ρ, it has been assumed that:

i) Just two of three lateral groups O-CH_2-CH_3 of silane molecule are hydrolyzed, as shown in Fig. A4.2a and A4.2b (consistent with ATR spectra shown in Chapter 4).

ii) In TGA curves, the relative weight loss with respect to raw NPs has been evaluated between 220°C to 550° to eliminate the weight loss contributions of water physically absorbed on filler surface (<200°C) and silanol group condensation (>550°C), see Chapter 4.

iii) Because of increasing temperature (TGA temperature ramp), the alkyl chain and the unreacted lateral group of silane molecules are degraded and replaced by an -OH group, as shown in Fig. A4.2c.

The complete calculations are here developed for NPs surface-modified by C_8 ($M_{silane\ C8}$=276 g/mol).

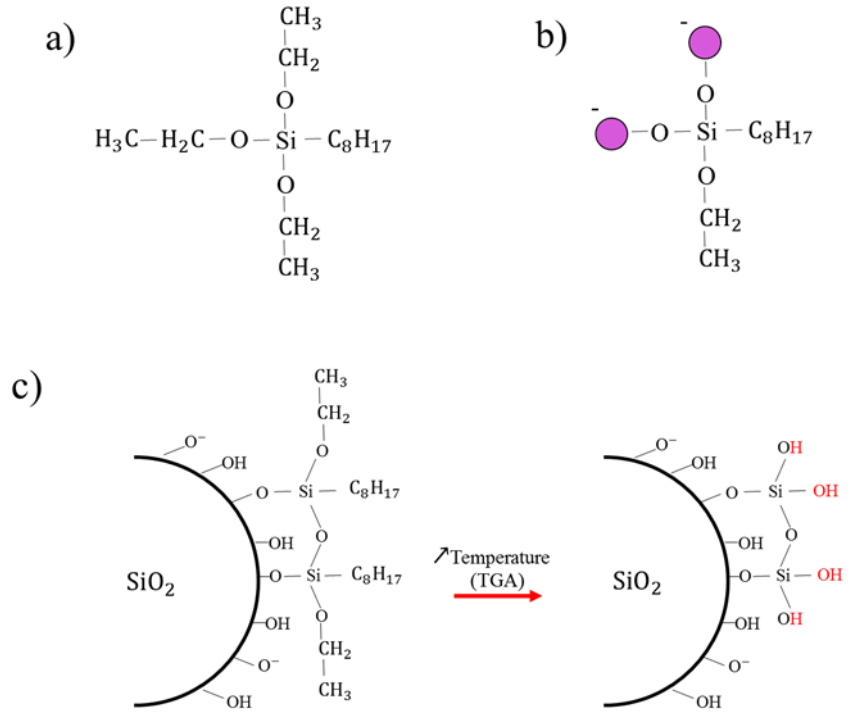

Figure A4.2 The C_8 molecule (a) can be hydrolyzed losing two of its three lateral groups (b). Then, the hydrolyzed silane molecule can react on silica particle surface (c). Finally, because of temperature increasing during TGA analysis, the alkyl chain and the residual lateral group are degraded and replaced by an –OH group

To determine the amount of reacted silane coating agent, and thus the grafting density, an equivalent molecular weight ΔM has been estimated considering the groups of the silane molecule which participate in the hydrolysis (Fig. A4.2b) and the TGA degradation (Fig. A4.2c).

$$\Delta M = M_{C8H17} + M_{CH2\text{-}CH3} - M_{OH} - 2\ M_H = (113 + 29 - 17 - 1)\ g/mol = 124\ g/mol$$

where M_{C8H17} is the molecular weight of the C_8 alkyl chain, $M_{CH2\text{-}CH3}$ is the molecular weight of lateral group of silane molecule; M_{OH} corresponds to the molecular weight of the –OH group which appears after the degradation of the alkyl chain and M_H is the molecular weight of the hydrogen that appears when the unreacted lateral group is burned during TGA measurements (Fig.A4.2c).

Then, considering 100g of surface-modified silica NPs, the relative weight loss with respect to bare NPs corresponds to mass of silane molecule which have been degraded because of temperature increasing ($mass_{loss}$). Thus, the moles of reacted coating agent (m) can be determined as

$$m = mass_{loss}/\Delta M \qquad [A4.1]$$

and the corresponding mass ($mass_{reacted\ C8}$) can be calculated as

$$\text{mass}_{\text{reacted C8}} = m\, M_{\text{silane C8}} \quad [A4.2]$$

This quantity can be normalized to the global amount of added coating agent to obtain the percentage of reacted agent. Knowing the average radius of silica NPs (R_{Si}=12.5 nm, see SAXS measurements), the grafting density ρ can be evaluated.

For completeness, we report the grafting densities for silica NPs surface-modified by C_8 C_{12} or C_{18} calculated considering the hydrolysis of one, two or three reactive groups (Table A4.1). The variation of the grafting densities would be approximately 0.15 nm^{-2} lower if only one or three lateral groups were assumed to have reacted.

Case a) : hydrolysis of 3 lateral groups

Coating agent	%w reacted coating agent	Grafting density (molecules per nm^2)	Monolayer thickness(nm)
C_8	82.7%	1.4	0.72
C_{12}	85.2%	1.4	0.89
C_{18}	71.8%	1.2	0.97

Case b) : hydrolysis of 2 lateral groups

Coating agent	%w reacted coating agent	Grafting density (molecules per nm^2)	Monolayer thickness(nm)
C_8	64.0%	1.1	0.55
C_{12}	72.2%	1.2	0.75
C_{18}	63.1%	1.1	0.84

Case c) : hydrolysis of 1 lateral groups

Coating agent	%w reacted coating agent	Grafting density (molecules per nm^2)	Monolayer thickness(nm)
C_8	51.6%	0.9	0.45
C_{12}	62.5%	1.0	0.64
C_{18}	57.1%	1.0	0.76

Table A4.1 Amount of reacted silane, grafting densities and equivalent monolayer thickness for different silane coating agents, assuming the hydrolysis of three (a), two (b) or one (c) lateral groups of the silane molecules.

Grafting density as a function of amount of coating agent

During the grafting reaction, the amount of coating agent can be varied to tune the dispersion of silica NPs in suspension and then in polymer matrix. In particular, C_8 has been added in water/ethanol mixture as 4%w, 8%w or 12%w with respect to filler content. For each of this C_8 content, C_{12} and C_{18} have been used in isomolar quantities (i.e., for samples prepared using C_8 as 4%w with respect to filler fraction, C_{12} and C_{18} are added in isomolar amounts).

The corresponding powder samples of surface-modified silica have been analyzed by TGA (see protocol details in section 2.3) to perform a quantitative evaluation of grafting reaction.

In Fig. A4.3a, the weight loss between 200°C and 550°C has been considered for samples prepared using C_8 at 4%w, 8%w or 12%w with respect to filler content. In the Fig. A4.3b and A4.3c, the weight loss in the same temperature range has been shown for silica particles surface-modified by C_{12} and C_{18}.

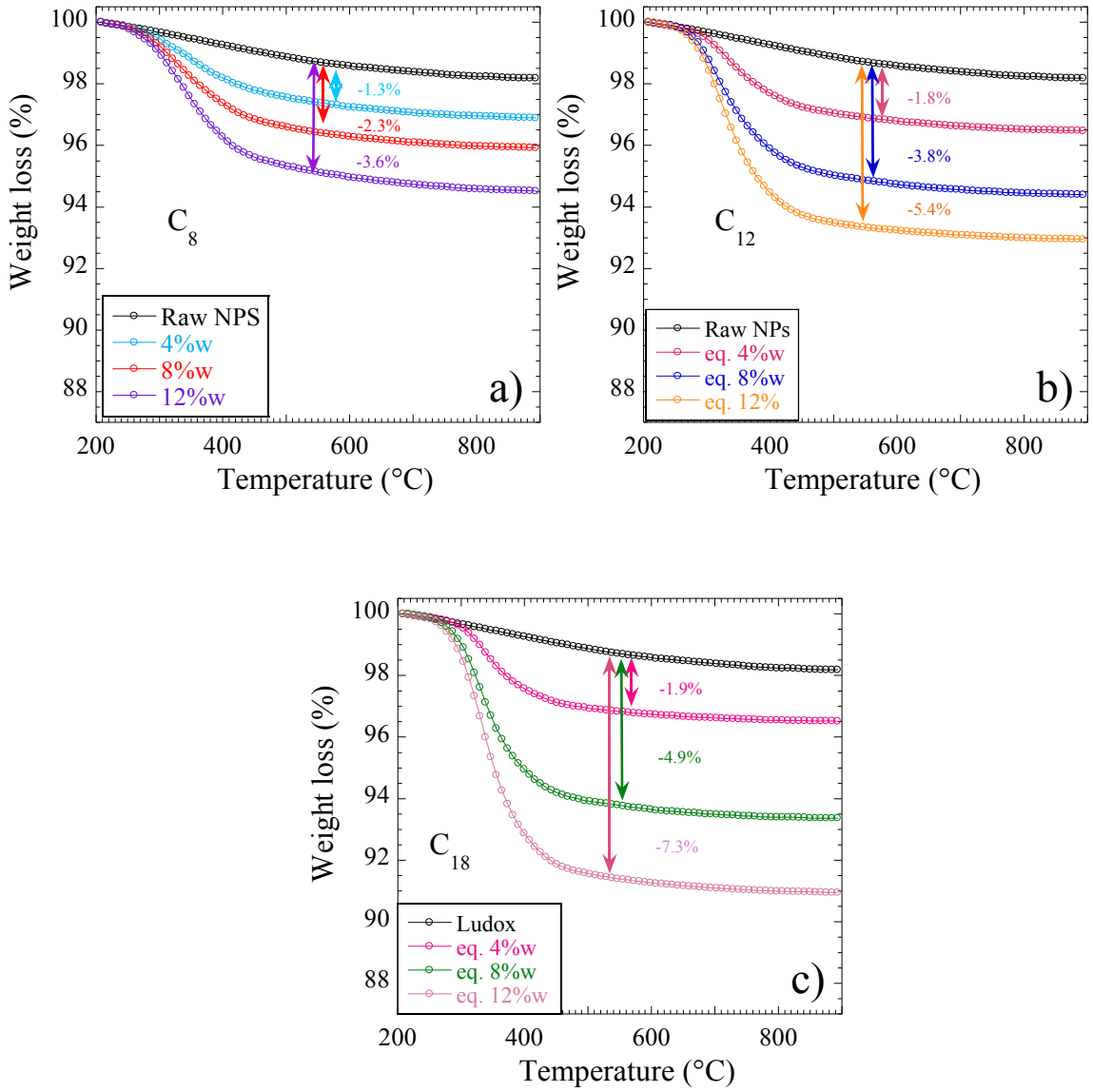

Figure A4.3 Weight loss between 200°C and 550°C has been considered for samples prepared using C_8 at 4%w, 8%w or 12%w with respect to filler content. The weight loss in the same temperature range have been evaluated also for silica particles surface-modified by C_{12} (b) and C_{18} (c).

Using the already mentioned method, the amount of reacted coating agent and the grafting density ρ have been estimated considering the hydrolysis of just two groups for each silane molecule. The outcomes are summarized in Table A4.2.

	C_8			C_{12}			C_{18}		
Sample name	**4%w**	**8%w**	**12%w**	**eq. 4%w**	**eq. 8%w**	**eq. 12%w**	**eq. 4%w**	**eq. 8%w**	**eq. 12%w**
%w reacted Silane	72.3%	64.0%	66.7%	69.0%	72.2%	69.1%	42.2%	63.1%	60.2%
Grafting density ρ	0.6	1.1	1.7	0.6	1.2	1.8	0.4	1.1	1.6
Monolayer Thickenss (nm)	0.3	0.6	0.9	0.4	0.8	1.1	0.3	0.8	1.3

Table A4.2 Amount of reacted silane, grafting densities and equivalent monolayer thickness for different amounts of added coating agent (i.e., different silane/Silica ratios).

As shown in Figure A4.4, the grafting density increases with the increase of coating agent content. Moreover, ρ results constant with the increase of the length of silane alkyl chain (from C_8, to C_{18}) for silica NPs surface-modified at 4%w and 8%w (isomolar). At 12%w (isomolar), the grafting density slightly increases with the increase of the molecular weight of coating agents. In fact, the different solubility of C_8, C_{12} and C_{18} in water/ethanol mixture can probably influence the silane hydrolysis and then their reaction on filler surface. Moreover, at this concentration some silane molecules could react between them and then on particle surface. This can affect the degradation of grafted molecules during the TGA measurements. In Fig. A4.5, for each coating agent, grafting density as shown as a function of the amount of silane expressed as silane/Silica ratio. The increase of this ratio determines an increase of the grafting density for all the three coating agents.

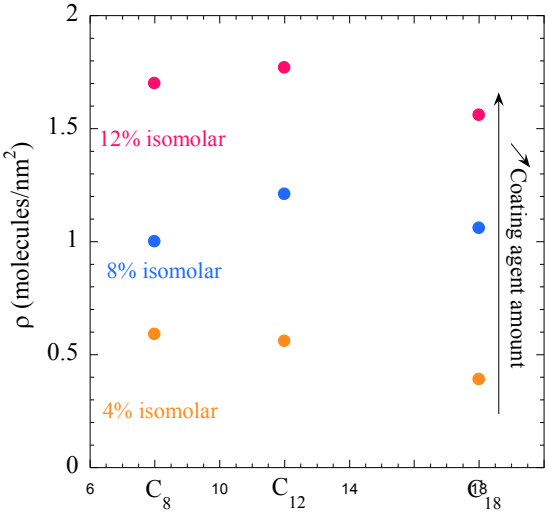

Figure A4.4 Grafting density ρ as a function of coating agents (length of alkyl chain). ρ recults constant for silica NPs surface-modified at 4%w and 8%w (isomolar) with the increase of the length of silane alkyl chain.

The grafting density at 12%w (isomolar) probably depends on solubility of each coating agent in water/ethanol mixture during the grafting reaction.

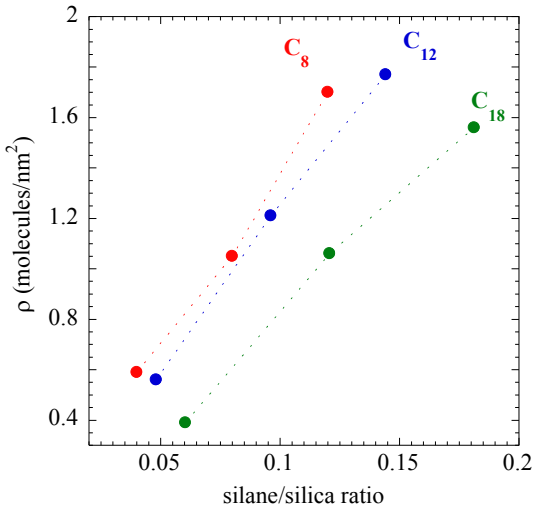

Figure A4.5 Grafting density (ρ) as a function of silica-silane ratio. The increase of this ratio determines an increase of the grafting density for all the three coating agent.

Grafting density as a function of the silane function

The surface-modification can be performed using coating agents with different silane functions, such as trimethoxy(octyl)silane (C_{8m}) and methoxy(dimethyl)octylsilane (C_{8mm}).

The grafting reaction has been performed according to the protocol described in the section 2.3 and the silanes are added in isomolar amounts with respect of C_8 (i.e., 8%w with respect to silica). The grafting density has been estimated by TGA analysis (Fig. A4.6) assuming the hydrolysis of two lateral groups for the C_{8m}; for the C_{8mm}, the hydrolysis of the only reactive group has been considered. The grafting densities for C_{8m} and C_{8m} are reported in Table A4.3 and compared to the result obtain for the C_8 coating agent.

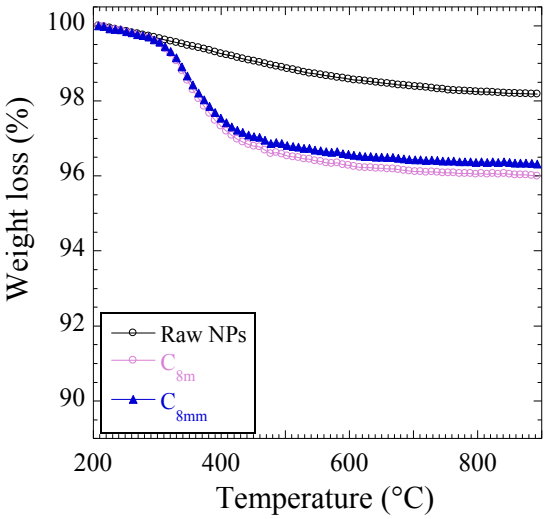

Figure A4.6 Weight loss between 200°C and 550°C has been considered for samples prepared using C_{8m} and C_{8mm}. Silane coating agents are added in isomolar amounts with respect of C_8 agent.

Coating agent	%w reacted coating agent	Grafting density (molecules per nm^2)	Monolayer thickness(nm)
C_8	64.0%	1.1	0.55
C_{8m}	72.3%	1.2	0.51
C_{8mm}	77.3%	1.3	0.53

Table A4.3 Amount of reacted silane, grafting densities and equivalent monolayer thickness for different silanes, C_8, C_{8m} and C_{8mm}

7.5. Appendix 5.1: Impact of silane function on surface-modified silica NP dispersion in precursor solvents and polymer matrix: the C_{18}-case

To shed light on the dispersion in different media of NPs surface-modified by silane with different silane functions, the grafting has been performed using different C_{18} silanes: octadecyl-triethoxysilane C_{18} (from Alfa Aesar, M_w =417 g/mol), octadecyl-trimethoxysilane C_{18m} (from Sigma-Aldrich, M_w =375 g/mol), and octadecyl-methoxy(dimethyl) silane C_{18mm} (from Sigma-Aldrich, M_w =343 g/mol), i.e., complementary study with respect to the C_8, C_{8m} and C_{8mm} case reported in Chapter 4. The characteristics of these coating agents are summarized in Table A5.1 and their structural formula are reported in Fig. A5.1.

Coating agent	Code	Linear formula	M_w (g/mol)	d (g/ml)	n (refractive ind.)
n-Octadecyltriethoxysilane	C_{18}	$C_{24}H_{52}O_3Si$	416.7	0.89 (at 25°C)	1.44
Trimethoxyoctadecylsilane	C_{18m}	$C_{21}H_{46}O_3Si$	374.7	0.88 (at 25°C)	1.44
Methoxydimethyloctadecylsilane	C_{18mm}	$C_{21}H_{46}O\,Si$	342.7	0.83 (at 25°C)	1.44

Table A5.1 Chemical properties of silane coating agents.

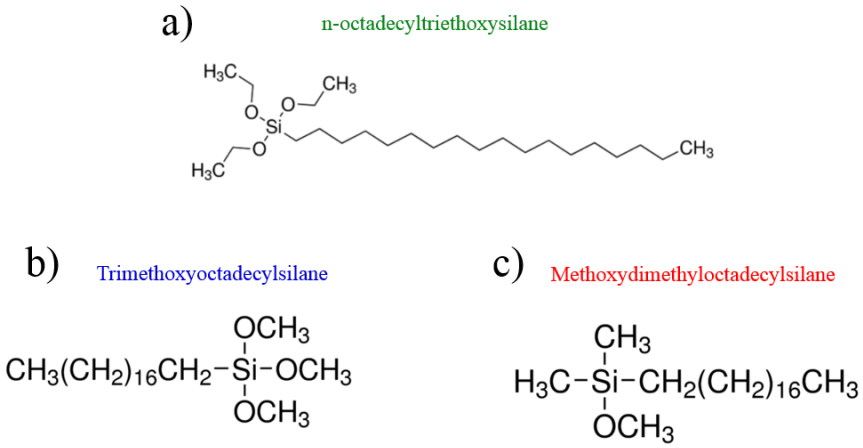

Figure A5.1 Structural formula of coating agents indicated in Table A5.1.

The grafting reaction has been performed according to the protocol described in the section 2.3. The grafting density has been estimated by TGA analysis (Fig. A5.4) assuming the hydrolysis of two lateral groups for the C_{18}- and C_{18m}; for the C_{18mm}, the hydrolysis of the only reactive group has been considered and the outcome is reported in Table A5.2. Also in this case, a structural characterization has been performed for the surface-modified NPs in precursor solvents and then in the finite nanocomposite.

Coating agent	%w Reacted coating agent	ρ (molecules.nm^{-2})	Monolayer thickness (nm)
C_{18}	63.1%	1.1	0.84
C_{18m}	63.1%	1.1	0.75
C_{18mm}	75.1%	1.3	0.88

Table A5.2 Grafting density for silane coating agents reported in Table A1 and determined by thermogravimetric analysis (TGA).

Hydroalcoholic suspensions: Fig. A5.2 shows the SAXS curves for silica NPs surface-modified by C_{18}, C_{18m}, and C_{18mm} suspended in the initial hydroalcoholic mixture where the grafting reaction took place (see section 2.3). The low-q scattering intensities seem to indicate that the standard octadecyltriethoxysilane (C_{18}) and the (C_{18m}) form bigger aggregates. The C_{18mm} sample shows a lower scattering intensity, and thus lower average aggregation. The evolution of the scattering curves of these samples is similar to the one observed for silica NPs suspended in ethanol/water mixture when surface-modified by C_8, C_{8m} or C_{8mm} (Fig. 4.10a), where the lowest intensity is observed for the C_{8mm} sample.

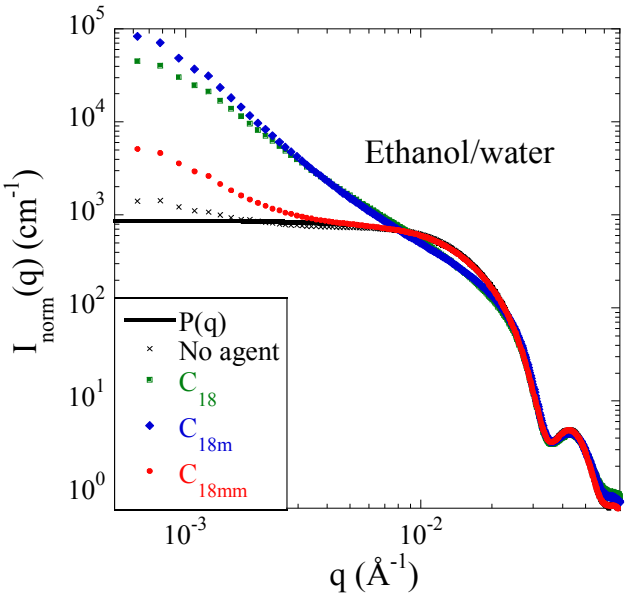

Figure A5.2 SAXS scattered intensities normed to NP form factor in water (continuous line, R_0 = 12.5 nm, 12%) of bare and surface-modified NPs (C_{18}, C_{18m}, C_{18mm}) suspended in in hydro-alcoholic medium (63%v ethanol, Φ_{Si} = 1%v).

MEK suspensions: Also in this case, changing the solvent by a dialysis procedure was expected to strongly impact on the dispersion of the surface-modified NPs (i.e., solvent polarity and solubility of the alkyl chains). The scattering curves for MEK suspensions are reported in Fig. A5.3. In this solvent, the variation of the C_{18}- silanes seems to have a strong impact on the NP dispersion, as compared to the C_8-silanes (Fig. 4.8a). Moreover, the order of the curves in this solvent is similar to the one found in the hydro-alcoholic suspension: the C_{18mm} seems to promote the best dispersion, showing a well-defined

repulsive peak at the intermediate q-range; the C_{18} and the C_{18m} show very close intensity values where no structural peaks are detected.

These results can be compared to the analogous C_8- surface modified NPs. In Fig. 4.11a, it has been showed that the best dispersion is reached when the NPs are surface-modified by triethoxyoctylsilane C_8, while among the C_{18}- agents, the best quality of the dispersion is ensured by the C_{18mm} grafting. This result could suggest that when the silane molecule is characterized by the shortest alkyl chain, the best dispersion is reached with a triethoxy- silane. On the other hand, for the agent with the longest alkyl chain the best dispersion is obtained using a mono-functionalized silane. Such an evidence indicates that the dispersion state of surface-modification can be tuned considering both the hydrophobicity and silane function of the coating agents. On the other hand, more experiments might be necessary to check the reproducibility of this effect. It can be concluded, however, that all NPs are quite well dispersed in MEK, and possibly C_{18mm}-modified NPs exceptionally well.

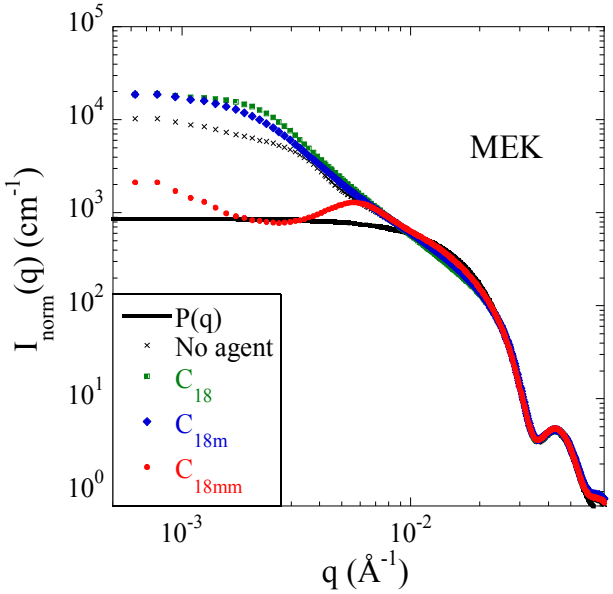

Figure A5.3 SAXS scattered intensities normed to NP form factor in water (R_0 = 12.5 nm, 12%) of bare and surface-modified NPs (C_{18}, C_{18m}, C_{18mm}) in MEK (Φ_{Si} = 1%v).

In nanocomposites: The final nanocomposites have been obtained by the mixing of NPs in MEK suspension with the polymer dissolved in the same solvent and subsequent solvent evaporation. Also in this case, the aim is to understand if the structural characteristics of the NPs in MEK suspensions predetermines the NP dispersion in the polymer matrix. If one compares the results for NCs, Fig. A5.4, to the one for MEK suspensions, Fig. A5.3, it can be observed that the overall intensities remain similar: the highest intensity values have been obtained for the C_{18} and C_{18m} silane, while the C_{18mm} allows to obtain a better dispersion (i.e., lower intensity and structural "shoulder" (i.e., Guiner-like behavior) possibly reminiscent of the peak observed in Fig. A5.3. This result confirms that the particle dispersion is transferred (at least partially) from the MEK suspension to the nanocomposite, as already observed in the case of the C_8- silanes.

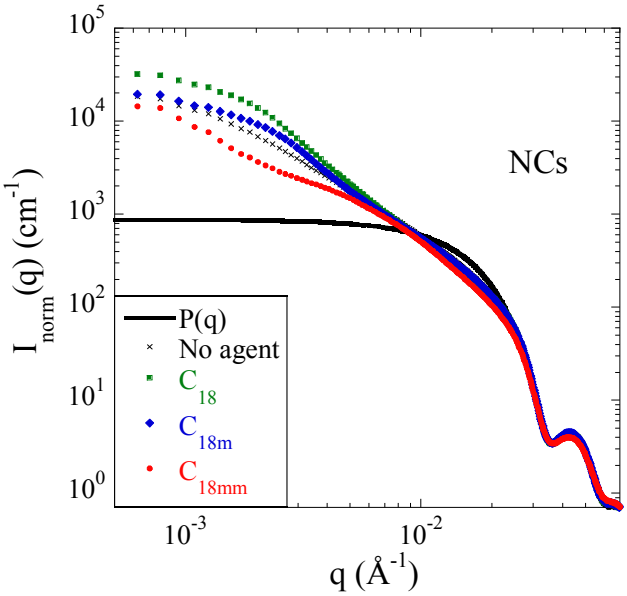

Figure A5.4 SAXS scattered intensities normed to NP form factor in water (continuous line, R_0 = 12.5 nm, 12%) of bare and surface-modified NPs (C_{18}, C_{18m}, C_{18mm}) in NCs. Silica volume fractions: for bare NPs, Φ_{Si} = 2.6%v; for C_{18}, Φ_{Si} = 1.4%v; for C_{18m}, Φ_{Si} = 3.2%v; for C_{18mm}, Φ_{Si} = 2.5%v.

The parameters characterizing the width of the mass distribution functions $<N_{agg}{}^2>/<N_{agg}>$ have been extracted from the data in Fig. A5.2, A5.3, A5.4 and they have been plotted for the three suspension media in Fig. A5.5. It can be observed that in the ethanol-water mixture, C_{18m}-surface modification forms the biggest aggregates. In MEK, all aggregates are rather small, with C_{18} favoring aggregation. In polymer nanocomposites, finally, C_{18m} induces the worst dispersion and C_{18mm} the best.

Concerning a possible transfer of the quality of the dispersion from MEK into the polymer nanocomposites, it is true that the order of the width of the mass distributions seems to be quite well conserved from MEK to the NCs.

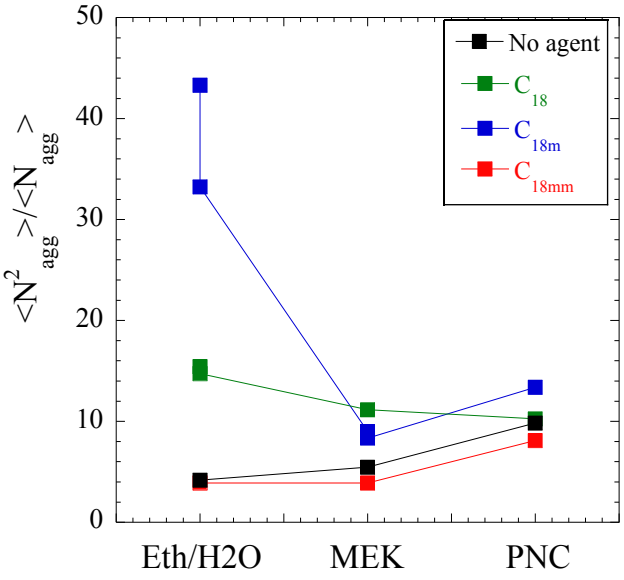

Figure A5.5 The width-parameter $<N_{agg}^2>/<N_{agg}>$ of the mass distribution functions for NPs surface modifies with C_{18}- agents with different silane functions and dispersed in the three suspension media (hydro alcoholic mixture, MEK, and in polymer).

Finally, the dispersion state of silica nanoparticles which are surface-modified C_{18}, C_{18m} or C_{18mm} in different suspending media (i.e., ethanol/water mixture, MEK and styrene-butadiene polymer) can be compared to the ones related to the NPs grafted by C_8, C_{8m} or C_{8mm} (see Fig. 4.14). In ethanol/water mixture, the mono-functionalized silanes (C_{8mm} and C_{18mm}) induce the lowest aggregation, comparable to the one of the bare nanoparticles. This could be linked to the fact that these molecules can only graft the silica surface and there are no other lateral groups that can react with neighboring molecules, as well as the conservation of surface silanols. On the other hand, the worst dispersion is obtained using C_8 and C_{18m}. In MEK, the aggregates are rather small for both C_8- and C_{18}- agents. A more detailed observation of the data reveals that the C_{18mm} induced a dispersion comparable to the one obtained using the C_8 silane. Concerning the dispersion in the polymer nanocomposites, it can be detected that the C_8 evidently promotes a better dispersion if compared to C_{8m} and C_{8mm} and the quality of the dispersion is well transferred from the correspondent MEK suspensions. Also for the C_{18}- agents the NP dispersion state seems to be transferred from the MEK suspensions to the nanocomposites, even if a small inversion between C_{18} and C_{18m} has been recorded. On the other hand, the values of the $<N_{agg}^2>/<N_{agg}>$ parameters for C_{18}, C_{18m} and C_{18mm} are similar than the one obtained for C_8, C_{8m} and C_{8mm} (Fig. 4.14) whereas the C_{8mm} clearly induces stronger aggregation. In other words, all aggregates seem to be approximately of comparable mass in MEK, and this is transferred into NCs with the notable exception of C_{8mm} favoring big aggregates.

A5.2 Impact of grafting density on surface-modified silica NPs dispersion in precursor solvents and polymer matrix

The amount of silane coating agent with different hydrophobicity (C_8, C_{12} and C_{18}) has been varied in order to modify the grafting density during the reaction of surface-modification. The characteristics of these coating agents are reported in section 2.1. The real grafting densities have been estimated by TGA and they are reported in appendix A4.

The variation of the silane grafting density is obtained through a variation of the silane/Silica ratio. In particular, the silane coating agent C_8 has been added at 4%w, 8%w or 12%w with respect to the silica mass. Then, the quantity of C_{12} and C_{18} to add has been fixed in order to obtain the same grafting density on filler surface as the C_8 analog (i.e., C_{12} or C_{18} added in isomolar amount with respect to C_8 at 4%w, 8%w of 12%w). The C_8 samples will be indicated as 4%w, 8%w or 12%w; the C_{12} and C_{18} will be named with the prefix "eq." (i.e., equivalent). The real silica/Silane ratio are reported in Table A5.3.

Also in this study, the dispersion of the surface-modified silica NPs has been investigated in the precursor solvents (i.e., ethanol/water mixture and MEK) and in the polymer matrix (i.e., nanocomposite).

	C_8			**C_{12}**			**C_{18}**		
Sample name	4%w	8%w	12%w	eq. 4%w	eq. 8%w	eq. 12%w	eq. 4%w	eq. 8%w	eq. 12%w
Silane/Silica ratio (%w)	4.0%	8.0%	12.0%	4.8%	9.6%	14.4%	6.0%	12.0%	18.1%

Table A5.3 Effective silane/Silica ratio used in grafting reactions with different amounts of silane coating agents.

Variation of C_8 amount

The scattering intensities of NPs surface-modified with different amounts of C_8 and dispersed in ethanol/water mixture, MEK and polymer matrix are reported in Fig. A5.6a, A5.6b, A5.6c, respectively. The silica concentration in the suspension is 1%v. The real silica content of NCs has been determined by TGA: for bare NPs, Φ_{Si} = 2.6%v; for C_8 at 4%w, Φ_{Si} = 2.7%v; C_8 at 8%w, Φ_{Si} = 1.2%v; C_8 at 12%w, Φ_{Si} = 1.9%v.

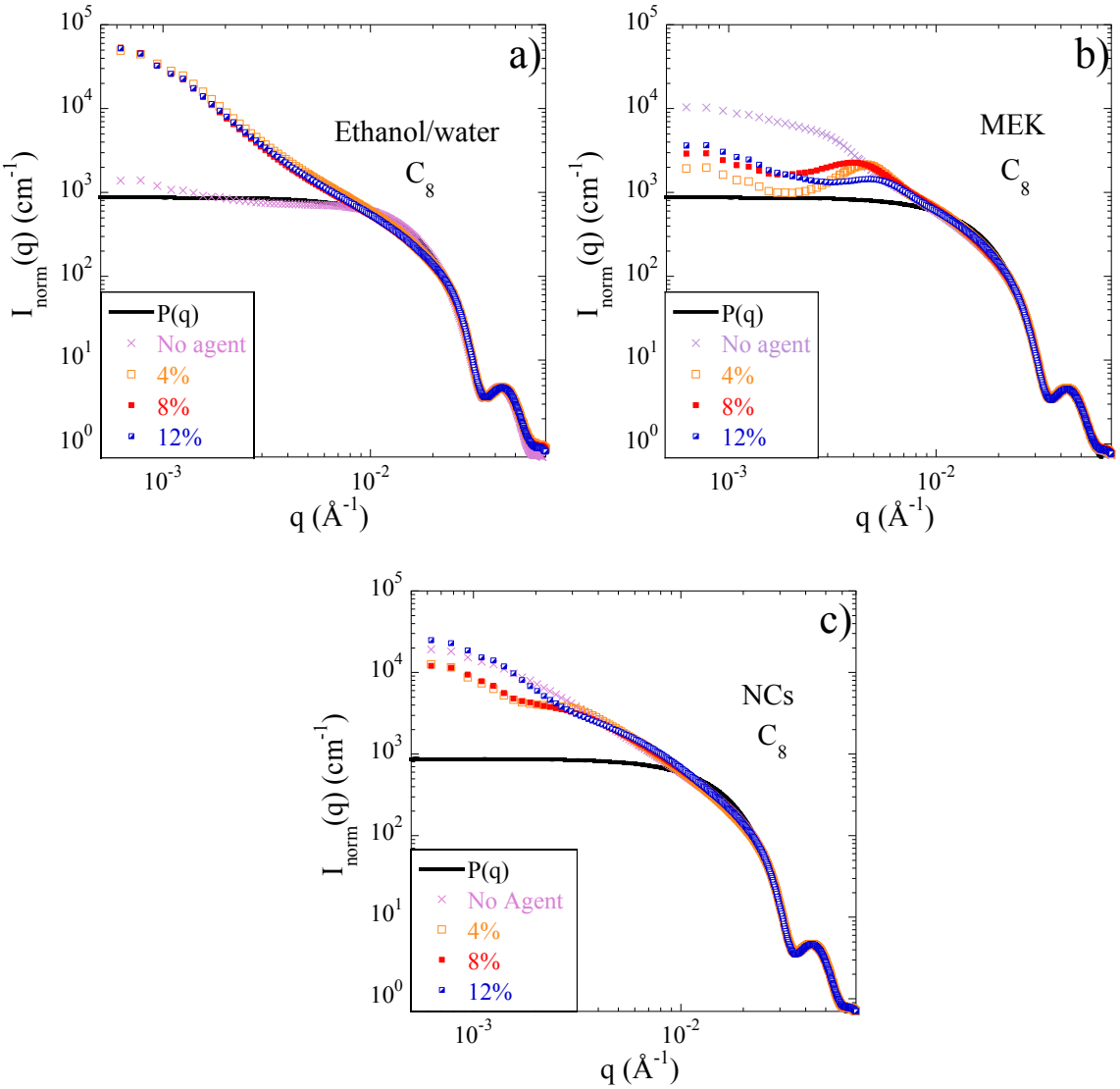

Figure A5.6 SAXS scattered intensities normed to NP form factor in water (continuous line, R_0 = 12.5 nm, 12%) of bare and surface-modified NPs with different amounts of C_8 silane coating agent (4%w, 8%w or 12%w with respect to silica content). The data are referred to surface-modified NPs dispersed in (a) ethanol/water mixture, (b) MEK and (c) polymer matrix (model NCs). Silica volume fractions: for bare NPs, Φ_{Si} = 2.6%v; for C_8 at 4%w, Φ_{Si} = 2.7%v; C_8 at 8%w, Φ_{Si} = 1.2%v; C_8 at 12%w, Φ_{Si} = 1.9%v.

In the hydroalcoholic suspensions, the low-q intensities increase without any relevant difference for the different coating agent amounts, revealing the occurrence of the grafting reaction (i.e., no low-q upturn for the bare NPs in the same solvent). When the particles are transferred in MEK, the shape of the scattering curves (i.e., well defined repulsive peak, except for the bare NPs) suggests that NPs form again aggregates of finite and smaller size. These structural characteristics seem to be transferred in the polymer nanocomposites. The scattering intensities of nanocomposites show a similar shape which is characterized by the presence of a shoulder possibly reminiscent of the structural peak observe in the correspondent MEK suspension. For all the surface-modified NPs, this low-q shoulder occurs approximately in the same q-regime.

Even if the low-q intensities are quite similar, the NC formulated at the highest coating agent amount (i.e., 12%w with respect to silica) shows the highest low-q scattering intensities. Such a result could suggest that the increase of the grafting density up to a certain value starts inducing aggregation rather than promote a better filler dispersion.

For a qualitative comparison, the TEM images of the same NCs analyzed by SAXS (Fig. A5.6c) are reported in Fig. A5.7. These pictures give an idea of the typical aggregation state of the particles even if the influence of the silane amount is difficult to evaluate by this technique. Moreover, the difference in the real silica volume fraction between the two samples could modify the result of the visual comparison.

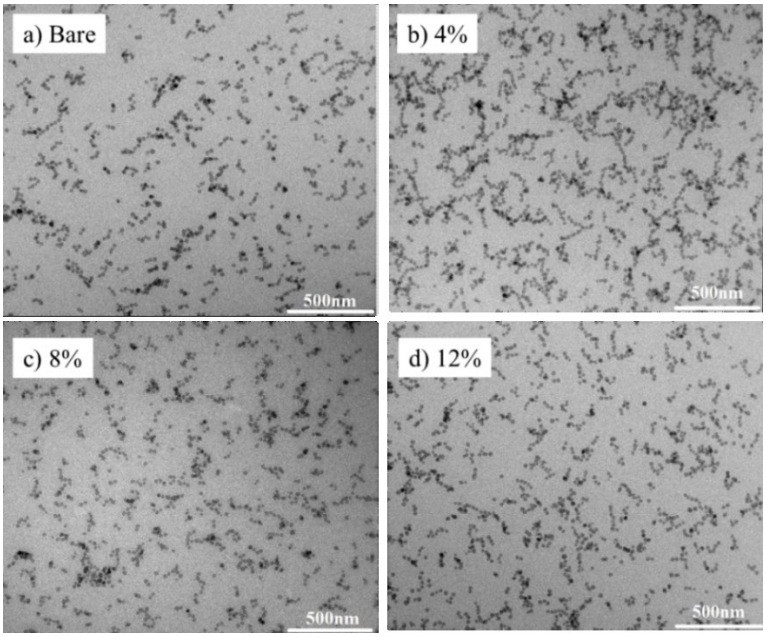

Figure A5.7 TEM images of NCs formulated with bare NPs or NPs surface-modified using different amounts of silane C_8 (i.e., 4%w, 8%w and 12%w with respect to silica content).

Variation of C_{12} amount

The scattering intensities of NPs surface-modified with different amounts of C_{12} and dispersed in ethanol/water mixture and MEK are reported in Fig. A5.8a, A5.8b, A5.8c, respectively. In both suspensions, the scattering curves reveal a behavior close to the one previously observed for the C_8-samples. In particular, it can be noticed that in MEK suspensions the order of low-q scattering intensities is the same that can be observed for the C_8- surface-modified NPs (A5.6b).

Unfortunately, the data for the equivalent NC samples are not yet available.

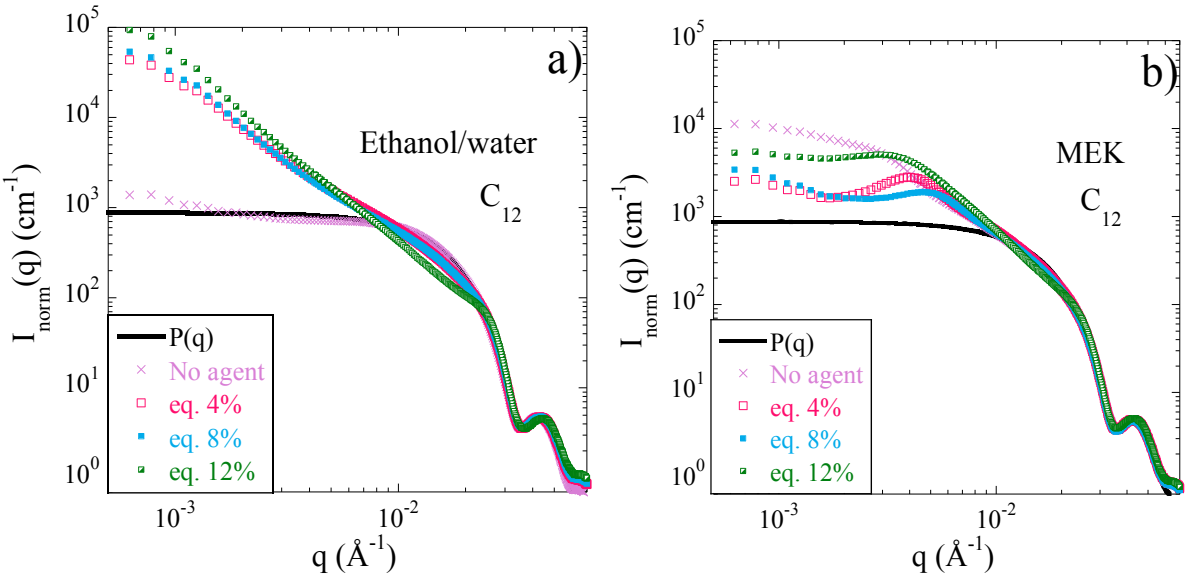

Figure A5.8 SAXS scattered intensities normed to NP form factor in water (continuous line, R_0 = 12.5 nm, 12%) of bare and surface-modified NPs with different amounts of C_8 silane coating agent (equivalent to 4%w, 8%w or 12%w with respect to silica content). The data are referred to surface-modified NPs dispersed in (a) ethanol/water mixture and (b).

Variation of C_{18} amount

The scattering intensities of NPs surface-modified with different amounts of C_{18} and dispersed in ethanol/water mixture, MEK and polymer matrix are reported in Fig. A5.9a, A5.9b, A5.9c, respectively. The silica concentration in the suspension is 1%v while the real silica content of NCs has been determined by TGA: for bare NPs, Φ_{Si} = 2.6%v; for C_{18} equivalent to 4%w, Φ_{Si} =2.5%v; for C_{18} equivalent to 8%w, Φ_{Si} = 1.4%v; for C_{18} equivalent to 12%w, Φ_{Si} =2.6 %v.

Also in this case, the low-q intensity increases in Fig. A5.9a proves the grafting reaction in the hydroalcoholic suspensions. While for C_8 and C_{12} the scattering intensities in the hydro-alcoholic suspensions were the same regardless of the silane amount (i.e., grafting density), for C_{18} the sample at eq. 4%w shows a lower upturn if compared to the ones of the samples at eq. 8%w and 12%w. Moreover, low-q scattering intensities of the C_{18} samples result higher than the ones of C_8 and C_{12} suspensions. The same trend is kept also once the surface-modified NPs are transferred in MEK, even if the intensities are almost in the same range. Comparing to Fig. A5.8b and A5.6b, it can be noticed that in Fig. A5.9b no well-defined structural peaks are detected. On the other hand, the equivalent 4%w (C_{18}) MEK suspension shows the lowest low-q intensity, as observed for C_8 and C_{12}.

These structural characteristics seem to be transferred in the polymer nanocomposites. Even if the low-q intensity are quite similar, the scattering results suggest that the equivalent 4%w promotes the best dispersion while the equivalent 12%w favors the aggregation, as detected for the C_8 silane.

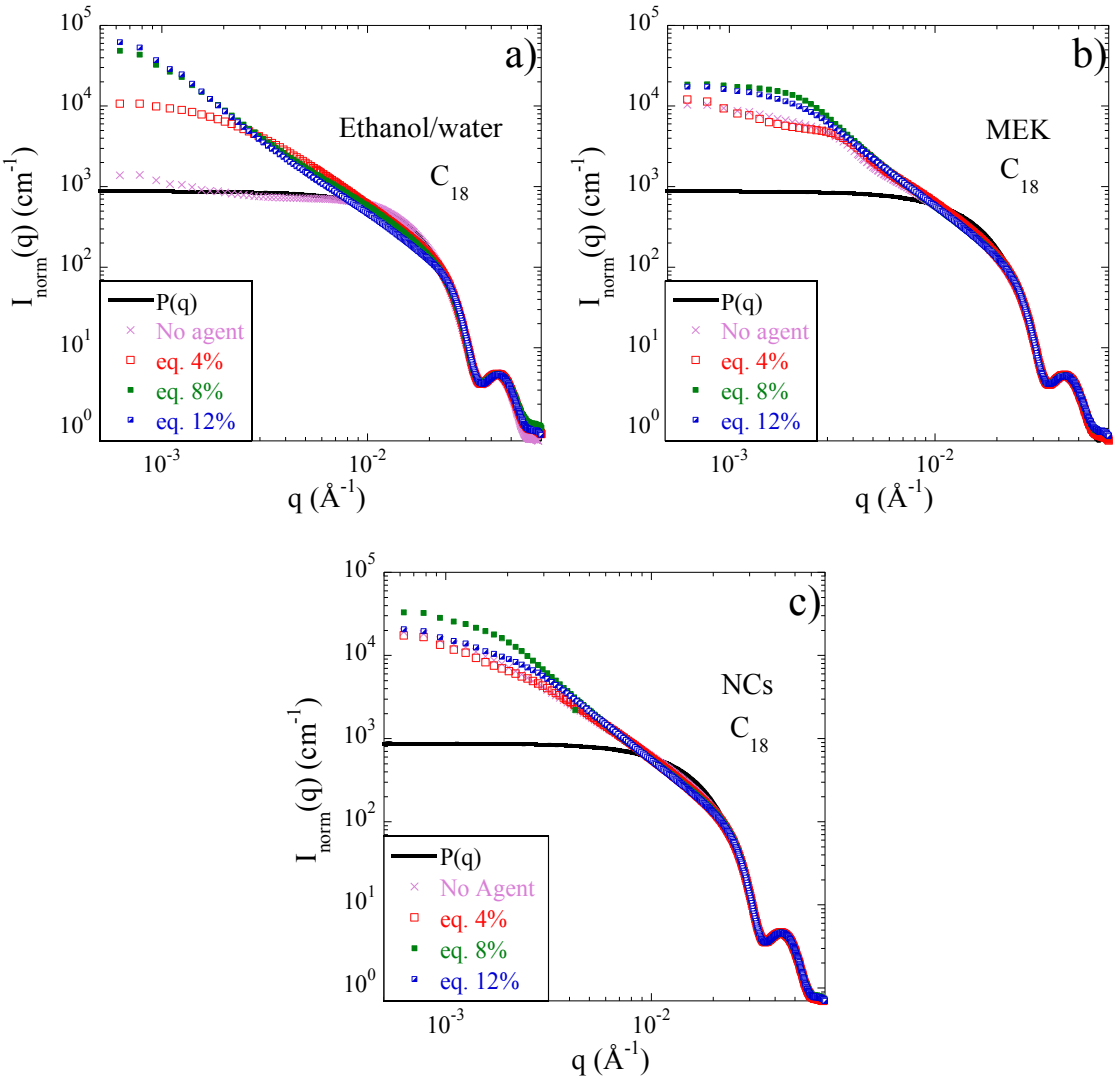

Figure A5.9 SAXS scattered intensities normed to NP form factor in water (continuous line, R_0 = 12.5 nm, 12%) of bare and surface-modified NPs with different amounts of C_{18} silane coating agent (equivalent to 4%w, 8%w or 12%w with respect to silica content). The data are referred to surface-modified NPs dispersed in (a) ethanol/water mixture, (b) MEK and (c) polymer matrix (model NCs). Silica volume fractions: for bare NPs, Φ_{Si} = 2.6%v; for C_{18} equivalent to 4%w, Φ_{Si} =2.5%v; for C_{18} equivalent to 8%w, Φ_{Si} = 1.4%v; for C_{18} equivalent to 12%w, Φ_{Si} =2.6 %v.

For nanocomposites formulated with C_{18} as coating agent, the impact of the silane content (i.e., grafting density) has also been investigated at different silica fractions. The scattering data, not reported here, have been analyzed to extract the average aggregation number $\langle N_{agg} \rangle$, and the next higher moment describing the width of the distribution, $\langle N_{agg}^2 \rangle / \langle N_{agg} \rangle$. In Fig. A5.10, these two parameters are plotted as a function of the silica volume fraction. As observed in Fig. 4.9 for the variation of silane hydrophobicity (see Chapter 4), the data reported in Fig. A5.10 suggest that all the systems behave in a very similar way.

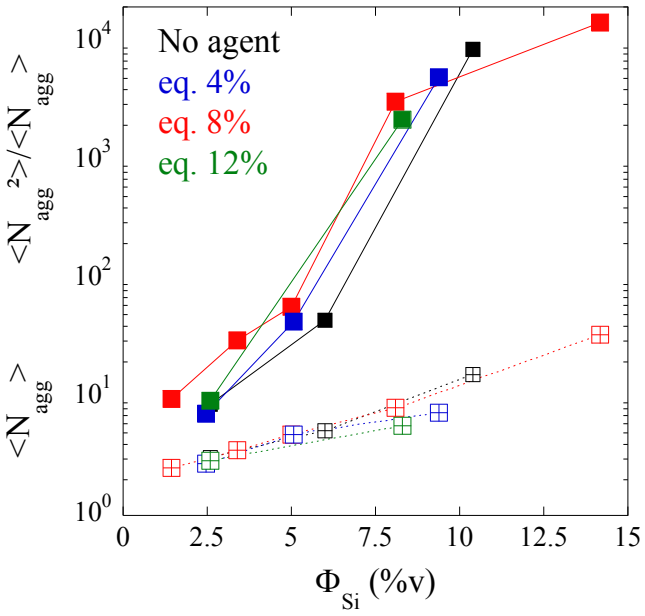

Figure A5.10 The average aggregation number $<N_{agg}>$ (empty symbols) and the normalized second moment of the distribution $<N_{agg}^2>/<N_{agg}>$ (plain symbols) of nanocomposites formulated at different grafting densities (i.e., different silane amounts) as a function of silica volume fraction Φ_{Si}.

Conclusions

Concerning the variation of silane amounts (i.e. grafting density) we showed that: i) the increase of the scattering intensities in the hydro-alcoholic suspensions confirms the occurrence of the grafting reaction, independently of the used silane and its amount (i.e., exception: equivalent 4%w C_{18}; ii) in the MEK suspensions, while C_8 and C_{12} show a well-defined repulsive peak at all the silane amounts, the C_{18} samples are characterized by "shoulders" which occur in the same q-regime. Moreover, the low-q scattering intensies of the C_8 and C_{12} suspensions are comparable, while the one for the C_{18} samples results higher than the others suggesting that this agent favors the NP aggregation. In Fig. A5.11a, a first estimation of the average aggregation number N_{agg} (i.e., estimated as I(q)/P(q) in the low-q regime) is reported as function of the equivalent silane/Silica ratio. It can be noticed that for all the three silanes, the 4%w samples (i.e., lower grafting density) show the best dispersion (i.e., the lowest low-q intensity); iii) concerning polymer nanocomposites, both C_8 and C_{18} samples show a similar low-q scattering intensities and reveling that the quality of the nanoparticle dispersion is transferred from the MEK suspension to the polymer matrix. The variation of the approximate N_{agg} as a function of the silane/Silica ratio (Fig. A5.11b) highlights that the best dispersion is obtained for the equivalent 4%w samples, while the worst is reached with the equivalent 12%w. Also in this case, the dispersion of the C_8 surface-modified NPs results better than the one obtained by the C_{18} grafting.

A more quantitative analysis (i.e., RMC simulations) could confirm the qualitative results presented above confirming that the highest amount of coating agent, and thus the highest grafting density, induces the stronger aggregation.

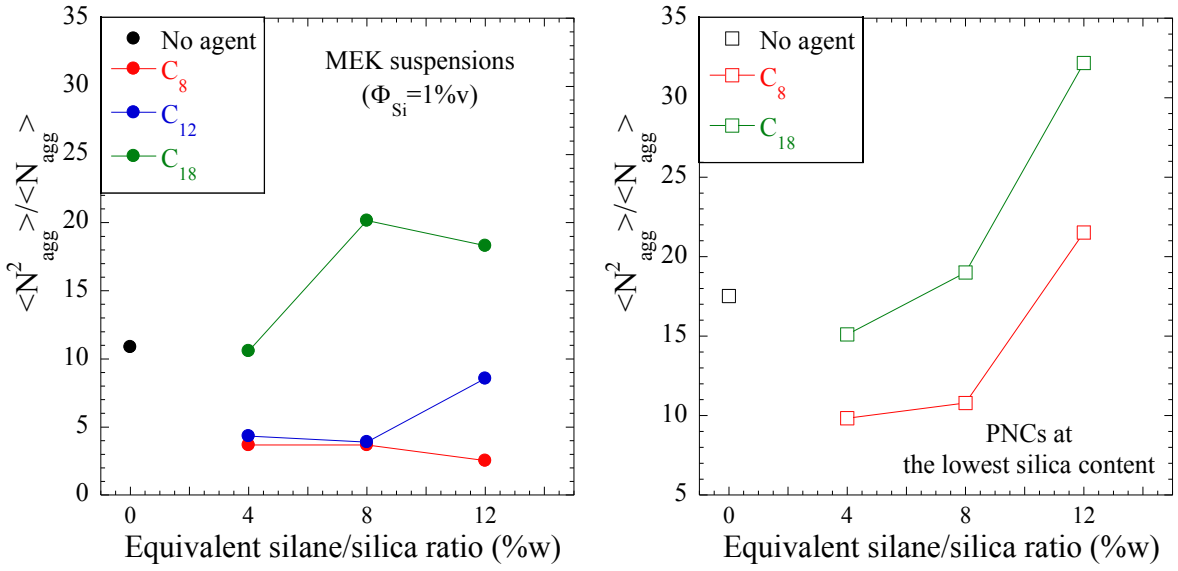

Figure A5.11 The evolution of the N_{agg} (i.e., I(q)/P(q) in the low-q regime) as a function of the equivalent silane/Silica ratio (i.e., different coating agent amounts and thus different grafting densities) for MEK suspensions (a) and polymer nanocomposites (b).

7.6. Appendix 6: Broadband Dielectric Spectroscopy (supporting information about Chapter 5)

Note on the normalization of dielectric spectra

Due to difficulties in estimating precisely the sample thickness and area, the dielectric spectra of the matrices with silanes have been normalized to the low-T (173 K) permittivity value of the pure matrix (2.25 and 2.31 at 253 K for SB_F and SB_NF, respectively). In the nanocomposites, the permittivity at 253 K has been rescaled to the value given by the equation

$$\varepsilon_\infty = \varepsilon_m \frac{[n\varepsilon_f + (1-n)\varepsilon_m] + (1+n)[\varepsilon_f - \varepsilon_m]\Phi_f}{[n\varepsilon_f + (1-n)\varepsilon_m] - n[\varepsilon_f - \varepsilon_m]\Phi_f}$$

where ε_∞ is the high-frequency limit of the dielectric constant, ε_m and ε_f are the frequency-independent dielectric constant of the polymer matrix and the filler, respectively; Φ_f is the volume fraction of the filler particles. This equation is reported in Kremer's book (Kremer and Schönhals 2003, Eq. 13.9) and it considers a simple model for two-phase heterogeneous materials with 5.5 for the dielectric permittivity of the silica (Baeza et al 2015b).

Fitting parameters of plasticized styrene-butadiene matrices

In Fig. A6.1a, the evolution of the HN shape parameters γ and δ (Eq. 5.2) used to describe the segmental relaxation of the styrene-butadiene SB_F matrices mixed with different amounts of C_{18} are reported as a function of the temperature. In particular, γ increases with the temperature, while δ decreases. Fig. A6.1b shows the linear decrease of the intensity of the segmental relaxation with the increase of the temperature.

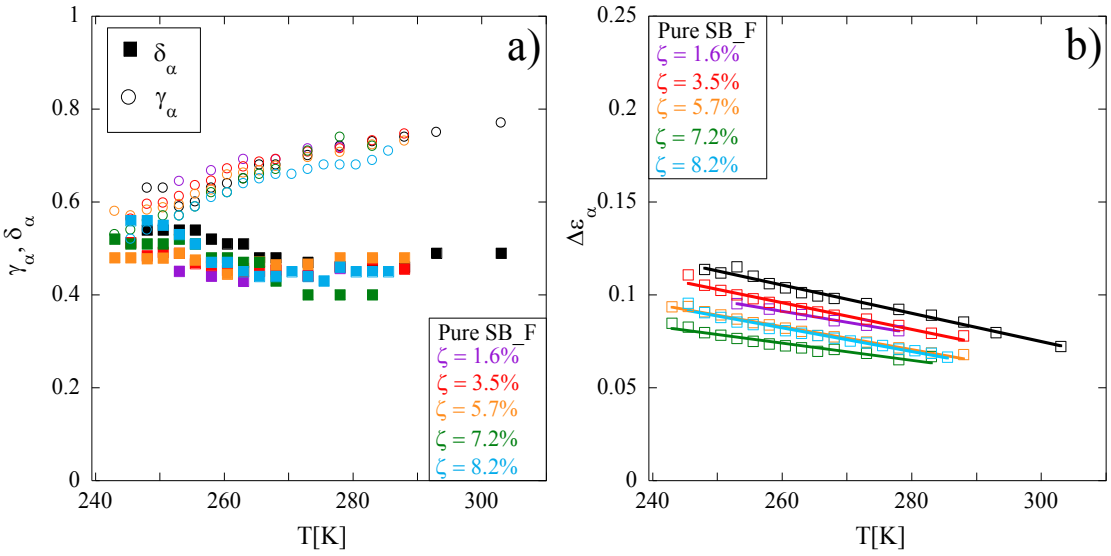

Figure A6.1 (a) Evolution of γ and δ parameters of the HN function used to describe the α-process as a function of the temperature. (b) Intensity of the α-process as a function of the temperature. Solid lines represent linear fit of the data.

Impact of polymer variation on MWS1 dynamics in non-grafted model NCs

The dynamics of the of the MWS1 process for non-grafted model NCs formulated with C_{18} at different amount of SB_F polymer are reported as a function of the temperature in Fig. A6.2. The variation of the composition of the polymer matrix seems not to affect the MWS1 process. This result suggests than the increase of the SB_F amount do not induce an increase of the residual water content in the sample.

The values of the γ_{MWS1} parameter (Eq. 5.2) used for the fitting of the MWS1 process are reported in the inset of Fig. A6.2 (δ_{MWS1} constant at 0.575).

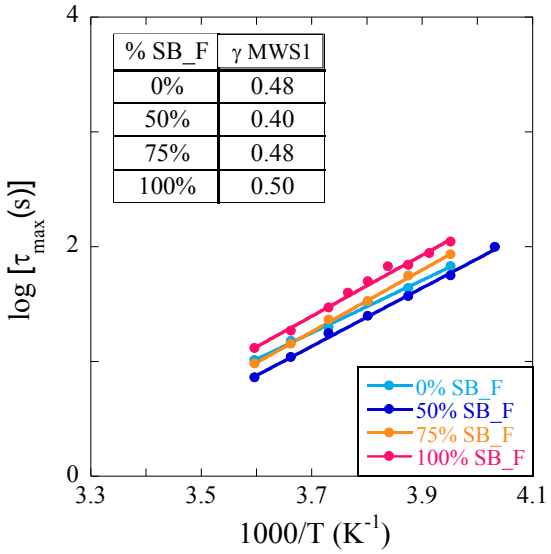

Figure A6.2 Relaxation times of MWS1 process as a function of the temperature. Inset: values of γ_{MWS1} parameter used in the HN fitting function.

Regarding the evolution of the MSW1-process with the content of SB_F, we found similar activation energies (E_{MWS1} between 43.8 and 51.4 kJ/mol) and time scales, which suggests that it is not affected by the amount of end-functionalized styrene-butadiene in agreement with previous works (Baeza et al. 2015b).

Fitting parameters of non-grafted model NCs at different silica content

In Fig. A6.3a, the evolution of the HN shape parameters γ and δ used to describe the segmental relaxation of the *non-grafted* model NCs formulated with SB_F polymer and C_{18} (12%w with respect to silica) are reported as a function of the temperature. In this case, the value of δ has been kept constant at 0.5. Fig. A6.3b indicates that for all the NCs, the process intensity linearly decreases linearly with the increase of the temperature.

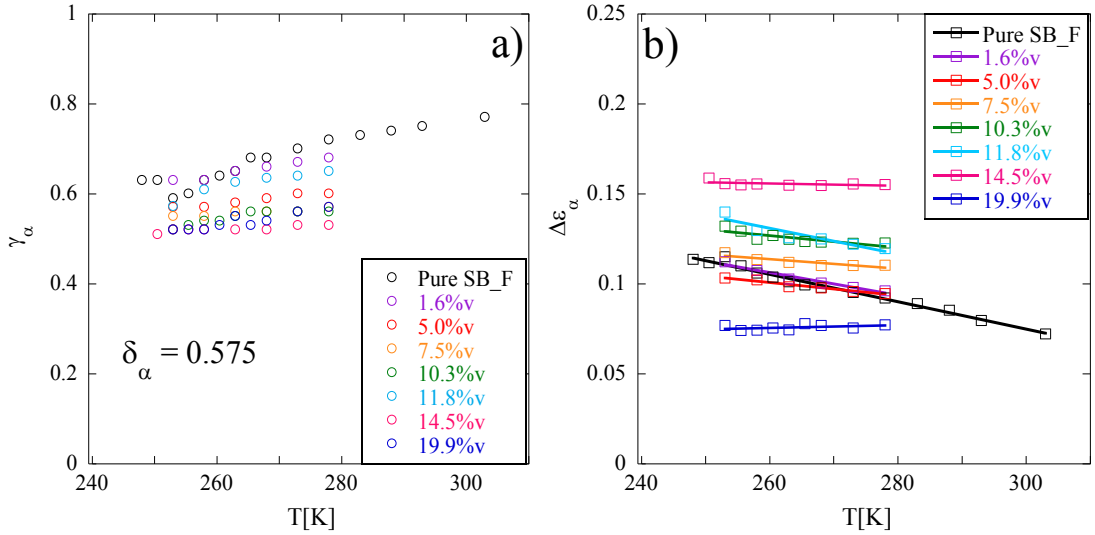

Figure A6.3 (a) Evolution of γ parameter of the HN function - Eq. 5.2 - used to describe the α-process as a function of the temperature. δ has kept constant at 0.575. (b) Intensity of the α-process as a function of the temperature. Solid lines represent linear fit of the data.

MWS1 dynamics in non-grafted model NCs at different silica content

Besides, we have also studied the evolution of the **MWS1**-process with the silica contents. The shape parameters γ are summarized in Table A6.1, and Fig. A6.4a shows the relaxation map of the MWS1 process for *non-grafted* NCs at different filler contents. The evolution of the relaxation times with the reciprocal temperature is well described by an Arrhenius law, which allows estimating activation energies of about 50 kJ/mol independently of the filler content. It can be observed that the MWS1 process accelerates with the increase of the filler content. This characteristic can be interpreted using the interlayer model, ILM, (eq. 2.49) developed by Steeman to predict the dielectric response of a glass-bead filled composites where a thin water layer is adsorbed at the filler-polymer interface (i.e., tri-phasic material composed by filler, matrix and interfacial-water layer) (Steeman and Maurer 1990; Steeman et al. 1991). The main elements of this model are: i) the dielectric constant of the matrix ($\varepsilon_m = n^2 = 2.25$, where n is the refractive index of the SB_F) and of the filler particles (ε_p= 5.5 (Steeman and Maurer 1990; Steeman et al. 1991)); ii) the volume filler fraction Φ_{Si}; iii) the water volume fraction in the sample Φ_l, which has been estimated by TGA (ramp at 3 K/min from 35°C to 100°C followed by a 4h isotherm). The values of Φ_l (%w) for each sample are reported in Fig. A6.4b. The Φ_l increases with increasing the silica fraction. The free parameter of the ILM is the conductivity of the water layer σ_l the thickness of which evolves with the water content in the nanocomposite. Considering the relaxation time of the MWS1 process at T=273 K (inset Fig. A6.4a) and using the eq. 2.49, the values of σ_l as a function of the filler content have been determined, as reported in the inset of Fig. A6.4b. In agreement with other works (Steeman et al. 1991; Otegui et al. 2013; Baeza et al. 2015b), the reported values of conductivity are lower than the one of the deionized water (5.5 μS/m). The increase of the layer conductivity with Φ_{Si} could be explained, e.g., by an increasing capture of ionic impurities at the filler-polymer interface.

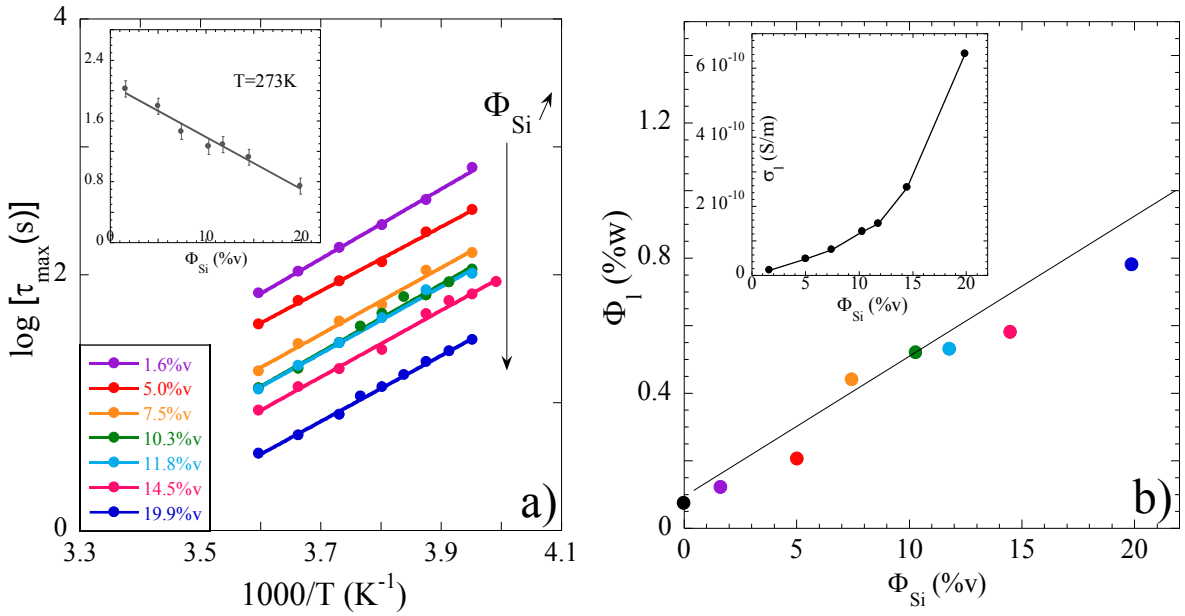

Figure A6.4 (a) Dynamics of MWS1 process as a function of the reciprocal temperature for *non-grafted* NCs at different filler fractions. Solid lines represent fits by means of the Arrhenius law. Inset: MWS1 relaxation times at T=273 K. (b) Residual water content in NCs estimated by TGA. Inset: conductivity of the interfacial water layer at T=273 K as a function of the silica content.

For the fitting of the MWS1 process, the δ_{MWS1} parameter of the HN function has been kept constant at 0.575. The value of the γ_{MWS1} parameter for each sample is specified in Table A6.1 The activation energy values obtained by the Arrhenius law are also indicated.

%v Si (nom)	%v Si (TGA)	γ MWS1	Ea (kJ/mol)
1.0%	1.6%	0.56	52.1
5.0%	5.0%	0.72	48.0
7.5%	7.5%	0.64	49.7
10.0%	10.3%	0.50	50.9
12.5%	11.8%	0.42	49.3
15.0%	14.5%	0.58	49.7
20.0%	19.9%	0.32	49.1

Table A6.1 Values of γ_{MWS1} parameter and of the activation energy of non-grafted model NCs at different filler contents.

For non-grafted model NCs at different silica content, the width of the peak of the segmental relaxation has been evaluated. As indicated in Fig. A6.5a, the width has been estimated at an abscissa y_w defined as $y_w = y_{max} - 0.25 * y_{max}$, where y_{max} is the abscissa which corresponds to the maximum of the segmental peak (T=258 K). The evolution of the peak width as a function of the silica volume fraction has been compared to the value of the parameter γ which takes into account the symmetric broadening of the segmental relaxation peak (Fig. A6.5b). These trends reflect the one of the segmental relaxation time (Chapter 5), which suggests that the plasticization also affects the shape of the α-process peak. A more detailed interpretation of these data has to be performed.

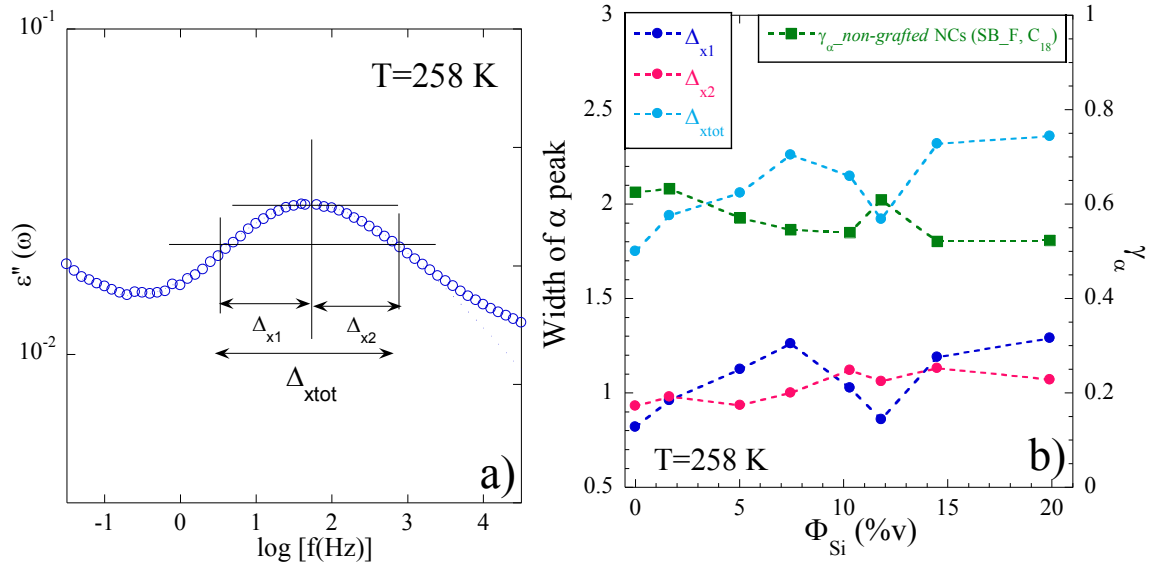

Figure A6.5 (a) Example of estimation of the width of the segmental relaxation peak (sample: 9.6%v silica, SB_F, C_{18} at silane/Silica ratio=18%). (b) Evolution of width peak and γ fitting parameter as a function of the silica filler content (T=258 K).

MWS1 dynamics in non-grafted model NCs with different amount of silane coating agent (C_{18})

In Fig. A6.6a and A6.6b, the dielectric spectra at T=258 K of non-grafted model NCs formulated with SB_F polymer and C_{18} at different amount are reported. The variation of the amount of added silane implies the variation of the C_{18}/Silica ratio (ψ) from 12% to 24%. Table A6.2 reports the values of the γ_{MWS1} parameters used for the fitting of the MWS1 process by the HN function (δ_{MWS1} constant at 0.575).

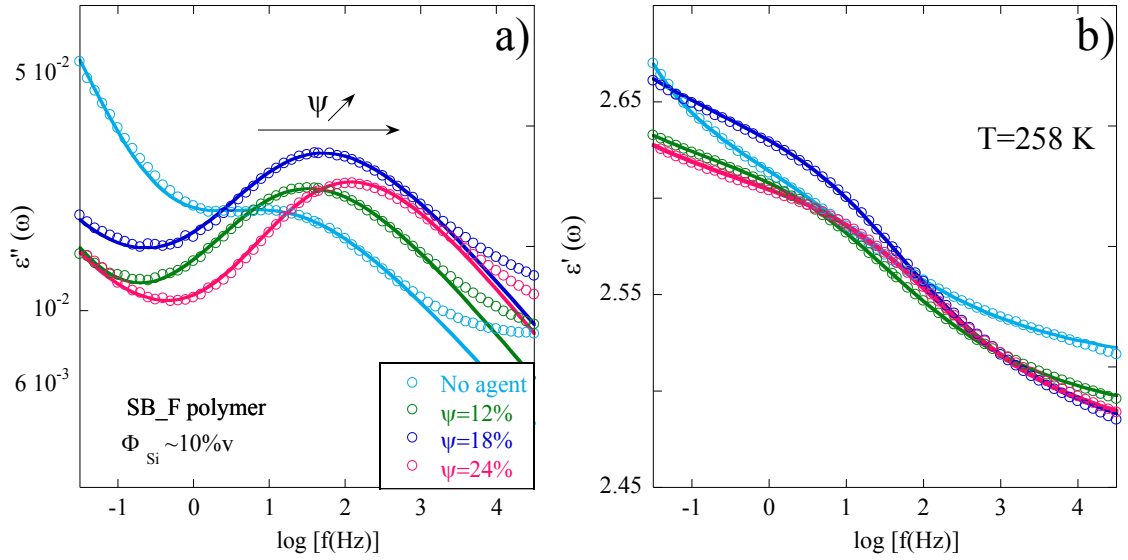

Figure A6.6 (a) Real and (b) imaginary part of the dielectric spectra for non-grafted model NCs at different amount of C_{18} (i.e., different C_{18}/Silica ratios).

Concerning the MWS1 process, it seems that the variation of the of the silane/Silica ratio do not strongly affect this process, as shown in Fig. A6.7. Table A6.2 reports the values of the γ_{MWS1} parameters used for the fitting of the MWS1 process by the HN function (δ_{MWS1} constant at 0.575). The activation energy estimated by the Arrhenius law are reported in the inset of Fig. A6.7. Only the sample formulated without any coating agent shows a lower relaxation time which can be explained considering the bigger amount of residual water with respect to the other samples (for NC without silane agent, Φ_I=0.8%w; for NC at ψ=12%w, Φ_I=0.5%w).

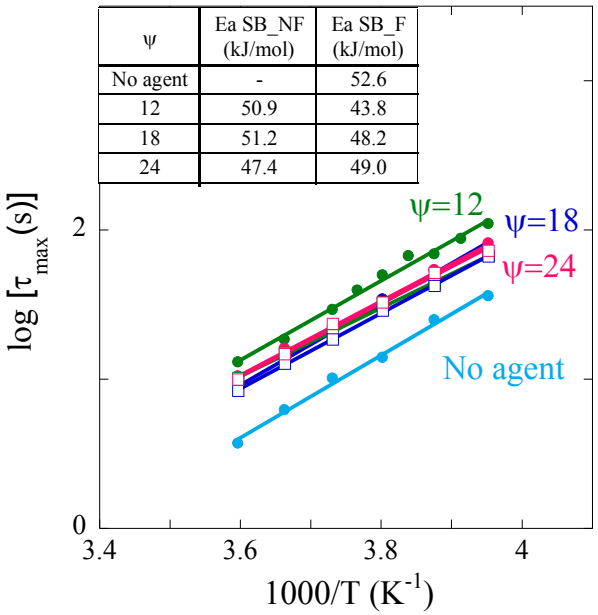

Figure A6.7 Dynamics of MWS1 process as a function of the temperature for *non-grafted* NCs at different C_{18}/Silica ratios. Solid lines represents fits by means of the Arrhenius law. Inset: activation energies of MWS1 process.

Sample	%v Si (TGA)	γ MWS1
(SB_F) ψ=12%	10.3	0.50
(SB_F) ψ=18%	9.6	0.45
(SB_F) ψ=24%	9.9	0.44
(SB_NF) ψ=12%	10.7	0.48
(SB_NF) ψ=18%	10.5	0.40
(SB_NF) ψ=24%	10.1	0.47

Table A6.2 Values of γ_{MWS1} used for the fitting of the MWS1 process in non-grafted model NCs at different amount of C_{18} (i.e., different C_{18}/Silica ratios).

7.7. Appendix 7: Rheological characterization of model nanocomposites

Rheology is a valid tool to determine the principal macroscopic-dynamical features of nanocomposite materials. As reported in literature (Jancar et al. 2010), most of the mechanical properties of NCs are related to the spatial organization of filler particles, polymer-filler interactions and chain conformations under deformation.

Here, we propose a mechanical characterization of our model nanocomposite system (Chapter 2.3). The first part of our work aims to address some technical issues (e.g. low thickness, presence of residual bubbles) in order to improve the rheological measurements. Then, the evolution of the reinforcement effect in NC is investigated as a function of the filler content in the linear viscoelastic regime.

Measurement set up

The investigated materials are model nanocomposites made of silica nanoparticles surface-modified with a silane coating agent (C_{18}, 12%w with respect of silica), and dispersed in a SB_F polymer matrix. Rheological tests have been carried out at the Foundation for Research & Technology (IELS-FORTH, Heraklion, Crete, Greece) under the supervision of Pr. Dimitris Vlassopoulos,

An ARES strain-controlled rheometer (TA instrument, USA) equipped with a force rebalance transducer (2KFRTN1) has been used for the rheological experiments. A homemade plate-plate geometry (upper plate diameter=6mm; bottom plate diameter=8mm) has been mounted, as shown in Fig. A7.1.

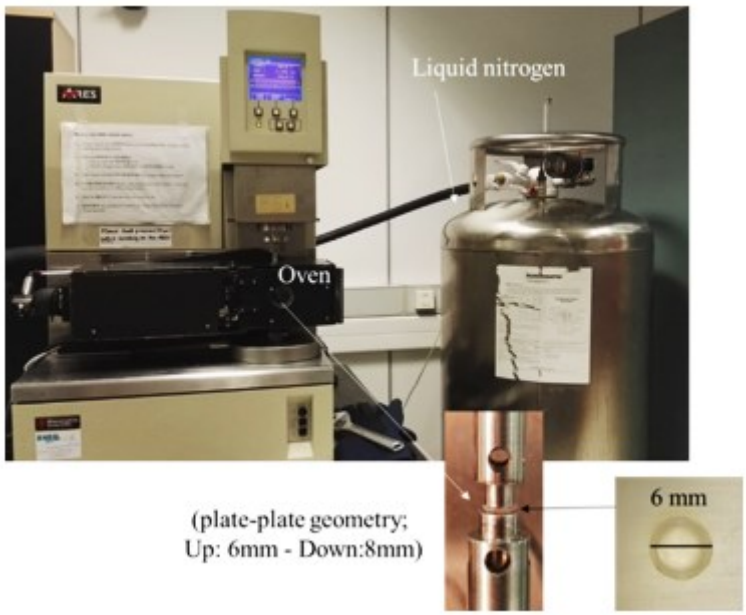

Figure A7.1 ARES rheometer equipped with an oven connected to a nytrogen tank to reach temperature below 0°C. A plate-plate homemade geometry has been used.

The ARES rheometer is equipped with a convection oven which allows controlling temperature from room temperature up to 300°C, with a resolution of 0.1°C. The oven is connected to a nitrogen gas

generator in order to provide inert atmosphere. For cryogenic measurements, a liquid nitrogen dewar can be used for lowering the temperature of the oven down to -100°C.
For the samples of interest, different kinds of tests have been performed:

1) Dynamic Strain Sweep Test (DSST), in order to define the Linear Visco-Elastic (LVE) regime ($\omega=2\pi f$ =10rad/s; T=80°C).
2) Dynamic Time Sweep Test (DTST), to verify the equilibrium condition of the sample in time (sample have been assumed at the equilibrium when the variation of dynamic moduli over 3 hours was less than 5%; ω =10rad/s; T=80°C, %strain in LVE regime).
3) Dynamic Frequency Sweep Test (DFST), in order to scan a frequency range between 100-0.1 rad/s (%strain in LVE regime). Temperature has been varied from 80°C to -20°C or -25°C. Below T= -25°C, measurements resulted out of torque and thus not reliable.

The samples have been loaded between the plates at T=80°C and squeezed to the proper gap, close to the thickness of the sample. After loading, each sample was allowed to relax for 30 min. Such time interval has been estimated to be sufficient to obtain a good thermal equilibration of the sample and the rheometric tools, and to reach a normal force close to zero. Whenever necessary, the part of sample exceeding the measuring geometry has been trimmed at the edge.

Sample molding for rheological measurements

As already mentioned, rheological measurements have been performed on model NCs formulated by solvent casting. The following technical issues are associated with the preparation of the specimens for rheological tests (see section 2.3):

1) The thickness of the NCs was around 0.15mm, a quite low value to perform gap-independent rheological measurements with a plate-plate geometry.
2) Residual bubbles or solvent trapped in the specimens affect torque measurements.

To overcome these problems, a specific molding procedure in vacuum has been developed. About 60mg of sample have been put between two Teflon disks (diam. 6mm) and inserted into a metallic cylinder. Then, the cylinder has been then placed into a vacuum chamber in contact with two heated platens of a hydraulic press, as shown in Fig. A7.2. The samples have been molded at T=100°C for 30min under vacuum. No extra pressure has been applied during the molding procedure.
Samples with a diameter of 6mm and thickness between 1-1.5mm have been obtained with the protocol described above. High-temperature and vacuum ensured the complete removal of residual air bubbles or solvent.

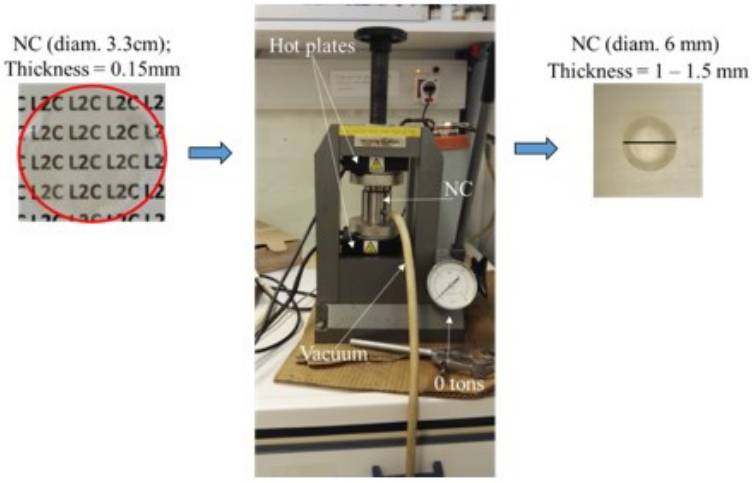

Figure A7.2 Hot-press with vacuum system used for molding nanocomposites for rheological measurements.

A crucial point in performing rheological measurements on nanocomposites is the equilibration of the samples. Due to the relaxation of internal stresses induced by the loading procedure, the dynamic moduli are expected to vary with time for a certain interval after the sample is loaded on the rheometer.

A preliminary time sweep (DTST) test has been performed on a pure SB_F matrix and on a NC with low filler content (just after molding). Fig. A7.3 shows that the value of the elastic modulus G' changes with time and it starts reaching an equilibrium state after about 15h. A variation in G' of 9% for the pure SB_F and 21% for NC with 0.9%v of silica has been found at the end of the test with respect to the initial value.

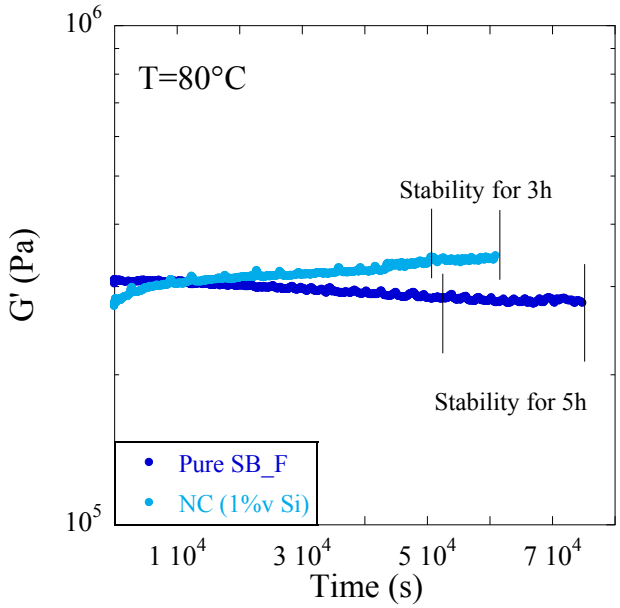

Figure A7.3 DTST measurements on pure SB_F and NC samples just after molding (without any preliminar equilibration).

Since more than 15h of equilibration are required for each sample, an alternative equilibration procedure has been developed in order to optimize the measurements. Nanocomposites have been put under

vacuum at T=80°C for a week and then molded according to the above described protocol. For each sample, a preliminary DSST has been performed to define the LVE regime. Then, an over-night DTST has been done to check the real equilibration of the sample. The strain values used during the DTST measurements are summarized in Table A7.1. Fig. A7.4 shows the evolution of the elastic modulus G' as a function of time for NCs at different silica volume fractions (Φ_{Si}) after the equilibration in the oven (vacuum, T=80°C, one week) and the molding in the press. These results indicate that samples are fully equilibrated at the end of the DTST.

Φ_{Si} (%v)	**0%**	**0.9%**	**4.3%**	**10.5%**	**13.6%**	**14.8%**	**17.3%**
Stain (%)	1%	0.6%	0.5%	0.5%	0.08%	0.1%	0.15%

Table A7.1 Strain values applied during the DFST test in order to work in the linear regime.

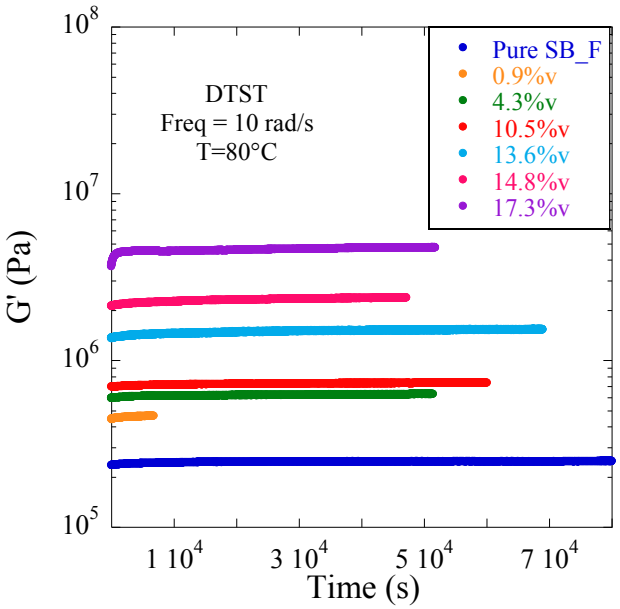

Figure A7.4 DTST measurements on NC at different silica volume fractions (Φ_{Si}) after equilibration in the oven (vacuum, T=80°C, one week) and molding in the press.

The equilibration and molding of the model nanocomposites are essential to correctly perform the rheological measurements. At the same time, it has to be into taken account that this preparation procedure could affect the structure of the sample. In this regard, some complementary tests have been performed to understand if the molding procedure modifies the organization of the fillers in the polymer matrix. For example, another way to shape the sample increasing its thickness is to overlap some layers of the NCs and put them into the oven under vacuum at T=80°C for three days ("multi-layer NC"). Then, comparing the results of the DFST tests at different temperatures for this multi-layer sample to the ones of the same sample molded with the protocol of compression molding in vacuum, no difference can be observe. This suggests that the molding procedure does not really affect the structure of the system. Some Small Angle X-ray Scattering measurements should be performed to confirm that the molding and the equilibration do not induce changes in the sample structure.

Master curve construction

After equilibration, frequency sweep measurements (DFST) have been performed on each samples at different temperatures (from 80°C to -20°C or -25°C). Reproducibility of the data has been verified for each sample: after the last dynamic measurement at the lowest temperature, the sample has been again heated up to 80°C and another DFST has been performed. In all the cases, the data have been found to overlap the first DFST at 80°C within an error bar smaller than 10%. This proved that the sample did not evolve during the frequency sweep tests at different temperatures.

As a first step, the pure SB_F has been characterized. Its elastic and viscous moduli (G' and G") at different temperatures are shown in Fig. A7.5a and Fig. A7.5b, respectively.

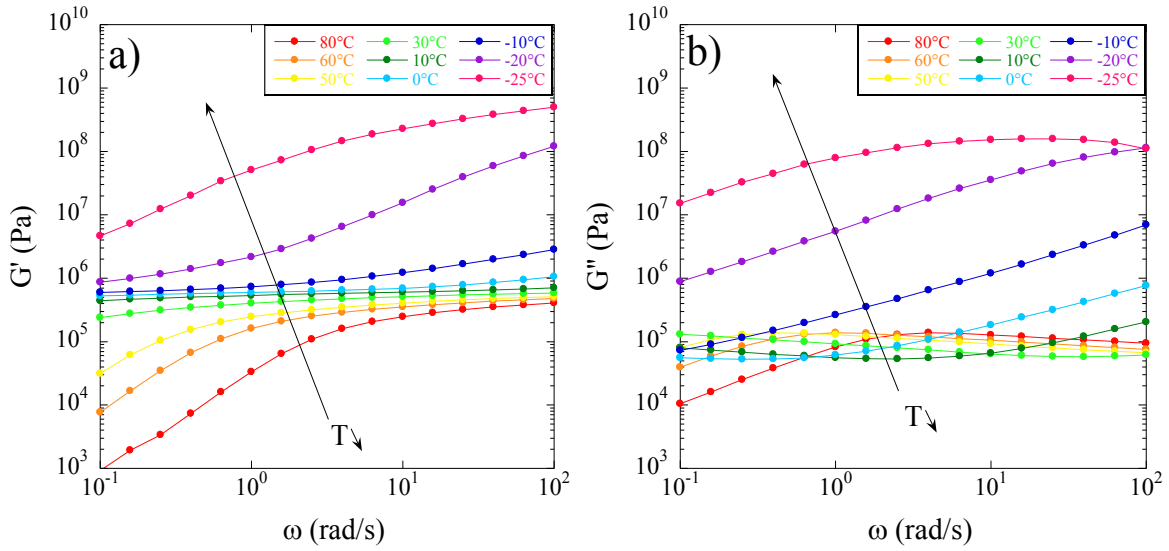

Figure A7. 5 Elastic (a) and viscous (b) modulus of pure SB_F polymer as a function of frequency obtained by DFST measurements at temperatures from 80°C to -25°C.

Using DFST data at several temperatures, the time-temperature superposition (TTS) can be applied to create a *master curve* which describes the viscoelastic behavior of the material of interest over several frequency decades (Ferry 1980). G' and G" curves at different temperatures have been horizontally shifted on data at the reference temperature (T_{ref}=50°C) using a shift factor named a_T. If necessary, a vertical shift factor b_T has been applied which always results of the order of 1 according to a weak variation of the density upon temperature (Brandrup et al. 1989). The final master curve for the pure SB_F is represented in Fig. A7.6. An important feature of this master curve is that it provides complete information about the polymer dynamics in the range of time scales from the segmental motion to reptation. From the cross-over between G' and G", three different characteristics times corresponding to three fundamental relaxation mechanisms can be identified (Mangal et al. 2016): i) the segmental relaxation time τ_g; ii) the entanglement relaxation time τ_e; iii) the terminal relaxation or reptation time τ_t.

The molecular weight between entanglements (M_e) is independent from the total molecular weight for a given polymer. For the pure SB_F, it can be estimated following the formula (Whitten and Brown 2007)

$$M_e = \frac{\rho RT}{G_0} \qquad [A7.1]$$

where ρ is the SB_F density, R is the gas universal constant (8.314 $JK^{-1}mol^{-1}$) and G_0 the value of G' in correspondence of the minimum of G" at the reference temperature. Thus, M_e for the pure SB_F is around 4 kg/mol.

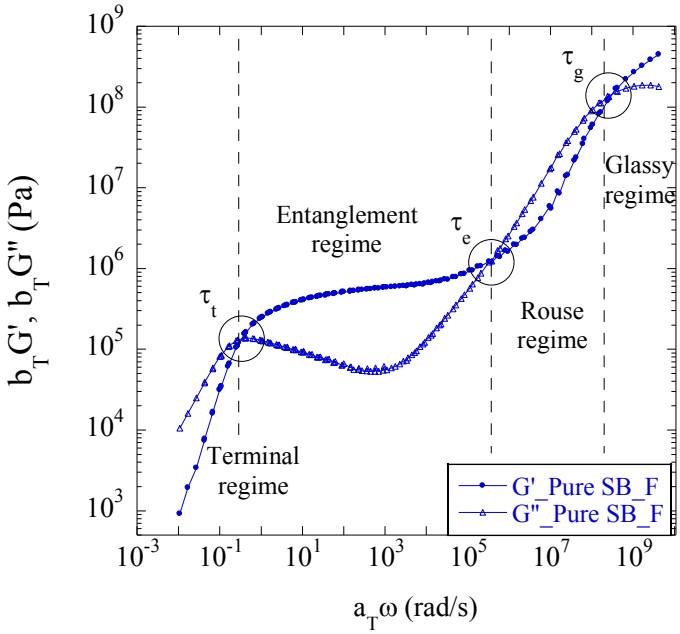

Figure A7.6 TTS master curve for neat styrene-butadiene (SB_F). Characteristic relaxation times (τ_g, τ_e, τ_t) can be extracted by the crossover between G' and G", as shown by Magal et al. (Mangal et al. 2016).

The horizontal (a_T) and vertical (b_T) shift factors used for building the master curve in Fig. A7.6, are reported in Fig. A7.7a. While b_T is always close to one, a_T varies significantly as a function of the temperature and its behavior can be described by the Williams-Landel-Ferry law (WLF, Eq. 1.9) (Williams et al. 1955) which is typically used to describe the time/temperature behavior of thermodynamically simple polymers above the glass transition temperature. A polymer system is considered thermodynamically simple when its characteristic relaxation times have the same temperature dependence. The horizontal shift factor a_T can be also defined as $a_T = \tau(T)/\tau(T_{ref})$ (Klüppel 2008), where τ(T) is a characteristic relaxation time at a generic temperature ($T>T_g$) and $\tau(T_{ref})$ is the characteristic relaxation time at the reference temperature (i.e. T_{ref} =50°C). Thus, the evolution of the relaxation time can be plotted as a function of 1000/T [K^{-1}] and fitted by the WLF law as shown in Fig. A7.7b

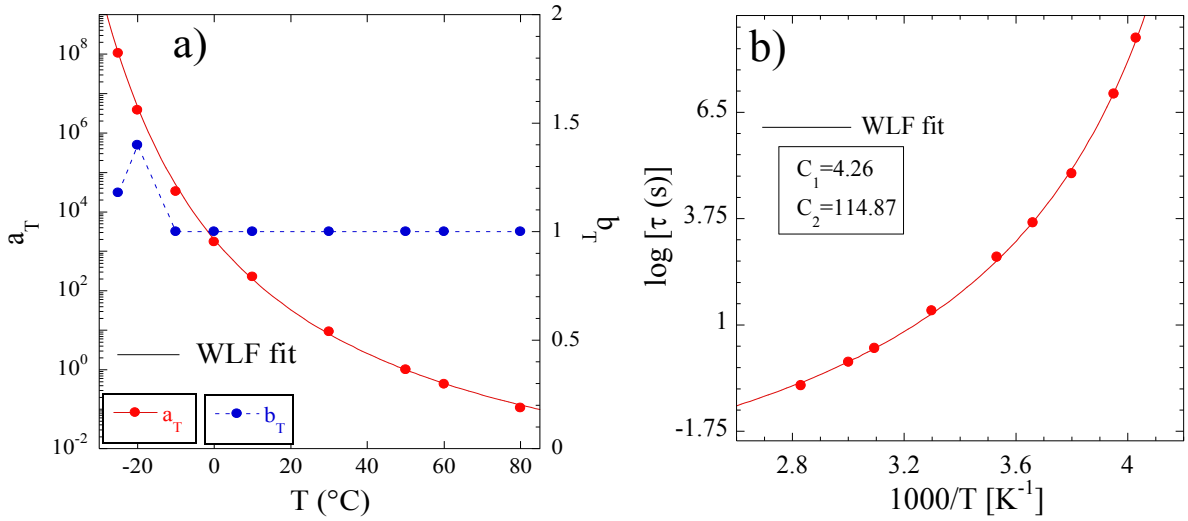

Figure A7.7 (a) Horizontal (a_T) and vertical (b_T) shift factors used for the TTS of the pure SB_F matrix. While b_T is always close to 1, a_T varies significantly as a function of the temperature and its behavior can be described by the Williams-Landel-Ferry (WLF) law; (b) The evolution of the polymer relaxation time as a function of 1000/T [K^{-1}] has been fitted by the WLF law in order to estimate the empirical constants C_1 and C_2, as reported in the inset.

Once evaluated the rheological behavior of the pure SB_F, the impact of the addition of fillers (silica volume fraction Φ_{Si} from 0%v to 17.3%v) on the mechanical properties can be studied.

As a general assumption, the TTS should not work for NCs because particles dynamics introduce other relaxation mechanisms that do not have the same dependence as the time scale of the pure polymer. However, analyzing the shape of the frequency-dependent dynamic moduli at different temperatures, it is reasonable to conclude that the TTS can still be applied to NCs in order to build apparent master curves provide an approximate, yet plausible description of the relaxation of the system at the reference temperature over a wide range of time scales. Also in this case, a vertical shift factor b_T of about 1 has been applied if necessary.

To correctly apply the TTS, all the frequency sweep measurements at temperature $T>T_g$ have to be shifted with respect to the specific T_g of the material. In our case, the Differential Scanning Calorimetry (TMDSC) measurements performed on model nanocomposites (see section 2.3) proved that all the samples have the same glass transition temperature. Thus, the same temperature (T=50°C) has been initially chosen as T_{ref} for all the NCs. On the other hand, once created all the master curves, the position of the high-frequency cross-over, which corresponds to the glass transition is not exactly at the same frequency for all the NCs. This difference could be explained considering that the samples analyzed by TMDSC had not be equilibrated as for NCs used during rheological measurements. Moreover, the mismatch of the high frequency data suggests that the mechanism of relaxation in nanocomposite systems is more complex than a simple extrapolation of the matrix behavior (Baeza et al. 2016a).

To quantitatively compare the rheological data, all the master curves have been horizontally shifted in order to match the same high-frequency cross-over of the pure SB_F. For clarity of representation and in order to better visualize the evolution of the data with the increase of the filler content, the NC master

curves have been split in three different plots: i) Fig. A7.8a reports the master curves for NCs at Φ_{Si}=0.9%v and Φ_{Si}=4.3%v; ii) Fig. A7.8b reports the master curves for NCs at Φ_{Si}=10.5%v and Φ_{Si}=13.6%v iii) Fig. A7.8c shows master curves for NCs at Φ_{Si}=14.8%v and Φ_{Si}=17.3%v. In the three plots, the NC master curves are compared to the one of the pure SB_F.

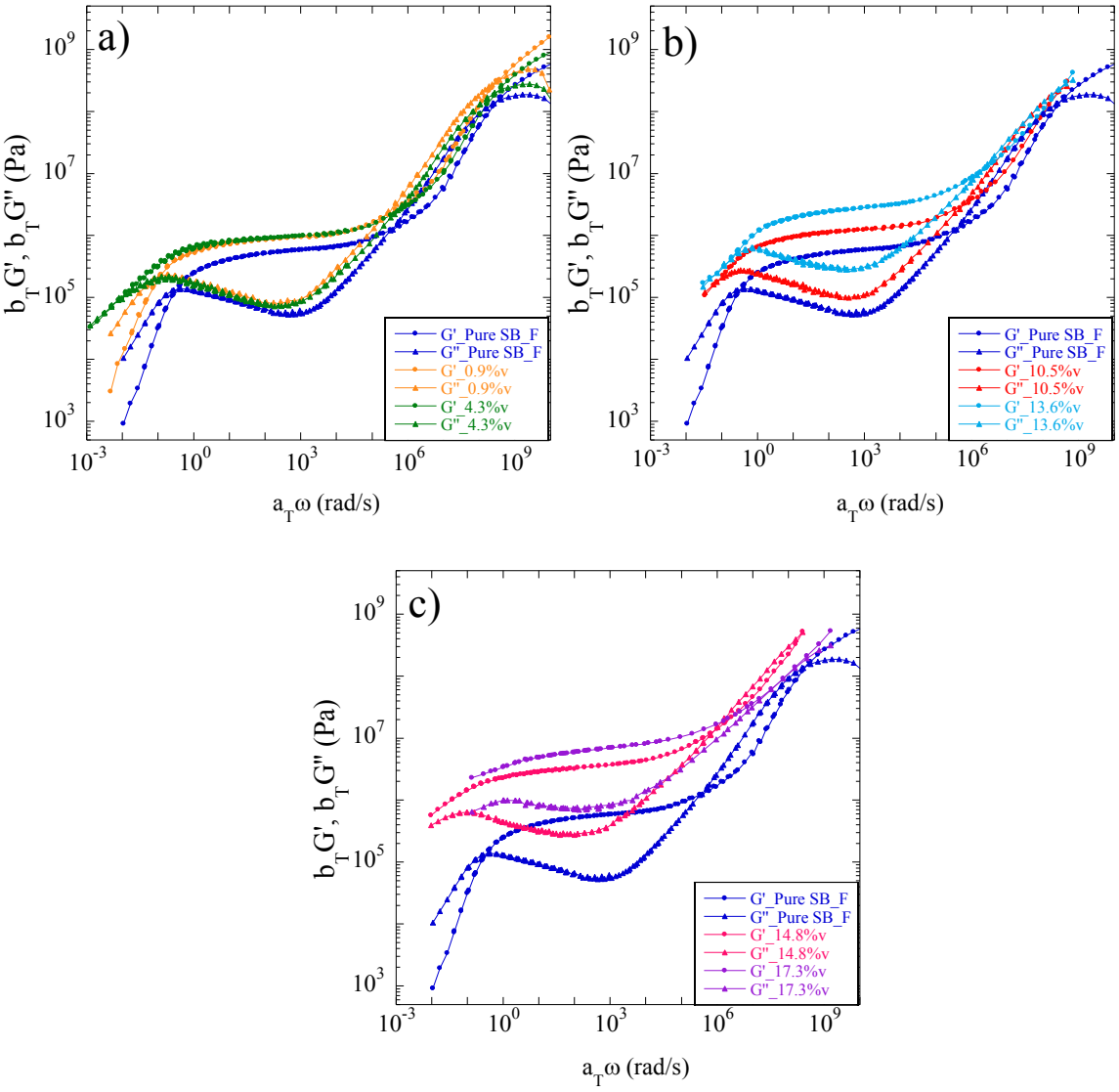

Figure A7.8 (a) TTS master curves for NCs at Φ_{Si}=0.9%v and Φ_{Si}=4.3%v; (b) TTS master curves for NCs at Φ_{Si}=10.5%v and Φ_{Si}=13.6%v, (c) TTS master curves for NCs at Φ_{Si}=14.8%v and Φ_{Si}=17.3%v. In each case, the master curve of NCs are compared with the one of the pure SB_F and they have been shifted at the pure SB_F high frequency cross-over in order to quantitatively compare all the data.

Data in Fig. A7.8 clearly show that the rheological properties of the samples considerably evolve in presence of silica fillers. A small variation of the filler fraction induces a remarkable increase of the viscoelastic moduli with respect to the pure polymer. Moreover, molecular dynamics are slowed down as proved by the fact that the low-frequency crossover is shifted to lower values (i.e. longer times). The change in the molecular dynamics is also reflected by the temperature dependence of the shift factors: even if the introduction of the filler particles has not been significantly changed the a_T shift factors (Fig.

A7.9a), it strongly modified the values and the shape of elastic and the viscous modulus. (Ren et al. 2000; Jouault et al. 2012). The vertical shift factors b_T used for TTS of nanocomposites are shown in Fig. A7.9b.

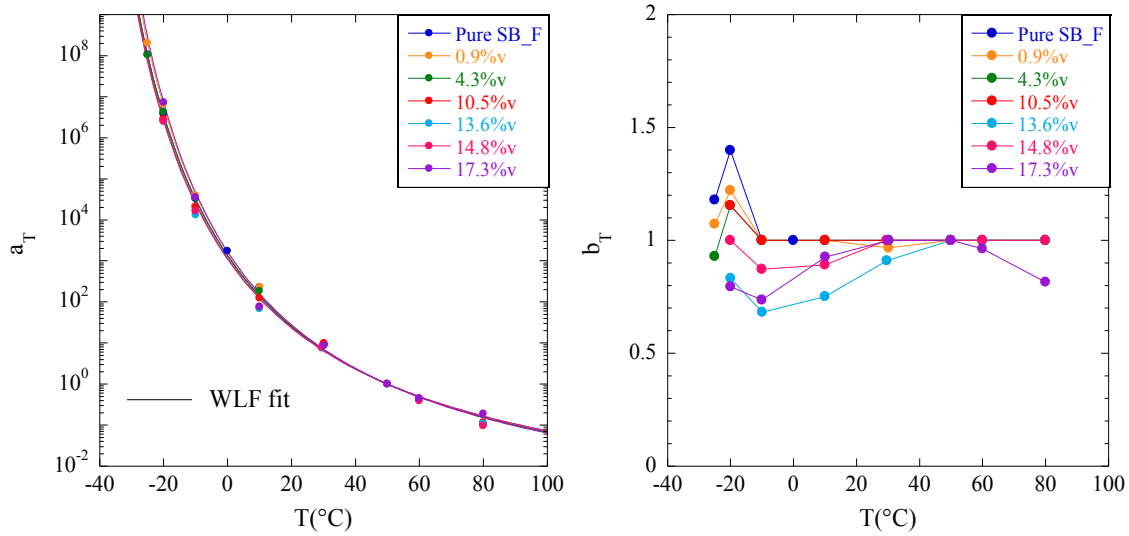

Figure A7.9 (a) Horizontal shift factors (a_T) used for the TTS of nanocomposite samples. a_T varies significantly as a function of the temperature but not from a sample to another (overlapped with a_T of pure SB_F). Its behavior is described by the WLF law (solid lines); (b) vertical shift factors (b_T) used for the TTS of nanocomposite samples.

The frequency spectrum of polymeric systems with high molecular weight is characterized by a plateau of the elastic modulus in the intermediate frequency regime (entanglement regime). The value of G' which corresponds to the minimum of G" is usually indicated as G'_0. Fig. A7.10 shows the relative reinforcement of the nanocomposites with respect to the pure matrix (reinforcement at small strain, $G'_0/G'_{0\_pure\ SB\_F}$) as a function of silica volume fraction. The $G'_0/G'_{0\_pure\ SB\_F}$ ratio represents the filler contribution to the elasticity of the system with respect to the pure matrix.

Firstly, the increase of $G'_0/G'_{0\_pure\ SB\_F}$ with the filler content can be observed. It is known in literature that the magnitude of the reinforcement effect is dependent on the volume concentration of the fillers (Stöckelhuber et al. 2017) since the presence of particles can reduce the mesh size ξ of the system ($G' = kT/\xi^3$, where k is the Boltzman constant and T is the absolute temperature (De Gennes 1979; Thomas 2016). The mechanism of reinforcement of the polymer matrix is generally described by an analogy with hydrodynamics (i.e., hydrodynamic reinforcement: volume effect proposed in analogy with the enhancement of the viscosity of liquids by the addition of particles) (Song and Zheng 2016). For comparison, the most common hydrodynamic reinforcement predictions (see Chapter 1), such as Einstein and Guth-Gold (Einstein 1906; Guth 1945) and the Krieger-Dougherty prediction (Krieger and Dougherty 1959) are also plotted in Fig.A7.10. In our case, the evolution of the hydrodynamic reinforcement as a function of the filler content is not well described by the simple Einstein or Guth-Gold models, while the Krieger-Dougherty equation with the Quemada approximation (Eq. 1.16) fits the data even at high filler concentration. The Krieger-Dougherty model generally allows to determine

maximum packing fraction values φ_c in hard spheres suspension**.** For spherical particles without any interactions, the packing volume fraction φ_c should be equal to 0.64. In a more complex systems, such as polymer NCs, the increase in the effective particle volume fraction leads to a drastic decrease of φ_c (Cassagnau 2008). In our case, the maximum packing fraction determined by fit results equal to 0.25. Even if this cannot be considered as a real quantitative description of the reinforcement effect, this result indirectly suggests that the reinforcement mechanism at high filler fractions is dominated by filler clustering whereas the polymer matrix acts like the embedding medium (Nusser et al. 2013). Thus, the increase of the filler content seems to impact on the relaxation phenomena which occur in NCs.

Moreover, the trend of the reinforcement factor shown in Fig. A7.10 indicates that the systems starts percolating around a filler content of 13%v, considering the strong increase of G'_0/ G'_{0_matrix} (Baeza et al. 2013a). This behavior has to be also compared to the shape of the NC master curves in the terminal-low frequency regime (see below).

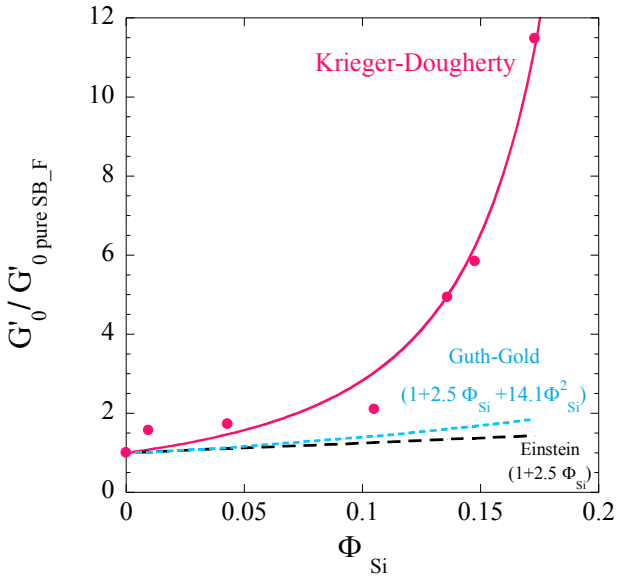

Figure A7.10 Reinforcement G'_0/ G'_{0_matrix} as a function of the filler content. The data have been fitted by different models (Einstein, Guth-Gold) but the Krieger-Dougherty with Quemada approximation seems to better describe the behavior of the reinforcement factor. Moreover, the G'_0/ G'_{0_matrix} around 0.13 seems to suggests that the system starts percolating.

As already mentioned, the master curves shown in Fig. A7.8a,b,c can be quantitatively compared since they are all at the same high frequency cross-over. It is possible to observe that the crossover linked to the relaxation time of an entanglement moves to higher frequency with the increase of the filler content. Thus, the entanglement relaxation time τ_e, evaluated as the inverse of the frequency of the entanglement corss-over, decreases with the increase of the filler content. Fig.A7.11 shows the τ_e of NCs normalized by the τ_e of the pure SB_F polymer ($\tau_e/\tau_{e_{pure\,SB}}$) as a function of the filler content.

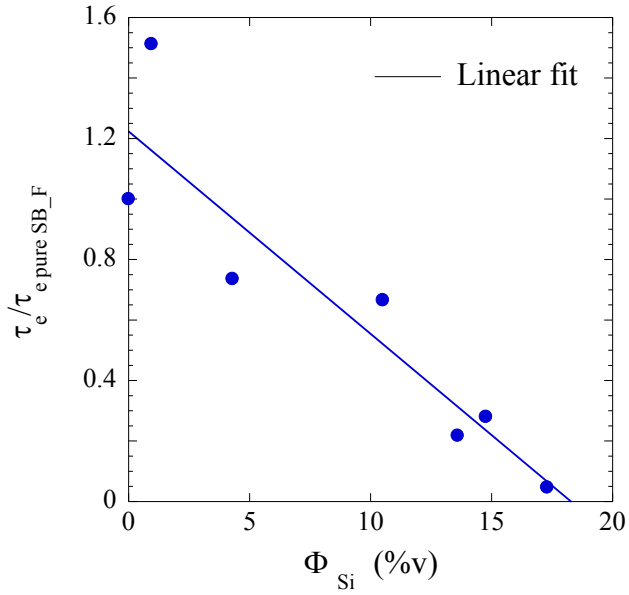

Figure A7.11. Normalized entanglement relaxation time of nanocomposite samples ($\tau_e/\tau_{e_{pure}SB}$). as a function of the filler content. The solid line represents a linear fit to indicate the decrease of decrese of $\tau_e/\tau_{e_{pure}SB}$ with the increase of the filler fraction. It can be considered as a the progressive reduction of the mesh size, because of the presence of the silica particle.

While in the pure polymer matrix the dynamics are dominated by entanglements of the polymer chains, the absorption interactions between the nanoparticles and the polymer chains in NC system hinder the chain motion. This behavior could be explained considering the absorption of the polymer on the filler surface which forms an interfacial region where segmental mobility of the polymer is reduced, i.e. glassy layer (Papon et al. 2012a). The absorption of polymer chains on nanoparticles induces the creation of a network where nanoparticles act as nodes connected by polymer strands: face-to-face inter-particle distance becomes smaller than the entanglements distance. Moreover, the polymer absorption on the particle surface induces the formation of "bridges" between polymer chains, as represented in Fig. A7.11. Thus, the presence of the nanoparticles dispersed in the polymer matrix promotes a reduction of the effective mesh size of the system, resulting in entanglement relaxation time with respect to the pure polymer matrix. This results suggest that the addition of the silica changes the nature of the relaxation processes, in agreement with some recent works (Chen et al. 2015; Baeza et al. 2016a).

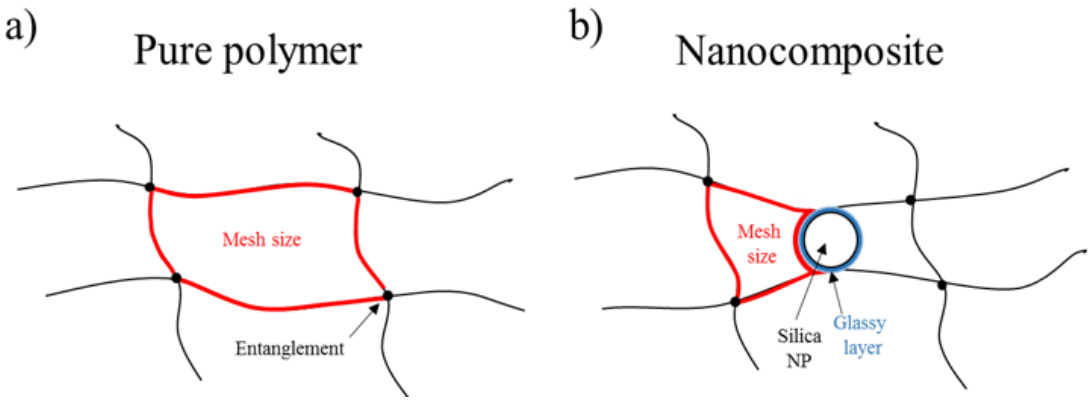

Figure A7.11 (a) Mesh size of pure polymer; (b) mesh size of nanocomposite where the NPs act like nodes between polymer chains inducing a chamgment in the network.

To better look at the behavior in the terminal flow regime (low frequency), all the master curves have been shifted at the same entanglement cross-over (Fig. A7.12). Even if the terminal crossover is not attained for all the samples, one can observe that the terminal crossover moves to lower frequencies with the increase of the filler content. This means that the addition of the filler induces an increase of the reptation time τ_t, which can be explained considering that polymer chains absorbed at the filler surface need a relaxation time as multiple decorrelation (simultaneous desorption) from the particle surfaces is necessary for diffusion (Zhang and Archer 2002). This behavior is described by Baeza *et al.* 2016 as a "train like motion", which explains the low frequency regime for samples at higher silica content as related to the desorption of segments bound to NPs.

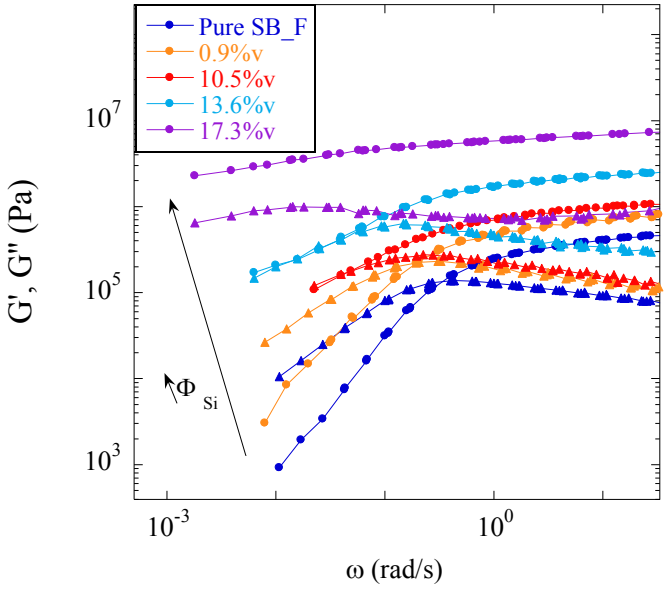

Figure A7.12 Terminal flow regime of master curves of NC samples which have been all shifted at the same entanglement cross-over (G', circle; G", triangles). Samples at 4.3%v and 14.8%v silica are not plotted for clarity reason.The terminal cross-over moves to lower frequencies with the increase of the filler content which can be explained considering the that the polymer chains absorbed at the filler surface need a longer relaxation time since they have to multiple-decorrelate (reptatation). Moreover, the increase of the filler content seems to induce a progressive broadening gel-like transition of the network dynamics.

The change in the network dynamics on NCs with respect to the pure polymer is also confirmed by the qualitative change of G' and G" in the terminal regime which is induced by the increase if the filler content. For samples with silica fractions up to 13%, the low frequency crossover between G' and G" occurs in the narrow frequency range. For samples with larger silica content, the transition from the plateau of G' to the terminal regime occurs over a much broader frequency range. Moreover, a power-law region appears before the terminal regime, with G' and G" that tend to be parallel before reaching the cross-over. Some additional creep measurements (i.e. progressive deformation at constant stress and at constant temperature) could help to better understand the terminal regime dynamics.

Bibliography

Bibliography

Akcora, P., et al., (2010). "Segmental dynamics in PMMA-grafted nanoparticle composites," Macromolecules,43 (19): 8275-8281.

Anderson, B., et al., (2009). "Rheology and microstructure of entangled polymer nanocomposite melts," Macromolecules,42 (21): 8370-8384.

Angell, C.A., (1995). "Formation of glasses from liquids and biopolymers," Science,267 (5206): 1924-1935.

Angell, C.A., (1991). "Relaxation in liquids, polymers and plastic crystals—strong/fragile patterns and problems," Journal of Non-Crystalline Solids,131 13-31.

Badley, R.D, et al., (1990). "Surface modification of colloidal silica," Langmuir,6 (4): 792-801.

Baeza, G.P., (2013). "Nanocomposites industriels simplifiés: analyse structurale et propriétés mécaniques", Université Montpellier 2.

Baeza, G.P., et al., (2013a). "Multiscale Filler Structure in Simplified Industrial Nanocomposite Silica/SBR Systems Studied by SAXS and TEM," Macromolecules,46 (1): 317-329.

Baeza, G.P., et al., (2013b). "Effect of Grafting on Rheology and Structure of a Simplified Industrial Nanocomposite Silica/SBR," Macromolecules,46 (16): 6621-6633.

Baeza, G.P., et al., (2014). "Mechanism of aggregate formation in simplified industrial silica styrene–butadiene nanocomposites: effect of chain mass and grafting on rheology and structure," Soft Matter,10 (35): 6686-6695.

Baeza, G.P., et al., (2015a). "A high-temperature dielectric process as a probe of large-scale silica filler structure in simplified industrial nanocomposites," Physical Chemistry Chemical Physics,17 (3): 1660-1666.

Baeza, G.P., et al., (2015b). "Depercolation of aggregates upon polymer grafting in simplified industrial nanocomposites studied with dielectric spectroscopy," Polymer, 73 131-138.

Baeza, G.P., et al., (2016a). "Network dynamics in nanofilled polymers," Nature communications 7, 11368.

Baeza, G. P., et al., (2016b). "Revealing nanocomposite filler structures by swelling and small-angle X-ray scattering," Faraday discussions,186 295-309.

Baeza, G. P., et al., (2016c). "Revealing nanocomposite filler structures by swelling and small-angle X-ray scattering," Farad. Discuss.,186 295-309.

Banc, A., et al., (2014). "Tuning structure and rheology of silica–latex nanocomposites with the molecular weight of matrix chains: a coupled SAXS–TEM–simulation approach," Macromolecules,47 (9): 3219-3230.

Batchelor, G.K., et al., (1972). "The determination of the bulk stress in a suspension of spherical particles to order c2," Journal of Fluid Mechanics,56 (3): 401-427.

Bergna, H., et al., (2005). Colloidal silica: fundamentals and applications. CRC Press.

Berriot, J., et al., (2003). "Gradient of glass transition temperature in filled elastomers," EPL (Europhysics Letters),64 (1): 50.

Blow, C.M., (1973). "Polymer/particulate filler interaction—the bound rubber phenomena," Polymer,14 (7): 309-323.

Bouty, A., et al., (2014). "Nanofiller structure and reinforcement in model silica/rubber composites: a quantitative correlation driven by interfacial agents," Macromolecules,47 (15): 5365-5378.

Bower, D.I., (2002). “An introduction to polymer physics”. Cambridge University Press.

Boyer, R.F., et al., (1947). "Effect of plasticizers on second-order transition points of high polymers," Journal of Polymer Science Part A: Polymer Chemistry,2 (2): 157-177.

Böhmer, R., et al., (1993). "Nonexponential relaxations in strong and fragile glass formers," The Journal of chemical physics,99 (5): 4201-4209.

Böhning, M., et al., (2005). "Dielectric study of molecular mobility in poly (propylene-graft-maleic anhydride)/clay nanocomposites," Macromolecules,38 (7): 2764-2774.

Bradford, E.B. (1963). "The morphology of synthetic latexes," Journal of Polymer Science: Polymer Symposia, Wiley Online Library.

Brandrup, J., et al., (1989). "Polymer handbook". Wiley New York.

Brochier, S., et al., (2011). "Hydrolysis-condensation kinetics of different silane coupling agents," Phosphorus, Sulfur, and Silicon,186 (2): 240-254.

Buera, M., et al., (1992). "Glass transition in poly (vinylpyrrolidone): effect of molecular weight and diluents," Biotechnology progress,8 (2): 144-148.

Burns, A., et al., (2006). "Fluorescent core–shell silica nanoparticles: towards "Lab on a Particle" architectures for nanobiotechnology," Chemical Society Reviews,35 (11): 1028-1042.

Capponi, S., (2011). "The structure and the dynamics of poly (vinyl methyl ether) PVME and in PVME concentrated water solution: a study by neutron scattering and fully atomistic molecular dynamics simulations". Servicio Editorial de la Universidad del País Vasco/Euskal Herriko Unibertsitatearen Argitalpen Zerbitzua.

Carrot, G., (2006). "Polymer grafting from 10-nm individual particles: proving control by neutron scattering," Soft Matter,2 (12): 1043-1047.

Cassagnau, Ph., (2008). "Melt rheology of organoclay and fumed silica nanocomposites," Polymer,49 (9): 2183-2196.

Castellano, M., et al., (2005). "Surface modification of silica: 1. Thermodynamic aspects and effect on elastomer reinforcement," Polymer,46 (3): 695-703.

Castellano, M., et al., (2007). "Influence of the silane modifiers on the surface thermodynamic characteristics and dispersion of the silica into elastomer compounds," The Journal of Physical Chemistry B,111 (17): 4495-4502.

Cerveny, S., et al., (2002). "Dielectric alpha- and beta-relaxations in uncured styrene butadiene rubber," Macromolecules,35 (11): 4337-4342.

Chen, G., et al., (2005). "Effects of surface properties of colloidal silica particles on redispersibility and properties of acrylic-based polyurethane/silica composites," Journal of colloid and interface science,281 (2): 339-350.

Chen, Q., et al., (2015). "Mechanical reinforcement of polymer nanocomposites from percolation of a nanoparticle network," ACS Macro Letters,4 (4): 398-402.

Cheng, S., et al., (2016). "Unexpected molecular weight effect in polymer nanocomposites," Physical review letters,116 (3): 038302.

Chevigny, C., et al., (2009). "Polystyrene grafting from silica nanoparticles via nitroxide-mediated polymerization (NMP): synthesis and SANS analysis with the contrast variation method," Soft Matter,5 (19): 3741-3753.

Choi, S.S., (2002a). "Difference in bound rubber formation of silica and carbon black with styrene-butadiene rubber," Polymers for Advanced Technologies,13 (6): 466-474.

Choi, S.S., (2002b). "Improvement of properties of silica-filled natural rubber compounds using polychloroprene," Journal of applied polymer science,83 (12): 2609-2616.

Choi, S.S., et al., (2004). "Filler-polymer interactions of styrene and butadiene units in silica-filled styrene–butadiene rubber compounds," Journal of Polymer Science Part B: Polymer Physics,42 (4): 577-584.

Colthup, N.B., et al., (1990). "Chapter 12 - Compounds containing boron, silicon, phosphorus, sulfur, or halogen," in Introduction to Infrared and Raman Spectroscopy (Third Edition).

Conzatti, L., et al., (2008). "Morphology and viscoelastic behaviour of a silica filled styrene/butadiene random copolymer," Macromolecular Materials and Engineering,293 (3): 178-187.

De Gennes, P.G., (1979). "Scaling concepts in polymer". Cornell University Press.

Debye, P., (1915). "Zerstreuung von röntgenstrahlen," Annalen der Physik,351 (6): 809-823.

Derjaguin, B., et al. (1993). "Theory of the stability of strongly charged lyophobic sols and of the adhesion of strongly charged particles in solutions of electrolytes," Progress in Surface Science,43 (1-4): 30-59.

Deshmukh, S.C., et al., (1995). "Investigation of SiO2 plasma enhanced chemical vapor deposition through tetraethoxysilane using attenuated total reflection Fourier transform infrared spectroscopy," Journal of Vacuum Science & Technology A: Vacuum, Surfaces, and Films,13 (5): 2355-2367.

Despert, G., et al., (2003). "Formation of micelle-decorated colloidal silica by adsorption of nonionic surfactant," Langmuir,19 (18): 7604-7610.

Dohi, H., et al., (2007). "Locating a silane coupling agent in silica-filled rubber composites by EFTEM," Langmuir,23 (24): 12344-12349.

Doi, M., et al., (1988). "The theory of polymer dynamics. " Oxford university press.

Donnet, J.-B., (1993). "Carbon black: science and technology. " CRC Press.

Einstein, A., (1906). "A new determination of molecular dimensions," Ann. Phys,19 (2): 289-306.

Feng, Y., et al., (2012). "Relationship between dispersion and conductivity of polymer nanocomposites: a molecular dynamics study," The Journal of Physical Chemistry B,116 (43): 13081-13088.

Ferry, J.D., (1980). "Viscoelastic properties of polymers. " John Wiley & Sons.

Frenkel, D., et al., (1986). "Structure factors of polydisperse systems of hard spheres: A comparison of Monte Carlo simulations and Percus–Yevick theory," The Journal of chemical physics,84 (8): 4625-4630.

Fulcher, G.S., (1925). "Analysis of recent measurements of the viscosity of glasses," Journal of the American Ceramic Society,8 (6): 339-355.

Gauthier, S., et al., (1996). "Study of grafted silane molecules on silica surface with an atomic force microscope," Langmuir,12 (21): 5126-5137.

Genix, A.C., e al., (2012). "Modeling of intermediate structures and chain conformation in silica–latex nanocomposites observed by SANS during annealing," Macromolecules,45 (3): 1663-1675.

Genix, A.C., et al., (2015). "Structure and dynamics of polymer nanocomposites studied by X-ray and neutron scattering techniques," Current Opinion in Colloid & Interface Science,20 (4): 293-303.

Genix, A.C., et al., (2016a). "Recent advances in structural and dynamical properties of simplified industrial nanocomposites," European Polymer Journal,85 605-619.

Genix, A.C., et al., "Determination of the local density of nanoparticle assemblies," (In preparation).

Genovese, D.B., (2012). "Shear rheology of hard-sphere, dispersed, and aggregated suspensions, and filler-matrix composites," Advances in colloid and interface science,171 1-16.

Goerl, U., et al., (1997). "Investigations into the silica/silane reaction system," Rubber chemistry and technology,70 (4): 608-623.

Grabowski, C.A., et al., (2013). "Dielectric Breakdown in Silica–Amorphous Polymer Nanocomposite Films: The Role of the Polymer Matrix," ACS applied materials & interfaces,5 (12): 5486-5492.

Guiner, A., et al., (1955). "Small angle scattering of X-rays," J. Wiley & Sons, New York.

Guth, E., (1945). "Theory of filler reinforcement," Journal of applied physics,16 (1): 20-25.

Hansen, J.-P., et al., (1990). "Theory of simple liquids. " Elsevier.

Hasegawa, R., et al., (1996). "Optimum graft density for dispersing particles in polymer melts," Macromolecules,29 (20): 6656-6662.

Havriliak, S., et al., (1967). "A complex plane representation of dielectric and mechanical relaxation processes in some polymers," Polymer,8 161-210.

Heinrich, G., et al., (2002). "Reinforcement of elastomers," Current opinion in solid state and materials science,6 (3): 195-203.

Holt, A.P., et al., (2014). "Dynamics at the polymer/nanoparticle interface in poly (2-vinylpyridine)/silica nanocomposites," Macromolecules,47 (5): 1837-1843.

Holt, A.P., et al., (2013). "Chain and segmental dynamics of poly (2-vinylpyridine) nanocomposites," Macromolecules,46 (10): 4168-4173.

Hunter, R.J., (2013). "Zeta potential in colloid science: principles and applications. " Academic press.

Immergut, E.H., et al., (1965). "Plasticization and plasticizer processes," Advances in chemistry series,48 1-26.

Ismail, H., et al., (1995). "Effects of multifunctional additive on mechanical properties of silica filled natural rubber compound," European polymer journal,31 (11): 1109-1117.

Jancar, J., et al., (2010). "Current issues in research on structure–property relationships in polymer nanocomposites," Polymer,51 (15): 3321-3343.

Janes, D.W., et al., (2011). "Dispersion morphology of poly (methyl acrylate)/silica nanocomposites," Macromolecules,44 (12): 4920-4927.

Jouault, N., et al., (2009). "Well-dispersed fractal aggregates as filler in polymer− silica nanocomposites: long-range effects in rheology," Macromolecules,42 (6): 2031-2040.

Jouault, N., et al., (2012). "Multiscale characterization of filler dispersion and origins of mechanical reinforcement in model nanocomposites," Polymer,53 (3): 761-775.

Jouault, N., et al., (2014). "Role of casting solvent on nanoparticle dispersion in polymer nanocomposites," Macromolecules,47 (15): 5246-5255.

Kadam, A.A., et al., (2016). "Plasticization of amorphous polystyrene by volatile organic compounds," Polymer Bulletin,73 (7): 1841-1853.

Kaewsakul, W., et al., (2012). "Optimization of mixing conditions for silica-reinforced natural rubber tire tread compounds," Rubber chemistry and technology,85 (2): 277-294.

Katz, H.S., et al., (1987). "Handbook of fillers for plastics." Springer Science & Business Media.

Khoee, S., et al., (2007). "Microstructure analysis of brominated styrene–butadiene rubber," Polymer Engineering & Science,47 (2): 87-94.

Kim, S., et al., (2009). "Drying of the silica/PVA suspension: effect of suspension microstructure," Langmuir,25 (11): 6155-6161.

Kim, S., et al., (2016). "Structural Development of Nanoparticle Dispersion during Drying in Polymer Nanocomposite Films," Macromolecules,49 (23): 9068-9079.

Klüppel, M., (2008). "Evaluation of viscoelastic master curves of filled elastomers and applications to fracture mechanics," Journal of Physics: Condensed Matter,21 (3): 035104.

Kosmalska, A., et al., (2003). "Adsorption of curatives and activity of silica toward elastomers," Macromolecular Symposia, Wiley Online Library.

Kosmulski, M., (2001). "Chemical properties of material surfaces." CRC press.

Kremer, F., et al., (2003). "Broadband Dielectric Spectroscopy." Springer-Verlag.

Krieger, I., et al., (1959). "A mechanism for non-Newtonian flow in suspensions of rigid spheres," Transactions of the Society of Rheology,3 (1): 137-152.

Kropka, J.M., et al., (2008). "Local Polymer Dynamics in Polymer− C60 Mixtures," Nano letters,8 (4): 1061-1065.

Kumar, N., et al., (2005). "Methods to disperse and exfoliate nanoparticles." Google Patents.

Kumar, S.K., et al., (2013). "Nanocomposites with polymer grafted nanoparticles," Macromolecules,46 (9): 3199-3214.

Lapra, A., et al., (2003). "Straining effects in silica-filled elastomers investigated by atomic force microscopy: from macroscopic stretching to nanoscale strainfield," Rubber Chemistry and technology,76 (1): 60-81.

Le Diagon, Y., et al., (2007). "Particle structuring under the effect of an uniaxial deformation in soft/hard nanocomposites," The European Physical Journal E: Soft Matter and Biological Physics,22 (1): 77-83.

Liff, S.M., et al., (2007). "High-performance elastomeric nanocomposites via solvent-exchange processing," Nature materials,6 (1): 76-83.

Lin, Y., et al., (2016). "Unexpected segmental dynamics in polystyrene-grafted silica nanocomposites," Soft matter,12 (41): 8542-8553.

Lindner, P., et al., (1991). "Neutron, X-ray and light scattering: introduction to an investigative tool for colloidal and polymeric systems,"

Mancke, R.G., et al., (1968). "Dynamic Mechanical Properties of Cross-Linked Rubbers. IV. Dicumyl Peroxide Vulcanizates of Styrene-Butadiene Rubber," Transactions of the Society of Rheology,12 (2): 335-350.

Mangal, R., et al., (2016). "Size-dependent particle dynamics in entangled polymer nanocomposites," Langmuir,32 (2): 596-603.

Mark, J.E., et al., (2013). "The science and technology of rubber. " Academic press.

Medalia, A.I., (1970). "Morphology of aggregates: VI. Effective volume of aggregates of carbon black from electron microscopy; Application to vehicle absorption and to die swell of filled rubber," Journal of Colloid and Interface Science,32 (1): 115-131.

Merabia, S., (2010). "Unique plastic and recovery behavior of nanofilled elastomers and thermoplastic elastomers (Payne and Mullins effects)," Journal of Polymer Science Part B: Polymer Physics,48 (13): 1495-1508.

Meth, J.S., et al., (2011). "Development of filler structure in colloidal silica–polymer nanocomposites," Macromolecules,44 (20): 8301-8313.

Metropolis, N., et al., (1953). "Equation of state calculations by fast computing machines," The journal of chemical physics,21 (6): 1087-1092.

Mijović, J., et al., (2006). "Dynamics in polymer− silicate nanocomposites as studied by dielectric relaxation spectroscopy and dynamic mechanical spectroscopy," Macromolecules,39 (6): 2172-2182.

Mittal, K.L., (2007). "Silanes and other coupling agents." CRC Press.

Mondragón, M.A., et al., (1995). "Vibrational analysis of Si(OC2H5)4 and spectroscopic studies on the formation of glasses via silica gels," Vibrational Spectroscopy,9 (3): 293-304.

Morton, M., (2013). "Rubber technology. " Springer Science & Business Media.

Mujtaba, A., et al., (2012). "Mechanical properties and cross-link density of styrene–butadiene model composites containing fillers with bimodal particle size distribution," Macromolecules,45 (16): 6504-6515.

Mujtaba, A., et al., (2014). "Detection of surface-immobilized components and their role in viscoelastic reinforcement of rubber–silica nanocomposites," ACS Macro Letters,3 (5): 481-485.

Musino, D., et al., (2017). "Synergistic Effect of Small Molecules on Large-Scale Structure of Simplified Industrial Nanocomposites," Macromolecules,

Musino, D., et al., "Impact of surface modification of silica nanoparticles on dispersion in precursor solvents and model polymer nanocomposites," (In preparation, a).

Musino, D., et al., "Aggregate formation of surface-modified nanoparticles in solvents and polymer nanocomposites," (Submitted, b).

Mélé, P., et al., (2002). "Reinforcement effects in fractal-structure-filled rubber," Polymer,43 (20): 5577-5586.

Nusser, K., et al., (2013). "Rheology and anomalous flow properties of poly (ethylene-alt-propylene)–silica nanocomposites," Macromolecules,46 (15): 6263-6272.

Oberdisse, J., (2002). "Structure and Rheological Properties of Latex− Silica Nanocomposite Films: Stress− Strain Isotherms," Macromolecules,35 (25): 9441-9450.

Oberdisse, J., et al., (2002). "Structure of Latex− Silica Nanocomposite Films: A Small-Angle Neutron Scattering Study," Macromolecules,35 (11): 4397-4405.

Oberdisse, J., (2006). "Aggregation of colloidal nanoparticles in polymer matrices," Soft matter,2 (1): 29-36.

Oberdisse, J., et al., (2007). "Structure of interacting aggregates of silica nanoparticles in a polymer matrix: small-angle scattering and reverse Monte Carlo simulations," Soft Matter,3 (4): 476-485.

Osterholtz, F.D., et al., (1992). "Kinetics of the hydrolysis and condensation of organofunctional alkoxysilanes: a review," Journal of Adhesion Science and Technology,6 (1): 127-149.

Otegui, J., et al., (2013). "Influence of Water and Filler Content on the Dielectric Response of Silica-Filled Rubber Compounds," Macromolecules,46 (6): 2407-2416.

Papon, A., et al., (2011). "Low-field NMR investigations of nanocomposites: polymer dynamics and network effects," Macromolecules,44 (4): 913-922.

Papon, A., et al., (2012a). "Solid particles in an elastomer matrix: impact of colloid dispersion and polymer mobility modification on the mechanical properties," Soft Matter,8 (15): 4090-4096.

Papon, A., et al., (2012b). "Glass-transition temperature gradient in nanocomposites: evidence from nuclear magnetic resonance and differential scanning calorimetry," Physical review letters,108 (6): 065702.

Paul, D.R., et al., (1978). "Polymer blends, vol. 2," Academic, New York,

Payne, A.R., (1965). "A note on the conductivity and modulus of carbon black-loaded rubbers," Journal of Applied Polymer Science,9 (3): 1073-1082.

Pedersen, J.S., et al., (1999). "Static properties of polystyrene in semidilute solutions: a comparison of Monte Carlo simulation and small-angle neutron scattering results," EPL (Europhysics Letters),45 (6): 666.

Penot, C., et al., (2006). "Rubber composition for a tire comprising a reinforcing inorganic filler and an (inorganic filler/elastomer) coupling system. " Google Patents.

Pérez-Aparicio, R., et al., (2013a). "Local chain deformation and overstrain in reinforced elastomers: an NMR study," Macromolecules,46 (14): 5549-5560.

Pérez-Aparicio, R., et al., (2013b). "Reinforcement in natural rubber elastomer nanocomposites: breakdown of entropic elasticity," Macromolecules,46 (22): 8964-8972.

Prucker, O., et al., (1998). "Mechanism of radical chain polymerizations initiated by azo compounds covalently bound to the surface of spherical particles," Macromolecules,31 (3): 602-613.

Pukánszky, B., et al., (1999). "Adhesion and surface modification," Mineral fillers in thermoplastics I,109-153.

Qu, L., et al., (2013). "Effect of silane coupling agent on filler and rubber interaction of silica reinforced solution styrene butadiene rubber," Polymer Composites,34 (10): 1575-1582.

Quemada, D., (1977). "Rheology of concentrated disperse systems and minimum energy dissipation principle," Rheologica Acta,16 (1): 82-94.

Ramier, J., et al., (2006). "Grafting of silica during the processing of silica-filled SBR: Comparison between length and content of the silane," Journal of Polymer Science Part B: Polymer Physics,44 (1): 143-152.

Ramier, J., et al., (2007a). "Influence of Silica and its Different Surface Treatments on the Vulcanization Process of Silica Filled SBR," Rubber Chem. Technol.,80 (1): 183-193.

Ramier, J., et al., (2007b). "Payne effect in silica-filled styrene–butadiene rubber: Influence of surface treatment," Journal of Polymer Science Part B: Polymer Physics,45 (3): 286-298.

Ranjan, R., et al., (2007). "Combination of living radical polymerization and click chemistry for surface modification," Macromolecules,40 (17): 6217-6223.

Ren, J., (2000). "Linear viscoelasticity of disordered polystyrene− polyisoprene block copolymer based layered-silicate nanocomposites," Macromolecules,33 (10): 3739-3746.

Rharbi, Y., et al., (1999). "Modes of deformation in a soft/hard nanocomposite: A SANS study," EPL (Europhysics Letters),46 (4): 472.

Rittigstein, P., et al., (2007). "Model polymer nanocomposites provide an understanding of confinement effects in real nanocomposites," Nature materials,6 (4): 278.

Robertson, C.G., et al., (2011). "Further consideration of viscoelastic two glass transition behavior of nanoparticle-filled polymers," Macromolecules,44 (5): 1177-1181.

Rubinstein, M., et al., (2003). "Polymer physics." Oxford University Press New York.

Russel, W.B., et al., (1989). "Colloidal dispersions." Cambridge university press.

Schaal, S., et al., (2000). "The effects of certain recipe ingredients and mixing sequence on the rheology and processability of silica-and carbon black-filled tire compounds," Rubber chemistry and technology,73 (2): 240-252.

Schmidt, G., et al., (2003). "Properties of polymer–nanoparticle composites," Current opinion in colloid & interface science,8 (1): 103-108.

Schmitt C.P., et al., (2015). "Surface modification of alumina-coated silica nanoparticles in aqueous sols with phosphonic acids and impact on nanoparticle interactions," Physical Chemistry Chemical Physics,17 (29): 19173-19182.

Schmitt C.P., et al., (2016). "Structure of alumina-silica nanoparticles grafted with alkylphosphonic acids in poly (ethylacrylate) nanocomposites," Polymer,97 138-146.

Scotti, R., et al., (2014). "Shape controlled spherical (0D) and rod-like (1D) silica nanoparticles in silica/styrene butadiene rubber nanocomposites: Role of the particle morphology on the filler reinforcing effect," Polymer,55 (6): 1497-1506.

Sindorf, D.W., et al., (1983). "Solid-state NMR studies of the reactions of silica surfaces with polyfunctional chloromethylsilanes and ethoxymethylsilanes," Journal of the American Chemical Society,105 (12): 3767-3776.

Smallwood, H.M., (1944). "Limiting law of the reinforcement of rubber," Journal of applied physics,15 (11): 758-766.

Song, Y., et al., (2016). "A guide for hydrodynamic reinforcement effect in nanoparticle-filled polymers," Critical Reviews in Solid State and Materials Sciences,41 (4): 318-346.

Steeman, P.A.M., et al., (1990). "An interlayer model for the complex dielectric constant of composites," Colloid & Polymer Science,268 (4): 315-325.

Steeman, P.A.M., et al., (1991). "Dielectric monitoring of water absorption in glass-bead-filled high-density polyethylene," Polymer,32 (3): 523-530.

Sternstein, S.S., et al., (2002). "Reinforcement mechanism of nanofilled polymer melts as elucidated by nonlinear viscoelastic behavior," Macromolecules,35 (19): 7262-7273.

Stockelhuber, K.W., et al., (2011). "Impact of filler surface modification on large scale mechanics of styrene butadiene/silica rubber composites," Macromolecules,44 (11): 4366-4381.

Stöber, W., et al., (1968). "Controlled growth of monodisperse silica spheres in the micron size range," Journal of colloid and interface science,26 (1): 62-69.

Stöckelhuber, K.W., et al., (2017). "Designing of Elastomer Nanocomposites: From Theory to Applications. " Springer.

Suzuki, N., et al., (2005). "Effects of rubber/filler interactions on deformation behavior of silica filled SBR systems," Polymer,46 (1): 193-201.

Tabatabaei, S., et al., (2006). "Experimental study of the synthesis and characterisation of silica nanoparticles via the sol-gel method, Journal of Physics: Conference Series, " IOP Publishing.

Tatou, M., et al., (2011). "Reinforcement and polymer mobility in silica–latex nanocomposites with controlled aggregation," Macromolecules,44 (22): 9029-9039.

Thomas, S., (2016). "Rheology and Processing of Polymer Nanocomposites. " John Wiley & Sons.

Treloar, L.R.G., (1975). "The physics of rubber elasticity. " Oxford University Press, USA.

Tung, W.-S., et al., (2016). "Temperature-Dependent Suppression of Polymer Diffusion in Polymer Nanocomposites," ACS Macro Letters,5 (6): 735-739.

Valentin, J.L., et al., (2006). "Characterization of the reactivity of a silica derived from acid activation of sepiolite with silane by 29 Si and 13 C solid-state NMR," Journal of colloid and interface science,298 (2): 794-804.

Vieyres, A., (2013). "Influence of filler/polymer interface on reinforcement, strain-induced crystallization and tear resistance in reinforced natural rubber." Université Claude Bernard-Lyon I.

Vilmin, F., et al., (2014). "Reactivity of bis [3-(triethoxysilyl) propyl] tetrasulfide (TESPT) silane coupling agent over hydrated silica: Operando IR spectroscopy and chemometrics study," The Journal of Physical Chemistry C,118 (8): 4056-4071.

Vogel, H., (1921). "The law of the relation between the viscosity of liquids and the temperature," Phys. Z,22 645-646.

Wang, W., et al., (2003). "Fabrication of near-infrared photonic crystals using highly-monodispersed submicrometer SiO2 spheres," The Journal of Physical Chemistry B,107 (44): 12113-12117.

Whitten, P.G., et al., (2007). "Polymer entanglement density and its influence on interfacial friction," Physical Review E,76 (2): 026101.

Williams, M.L., et al., (1955). "The temperature dependence of relaxation mechanisms in amorphous polymers and other glass-forming liquids," Journal of the American Chemical society,77 (14): 3701-3707.

Wolf, B., et al., (2007). "Shear thickening of an emulsion stabilized with hydrophilic silica particles," Journal of Rheology,51 (3): 465-478.

Wolff, S., et al., (1992). "Filler—elastomer interactions. Part IV. The effect of the surface energies of fillers on elastomer reinforcement," Rubber chemistry and technology,65 (2): 329-342.

Wool, R.P., (1993). "Polymer entanglements," Macromolecules,26 (7): 1564-1569.

Wu, Y.-P., et al., (2008). "The influence of in situ modification of silica on filler network and dynamic mechanical properties of silica-filled solution styrene–butadiene rubber," Journal of applied polymer science,108 (1): 112-118.

Wu, Z., et al., (2007). "Controlling the hydrophobicity of submicrometer silica spheres via surface modification for nanocomposite applications," Langmuir,23 (14): 7799-7803.

Wypych, G., (2004). "Handbook of plasticizers. " ChemTec Publishing.

Wypych, G., (2016). "Handbook of fillers. " Elsevier.

Wyss, H.M., (2003). "Microstructure and mechanical behavior of concentrated particle gels." Elsevier.

Yatsuyanagi, F., et al., (2001). "Effects of secondary structure of fillers on the mechanical properties of silica filled rubber systems," Polymer,42 (23): 9523-9529.

Yatsuyanagi, F., (2002). "Effects of surface chemistry of silica particles on the mechanical properties of silica filled styrene–butadiene rubber systems," Polymer journal,34 (5): 332-339.

Yrieix, M., (2016). "Impact du couplage charges/matrice sur les propriétés rhéologiques de nanocomposites silice/élastomère: application aux défauts volumiques d'extrusion." Université de Lyon.

Zaborski, M., et al., (2003), *Activity of fillers in elastomer networks of different structure*, Macromolecular Symposia, Wiley Online Library.

Zhang, L., et al., (2000). "Morphology and mechanical properties of clay/styrene-butadiene rubber nanocomposites," Journal of Applied Polymer Science,78 (11): 1873-1878.

Zhang, M.Q., et al., (2001). "Atomic force microscopy study on structure and properties of irradiation grafted silica particles in polypropylene-based nanocomposites," Journal of applied polymer science,80 (12): 2218-2227.

Zhang, Q., et al., (2002). "Poly (ethylene oxide)/silica nanocomposites: structure and rheology," Langmuir,18 (26): 10435-10442.

Zhao, D.,et al., (2014). "Controlling the thermomechanical behavior of nanoparticle/polymer films," Acs Nano,8 (8): 8163-8173.

Zhuravlev, L.T., (2000). "The surface chemistry of amorphous silica. Zhuravlev model," Colloids and Surfaces A: Physicochemical and Engineering Aspects,173 (1): 1-38.

Résumé en français du travail de thèse

Impact de la modification de surface de nanoparticules sur la structure et la dynamique de nanocomposites silice-polymère

Les matériaux nanocomposites obtenus par dispersion de charges nanométriques dans un polymère ont des nombreuses applications industrielles grâce à l'amélioration des propriétés des matrices. La dispersion des charges pendant le procès de préparation des nanocomposites est déterminée par les interactions entre charges et polymère. L'état final de dispersion impacte les propriétés structurales et dynamiques. La détermination des propriétés macroscopiques - mécaniques, électriques, ou autres – induites par la structure et la dynamique du matériau nanocomposite est une question fondamentale à laquelle nous avons essayé de répondre lors de cette thèse.

Nous présentons ici une étude concernant les nanocomposites de silice-polymère (styrène-butadiène, SB) non réticulés où la compatibilité entre les charges et le polymère est rendu possible par l'introduction de petites molécules, telles que des agents de recouvrement (silanes). Ces molécules sont capables de modifier les propriétés de surface des particules de silice en les rendant plus hydrophobes – ce qui améliore les interactions avec un polymère hydrophobe (SB). Cette approche permet de mieux contrôler la dispersion de la charge dans la matrice de polymère, ce qui modifie les propriétés structurelles, dynamiques et mécaniques du matériau final.

Notre partenariat avec Solvay, nous a permis de reproduire avec succès la formulation des nanocomposites industrielles simplifiés non réticulés, selon le protocole proposé dans les travaux de Baeza et al. (Baeza et al. 2013a). Dans ce système, obtenu par l'incorporation de silice hautement dispersible dans le styréne-butadiéne, nous avons fait le choix de limiter le nombre d'ingrédients dans la formulation (i.e., les nanoparticules, le polymère, l'agent de recouvrement et un catalyseur). Le but de cette limitation étant de mieux apprendre l'impact de chaque composant sur les propriétés des échantillons. En couplant des expériences de diffusion des rayons-X aux petits angles (DXPA) avec de la microscopie électronique à transmission (MET), la dispersion de la silice dans la matrice polymérique a été étudiée en fonction des différents paramètres comme la variation de polymère fonctionnel ou la quantité d'agent de recouvrement. Un exemple d'image acquise par MET pour un nanocomposite industriel simplifié est montré en Fig. R1. Nous avons quantifié l'effet des agents de recouvrement selon la longueur de leur chaîne alkyle (C_8, C_{12} et C_{18}) sur la structure en termes de formation d'agrégats. Nous avons montré que la longueur de la chaîne alkyle du silane n'a pas d'impact sur la microstructure des nanocomposites mais que l'augmentation de la quantité de silane favorise la réduction de la taille des agrégats de silice. De plus, nous avons clarifié le rôle du catalyseur, diphényl-guanidine (DPG), couramment utilisé dans la fabrication de pneus. Nous avons mis en avant l' effet synergique existe entre DPG et agent de recouvrement: les DPG est nécessaire pour favoriser l'effet compatibilisant du silane.

Cette étude a été étendue aux nanocomposites industrielles simplifiés réticulés, obtenus par vulcanisation. Même dans ce cas, nous avons révélé que l'action synergique de la DPG et du silane est essentielle pour régler la dispersion de la charge et donc la structure finale du matériau composite.

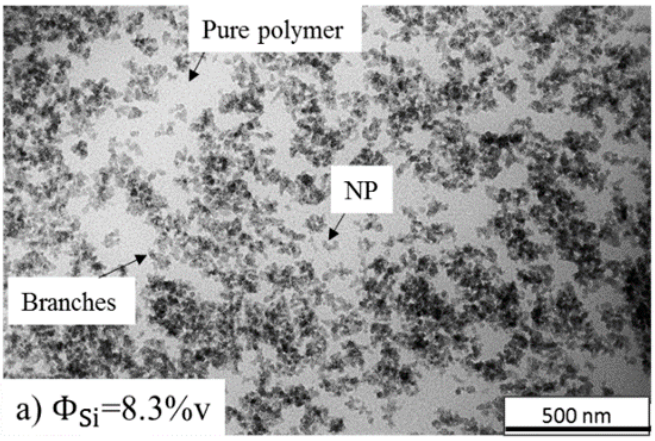

Figure R1 Image MET d'un nanocomposite industriel simplifié formulé en utilisant C_8 comme agent de recouvrement à un taux de silice de 8,3% v, en présence de DPG. Les régions occupées du polymère pur sont bien visibles. Selon l'échelle de gris, des nanoparticules primaires peuvent être observées.

L'étude des nanocomposites industrielles simplifiées a été étendue à un nouveau système modèle silice-styrène/butadiène, entièrement développé dans le cadre de ma thèse au Laboratoire Charles Coulomb. Ce système a été formulé par une procédure en plusieurs étapes, où les nanoparticules de silice colloïdale modifiées sont dispersées dans la matrice de polymère styrène-butadiène en présence d'un solvant (méthyl-éthylcétone, MEK). Le nanocomposite est obtenu après l'évaporation complète de ce solvant. Afin de réaliser un système modèle équivalent su système industriel, le premier objectif était de modifier la surface des nanoparticules de silice en suspension en utilisant des agents de recouvrement. Nous avons développé avec succès une méthode efficace pour modifier la surface des billes de silice dans un mélange éthanol / eau, en obtenant une densité de greffe d'environ 1 molécule / nm^2. Ce taux de greffage a été estimé par analyse thermogravimétrique (ATG), Fig. R2a.

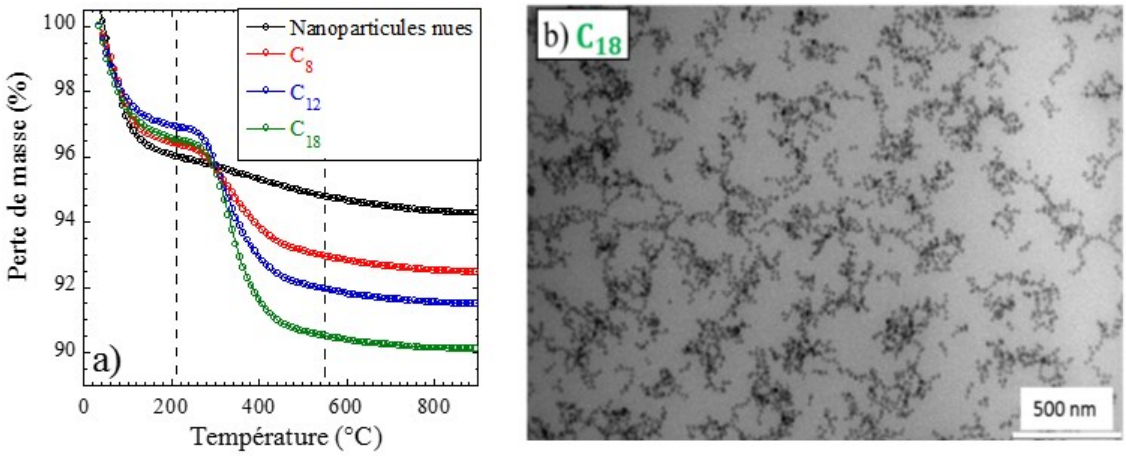

Figure R2 (a) La perte de masse entre la température ambiante et 900 ° C est liée à l'évaporation de l'eau absorbée physiquement sur les NP (jusqu'à 200 ° C), à la décomposition des molécules de silane greffées (entre 200 ° C et 550 ° C) et à la condensation des groupes silanol sur la surface de la silice (jusqu'à 900 ° C). (b) Image MET de un nanocomposite modèle.

Par une procédure d'échange de solvant (dialyse), nous avons ensuite transféré et stabilisé les particules modifiées dans le solvant (MEK) utilisé pour solubiliser le polymère. Grâce à cette étape, la suspension de particules greffées peut être mélangée avec le polymère pour obtenir le nanacomposite modèle. Un exemple d'image MET de un nanocomposite modèle est montré in Fig. R2b. Pour ce système, la modification de la surface a été effectuée avec des molécules de silane qui diffèrent: i) par la longueur de chaîne d'alkyle (C_8, C_{12} et C_{18}), comme pour les nanocomposites industrielles simplifiées; ii) par la nature de la fonction permettant le greffage, telle que le triéthoxy, le triméthoxy, le monométhoxy-octylsilane (indiqués C_8, C_{8m} et C_{8mm}).

Pour la caractérisation structurale de ce système modèle, nous avons couplé des mesures de diffusion des rayons-X aux petits angles avec de simulations de Monte Carlo inverse. Les résultats nous ont permis d'étudier l'état de dispersion des nanoparticules de silice greffées dans le mélange éthanol/eau et dans la MEK, et même dans le matériel nanocomposite final. Dans chaque milieu, nous avons pu déterminer les fonctions de distribution des nombres d'agrégations, et en extraire la masse des agrégats en présence ou absence d'interaction. Nous avons prouvé qu'après la réaction en solution hydro-alcoolique, les particules étaient plutôt agrégées, alors qu'après leur transfert dans la MEK, les expériences des DXPA ont révélé la répulsion entre agrégats plus petits. Cela suggère que l'agrégation est réversible, et que c'est la couche greffée qui protège les particules d'une agrégation irréversible. En ce qui concerne la modification de la surface des nanoparticules par des silanes avec une hydrophobicité différente, nous avons montré que les interactions de particules en suspension n'étaient que légèrement affectées par le type de greffe, et que le C_{18} (i.e., silane avec la chaîne d'alkyle la plus importante) induit toujours les nombres d'agrégation les plus élevés. Lorsque la modification de surface a été effectuée par des silanes avec différentes fonctions, les distributions de masse des agrégats semblent être conservées de la MEK

aux nanocomposites. D'autre part, seul les billes modifiées par le C_8 conservent une distribution de masse comparable, alors que cette distribution devient plus large pour le C_{8m} et le C_{8mm}.

Pour le système modèle, l'impact des agents de recouvrement sur les propriétés dynamiques (relaxation α) du système modèle a été étudié par spectroscopie diélectrique, BDS. Tout d'abord, nous avons montré comment les agents de recouvrement peuvent être utilisés pour induire la plastification de la matrice de polymère styrène-butadiène. Cela se traduit par une diminution du temps de relaxation du processus α et donc à une réduction de la température de transition vitreuse (mesurée par calorimétrie). En ce qui concerne les nanocomposites, nous avons étudié deux types de systèmes: i) les nanocomposites modèles *greffés*, où le silane est chimiquement attaché à la surface des nanoparticules de silice avant leur dispersion dans la matrice de polymère. Dans ce cas, la dynamique de la relaxation α n'est pas modifiée par le traitement de surface des nanoparticules; ii) les nancomposites modèles *non greffés*, où l'agent de recouvrement vient d'être ajouté après la dispersion de la silice dans la matrice de polymère. Dans ce cas, un effet de plastification n'est induit que quand l'échantillon est formulé avec du polymère avec des chaînes fonctionnalisées et du C_{18} comme agent de recouvrement, Fig. R3.

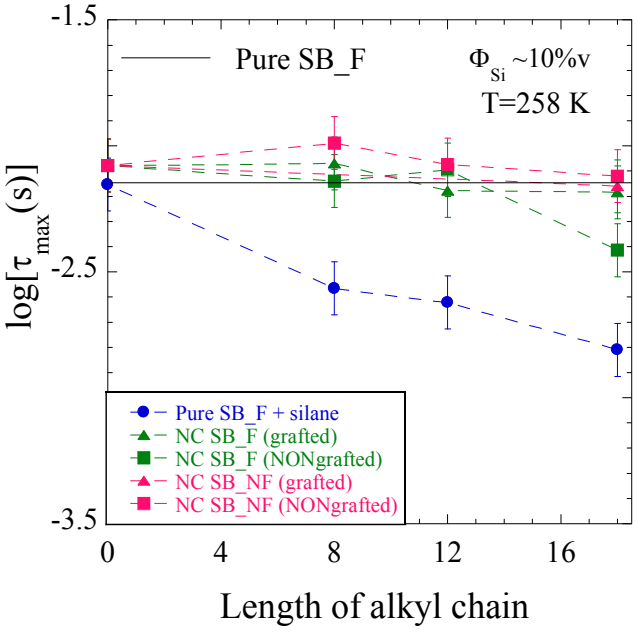

Fig. R3 Temps de relaxation de la relaxation α à T = 258 K pour les nanocomposites modèles *greffés* et *non greffés* en fonction de la longueur de chaîne alkylique du chaque silane. La ligne noire indique le niveau de la matrice SB_F pure. Les barres d'erreur ont été estimées compte tenu de la variation du temps de relaxation entre deux points expérimentaux consécutifs en fréquence.

Nous avons interprété ce résultat en tenant compte soit de l'interaction favorable entre les silanes et le groupe fonctionnel des chaînes de polymères, soit de l'interaction favorable du groupe terminal du polymère avec les groupes hydroxyles de la silice qui empêchent les molécules de silane d'être adsorbées sur la surface de la silice. Ainsi, dans les nanocomposites modèles non greffés préparés avec le polymère SB_F et C_{18}, nous avons étudié l'impact de la variation du taux de silice (i.e., fraction

volumique de silice). Nous avons estimé la quantité de silane présent dans la fraction polymérique du composite, révélant que l'amplitude de l'effet de plastification augmente jusqu'à une fraction de silice de environ 11,8% v: l'augmentation du taux de charge correspond à une diminution de la fraction de polymère et par conséquent à l'augmentation du nombre de molécules de silane par chaîne de polymère. Pour de taux de silice supérieur à 11,8% v, la formation d'un réseau percolée semblait prévaloir sur la plastification car une augmentation du temps de relaxation α est enregistrée. De plus, la variation du rapport C_{18}/silice indique que la plastification peut également être induite dans une matrice polymère entièrement non fonctionnalisée, pour des quantités de silane suffisamment élevées, au-delà de la saturation de la surface des billes de silice.

Les résultats de ce travail de thèse ont montré comme la formulation de matériaux nanocomposites avec agents de recouvrement peut impactée leur propriétés structurales (i.e., taille des agrégats et fonctions de distribution des nombres d'agrégations) et dynamiques (i.e., effet de plastification).
L'ensemble des ces résultats peut aider à une meilleure compréhension des caractéristiques fondamentales des matériaux composites et à promouvoir une conception rationnelle de leur formulation.

Impact of nanoparticle surface modification on the structure and dynamics of silica-polymer nanocomposites

Nanocomposite materials made by dispersion of nano-scale fillers in a soft polymer matrix attract industrial interest because of their enhanced properties. During their formulation, filler-filler and filler-polymer interactions affect the dispersion of the particles, and thus the final nanocomposite structure. The filler dispersion as well as dynamical properties control many material properties and in particular the mechanical response of these materials.
In this PhD work, we propose the study of nanocomposites made by dispersion of nano-metric hydrophilic silica particles in a soft hydrophobic polymer matrix of styrene/butadiene (SB), which is commonly used in car tire manufacturing. Since coating agents can react with the filler surface tuning the silica-silica and the silica-polymer interactions, they have been used to promote the compatibility between silica and SB. Firstly, we investigate "simplified industrial nanocomposites" obtained by solid mixing of SB and millimetric silica pellets. By a multiscale approach (microscopy and X-ray scattering, SAXS) we show that: i) the presence of a catalyzer (DPG) unambiguously amplifies the action of the coating agent; ii) the increase of silane content induces the progressive decrease of silica aggregate size. The study of the simplified industrial nanocomposites has been extended to a silica/SB model system. We developed an efficient method to surface-modify colloidal silica NPs in ethanol/water, to stabilize them in the same solvent (MEK) used to dissolve the polymer, and to obtain the final model nanocomposite by solvent casting. For the structural characterization of this multi-step system, we propose a combined SAXS-reverse Monte Carlo approach which allows to investigate the dispersion state of surface-modified silica NPs in precursor solvents (i.e., ethanol/water and MEK) and in the polymer matrix. The filler dispersion is influenced by the characteristics of the grafted silane molecule (varying hydrophobicity, grafting function, and density) and it is shown the quality of the dispersion state is maintained from the precursor suspension to the nanocomposite. Moreover, Broadband Dielectric Spectroscopy (BDS) has been used to investigate the role of silane coating agents in the segmental dynamics of model nanocomposites. We show that the silane molecules can act as *plasticizers* in pure styrene-butadiene matrices, inducing a significant decrease of the glass transition temperature. We also prove that the chemical surface-modification of the fillers does not affect the segmental dynamics (α-relaxation) in nanocomposites, whereas the presence of "free" silane molecules in the polymer bulk can induce a detectable plasticization effect.

Impact de la modification de surface de nanoparticules sur la structure et la dynamique de nanocomposites silice-polymère

Les matériaux nanocomposites obtenus par la dispersion de charges nanométriques dans un polymère ont de nombreuses applications industrielles à cause de l'amélioration des propriétés des matrices. La dispersion des charges pendant le procès de préparation des nanocomposites est déterminée par les interactions entre charges et avec le polymère. L'état final de dispersion impacte les propriétés structurales, dynamiques et mécaniques du matériau.
Dans ce travail de thèse, nous proposons l'étude de nanocomposites produits par dispersion de billes de silice hydrophiles dans une matrice de polymère hydrophobe, i.e., styrene-butadiene (SB), couramment utilisé dans les pneumatiques. Nous avons notamment étudié l'impact des agents de recouvrement - des silanes réagissant avec la surface des charges – qui sont utilisés afin de promouvoir la compatibilité entre la silice et le SB.
Dans un premier temps, nous avons étudié des matériaux composites industriels simplifiés obtenus par l'incorporation de silice hautement dispersible dans le SB. En couplant des expériences de diffusion des rayons-X aux petits angles (DXPA) avec de la microscopie, nous avons montré que : i) la présence d'un catalyseur (DPG) amplifie l'effet de l'agent de recouvrement; ii) l'augmentation de la quantité de silane favorise la réduction de la taille des agrégats de silice. De plus, un système modèle équivalent au système industriel simplifié a été développé, mais avec une silice colloïdale. Nous avons mis au point une nouvelle méthode pour modifier la surface des billes de silice en suspensions dans en mélange eau/éthanol. Ces nanoparticules sont ensuite stabilisées dans le même solvant utilisé pour la dissolution du SB, le MEK. Enfin, le composite modèle est obtenu par évaporation du solvant. La dispersion des billes de silice greffées a été étudiée en suspension (i.e., dans le mélange eau/éthanol et MEK) et dans le nanocomposite, en couplant DXPA avec des simulations de Monte-Carlo inverse. Nous avons montré que la qualité de la dispersion dépend du type de silane utilisé et qu'elle est transférée du solvant (MEK) au composite. De plus, l'impact des agents de recouvrement sur les propriétés dynamiques (relaxation α) du système modèle a été étudié par spectroscopie diélectrique, BDS. Nous avons découvert que les agents de recouvrement peuvent plastifier le SB pur, en induisant une baisse significative de la température de transition vitreuse. Dans les composites, la modification de l'état de surface des billes par l'agent de recouvrement n'altère pas la relaxation α. Cependant, la présence de molécules de silane libres dans la matrice polymère du nanocomposite peut également induire un effet de plastification.